UNIVERSITY OF THE
WITWATERSRAND,
JOHANNESBURG

Petrogenesis and detailed geochemical and isotopic studies of the Epembe carbonatite and syenite rocks, NW Namibia

Mbili Tshiningayamwe

A thesis submitted to the Faculty of Science, University of the Witwatersrand, Johannesburg, in fulfilment of the requirements for degree of Doctor of Philosophy

School of Geosciences

Johannesburg, 2022

Declaration

I declare that this thesis is my own, unaided work. It is being submitted for the degree of Doctor of Philosophy at the University of the Witwatersrand, Johannesburg. It has not been submitted before for any degree or examination

(Signature of candidate)

31 March 2022

Abstract

Although many carbonatite occurrences world-wide show temporal and spatial association with silica under-saturated alkaline rocks (e.g. nephelinites, ijolites, nepheline syenites) their petrogenetic relationship is still a matter of debate. In the Epembe area of northwestern Namibia, there is an occurrence of a carbonatite associated with alkaline rocks. Such an occurrence provides an ideal opportunity to investigate their petrogenesis and the petrogenetic relationship between them if any. The rocks were studied using whole rock geochemistry, U-Pb geochronology, mineral and isotope geochemistry.

The Epembe Alkaline Carbonatite Complex (EACC) was emplaced along a fault zone into medium- to high-grade Palaeoproterozoic basement rocks of the Epupa Metamorphic Complex (EMC) and extends over a distance of 9 km in a south-easterly direction with a width of 1 km. Alkaline rocks constitute the main lithologies and are cross-cut by a calcite-carbonatite dyke. The alkaline rocks can be classified as syenite and nepheline-bearing syenites, with alkalic, metaluminous and ferroan affinities. The syenite occurs as a discontinuous intrusion which separates the nepheline syenite from the EMC, while the carbonatite cross-cuts the nepheline syenite body along strike. The syenite comprises alkali feldspar and clinopyroxene with accessory apatite and magnetite. The nepheline syenite comprises major to minor alkali feldspar, nepheline, biotite and cancrinite, while plagioclase, apatite, sphene, zircon, calcite and magnetite occur as accessory phases. The carbonatite consists of calcite, apatite, pyrochlore, pyroxene (aegirine), biotite, zircon, alkali feldspars and plagioclase in varying amounts. Based on zircon U-Pb dating, a $^{206}Pb/^{238}U$ weighted mean age of 1220 ± 3 Ma (2SE, MSWD = 1.3) was determined for the syenite emplacement, whereas two nepheline syenite samples give identical magmatic ages of 1209 ± 3 ($^{206}Pb/^{238}U$ weighted mean age, 2SE, MSWD = 1.1) and 1205 ± 13 Ma (concordia intercept age, 2SE, MSWD = 2). The nepheline syenite ages correspond with the concordia age of 1198 ± 5 Ma (2SE, MSWD = 1.1) of the carbonatite interpreted as magmatic. The nepheline-normative syenites define broadly linear trends in Harker plots consistent with evolution by fractional crystallization involving pyroxene and apatite. The rare earth element (REE) pattern of the syenite shows a negative Eu anomaly, consistent with plagioclase fractionation. The syenite

is characterized by the absence of a negative Nb anomaly on a Primitive Mantle (PRIMA)-normalized diagram with Ce/Pb and Nb/U ratios of 12 and 19, respectively, suggesting that it was not affected by crustal contamination during ascent and emplacement. The absence of a crustal signature indicates that the syenite is not related to the nepheline syenite by combined assimilation and fractional crystallization, and was likely emplaced as a distinct magma batch derived from the mantle. REE patterns of the nepheline syenite and carbonatite are coherent showing LREE enrichment relative to HREE. On a PRIMA-normalized multi-element diagram both the carbonatite and syenite display relative depletions of Zr, Hf and Pb and relative enrichment of Sr. Low Mg, Cr and Ni contents of the carbonatite and nepheline syenite suggest that these rocks crystallized from an evolved parental magma rather than a primitive mantle-derived melt. Geochemical similarities between the carbonatite and nepheline syenite also suggest that the Epembe carbonatite is not a product of immiscible separation between a carbonate and silicate melt. Instead, the carbonate may represent a melt fraction that formed after partial crystallization of the nepheline syenite.

Apatite grains from one syenite, six nepheline syenite and five carbonatite samples were examined using cathodoluminescence (CL) imaging, trace element and Sr-Nd isotope compositions as well as U-Pb geochronology. Syenite-hosted apatite is homogenous in CL and contains the highest concentration of REE (9189-44100 ppm) with light (L) REE enrichment (La_N/Yb_N = 4-91) relative to heavy (H) REE and negative Eu anomalies (Eu/Eu* = 0.4-0.9). These features are attributed to the formation of apatite in an evolved mantle-derived melt associated with plagioclase fractionation. Nepheline syenite-hosted apatite is also generally homogeneous in CL, while core-rim zoning and patchy textures are only observed occasionally. Both texturally homogeneous and core-rim zoned apatite are enriched in LREE (La_N/Yb_N = 32-94) relative to HREE, consistent with a magmatic origin. Core-rim zoned apatite is characterized by a rim-ward increase in REE concentrations accompanied by uniform Sr and Nd isotopic compositions, which can be attributed to the re-equilibration of early-formed apatite (core) with later infiltrating melt enriched in REE, causing the formation of apatite overgrowths (rims). Patchy apatite is depleted in Na, Y and REE, particularly the LREE (La_N/Yb_N = 4-19) and is enriched in Sr relative to apatite from other nepheline syenite, reflecting interaction with fluids (metasomatism). The strontium

isotope composition of metasomatic apatite and magmatic apatite is indistinct suggesting a magmatic origin of the fluids responsible for alteration. Carbonatite apatite is LREE-enriched (La_N/Yb_N = 24-161) relative to HREE and displays core-rim zoning in CL accompanied by a rim-ward increase in REE, attributed to mineral fractionation. No Eu anomalies (Eu/Eu* = 1) in chondrite-normalized REE patterns are observed in any apatite hosted by nepheline syenite and carbonatite. A LA-ICPMS U-Pb age of 1216 ± 11 Ma (MSWD = 4.3, 2 SE) for syenite apatite constrains emplacement of the syenite, while magmatic nepheline syenite apatite ages of 1193 ± 14 Ma, 1197 ± 17 Ma and 1194 ± 16 Ma (MSWDs < 4.0, 2 SE) have been determined. The Sr and Nd isotopic composition of apatite in syenite ($^{87}Sr/^{86}Sr_{(i)}$ = 0.7035-0.7048; $\varepsilon_{Nd(t)}$ = +2.5 to +3.2), nepheline syenites ($^{87}Sr/^{86}Sr_{(i)}$ = 0.7031-0.7037; $\varepsilon_{Nd(t)}$ = +1.5 to +4.4) and carbonatite ($^{87}Sr/^{86}Sr_{(i)}$ = 0.7031-0.7033; $\varepsilon_{Nd(t)}$ = 0 to +3.3) overlap, pointing to a common but heterogeneous mantle source, possibly involving HIMU and EMI mantle endmembers.

Lastly, cathodoluminescence (CL) imaging combined with trace elements (including REE) as well as Hf isotope compositions of zircon grains extracted from one syenite, five nepheline syenite samples and one carbonatite sample are presented. Carbonatite and syenite zircons are generally unaltered and characterized by steeply rising REE patterns in chondrite-normalized diagrams, with positive Ce anomalies (Ce/Ce* = 1-8). Syenite zircon further displays significant negative Eu anomalies (Eu/Eu* = 0.2-0.4) attributed to earlier plagioclase formation and fractionation. These features are consistent with zircon formation in a magmatic environment. In the nepheline syenite samples, two zircon types are recognized. Type 1 zircon is magmatic, with homogeneous-grey, unzoned and oscillatory-zoned domains in CL, while type 2 zircon is hydrothermally altered and displays a cloudy appearance in CL. Type 2 zircon is characterized by enrichment in LREE (101-853 ppm), Nb (97-339) and Ti (63-140 ppm) when compared to magmatic type 1 zircon (LREE = 17-93 ppm, Nb = 7-59 and Ti = 2-15 ppm). The Hf isotope composition of type 1 and type 2 zircon is indistinct suggesting that the fluids involved in zircon alteration were sourced from within the complex. The similarity of $\varepsilon_{Hf(t)}$ values in zircon from syenite (+0.5 ± 0.4 to +1.5 ± 0.4), nepheline syenite (+1.6 ± 0.3 to +2.7 ± 0.5) and carbonatite (+0.5 ± 0.4 to +1.9 ± 0.2) is consistent with the melts having been derived from a moderately depleted mantle.

The data presented in this study are best explained by partial melting of a heterogeneous mantle at ca. 1200 Ma, which resulted in the formation of an alkali basalt and a carbonated-alkali basaltic melt. The alkali basalt melt ascended first utilizing an existing fault system and evolved to form the syenite. Subsequently, the carbonated-alkali basaltic melt percolated upwards and differentiated to form the nepheline syenite and calcite-carbonatite. Finally, metasomatic interaction occurred between magmatic derived fluids and primary assemblages.

Acknowledgements

The Centre of Excellence for Integrated Mineral and Energy Resource Analysis (CIMERA) is thanked for funding this project.

I would like to thank Professor Fred Kamona for initiating this research as well as the Gecko mineral exploration company, particularly Rainer Ellmies, Matilde Nambahu and Kaarina Ndalulilwa for granting me access to the study area. Thanks are also extended to Doctor Teklay Mengist and Josiah Shilunga who offered academic support throughout the academic journey. I would also like to thank Caiphus Majola for assisting with sample preparation as well as Professor Alexander Ziegler for offering microprobe training. Thanks are extended to my parents, brothers and sisters for their continuous love, support, encouragement and prayers throughout this journey. Finally, I would like to thank my supervisors, Professor Robert Bolhar and Professor Paul Nex for their guidance during this study. This work wouldn't have been possible without their supervision. Thank you all.

Table of Contents

List of Figures

List of Tables

1. Introduction

1.1 Carbonatites and associated alkaline rocks

Carbonatites are defined as igneous rocks composed of more than 50 modal % carbonate (calcite, dolomite or ankerite) minerals (Woolley and Kempe, 1989). Carbonatites occur as both extrusive and intrusive igneous rocks (Le Bas, 1987). There are approximately 527 (compared to 330 in 1989: Woolley, 1989) known carbonatite occurrences worldwide ranging in age from Archean to the present-day, with more than half of these occuring in Africa (Woolley and Kjarsgaard, 2008). The following features characterize the spatial distribution of carbonatites (Woolley, 1989): (1) Many carbonatites are related to orogenic belts, including constructive and destructive plate boundaries, (2) carbonatites can be associated with oceanic fracture zones, (3) carbonatites commonly occur on uplifted or domed areas, which vary from tens to thousands of kilometers in diameter and (4) carbonatites are associated with major faulting. The majority of carbonatites occur as small intrusive complexes associated with alkaline silicate rocks, including nepheline syenite, ijolite and urtite (e.g. Le Bas, 1987; Harmer and Gittins, 1998). Few carbonatites are found together with peridotites, pyroxenites, group 1 kimberlites or lamprophyres (Bell et al., 1999).

Although many carbonatite occurrences world-wide show temporal and spatial association with silica under-saturated alkaline rocks, their petrogenetic relationship is still debated. Geochemical and isotopic compositions from various studies indicate that these rocks are originally mantle-derived (e.g. Harmer and Gittins, 1998; Wu et al., 2011; Zhu et al., 2017). Experimental studies and those of natural carbonatite-alkaline associations show that carbonatite magmas can be formed by direct partial melting of a carbonated mantle peridotite (Harmer and Gittins, 1998, Wallace and Green, 1998), or that carbonatites represent residual melts, fractionated from a nephelinitic parental magma (Gittins and Jago, 1998; Brassiness et al., 2005; Mitchell, 2005; Wang et al., 2014). Alternatively, carbonatites may be products of liquid immiscibility involving a carbonate saturated silicate melt (Lee and Wyllie, 1998; Bodeving et al., 2017).

An important question concerns the exact mantle source region and characteristics from which the carbonatite and associated alkaline rocks were derived. Alkaline magmas can form from the asthenospheric mantle by small degrees of partial melting (Fitton, 1987), or partial melting of a metasomatized, large ion lithophile element (LILE) and light rare earth element (LREE) enriched upper mantle (Dawson, 1987), or from the interaction of asthenospheric mantle-derived magma with the lithosphere during ascent (Menzies, 1987). The formation of the most evolved rock types of alkaline suites, such as syenites, can be by fractionation from alkali basaltic parents combined with input from continental crust (Foland et al., 1993; Jung et al., 2007), or by small degree partial melting of enriched lower continental crust (e.g. Drüppel el., 2007). Available isotope data indicates that carbonatites exhibit large isotopic variations, requiring a number of different sources ranging from enriched to depleted mantle located in the asthenosphere (Nelson et al., 1988; Bell and Simonetti, 2009) or in the subcontinental lithospheric mantle (e.g. Wu et al., 2011).

Despite carbonatite and alkaline rocks being volumetrically insignificant, these rocks have unique geochemical signatures, reaching significant concentrations of economically important minerals and elements (Fitton and Upton, 1987). For instance, carbonatites and associated rocks represent the main economic source of rare earth elements (REE) and niobium (Nb) worldwide, and are significant source materials for phosphate (Mariano, 1989; Smith et al., 2016). The importance of REE (particularly Nd, Pr and Dy) is related to their use in the production of high-technology devices, chemical catalysts, metal alloys, glass polishing and permanent magnets (for wind turbines) (Verplanck, 2017). Between 2010 and 2012, the People's Republic of China as the major producer of REE decided to stockpile its REE resources and ban the export of these elements (Paulick and Machacek, 2017). This action has led to an increased demand of REE and associated REE exploration activities in other countries, including Namibia.

1.2. Epembe Alkaline Carbonatite Complex (EACC)

The EACC was emplaced along a NW-trending fault zone within basement gneisses of the Epupa Complex EC), resulting in a linear structure measuring 9 km long and 1 km wide. It consists of

syenite, nepheline syenite, a carbonatite dyke, lamprophyre dykes and a fenite (Ferguson et al., 1975). The area is located in the Kunene region of Namibia, about 800 km north of the capital city, Windhoek. The nearest town is Opuwo, approximately 90 km south of the EACC. The EACC lies within EPL 3299 belonging to Gecko Exploration Pty Ltd. The main economic minerals are apatite (P, REE) and pyrochlore (Ta, Nb, U). Previous work around the EACC involved detailed geological mapping of the central parts of the complex (Bull, 2013), characterization of pyrochlore (Falshaw, 2012) and U-Pb dating of zircon (Littmann et al., 2000 in Drüppel et al., 2005; Simon et al., 2017). Kapuka (2019) investigated the distribution of REE using whole rock geochemistry, whereas fenitization processes associated with the emplacement of the complex were examined by Ferguson et al. (1975).

1.3. Apatite and zircon - geochemistry and geochronology

Apatite is a common accessory phase in carbonatites and associated rocks (Chakhmouradian et al., 2017; Decrée et al., 2020). The crystal structure of apatite accommodates a wide range of chemical substitutions (Pan and Fleet, 2002). Apatite typically forms early, but also crystallizes throughout magmatic differentiation, up to late-stage crystallization (Chakhmouradian et al., 2017), making it a good indicator for magma evolution (Bühn et al., 2001; Wang et al., 2014; Mitchell et al., 2017). Back scattered electron and cathodoluminescence imaging can reveal apatite textures, which in combination with trace element geochemistry allows the distinction between primary and secondary apatite (Broom-Fendley et al., 2017; O'Sullivan et al., 2020; Decrée et al., 2020). Compared to primary apatite, secondary apatite commonly occurs as turbid overgrowths and alteration patches accompanied by a decrease in REE (particularly LREE) relative to igneous apatite (Harlov et al., 2002; Decrée et al., 2020).

The LREE and Sr are among some of the elements that substitute in the apatite structure (Hograth, 1989; Pan and Fleet, 2002). Therefore, measurement of $^{87}Sr/^{86}Sr$ and $^{143}Nd/^{144}Nd$ ratios in apatite, corrected to a specific age (defined by zircon U-Pb geochronology) allows for the calculation of an epsilon value, which is a measure of the deviation of Sr or Nd from the Chondritic Uniform Reservoir (CHUR) at a particular age. This information pertains to the source from which

the rocks were derived. For instance, radiogenic Nd compositions (positive $\varepsilon_{Nd(t)}$) may indicate derivation from the Depleted Mantle (DM), whereas unradiogenic Nd composition (negative $\varepsilon_{Nd(t)}$) may imply derivation of the parental melt from an enriched source, such as continental crust or Enriched Mantle (EM).

Given the capability to host U and Th, apatite has also been employed in geochronology (e.g. Chew et al., 2011; Kirkland et al., 2018; O'Sullivan et al., 2021) and in high-temperature thermocronological studies, which assume closure temperatures of the U-Pb system of 350-550 °C (Chamberlain and Bowring, 2000; Shoene and Bowring 2007). Due to the relatively lower U-Pb closure temperature of apatite relative to zircon (> 900°C: Cherniak and Watson, 2000; Shoene and Bowring, 2007), apatite U-Pb ages may not be interpreted in terms of timing of magmatic activity. Instead, apatite U-Pb data yields critical information on the timing of thermal events and the cooling history of rocks (Gaweda et al., 2014; Kirkland et al., 2018). A challenging aspect of U-Pb apatite geochronology is the presence of significant and variable non-radiogenic Pb (or common lead, Pbc), which can be corrected in LA-ICPMS-based analysis (Chew et al., 2011).

Zircon is ubiquitous in the Earth's crust and is characterized by its low solubility in almost any melt and fluid compositions and durability during mechanical transport (Hanchar and Miller, 1993). However, zircon is not immutable to all major geological events (e.g. partial dissolution, metamictization, and overgrowth) and tends to preserve some of these events as distinct structural entities on pre-existing zircon grains observable in BSE and CL imaging (Hanchar and Miller, 1993; Corfu et al., 2003). Because of this, zircon quite commonly consists of distinct segments, each preserving a particular period of zircon formation (Corfu et al., 2003). Its capability to host significant amounts of U, Th, Hf and REE (Belousova et al., 2002a; Hoskin and Schaltegger, 2003) makes it useful in U-Pb geochronology and in the determination of magma sources by employing the Lu-Hf isotope system (Kinny and Maas, 2003). Therefore, combined imaging with chemical and isotopic analyses of different segments in zircon can provide detailed petrogenetic information (e.g. Pidgeon, 1998; Tichomirowa et al., 2013; Doroshkevich et al., 2021; Bolhar et al., 2021a).

1.4. Problem statement

Although few studies have been carried out around the Epembe Alkaline Carbonatite Complex (EACC), none of these studies focussed on constraining the magma sources of the Epembe syenite, nepheline syenite and carbonatite as well the genetic relationship between these rock types. This study presents detailed geochemical data to better constrain sources and processes that were involved at Epembe, utilizing whole rock geochemistry, mineral chemistry, geochronology and isotopic analysis. Thus, the research will provide new knowledge on the sources and evolution of Epembe syenite, nepheline syenite and carbonatites.

1.5. Aims and objectives

The aim of this study is to use whole rock geochemistry, accessory mineral (apatite, zircon) geochronology (U-Pb) and geochemistry (Sr, Nd and Hf isotopes and trace elements) in order to refine aspects of the petrogenesis of the Epembe syenite, nepheline syenite and carbonatite. Specifically, the objectives of the study are to:

- Examine the whole rock petrographic characteristics
- Determine the whole rock geochemistry
- Carry out U-Pb geochronology of zircon and apatite
- Determine the morphology and trace element content as well as Sr-Nd isotopic compositions of apatite
- Determine the morphology and trace element content as well as Hf isotopic compositions of zircon

1.6. Research questions

The following aims were addressed:

a. What are the apatite and zircon U-Pb ages and do these ages constrain specific magmatic or post-magmatic events?

b. Are there any geochemical variations among elements in nepheline syenite whole rock samples indicative of magma evolution by fractional crystallization?

c. Do the whole rock geochemical characteristics of the syenite carry fingerprints of crustal contamination of the source or during magma ascent and emplacement?

d. Do compositions of the carbonatite display systematic enrichments or depletions in certain elements when compared to that of the nepheline syenite in favour of magma origin by liquid immiscibility or fractional crystallization?

e. What are the textures and chemical composition of apatite and zircon as indicators of magma evolution and post-magmatic alteration?

f. What are the isotopic compositions of apatite and zircons as tracers of magmatic sources?

1.7. Structure of thesis

This thesis is divided into six chapters, with chapters 3, 4 and 6 forming parts of scientific articles in various stages of the publication process. The article corresponding to Chapter 3 has been submitted to the Journal of African Earth Sciences with manuscript number AES10110, while the article corresponding to Chapter 4 has been submitted to Lithos (manuscript number LITHOS10168). The article for Chapter 5 has been submitted to the South African Journal of Geology (manuscript number SAJG 2629). Chapter 1 outlines the scope of this study, provides necessary background and the identified research gaps and also outlines the approaches in addressing some unresolved issues. Chapter 2 summarises the geology of the Epupa, Kunene and the Epembe Alkaline Carbonatite complexes. Chapter 3 presents the field observations, petrographic and whole rock geochemical characteristics of the syenite, nepheline syenite and carbonatite. Chapter 4 is dedicated to the study of apatite textures, chemical composition, U-Pb geochronology and Sr-Nd isotopes, while Chapter 5 examines the textures, chemistry, U-Pb geochronology and Lu-Hf isotope composition of zircons. Chapter 6 provides a synthesis of the results and interpretations of Chapters 3, 4 and 5. Detailed methodologies are presented in each specific chapter. Appendices at the end of the thesis contain all analytical data produced in this study.

1.8. Contributions to written work

Chapter 3:

Mbili Tshiningayamwe, Robert Bolhar, Paul A. M. Nex, submitted to *Journal of African Earth Sciences*. Manuscript number: AES10110

Mbili Tshiningayamwe – 70% (collected samples, produced all written work, including all figures, performed mineral separation on all samples, obtained whole rock element data)

Robert Bolhar – 20% (main supervisor, assisted with sample collection, edited and corrected manuscript drafts)

Paul A. M. Nex – 10% (co-supervisor, edited and corrected manuscript drafts)

Chapter 4:

Mbili Tshiningayamwe, Robert Bolhar, Paul A. M. Nex, Henriette Ueckermann and Qing Chang submitted to *LITHOS*. Manuscript number: LITHOS10168 (revised)

Mbili Tshiningayamwe - 70% (produced all written work, including all figures, performed mineral separation on all samples)

Robert Bolhar – 15% (main supervisor, measured U-Pb and trace element compositions in apatite as well as data reduction, edited and corrected manuscript drafts)

Paul A. M. Nex – 5% (co-supervisor, edited and corrected manuscript drafts)

Henriette Ueckermann – 5% (assisted with Sr and Nd isotope analysis in apatite)

Qing Chang - 5% (assisted with Nd isotope analyses in apatite)

Chapter 5:

Mbili Tshiningayamwe, Robert Bolhar, Paul A. M. Nex submitted to *South African Journal of Geology*. Manuscript number: SAJG 2629 (under revision)

Mbili Tshiningayamwe – 70% (Produced all written work, including all figures, performed mineral separation on all samples)

Robert Bolhar – 20% (main supervisor, carried out trace element and U-Th-Pb measurements as well as data reduction, edited and corrected manuscript drafts)

Paul A. M. Nex – 10% (co-supervisor, edited and corrected manuscript drafts)

2. Geological setting

The Epembe Alkaline Carbonatite Complex intruded the Palaeoproterozoic Epupa Metamorphic Complex (EMC) basement (Fig. 2.1) (Ferguson et al., 1975). Brandt et al. (2003) sub-divided the EMC into two distinct units on the basis of metamorphic grade, namely the Orue and Epembe units, separated by E-W and NE-SW trending, sub-vertical shear zones. The Orue unit is characterized by upper amphibolite facies ortho- and paragneisses, while the Epembe unit consists of ultra-high temperature granulites. The Orue unit displays distinct banding and is predominantly composed of granitic gneisses, with lenses and bands of foliated amphibolite, from a few cm up to 10s of m in thickness with a tectonic foliation, which is generally parallel to banding (Brandt et al., 2003). Tegtmeyer and Kröner (1985) reported a zircon U-Pb crystallization age of 1795 ± 33/-29 Ma for a granitic augen gneiss belonging to the Orue unit. The Epembe unit is a fault-bounded, weakly-banded two pyroxene mafic granulite with some interlayered enderbitic, orthopyroxene-bearing felsic orthogneiss at its eastern and western ends (Brandt et al. 2003). Seth et al. (2003) obtained $^{207}Pb/^{206}Pb$ ages for magmatic zircon from the Epembe granulite ranging from 1810 ± 11 to 1635 ± 13 Ma. Metamorphic zircon ages of the Orue and Epembe Units are considerably younger, at 1340 - 1320 Ma and 1520 - 1510 Ma, respectively (Seth et al., 2003, 2005).

The Palaeoproterozoic basement rocks of EMC were intruded by massif-type anorthosites of the Kunene Complex (KC) (Fig. 2.1a), which covers an area of approx. 15 000 to 18 000 km^2 (Ashwal and Twist, 1994). The anorthosite is likely to be larger, though, since the eastern margin of the intrusion is covered by Kalahari sediments (Bybee et al., 2019). The anorthosite body is exposed on both sides of the Namibia-Angola border. On the Namibian side, it extends in a NW-SE direction consisting of tectonized, pervasive, pale anorthosite (Drüppel et al. 2005) and several subzones of unaltered leucotroctolite forming the so-called Zebra Mountains (Maier et al., 2013). The pale anorthosite is rich in orthopyroxene, especially in areas close to the granitic gneiss (Maier et al., 2013). On the basis of Nd, Sr and Pb isotopic data, the older pale anorthosite appears to be more crustally-contaminated than the leucotroctolite (Gleißner et al., 2011). The pale anorthosite possibly acted as a buffer, which prevented the leucotroctolite from extensive

crustal contamination (Gleißner et al., 2011). Other minor rocks include an irregular mass of anorthosite (> 10 m in diameter), several lamprophyres and fine-grained mafic dykes of unknown age (Maier et al., 2013). Contacts between the EMC and KC tend to be obliterated by ductile shear zones and brittle faults, except for some localities where the leucocratic anorthosite is in contact with the Orue unit, exposing the metamorphic aureole of garnet-cordierite-sillimanite hornfels with a garnet Pb-Pb age of 1341 ± 47 Ma (Seth et al., 2005). The emplacement age of the main body of the KC is well constrained at 1363 ± 17 Ma (U-Pb baddeleyite; Maier et al., 2013). More recently, Brower (2017) reported that the KC was emplaced during a series of magmatic events, with at least four age groups identified on the basis of remote sensing data combined with zircon and baddeleyite U-Pb geochronology. These groups are characterized by ages of 1438.4 ± 1.1 Ma, 1400.5 ± 1.3 Ma, 1390.4 ± 2.3 Ma and 1379.8 ± 2.0 Ma (Brower, 2017). In addition, Bybee et al. (2019) reported a U-Pb zircon age of 1500 ± 1.2 Ma for pegmatitic pods entrained from cumulate zones at the base of the crust. In the adjacent basement rocks close to the southernmost margin of the KC numerous NE trending alkali granites and syenodiorite dykes (40 km by 2-3 km) occur with a U-Pb zircon age of 1376 ± 2 Ma (Drüppel et al., 2007), corresponding to magmatic ages of the Kunene anorthosite. A U-Pb baddeleyite age of 1220 ± 15 Ma was determined for a troctolite body at Ohameramba proposed to be a late intrusive pulse of the Kunene anorthosite magmatism (Maier et al., 2013).

On the Namibian side, two groups of alkaline rocks are found along the margin of the Kunene Complex, mainly carbonatite dykes cross-cutting alkaline rocks. The two groups are collectively named the Epembe-Swartbooisdrif Alkaline Province due to possible genetic relationships (Ferguson et al., 1975). The Swartbooisdrif Alkaline Carbonatite Complex (SACC) is exposed about 35 km east of the EACC and consists of plugs and irregular bodies of altered nepheline syenite, syenite and ferrocarbonatite dykes**.** The EACC (Fig. 2. 1) is emplaced along a NW-trending fault zone within basement gneisses of the Epupa Complex, resulting in a linear shape and measures 9 km long with a width of 1 km. It consists of a syenite, nepheline syenite, a carbonatite dyke, lamprophyre dykes and a fenite (Ferguson et al., 1975). Nepheline syenite is the main rock type, while syenite occurs as minor intrusions which separates the nepheline syenite from the Epupa gneisses in places. The carbonatite cross-cuts the main nepheline syenite

body in a south easterly direction and measures 6.5 km long and 250 m wide, with a sub-vertical dip. Fine-grained, phyric lamprophyre dykes cut the nepheline syenite and the country rock gneiss. Most are short, between 20 and 60 cm wide and trend E-W or WNW. They increase in number closer to the fault zone and are most abundant near the northwestern end of the Epembe carbonatite (Menge, 1996). Syenite dykes of the Swartbooisdrif area have been dated at 1385 ± 5 Ma and 1335 ± 2 Ma using zircon, and are coeval with the Kunene anorthosite (Littmann et al., 2000, in Drüppel et al., 2005). In contrast, syenitic rocks from EACC are much younger and gave U-Pb zircon ages of ca. 1216-1213 Ma (Littmann et al., 2000, in Drüppel et al., 2007). Simon et al., (2017) obtained a SIMS U-Pb zircon magmatic age of 1184 ± 10 Ma for the main Epembe carbonatite dyke intrusion.

On the Angolan side, the KC has been intruded by alkaline and carbonatite rocks of the Lupongola Complex. (Alberti et al., 1999), which form a ring-shaped structure consisting of brecciated carbonatite pods, dykes and veins associated with syenites in discontinuous outcrops. A north to northwest trending dyke system (carbonatites and phonolites) cross-cuts the ring structure and extends for several kilometers in the gabbro-anorthosite country rocks (Alberti et al., 1999). The age of this carbonatite is unknown, but is assumed to be Mesoproterozoic based on Sr and Nd isotopic similarities with Precambrian carbonatites (Alberti et al., 1999). A summary of geochronological data is provided in Table 2.1.

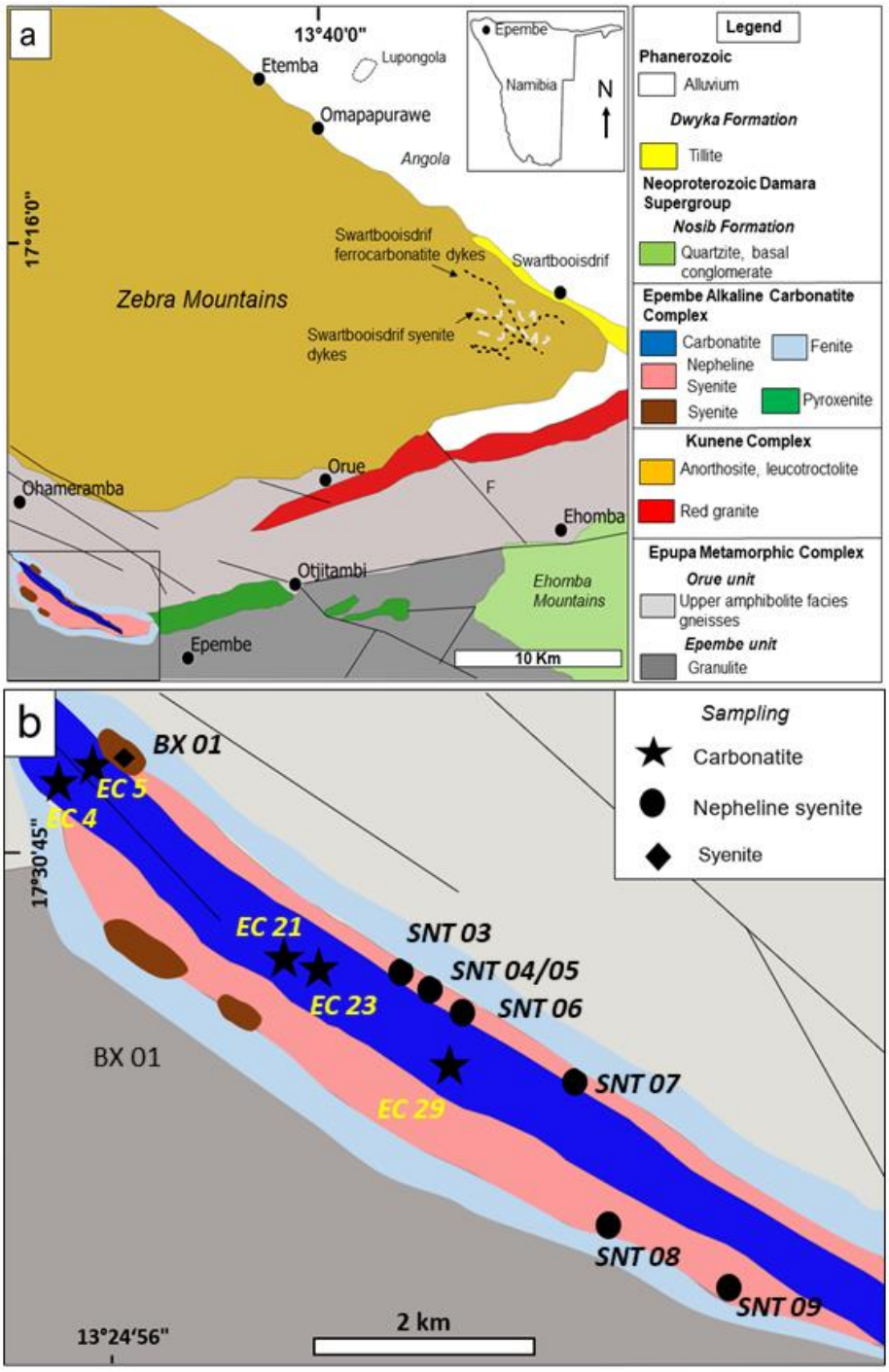

Fig. 2.1: (a) Geological map of the Namibian portion of the Kunene Complex and surrounding rocks modified from Ferguson et al. (1975), Menge (1998) and Brandt et al. (2003). (b) Sketch map of the study area (shown by rectangle in the lower left corner of Fig. 2.1a) showing sample locations.

Table 2.1: Summary of available magmatic ages for geological units around the study area

Geological time division	Unit	Lithology	Age (Ma)
Mesoproterozoic	Epembe-Swartbooisdrif Alkaline Province	Swartbooisdrif carbonatite	1140 - 1120, U-Pb Pyrochlore (Littmann et al., 2000 in Drüppel et al., 2005)
		Epembe carbonatite	1184 ± 10, U-Pb zircon (Simon et al., 2017)
		Epembe nepheline syenite,	1216 – 1213, U-Pb zircon (Littmann et al., 2000, in Drüppel et al., 2007)
	Other	Syenodiorite	1376 ± 2, U-Pb zircon (Drüppel et al., 2007)
	Kunene Complex	Troctolite	1220 ± 15, U-Pb baddeleyite (Maier et al., 2013)
		Deformed anorthosite	1363 ± 17, U-Pb baddeleyite (Maier et al., 2013)
		Leucotroctolitic rocks	1379.8 ± 2.0 zircon/baddeleyite (Brower, 2017)
		Swartbooisdrif syenite	1385 ± 5 and 1335 ± 2, U-Pb zircon (Littmann et al., 2000, in Drüppel et al., 2007)
		Leucotroctolitic rocks	1390.4 ± 2.3 zircon/baddelyite (Brower, 2017)
		Leuconorite	1400.5 ± 1.3 zircon/baddeleyite (Brower, 2017)
		Leucotroctolitic rocks	1438.4 ± 1.1 zircon/baddeleyite (Brower, 2017)
		Pegmatite pods	1500 ± 13 U-Pb (Bybee et al., 2019)
Palaeoproterozoic	Epupa Metamorphic Complex	Granitic augen gneiss	1795 ± 33/-29, U-Pb zircon, Tegtmeyer and Kröner (1985)
		Ultra-high grade granulites	1810 ±11 to 1635 ±13, $^{207}Pb/^{206}Pb$ zircon (Seth et al., 2003)

3. Petrology and geochemistry of the Epembe syenites and carbonatite, northwest Namibia

3.1. Introduction

The genetic relationship between carbonatites and alkaline rocks remains a matter of debate. A large body of geochemical and isotopic compositions indicate that they are originally from the mantle (e.g. Harmer and Gittins, 1998, Wallace and Green, 1988). Experimental results and studies of natural carbonatite and alkaline rock associations show that carbonatite magmas can form by partial melting of a carbonated mantle peridotite (Harmer, 1999; Harmer and Gittins, 1998; Wallace and Green, 1988). Alternatively, carbonatites may be residual melts fractionated from a nephelinite parental magma (Gittins and Jago, 1998; Brassiness et al., 2005; Wang et., 2014) or a product of liquid immiscibility of a carbonate-saturated silicate melt (Lee and Wyllie, 1998; Veksler et al., 2012; Bodeving et al., 2017). There is, however, no consensus on which of these models best explains the genesis of carbonatites, possibly because a single model cannot satisfactorily account for the wide range of compositions and associations displayed by carbonatites globally.

In northern Namibia, there is an occurrence of a carbonatite associated with alkaline rocks, in the Epembe area, and such an association provides an opportunity to investigate the possible relationship among these rock types. However, none of the previous work carried out involved a comparative study of the carbonatite and associated alkaline rocks. Existing studies include: a detailed investigation of the occurrence and compositions of pyrochlore from the northern tip of the carbonatite dyke (Falshaw, 2012), detailed mapping of the central portion of the dyke (Bull, 2013) and a geochemical investigation of REE distribution within the carbonatite dyke (Kapuka, 2019). Simon et al. (2017) presented SIMS U-Pb geochronological data of carbonatite zircon, while Ferguson et al. (1975) studied fenitization processes related to the emplacement of the complex.

The aim of the present study is to present petrological and geochemical data from the carbonatite and syenitic rocks in order to investigate the evolution of the complex and to evaluate the three models that have been proposed for the formation of carbonatites.

3.2. Methodology

Field work was carried out over period of two years during two visits. The first focused on the collection of carbonatite samples, whereas the second focused on sampling the associated syenite units. Prior to field work, a preparation phase involved a literature review of the geology of the area. Google earth and landsat imagery was used to investigate the nature of the terrain and routes around the study area.

The first geological field visit and sampling campaign was carried out from the 5th to the 14th of May 2018, while the second one was from the 2nd to the 4th of January 2020. A total of 30 carbonatite samples were collected along and across the 6.5 km long carbonatite dyke. The samples were collected at intervals of approximate 400 m along and 80 m across the strike of dyke although the lack of continuous outcrop meant greater distances between some samples. With regards to the syenites, a total of 8 samples were collected from the main syenite intrusion which is cross-cut by the carbonatite dyke. A list of all collected samples is provided in table 3.1. Although previous studies have recognized different carbonatite types/pulses based on geological mapping (Bull, 2013), textures and mineral phases (Falshaw, 2012; Simon et al. 2017), the major element geochemical data (Appendix 2, Fig. 3.6) of the 30 carbonatite samples collected are similar and thus the carbonatite is treated as a whole in this study, in order to avoid being repetitive.

Table 3.1: List of all collected samples and their GPS locations. UTM zone 33K.

Sample	Easting (m)	Southing (m)	Rock type
EC1	331710	8063052	carbonatite
EC2	331772	8063102	carbonatite
EC4	331939	8063015	carbonatite
EC5	331960	8063086	carbonatite
EC6	331991	8063147	carbonatite
EC7	332117	8062730	carbonatite
EC8	332169	8062780	carbonatite
EC9	332210	8062846	carbonatite
EC10	332422	8062566	carbonatite
EC11	332524	8062456	carbonatite
EC12	332593	8062513	carbonatite
EC13	332805	8062036	carbonatite
EC14	332870	8062120	carbonatite
EC15	332780	8061810	carbonatite
EC16	332876	8061836	carbonatite
EC17	333330	8061572	carbonatite
EC18	333542	8061799	carbonatite
EC19	333565	8061233	carbonatite
EC20	333801	8061621	carbonatite
EC21	333866	8061380	carbonatite
EC22	334085	8061126	carbonatite
EC23	334119	8061198	carbonatite
EC24	334163	8061265	carbonatite
EC25	334437	8060843	carbonatite
EC26	334514	8060887	carbonatite
EC27	334514	8060887	carbonatite
EC28	334977	8060665	carbonatite
EC29	335046	8060756	carbonatite
EC30	335434	8060442	carbonatite
EC31	335480	8060534	carbonatite
BX 01	331818	8063271	syenite
SNT 03	334335	8060999	nepheline syenite
SNT 04	334728	8060986	nepheline syenite
SNT 05	334470	8061146	nepheline syenite
SNT 06	334469	8061155	nepheline syenite
SNT 07	334803	8060931	nepheline syenite
SNT 08	336120	8060047	nepheline syenite
SNT 09	336422	8059884	nepheline syenite

3.2.1. Whole rock geochemistry

Samples were crushed using a jaw crusher to 3 to 4 cm diameter and then milled to very fine powders using a rotary swing mill at the University of the Witwatersrand (Wits). Acetone was used to clean the equipment in between samples in order to avoid contamination. Prior to crushing, weathering on samples was removed using a rock cutting machine. Samples were analyzed for major and trace element concentrations in the Earthlab at Wits. Concentrations of major element oxides were determined using the Norrish Fusion 1 technique using in-house correction procedures and a Panalytical (Philips PW2404) X-ray fluorescence spectrometer. The elements were fused using Johnson Matthey Spectrolflux 105 at 1100 °C, and raw data corrected using in-house software. Standard calibrations were made up using synthetic oxide mixtures and certified reference materials (CRMs) as well as in-house standards. CRMs include USGS and NIM (South Africa) series, namely: GSP-2, BCR2, W-2, PCC1, BHVO2, AGV2 and G2 DTS1, NIM-S, NIM-N, NIM-G, NIM-P, NIM-D. All the standards are used as calibrations for initial runs and then analyzed as unknowns. For preparation of fusion disks and glass beads, 0.35 g of sample powder and 2.5 g of lithium tetra-borate flux were used. Precision is taken as 1 % for elements with concentrations > 5 wt% and 5 % for elements with concentrations < 5 wt%. Trace elements were determined using the Perkin Elmer DRC-e Inductively Coupled Plasma Mass Spectrometry (ICP-MS) and analysed against certified primary solution standards. International reference materials AGV-2, BCR-1 and BR-1 were analysed with every run. Agreement to accepted values of the standards was better than 10 % for all elements and in many cases better than 5 %. Dissolution of 50 mg of sample was carried out with high purity HF-HNO_3 using a MARS microwave digester. Using the microwave digester allow to dissolve refractory minerals (common in these samples) compared to using an open beaker or hotplate.

3.3. Results

3.3.1. Geological field observations

Most of the study area is covered by gravel and vegetation (Fig. 3.1a). The carbonatite forms linear hills, roughly 20 m above the surrounding area. In comparison to the carbonatite, the

syenitic rocks are less well-exposed and occur as low-lying outcrops together with the basement rocks and fenites.

There are compositional and textural variations within the syenitic rocks (Fig. 3.1. b-g), although the most common variety is a light grey medium-grained rock. Other textural varieties comprise pegmatites, glomeroporphyritic syenites, pegmatitic zones (Fig. 3.1c) and banded types. Pegmatites form small bodies measuring 5 m by 3 m in size, whereas pegmatitic zones and glomeroporphyritic textures are found within the main syenite body. The banded syenite occurs towards the south-eastern end of the intrusion and is characterized by light and dark bands with an equigranular medium-grained texture. Reddish coloration resulting from Fe-oxide staining was also observed on the surface of some parts of the intrusion. Since the main medium-grained intrusion does not appear to be foliated, it is not possible to measure the attitude of these rocks. Contacts with the basement rocks were not observed. However, the syenitic rocks display sharp contacts with the carbonatite. At some contacts, the syenite has been brecciated by the carbonatite emplacement (Fig. 3.2a). In addition, carbonatite veins of variable sizes (up to 5 cm wide) and orientation penetrate the syenites and sometimes these carbonatite veins show chilled margins.

The carbonatite is heterogeneous, both in color, texture and mineralogy (Fig. 3.2. a-h). Towards the south-eastern end of the dyke, the carbonatite thins into several smaller carbonatite dykes parallel to the main carbonatite body extending into the country rocks. Color variations include white, pink and grey with pink being dominant. Occasionally, there is a brown ferriginous staining caused by weathering of iron oxides. The texture varies from fine- to medium-grained mainly consisting of calcite indicating that it is a calcite carbonatite. In some parts, the carbonatite contains silicate and carbonate rock inclusions (Fig. 3.2c, d). Accessory minerals, such as pyroxene, apatite, biotite and zircon, are visible on the outcrop or in hand specimens possibly due to their slow rate of weathering compared to calcite. Late-stage calcite veins are observed cross-cutting the carbonatite throughout. These veins vary in width up to 2 cm and appear as unoriented, anastomosing veinlets exploiting any zones of weakness in the carbonatite host.

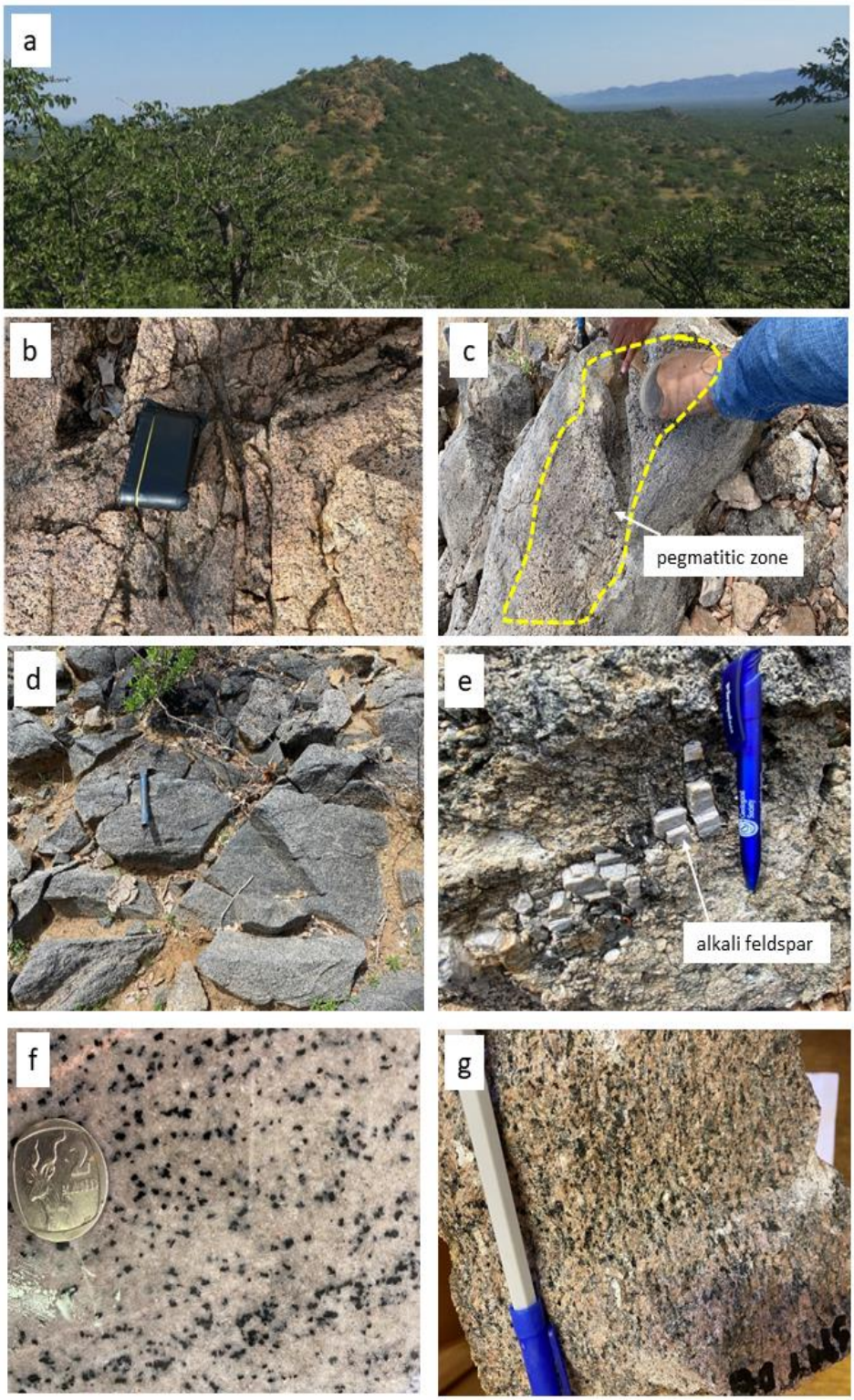

Fig. 3.1: Field outcrops (a-e) and hand specimen photographs (f, g). (a) Epembe carbonatite hills (photo taken looking north-west). (b) Reddish syenite. (c) Pegmatitic domain in a grey syenitic

rock. (d) Dark grey colored fine-grained outcrop. (e) Alkali feldspar glomerocrysts in syenitic outcrop. (f) Medium grained biotite rich syenite, sample SNT 03. (g) Very coarse grained syenitic sample. Sample SNT 06.

Fenites, defined as aureoles of high temperature altered country rocks found in close spatial relationship with carbonatites and alkaline rocks (Elliot et al., 2018), have been observed at Epembe. This fenitization (e.g. Fig. 3.2h) is irregularly developed around the carbonatite and syenitic rocks, although absent in some areas. Fentized country rocks display a brick red colour. Both the syenites and carbonatites display a similar style of metasomatism, which can extend up to 1 km into the surrounding rocks. Fenitization is highest close to the syenite and carbonatite and these areas show development of shearing and brecciation. Textural changes associated with fenitization include the replacement of gneissic foliation by a more massive texture. Mineralogical changes during fenitization involves the disappearance of quartz and an increase in the abundance of mafic minerals. Biotite is altered to chlorite, while hornblende is altered to chlorite and epidote (Ferguson et al., 1975).

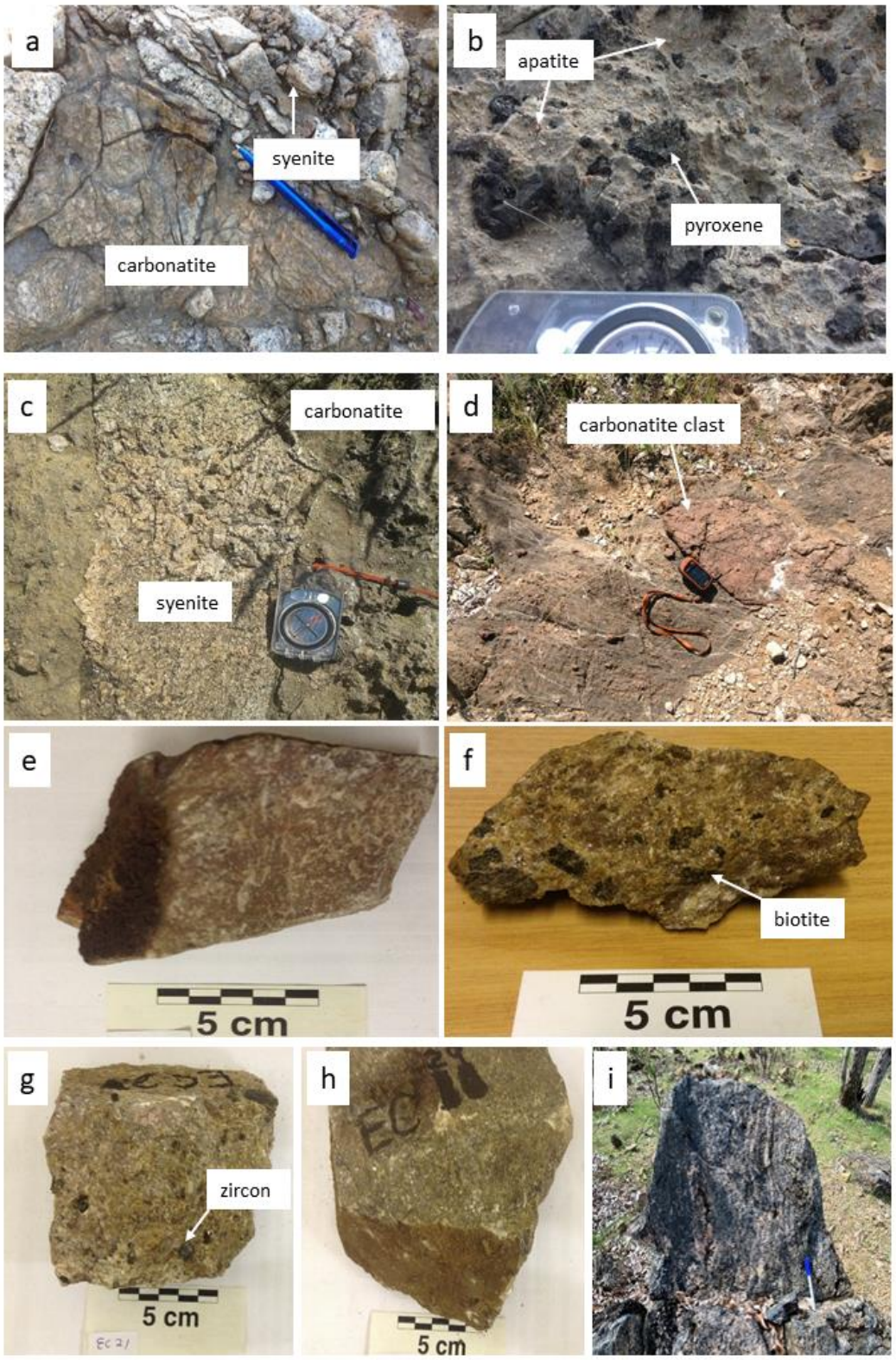

Fig. 3.2: Field outcrops (a-d) and hand specimen (e-h) photographs of the Epembe carbonatite and fenite (i). (a) Brecciated syenite near the contact with the carbonatite. (b) Apatite and

pyroxene grains on weathered carbonatite surface. (c) Syenitic xenolith in carbonatite. (d) carbonatite with carbonate clast. (e) Carbonatite sample EC 4. (f) Carbonatite sample EC 5. (g) Carbonatite sample EC 21. (h) Carbonatite sample EC 23.

3.3.2. Petrography

Petrographically, there are textural variations within the syenitic rocks, but a medium-grained texture is the most common. The mineral assemblage comprises major to minor alkali feldspar, nepheline, biotite and cancrinite, while plagioclase, apatite, sphene, zircon, calcite and magnetite occur as accessory phases (Fig. 3.3a-d). Zircon and apatite are rarely visible under the petrographic microscope and their presence was confirmed by mineral separation. Alkali feldspar is the dominant mineral and occurs as euhedral, anhedral and subhedral elongated grains with a grain size of < 1 to > 5 mm. Some alkali feldspar grains display embayments on the edges. Parallel alignment of elongated alkali feldspar is also observed in one sample (Fig. 3.3a). Most of the alkali feldspar grains show cross-hatched twinning, while a few show carlsbad twinning. Perthitic exsolution textures are common in these alkali feldspars and they can be grouped as plate, spindle, sinous and braided types. Medium-grained anhedral and subrounded nepheline is usually disseminated or occurs as interstitial grains between alkali feldspars. Nepheline can also be tabular or elongated in shape. Coarser-grained nepheline is intimately associated with alkali feldspar where it appears to penetrate the alkali feldspars. Biotite with a grain size of 1 to 4 mm is characterized by flaky, anhedral and subhedal grain shapes. Biotite may occur in clusters, where grains display a mosaic arrangement but are mostly disseminated within the alkali feldspar matrix. Biotite sometimes contains inclusions of alkali feldspar or may occupy interstices between alkali-feldspars. Euhedral to subhedral sphene up to 3 mm in size is observed in nepheline syenite sample SNT 08 (Fig. 3.3c), where it appears as scattered grains. Plagioclase is found as isolated subhedral grains up to 1 mm in length (Fig. 3.3b). Anhedral calcite occupies interstices between alkali feldspar. Apart from the nepheline-bearing syenites, one syenite sample (BX 01) collected towards the north-eastern part of the carbonatite dyke shows somewhat different mineral abundances when compared to the nepheline syenites. It is medium-grained, with a granular texture and comprises alkali feldspar and anhedral (up to 8 mm)

pyroxene (aegirine) (Fig. 3.3d), with inclusions of magnetite and elongated apatite. In this sample no biotite was observed.

The textural evolution of the carbonatite is diverse, however, the mineralogy is generally simple. The typical major and minor mineral assemblage of the carbonatite samples includes calcite, apatite, pyrochlore, pyroxene (aegirine), biotite, zircon and alkali feldspars and lath-shaped plagioclase (Fig. 3.3e-h). Monazite and magnetite are present as accessory phases. Magmatic calcite occurs in the samples, as a fine to/or medium-grained matrix, with a modal abundance of 64 to 83 vol% attesting that the Epembe carbonatite is a calcite-carbonatite. Calcite can also occupy interstices between apatite and pyrochlore cumulates. Porphyroblastic (core and mantle) structures are common in these samples and are characterized by twinned calcite porphyroblasts fringed by smaller calcite grains devoid of twinning (Fig. 3.3f). Twin lamellae in the porphyroblasts are sometimes bent. In hand specimen late-stage calcite veins are observed cross-cutting the carbonatite. The veins appear as un-orientated, anastomosing veinlets up to 2 cm wide, along planes of weakness. Apatite is the second most abundant phase occurring throughout the carbonatite, with ovoid, elongate, euhedral hexagonal and subhedral grain shapes (Fig. 3.3e, g). On average, the grain size of apatite is 0.5 mm. The apatite grains are disseminated in a calcite matrix or display a flow texture. Occasionally apatite occurs in clusters and as inclusions within pyrochlore and zircon. Pyrochlore is brownish or opaque with subhedral shapes (and a dark rim) dispersed in a calcite matrix. Most of the pyrochlore displays an intimate association with apatite and aegirine. Pyrochlore grain size is usually < 1 mm, but larger grains up to 6 mm are also observed. Zircon occurs as disseminated fine- to medium-sized grains with subhedral and euhedral grain shapes (Fig. 3.3g). Mineral inclusions of calcite are common in zircon. Biotite appears as dark or brownish large grains in clusters with a basal cleavage, which is in some cases deformed. Some biotite and monazite are very fine-grained and were observed during BSE examination. These biotites form elongate grains up to 200 µm occupying interstices between apatite and calcite. Monazite occurs as bright, anhedral grains disseminated within the matrix or around apatite. Magnetite occurs as fine-grained opaque grains, which often occupy micro-fractures. Alkali-feldspars occur as dispersed anhedral grains (Fig. 3.3h) or form globular structures which are up to 6 mm in diameter. Xenoliths of syenitic rocks in the carbonatite occur

as rounded, elongated and angular blocks wrapped in a flow texture. The xenoliths vary in size from ~15 cm to up to half a meter in length in areas close to the contact with the country rocks. A summary of the studied samples and estimated mineral modal abundances is presented in Table 3.1.

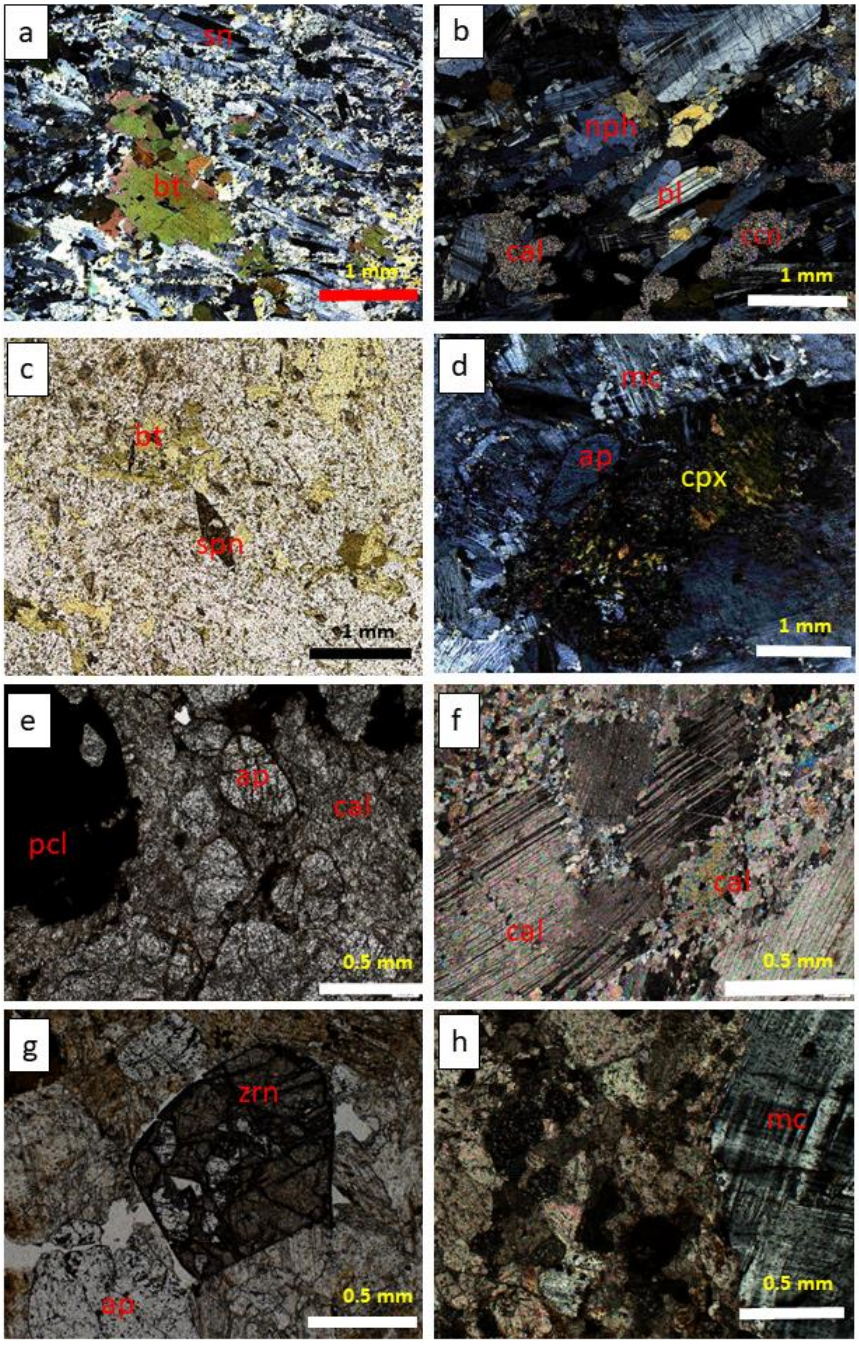

Fig. 3.3: Selected thin section microphotographs of the Epembe nepheline syenite (a, b, c), syenite (d) and carbonatite (e, f, g, h). (a) Parallel alignment of simple-twinned alkali feldspar in sample SNT 03, XPL. (b) Nepheline syenite sample SNT 07 showing plagioclase, XPL. (c) Nepheline syenite sample SNT 08 showing euhedral sphene and anhedral biotite, PPL. (d) Syenite sample BX 01, XPL. (e) Apatite and pyrochlore within a calcite matrix, sample EC 4, PPL. (f) Calcite displaying core and mantle structure, sample EC 5, XPL. (g) Carbonatite sample EC 21 showing euhedral fractured zircon with apatite inclusions, PPL. (h) Large microcline grain in carbonatite EC 29, PPL. Abbreviations: mc=microcline, sa=sanidine, pl=plagioclase, cpx=clinopyroxene, bt=biotite, spn=sphene, nph=nepheline, ccn=cancrinite, cal=calcite, ap=apatite, pcl=pyrochlore, zrn=zircon.

Table 3.2: Simplified description of the studied samples, mineral modal abundances (in percent) and GPS coordinates.

Location		Texture	alkali feldspar	nepheline	biotite	clinopyroxene	cancrinite	calcite	apatite	pyrochlore	zircon	accessory phases
	UTM zone 33K		vol (%)	vol (%)	vol (%)	vol (%)	vol (%)	vol (%)	vol (%)	vol (%)	vol (%)	
BX 01	331818 m E 8063271 m S	Pink, medium grained	90	-	-	10	-	-	-	-	-	Ap, Mag
SNT 03	334335 m E 8060999 m S	Grey, medium grained	85	5	10	-	-	-	-	-	-	Ap
SNT 04	334728 m E 8060986 m S	Grey, medium grained	75	10	5	-	10	-	-	-	-	Ap, Zir, Pl
SNT 05	334470 m E 8061146 m S	Grey, medium grained	80	5	5	-	10	-	-	-	-	Ap, Zir
SNT 06	334469 m E 8061155 m S	Pink, very coarse grained	70	5	10	-	15	-	-	-	-	Ap, Zir, Cal
SNT 07	334803 m E 8060931 m S	Grey, medium grained	70	15	5	-	10	-	-	-	-	Ap, Zir, Pl, Cal
SNT 08	336120 m E 8060047 m S	Grey, medium grained	70	15	15	-	-	-	-	-	-	Sph
SNT 09	336422 m E 8059884 m S	Grey, medium grained	75	5	10	-	10	-	-	-	-	Ap, Zir
EC 4	331939m E 8063015m S	Pink, fine grained	-	-	-	-	-	83	14	3	-	Mag
EC 5	331960m E 8063086m S	Pink, porphyroblastic	-	-	4	4	-	11	12	13	-	-
EC 21	333866m E 8061380m S	Pink, equigranular medium grained	-	-	15	-	-	64	19		2	-
EC 23	334119m E 8061198m S	Grey, equigranular medium grained	-	-	-	6	-	74	20	-	-	Mag
EC 29	335046m E 8060756m S	Grey, fine grained	6	-	3	-	-	74	17	-	-	Mnz

Abbreviations: Ap=apatite, Zir=zircon, Pl=plagioclase, Mag=magnetite, Cal=calcite, Sph=sphene, Mnz=Monazite

3.3.3. Major element geochemistry

Whole rock geochemical results of the studied samples are presented in Appendix 2. Using the TAS (total alkalis vs silica) plutonic classification diagram of Middlemost (1994), the samples overlap the fields of foidolite, foid syenite, foid monzosyenite and syenite (Fig. 3.4a). Based on the petrographic observations, the main foid mineral is nepheline and therefore these rocks are all referred to as nepheline syenites. The nepheline syenites have a limited SiO_2 range (48-52 wt%). The low alkali content (K_2O: 6.3-8.7 wt%; Na_2O: 3.3-8.3 wt%) relative to Al_2O_3 (18-21 wt%) results in the nepheline syenites being classified as metaluminous (Fig. 3.4b). The CaO (3-6 wt%) content is variable, whereas MnO (0.06-0.1 wt%), TiO_2 (0.3-0.9 wt%) and P_2O_5 (0.1-0.9 wt%) concentrations are less variable. The syenite sample BX 01, is broadly geochemically similar to the nepheline syenites, however, it is characterized by relatively higher SiO_2 (59 wt%) and lower Al_2O_3 (18 wt%) and CaO (2.6 wt%). The magnesium number (Mg# = atomic Mg/atomic Mg + Fe *100) is 0.20 to 0.29 for the nepheline syenites, while it is 0.22 for the syenite sample. Based on the geochemical characteristics, the syenitic samples are further classified as ferroan rocks (Fig. 3.4c: after Frost et al., 2001). Using the Fe-index and modified alkali index of Frost et al. (2001), all the samples are classified as alkalic rocks (Fig. 3.4d). Compositional variability is displayed in Harker diagrams (Fig. 3.5). Despite the limited range of SiO_2 content some systematic variability is observed. The oxides CaO, MgO, Fe_2O_3 and P_2O_5 tend to decrease with increasing SiO_2 abundance, whereas K_2O + Na_2O and Al_2O_3 tend to increase with increasing SiO_2 among the nepheline syenites. Titanium (not shown) is not correlated with SiO_2.

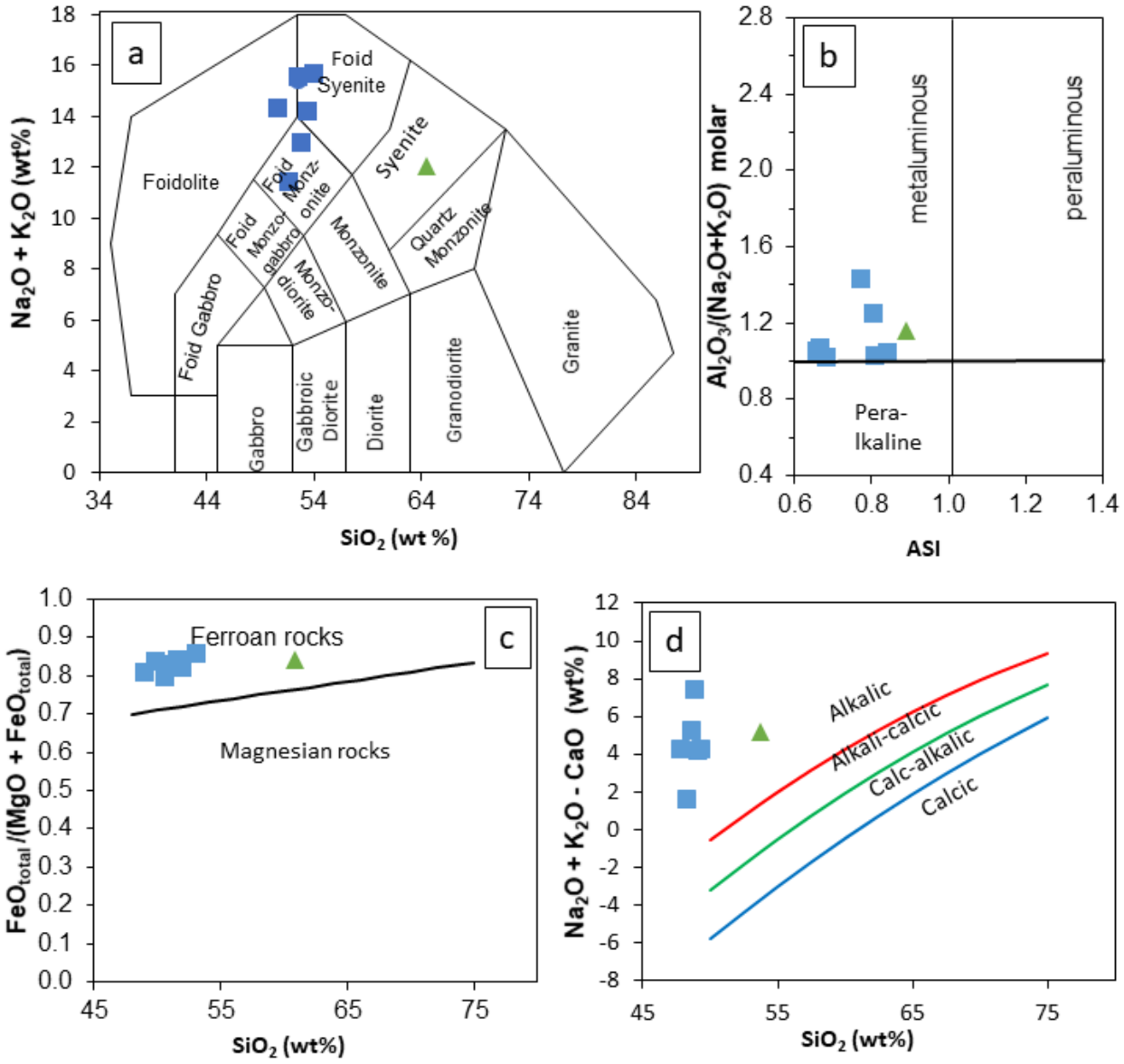

Fig. 3.4: Geochemical classifications for the Epembe syenitic rocks. (a) Total alkalis (Na_2O+K_2O) vs. SiO_2 plot after Middlemost (1994). (b) Shand's (Shand, 1927) alkalinity index [plot of $Al_2O_3/(Na2O+K_2O)$molar vs. $Al_2O_3/(Na_2O+K_2O+CaO)$molar]. (c) Plot of $FeO_{total}/(MgO + FeO_{total})$ vs. SiO_2 after Frost et al. (2001). (d) Plot of the modified alkali-lime index Na_2O+K_2O-CaO vs. SiO_2 after Frost et al. (2001). Symbols: blue filled squares (nepheline-bearing syenite), green filled triangle (syenite)

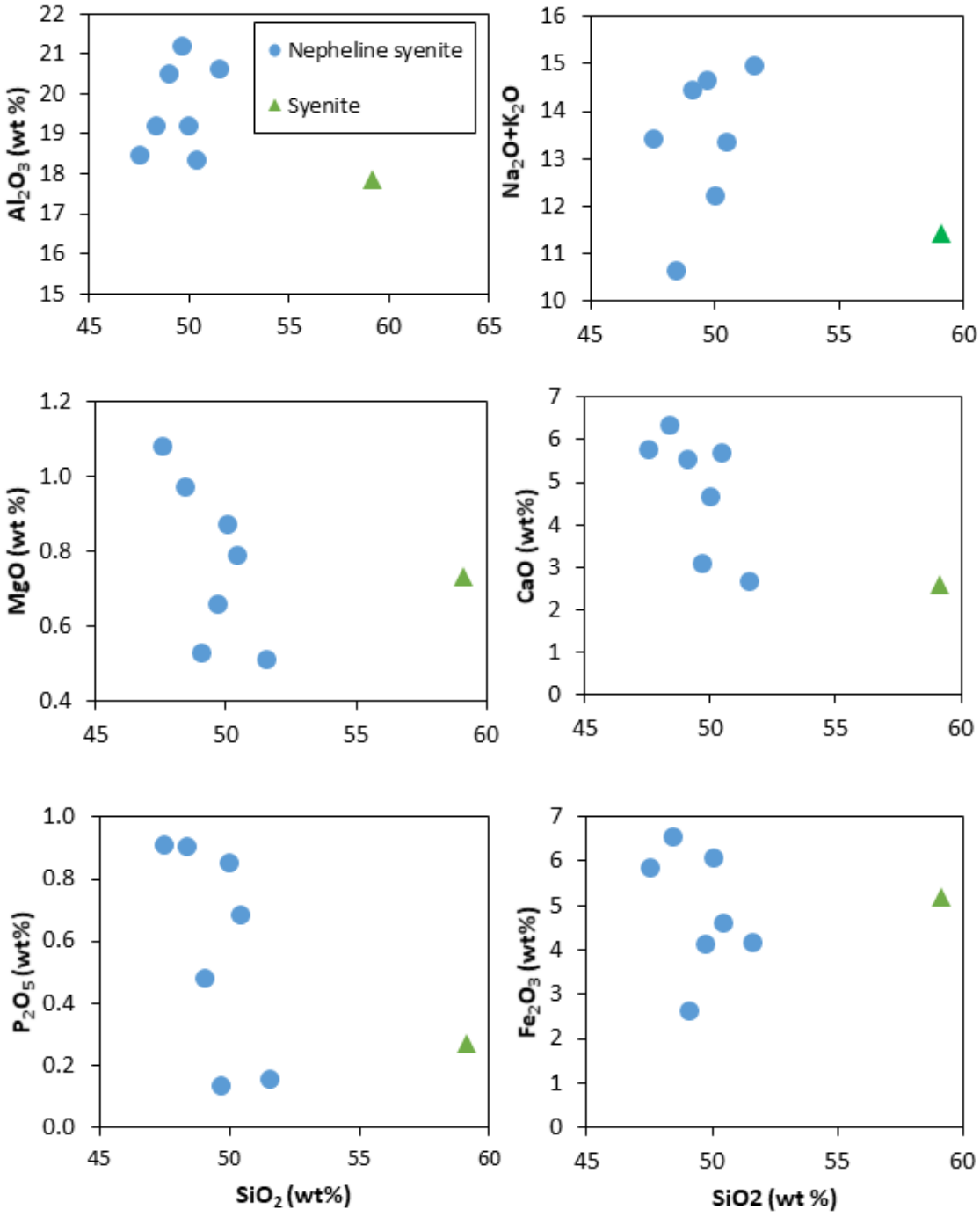

Fig. 3.5: Selected major elements vs. SiO_2 for the Epembe syenitic rocks

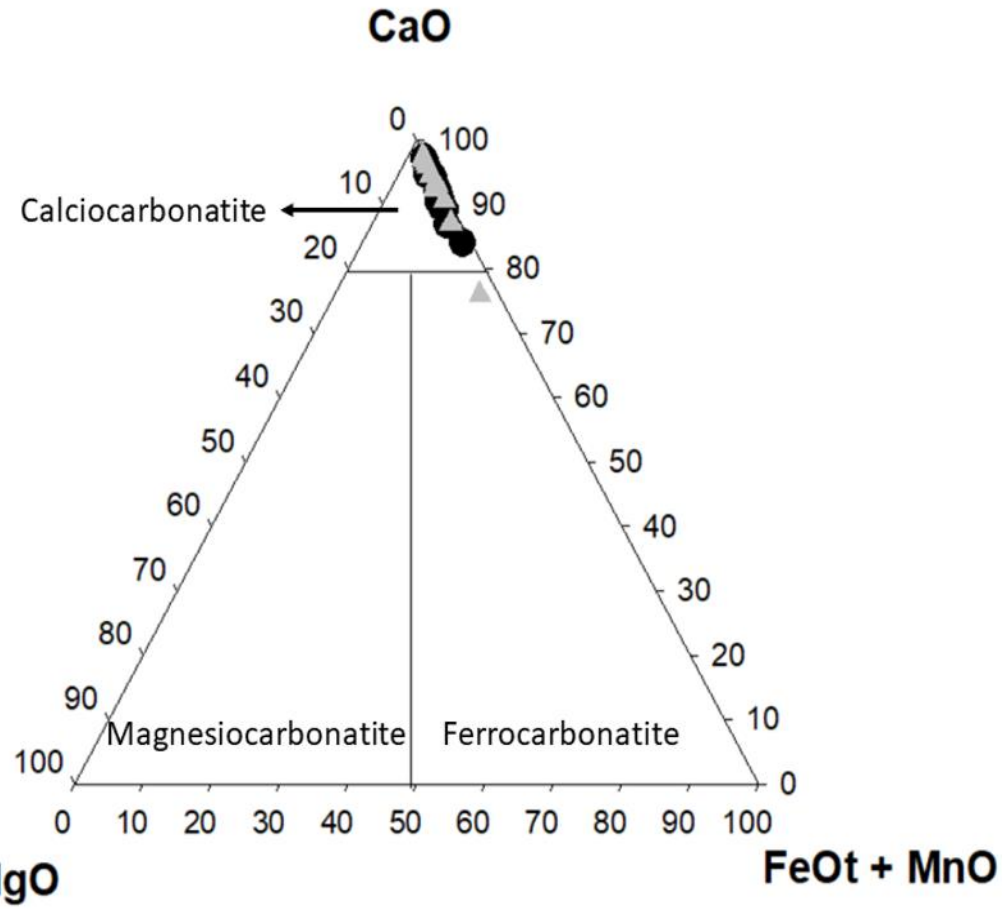

FIg. 3.6: Ternary geochemical classification diagram for carbonatites (after Woolley and Kempe 1989). Black filled circles represent data from this study and grey triangles represent data from Kapuka (2019).

3.3.4. Trace element geochemistry

Based on a literature survey, this study presents the first trace element data for the Epembe syenitic rocks. In a PRIMA-normalized multi-element diagram (Fig. 3.7), the Epembe nepheline syenite and carbonatite display similar trace element patterns for certain elements such as Pb, Sr, Hf and Zr. Strontium shows positive anomalies, whereas Pb, Hf and Zr display negative anomalies. Some variability is observed for Th, U, Nb and Sn in the nepheline syenite and carbonatite samples. The elements Cs, Rb and Ba are enriched in the nepheline syenite compared to the carbonatite by up to an order of magnitude. Conversely, Sr and Pb concentrations are

enriched in the carbonatite (Sr = 4242-11261 ppm, Pb = 8-23 ppm) relative to the nepheline syenite (Sr = 1503-2510 ppm, Pb = 1-4 ppm), while Zr and Hf concentrations are similar for both the carbonatite and syenite. Although variable, U, Th and Nb appear to be enriched in the carbonatite relative to the nepheline syenite samples. The syenite sample (BX 01) displays a similar PRIMA-normalized multi-element pattern with the nepheline syenite samples, however, the syenite lacks significant Pb and Sr anomalies. Most of the trace elements show varying uncorrelated contents within the syenitic rocks (Fig. 3.8), Rb, Sr, Nb and Zr are not correlated with SiO_2.

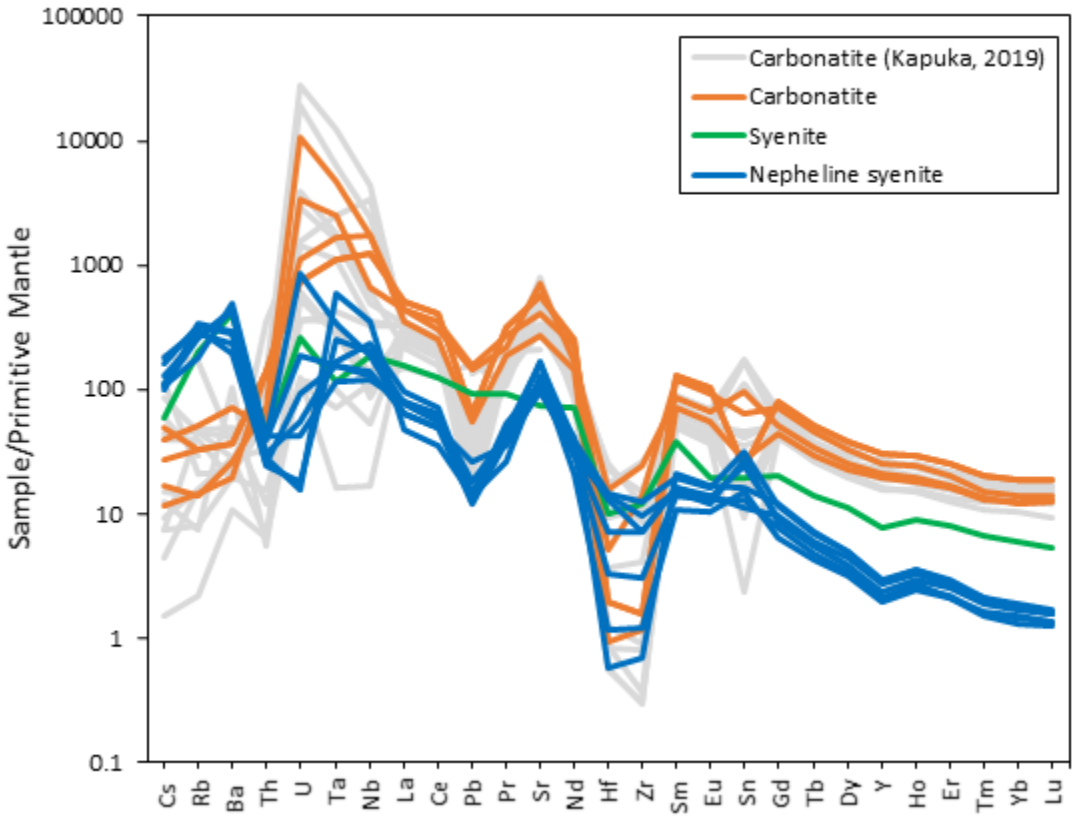

Fig. 3.7: Primitive Mantle-normalized multi-trace element patterns for Nepheline syenite, syenite and carbonatite samples from Epembe. Normalization values are from Lyubetskaya and Korenaga (2007).

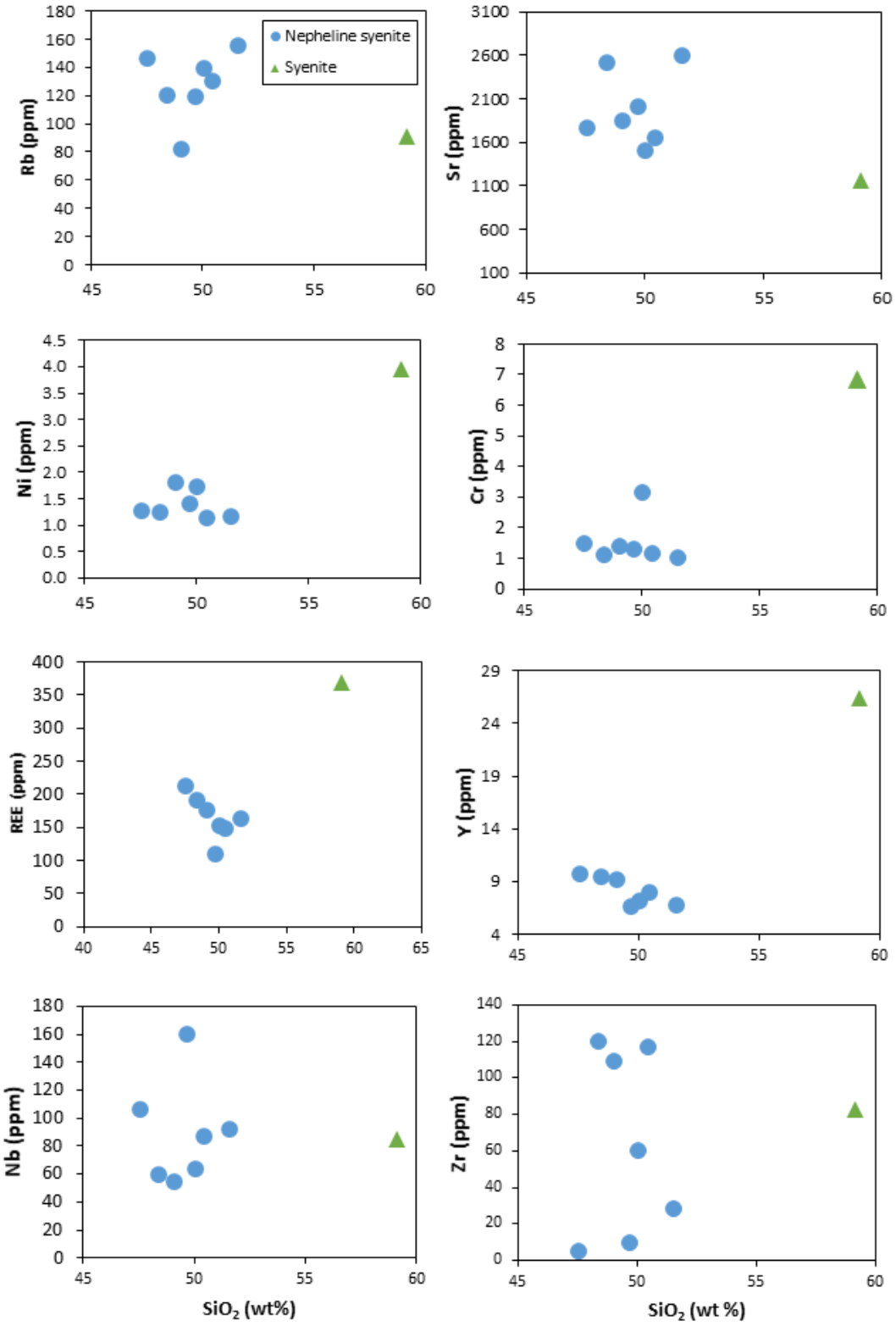

Fig. 3.8: Selected trace elements vs. SiO_2 for the Epembe syenitic rocks

3.3.5. REE geochemistry

In a chondrite-normalized REE diagram (Fig. 3.9), the Epembe nepheline syenite and carbonatite samples display coherent REE patterns. Among the different rock types, the carbonatite shows the strongest REE enrichment (REE (t) = 767-1248 ppm, where t = total), followed by the syenite (REE(t) = 369 ppm) and then the nepheline syenite (REE(t) = 110-214 ppm). The carbonatite, nepheline syenite and syenites samples are all light (L) REE enriched relative to heavy (H) REE with La_N/Yb_N ratios of 25-35, 31-53 and 26, respectively. The Eu anomalies ($Eu/Eu^* = Eu_N/(0.5Sm_N + 0.5Gd_N)$) are absent in carbonatite and nepheline syenite samples ($Eu/Eu^* = \sim 1$), while the syenite displays a minor negative Eu anomaly ($Eu/Eu^* = 0.7$). Total REE content appears to decrease with increasing SiO_2 content among the nepheline syenite samples (Fig. 3.8).

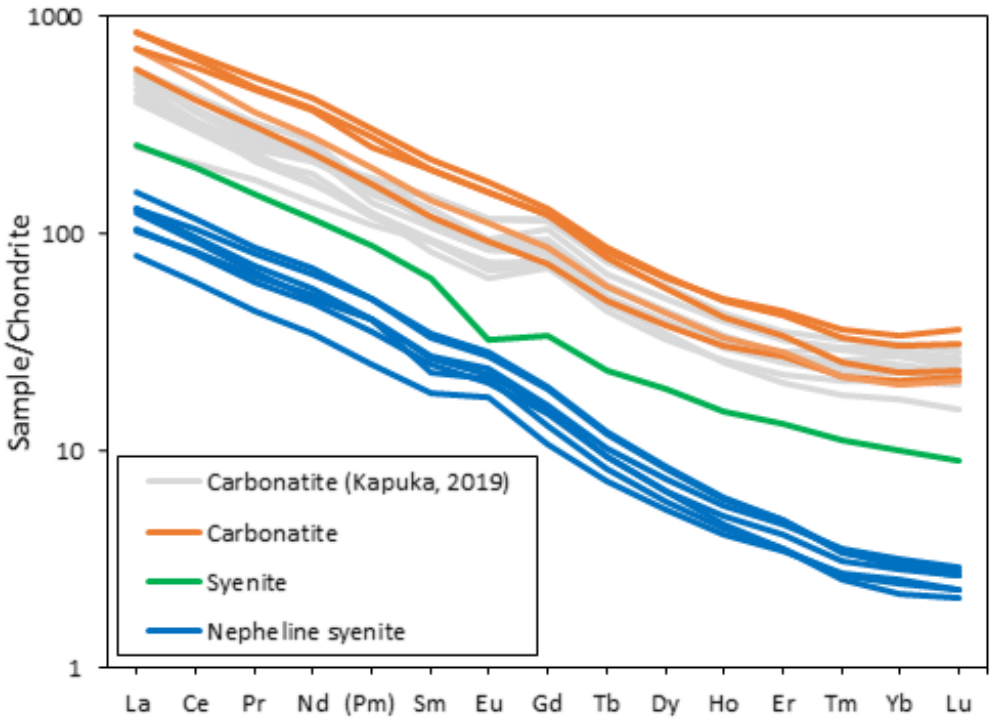

Fig. 3.9: Diagram showing whole rock chondrite-normalized REE patterns for Nepheline syenite, syenite and carbonatite samples from Epembe. Normalization values for chondrite from Boynton (1984)

3.4. Discussion

3.4.1. Evolution of the silicate rocks and the carbonatite

3.4.1.1. Silicate rocks

As shown in Fig. 3.5, CaO, Fe_2O_3, P_2O_5 and MgO tend to decrease with increasing SiO_2 concentration, whereas Al_2O_3, K_2O+Na_2O increase with increasing SiO_2. Since SiO_2 concentrations increase with differentiation in magmatic silicate rocks, the observed trends are consistent with fractional crystallization of pyroxene and apatite. Although CaO decreases with increasing SiO_2, it cannot be related to plagioclase fractionation in the absence of decreasing Al_2O_3 with increasing SiO_2. Moreover, the trace elements Ba and Sr, which have an affinity for plagioclase, do not show any correlation with SiO_2, and the nepheline syenites do not show any significant negative Eu anomaly (Fig. 3.9), which would be expected if prior plagioclase formation and removal occurred during the evolution of the parental magma. Nickel and Cr values are low (< 3 ppm), even in the most primitive nepheline syenite samples, which implies that these rocks are the product of crystallization from an evolved magma, consistent with the low Mg# (0.20-0.29). The REE decrease with increasing SiO_2 (Fig. 3.8), suggests that the REE have been fractionated by apatite. Control by apatite on REE in magmatic systems has been documented in a number of studies (e.g. Mao et al., 2016; Chakhmouradian et al., 2017). Since Ti, Nb and Zr concentrations do not decrease with increasing SiO_2 (Fig. 3.5), it appears that crystal fractionation involving titanite and zircon was not significant during the evolution of the nepheline syenites. Biotites generally occupy interstices between alkali-feldspar and sometimes contain alkali feldspar inclusions suggesting that it crystallized relatively late, presumably after alkali-feldspar.

The nepheline syenite samples are enriched in light REE over the heavy REE (La_N/Yb_N = 31-53), a common characteristic of alkaline rocks (Dostal, 2017), sometimes reaching economic concentrations (e.g. Khibinny, Kola Peninsula; Kogarko, 2018). Enrichment of LREE can be due to fractional crystallization, hydrothermal enrichment, magma composition and small degree partial melting of a garnet-bearing mantle source (Dostal, 2017; Eby et al., 1998; Kogarko, 2018; Smith et al., 2016), and also contamination by local crust. The regular REE pattern of these rocks suggests that the LREE enrichment is not a result of hydrothermal processes. Also, late-stage REE hydrothermal phases, such as monazite commonly found in association with apatite, were not

observed in BSE examination. Eenrichment of LREE in these rocks due to fractional crystallization can also be excluded as it has been shown above that the REE are sequestered by early formed apatite. Crustal contamination is not significant as parental magmas to alkaline rocks tend to be enriched in REE, such that effects of crustal contamination may not be detectable. Moreover, if crustal contamination occurred, it would result in the disappearance of the nepheline normative character of the nepheline syenites by interaction with quartz normative crust. Thus, the enrichment of LREE in the studied nepheline syenites is likely to be a feature of the parental magma, resulting from small degree partial melting of a garnet bearing-source, since garnet retains the heavy REE (e.g. Eby et al., 1998; Dostal, 2017). Given the relatively large ionic radii of the LREE (La-Eu) in comparison to the HREE (Gd-Lu), light REE will behave incompatibly during melting. Another feature supporting the existence of garnet in the source is the low Zr, Hf concentrations relative to the LREE (Fig. 3.7). Zirconium (and Hf) is compatible in garnet (K_d = 3.98, Sweeney et al., 1992) and thus can be retained in the source.

Although the syenite contains high SiO_2 relative to the nepheline syenites**,** it does not show any correlation with the nepheline syenites (Figs. 3.5 and 3.8) and its REE content is much higher when compared to the nepheline syenites (Fig. 3.9). Accordingly, its relationship with nepheline syenites cannot be explained by fractional crystallization alone. However, co-existence of silica-undersaturated and silica-oversaturated syenites can be explained by mixing of mantle-derived silica-undersaturated alkaline magmas with granitic magmas formed by melting of lower crustal material above a zone of mafic underplating (Jung et al., 2007). The involvement of continental crust in the petrogenesis of the Epembe syenite can be evaluated using PRIMA-normalized whole rock geochemistry. According to Hofmann (1997), elevated incompatible trace element abundances are typical for magmas derived from enriched mantle plumes associated with OIBs, such as EM1 and HIMU, whereas negative Nb and positive Pb anomalies are typical for crustal rocks. The ratios Nb/U and Ce/Pb are magma source sensitive (Hofmann, 1997) and can therefore also be used to evaluate the possibility of crustal involvement. The syenite sample is characterized by an absence of positive Pb, no negative Nb (Fig. 3.7) with Ce/Pb and Nb/U ratios of 12 and 19, respectively. In contrast, the Nb/U ratio for the continental crust and island arc volcanics is ~10, while their Ce/Pb ratios are 4-5 times lower than the OIB value of 25 (Hofmann,

1997). Therefore, the Ce/Pb and Nb/U ratios and no negative Nb, which all are different from continental crust and island arc volcanics signatures, argue against a crustal contribution to the syenite magma, during ascent and emplacement or in its source. This then suggests that the syenite evolved from an independent upper mantle derived parental melt in which the presence of a negative Eu anomaly is consistent with earlier plagioclase fractionation.

Three main hypotheses have been proposed for the formation of silica-undersaturated magmas. The first involves partial melting of a metasomatized enriched mantle or lower crust (e.g. Eby et al., 1998) and the second, the generation of a residual melt by fractional crystallization of an alkali basalt perental melt (Eby et al., 1998; Bodeving et al., 2017). The third involves mixing of a silicic melt, generating hybrid liquids (Jung et al., 2007). The geochemistry of the silica-undersaurated alkaline rocks at Epembe and their evolution points towards the second hypothesis. As shown above, the nepheline syenites are interpreted to have undergone fractional crystallization involving pyroxene and apatite, while negative Eu anomalies in the Epembe syenite suggest that its initial magma underwent plagioclase fractionation. A mantle origin of the Epembe nepheline syenite and syenite samples can be demonstrated on the basis of Sr-Nd-Hf isotiopic compositions (see chapters 4 and 5). Since different evolutionary paths have been proposed for the two different rock types, these rocks may have been derived from distinct parental melts with alkali basalt affinities. There is an occurrence of a pyroxenite in the surrounding of the study area (Fig. 2.1), however, at present there is no geochemical data for this unit which could allow for investigation of a genetic relationship to the Epembe nepheline syenites or syenite. However, it is likely that this pyroxenite may represent the least evolved silicate unit in the evolution of either the Epembe nepheline syenite or syenite and thus further geochemical studies are required to address this.

3.4.1.2. Carbonatite

Amongst all the carbonatite occurrences studied so far, only a few have retained their original magmatic textures and compositions (Chakhmouradian et al., 2016). Petrographic investigation of the Epembe carbonatite shows that recrystallization textures are common in calcite, particularly mechanical twining and “core and mantle structures”. These features attest to post-

magmatic deformation of the carbonatite. Given that such ductile deformation mechanisms occur at depth (Chakhmouradian et al., 2016), the Epembe carbonatite was emplaced at deeper crustal levels. Even though the carbonatite appears to have been deformed, some of the magmatic features appear to have been preserved and are seen in the enrichment of incompatible elements up to 10 000 times primitive mantle values, depletion in Zr and Hf, LREE abundances of up to 100 times chondrite values with $La_N/Yb_N > 24$, and Y/Ho = 28 similar to many other magmatic carbonatite occurrences worldwide (e.g. Nelson et al., 1988; Woolley and Kempe, 1989).

The major and minor mineral assemblage of the carbonatite samples includes calcite, apatite, pyrochlore, pyroxene (aegirine), biotite, zircon and alkali feldspars and lath-shaped albite. The occurrence of apatite in clusters or as disseminated grains within a calcite matrix and sometimes as inclusions within zircon, in addition to its intimate association with pyrochlore implies that apatite and pyrochlore (where available) were the earliest minerals to reach the liquidus, followed by calcite, zircon, aegirine, feldspar, biotite and magnetite. The crystallization of apatite before calcite is consistent with experimental studies, which show low solubility of this mineral in carbonatitic melts (Hammouda et al., 2010). Such early apatite formation will sequester the REE early in the evolution of the carbonatite. As for the nepheline syenite, the LREE enrichment relative to HREE in the carbonatite is attributed to the presence of garnet in the melt source region. One notable feature of the carbonatite samples is the variable U, Th and Nb concentrations in the PRIMA-normalized diagram (Fig. 3.7), especially when compared with other data (Kapuka, 2019). Such variability can be explained by the variable pyrochlore abundance and compositions from the Epembe carbonatite (Falshaw, 2012). Assimilation of wall rock material by carbonatite melts is common and it is manifested in the resorption of xenoliths and precipitation of silicate minerals (Chakhmouradian et al., 2016). Thus, the occurrence of feldspar, biotite and disaggregated silicate lithologies in the Epembe carbonatite are interpreted to be due to crustal contamination by associated silicate rocks during carbonatite emplacement. This is in line with silica activity calculations which show that phases such as feldspars are not likely to crystallize in carbonatites as the silica activity is too low to crystallize these minerals (Barker, 2001). Further evidence supporting assimilation in the carbonatite is from the whole rock SiO_2

concentrations of up to 11 wt% which have been reported by Kapuka (2019). Elsewhere, wall rock assimilation has also been reported to be responsible for the presence of silicate minerals and xenoliths in carbonate-rich rocks from Dahomeyide orogeny, southeastern Ghana (Nude et al., 2009).

3.4.2. Petrogenetic relationship between the carbonatite and nepheline syenite

As stated earlier, carbonatite magmas are thought to form by direct partial melting of a carbonated mantle peridotite (Harmer and Gittins, 1998; Wallace and Green, 1988; Harmer, 1999), or represent residual melts that fractionated from a nephelinite parental magma (Gittins and Jago, 1998; Brassiness et al., 2005; Mitchell, 2005; Wang et., 2014). Carbonatites may also be viewed as a product of liquid immiscibility arising from a carbonate-saturated silicate melt (Lee and Wyllie, 1998; Bodeving et al., 2017). The association of the Epembe carbonatite with a nepheline syenite provides an opportunity to evaluate the above models based on the presented data. This is also motivated by the idea that both these rock types are age similar and have overlapping Sr-Nd-Hf isotopic copmositions (see chapters 4 and 5).

Studies which invoke the formation of a carbonatite magma by direct partial melting of carbonated mantle peridotite (lherzolite or harzburgite) show that the resulting carbonatite is dolomitic in composition (e,g. Wallace and Green, 1988; Wyllie and Green, 1988). These studies are based on high pressure (> 2 GPa) experiments. It is however possible to generate carbonatites with high values of Ca/Ca + Mg i.e alkali-bearing carbonatites, at lower pressure. For instance, experiments of Dalton and Wood (1993) yielded a calcite-carbonatite with a Ca/Ca + Mg value of ~0.88 (the corresponding value for the Epembe calcite-carbonatite is 0.93 on average). It has also been proposed that calcite-carbonatites can be produced by interaction of a rising dolomite-carbonatite magma with harzburgite or lherzolite, forming wehrlite (Harmer and Gittins, 1998; Wyllie and Lee, 1998). Irrespective of whether the calcio-carbonatite forms as a result of partial melting at low pressure or from reaction of dolomite-carbonatite with harzburgite or wehrlite, it will have elevated contents of elements like Ni and Cr, which are concentrated in the latter rocks. In contrast, the Epembe calcite-carbonatite has low contents of these elements (< 35 ppm). In

view of these observations, it is therefore concluded that the Epembe calcite-carbonatite did not originate by direct partial melting of the mantle or from a dolomite-carbonatite.

Harmer and Gittins (1998) showed that carbonatites in several African carbonatite alkaline complexes are primary, however, they did not completely rule out the formation of carbonate melts from a carbonated parent silicate melt by liquid immiscibility. Instead, they suggest that liquid immiscibility is possible at low pressures and temperatures in the crust. The role of a liquid immiscibility gap for controlling a carbonated silicate melt has also been demonstrated for temperatures and pressures similar to those prevalent in the crust (Lee and Wyllie, 1998). At the point of liquid immiscibility, both the carbonate and silicate must be in geochemical equilibrium (Harmer, 1998). Upon separation, geochemical parameters are expected to partition systematically between the two melts and this has been constrained experimentally. For instance, at pressures of 72-100 MPa and temperatures of 650-1100 °C most REE partition into the silicate liquid, while La, Sr, Ba partition into the carbonate liquid (Veksler et al., 2012). Most of the high field strength elements (HFSE) preferentially partition into the silicate liquid with Zr and Hf being the most concentrated (Veksler et al., 2012). A study of carbonatite and associated silicate rocks from Lofdal, Namibia, documented relative negative Ta, Nb and Hf anomalies in carbonatites, while the associated silicate rocks display positive anomalies (Bodeving et al., 2017). Such behaviour of HFSE supports immiscible separation of a carbonate-silicate pair. Apart from carbonate-silicate liquid immiscibility being possible at crustal pressure, Martin et al. (2013) showed that liquid immiscibility is also possible at 1-3 GPa and 1150-1260 °C in their hydrous experiments and instead suggested that liquid immiscibility is controlled by H_2O concentration of the melt.

In order to evaluate if the Epembe carbonatite was derived from the associated nepheline syenites by liquid immiscibility, modelling was applied using experimentally-determined partition coefficients (K_d = concentration in carbonatite/concentration in silicate). Martin et al. (2013), however, pointed out that this approach is not straightforward as most carbonatites do not represent true melt compositions but are heavily modified during the late or post-magmatic stage. Nevertheless, an immiscible silicate fraction was selected that is compositionally similar to the Epembe nepheline syenites (RQ-21 and C4-41 from Veksler et al., 2012; LM-63 and LM-73

from Martin et al., 2013). Most of the experimental, immiscible melt products, including silicates and carbonates, however, were enriched in alkalis (Na and K), relative to the Epembe nepheline syenite and carbonatite samples. This mismatch is likely to be related to the loss of alkalis during fenitization in the Epembe rocks (Ferguson et al., 1975). The partition coefficients (K_d) for C4-41 and RQ-21 (Veksler et al., 2012) shown on spider-diagram (Fig. 3.10a) and REE patterns (Fig. 3.10b) are similar in form to those of the Epembe carbonatite/nepheline syenite in some of the elements, such as La, Sm, Zr, Hf, but most importantly the K_d absolute values are very different without any overlap. Based on the experimental study of Veksler et al. (2012), it would be expected to find low Ba, high REE, HFSE concentrations in the nepheline syenite compared to the carbonatite at Epembe if liquid immiscibility operated, which is not the case. When displayed in in trace element diagrams (Fig. 3.10a, b), the partition coefficients for experiment LM-63 and LM-73 (Martin et al., 2013) show similarities for more elements (Cs, Ba, Nb, La, Ce, Pr, Sr, Zr, Hf, Sm and Eu) when compared with the Epembe carbonatite/nepheline syenite, with some K_d absolute values overlapping for elements (La, Ce, Pr, Sm and Eu). This similarity in K_d values may in part be due to similarities in H_2O concentration of the melts in the two studies (Martin et al., 2013). However, the H_2O content of the Epembe rocks has not been constrained so far. Most importantly though, for liquid immscibility to operate, the partition coefficient values shown in spider diagrams and REE diagrams should display similar forms for all elements for both the experimental study and the natural carbonate-silicate system (Veksler et al., 2012; Martin et al., 2013; Bodeving et al., 2017). Unless some mismatches in K_d values can be attributed to other processes such as late-stage hydrothermal alteration, at Epembe the mismatches in K_d values (e.g. the heavy REE with those of the experimental studies: Fig. 3.10) cannot be attributed to such a process because hydrothermal REE minerals are not significant at Epembe. Instead, there is abundant magmatic apatite, which is likely the host of the REE (chapter 4). In summary, provided that partition coefficient mismatches between this study and those from experimental studies are valid (Fig. 3.10), it is unlikely that the Epembe carbonatite seperated from the associated nepheline syenite by liquid immiscibility.

The remaining hypothesis is the origin of a carbonatite melt by fractional crystallization of a coexisting carbonated silicate magma (Brassiness et al., 2005; Mitchell, 2005; Wang et.,

2014). In the case of Epembe, such a hypothesis is possible considering the close spatial association of the carbonatite and alkaline silicate rocks. According to this hypothesis, the calcite-carbonatite would represent the last residual liquid produced by fractional crystallization of the alkali-basalt magma (earlier it was proposed that alkali basalt is the parental melt to the Epembe nepheline syenite). The observation that the carbonatite intruded the nepheline syenite supports this hypothesis. Further possible is provided by the behavior of REE, Ta and Nb, which, being incompatible are expected to accumulate in the residual liquid. Indeed, these elements are enriched in the carbonatite relative to the nepheline syenites. It has also been shown experimentally that carbonate melts have low viscosities and can separate from their source even at low degrees of partial melting and are capable of percolating through wall rocks (Hunter and Mackenzie, 1989; Hammouda and Laporte, 2000). Therefore, it is likely that the Epembe carbonatite magma formed after partial crystallization of the associated nepheline syenites and then intruded its own and related nepheline syenite rocks.

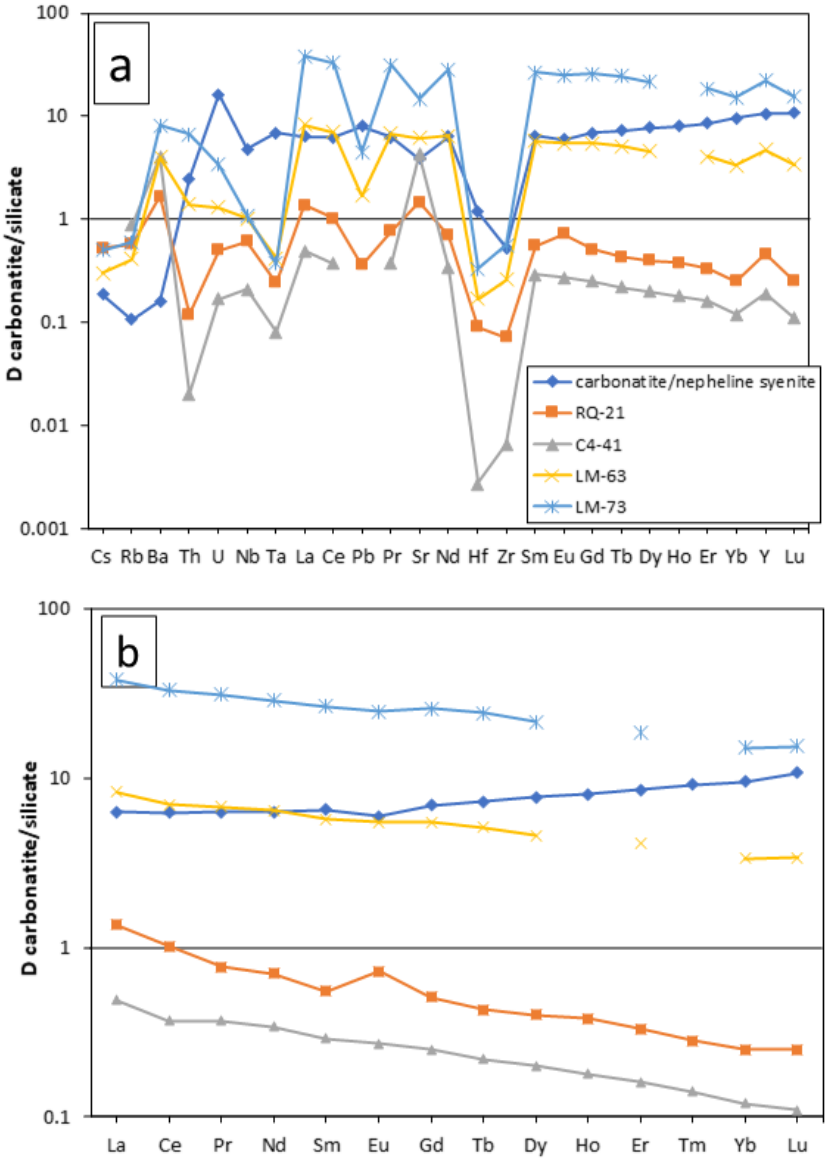

Fig. 3.10: (a) Ratios for selected trace elements compared to experimentally determined carbonate-silicate partition patterns for same elements in quenched melts (RQ-21 and C4-41: Veksler et al., 2012; LM-63 and LM-73: Martin et al., 2013). (b) Ratios for rare earth elements compared to experimentally-determined carbonate-silicate partition patterns for same elements in quenched melts (RQ-21 and C4-41: Veksler et al., 2012; LM-63 and LM-73: Martin et al., 2013).

3.5. Conclusion

This study presents petrological and geochemical data of the Epembe syenitic rocks and carbonatite. The syenitic rocks include a syenite and nepheline-bearing syenites. All, are alkalic, metaluminous and ferroan. The associated calcite-carbonatite displays post-magmatic deformation features, however, it appears to have retained its igneous geochemical characteristics. The presence of feldspars and biotite, silicate xenoliths and elevated SiO_2 content in this rock are consistent with assimilation of country rock material during its emplacement. The nepheline syenites appear to have evolved via fractional crystallization involving pyroxene and apatite, while the syenite evolved from a distinct mantle-derived melt unrelated to the nepheline syenites. Trace element similarities between the carbonatite and nepheline syenite suggest these rocks are related and that the carbonatite may be a melt fraction that formed after partial crystallization of the nepheline syenite.

4. The use of apatite trace element mineral chemistry and Sr-Nd isotopic determinations for investigating the petrogenesis of syenites and carbonatites. A case study of the Epembe alkaline-carbonatite complex, Namibia

4.1. Introduction

Carbonatites are an unusual type of igneous rock with more than 50 modal % carbonate minerals (Woolley and Kempe, 1989). Syenites on the other hand, are igneous rocks with less than 20 modal % quartz and more than 65 modal % alkali feldspar (Streckeisen, 1976). Carbonatite and related alkaline complexes are the main economic suppliers of rare earth elements (REE) and niobium (Nb) worldwide, and are significant producers of phosphate (Mariano, 1989; Smith et al., 2016). Phosphates from these rocks have been mined in South Africa, Zimbabwe, Sri Lanka and Brazil for the production of fertilizer (Pell, 1996). In addition, it has been shown that phosphate minerals are a potential source for REE production, which could alleviate the shortage of REE supply globally (Ihlen et al., 2013; Mariano and Mariano, 2012). For instance, magmatic apatite usually contains more than 0.35 wt% REE (Ihlen et al., 2014). Apatite hosted by carbonatites and related alkaline complexes typically forms early during magma emplacement, but can also crystallize throughout magmatic differentiation, and up to late metasomatic and hydrothermal stages (Belousova et al., 2002b; Bühn et al., 2001; Chakhmouradian et al., 2017). Apatite in carbonatite and associated alkaline rocks is usually enriched in REE and such enrichment may be dependent on the processes forming apatite (Decrée et al., 2020).

The objective of this study has been to assess the relative crystallization stages pertinent to apatite formation in syenitic rocks and carbonatite of the Epembe Complex, Namibia, by means of petrographic observations and geochemical and isotopic analysis. Petrographic examination of apatite was based on cathodoluminescence imaging. Amongst other factors, the luminescence of apatite in CL is related to constituent elements, such as Mn and REE (Gros et al., 2016). Thus, combined cathodoluminescence imaging and in-situ trace element analysis aids in distinguishing between magmatic and non-magmatic apatite as well as helping to trace magmatic events. An important motivating aspect of the study was that, if any mining activities are to

commence at Epembe in the near future, REE may be considered as a by-product of mining of the phosphate concentrate or vice versa.

Given its capability to host U and Th, apatite has also been employed in geochronology (e.g. Chew et al., 2011; Kirkland et al., 2018; O'Sullivan et al., 2021) and in thermochronological studies, which show that the closure temperature of the U-Pb system in apatite is ca. 350-550 °C (Chamberlain and Bowring, 2001; Schoene and Bowring, 2007). Due to the low U-Pb closure temperature of apatite relative to zircon (> 900 °C: Cherniak and Watson, 2001; Schoene and Bowring, 2007), apatite U-Pb ages may not be interpreted in terms of the timing of magmatic activity. However, apatite U-Pb data yield valuable information on the timing of thermal events and the cooling history of rocks (Gawęda et al., 2014; Kirkland et al., 2018; O'Sullivan et al., 2021)

Whole rock Sr and Nd isotope geochemistry has been widely used in constraining magma sources, however, this approach does not allow small-scale isotopic heterogeneities to be detected, which can be recorded in apatite as distinct zonations. Nevertheless, in-situ isotopic studies of apatite have remained rare so far. The few studies using in-situ isotopic analyses on apatite in the context of carbonatites and alkaline rocks include: Decrée et al. (2020) using Sr isotopes and Wu et al. (2011), Mitchell et al. (2017) using both Sr and Nd isotopic compositions of apatite from the Phalaborwa Igneous Complex, South Africa, and of apatite from the Blue River carbonatites, Canada.

A secondary purpose of this study was to carry out in-situ U-Pb analysis by LA-SF-ICPMS and Sr-Nd by LA-MC-ICPMS in order to further explore the magmatic sources and the emplacement and cooling history of the Epembe Complex.

4.2. Methodology

Apatite grains were extracted from twelve rock samples (BX 01, SNT 03, SNT 04, SNT 05, SNT 06, SNT 07, SNT 09, EC 4, EC, 5, EC 21, EC 23 and EC 29) using standard techniques (heavy liquid separation, magnetic separation and hand picking) followed by mounting and polishing

4.2.1. Electron probe micro-analysis (EPMA)

Major and minor element analyses of apatite were conducted using a CAMECA SX-5 FE EPMA equipped with five spectrometers, at the microscopy and microanalysis unit (MMU) of the University of the Witwatersrand. Carbon-coated thin sections and mineral mounts were investigated using BSE, CL and EDS methods for mineral identification, fractures, inclusions and zoning patterns. A beam current of 20 nA, an accelerating voltage of 15 kV and a beam diameter of 10 µm were employed and the following natural and synthetic standards were used: Apatite (F, P, Ca), quartz (Si), tugtupite (Cl), albite (Na) and monazite (La, Ce). Crystals used are as follow: LPET (P, Cl, Ca, La, Ce), TAP (Si, Na) and PCO (F). Peak counting times were 20 s for Na, Ca, P, La, Ce, Cl and 30 s for F, Si.

4.2.2. Trace element analysis by LA-ICPMS

Trace element analysis as well as U-Pb measurements on apatite were carried out in the Earthlab at the University of the Witwatersrand, using an Australian Scientific Instruments (ASI)/Applied Spectra Resolution 193 nm ArF excimer (SE 155) system coupled to a Thermo Scientific Fisher sector-field ICPMS (Element XR). Measurements were performed in low resolution and electrostatic scanning (E-scan) modes. Data were acquired by single spot analysis (60 µm diameter), using a repetition rate of 10 Hz and a fluence of 2.5 Jcm^{-2}. The total acquisition time was 60 sec, comprising 15 s of pre-ablation and blank measurement followed by 20 sec of measurement. Laser sampling took place in a SE155 dual-volume ablation cell (Laurin Technic, Canberra, Australia) using a mixed He-Ar atmosphere and a small volume of N_2 to enhance signal stability and sensitivity. The following gas flows were applied: He (300-450 ml/min), Ar (800-1200 ml/min) and N_2 (2-6 ml/min), respectively. For trace element analysis, synthetic glass NIST 612 (Jochum et al., 2011) served for calibration, while NIST 610 (Gao et al., 2002) and Durango apatite (Chew et al. 2016) were analyzed as unknowns to evaluate accuracy and precision. The LA-ICPMS system was tuned during line scans using NIST 612 glass for maximum sensitivity of ^{6}Li, ^{115}In and ^{238}In, while maintaining oxide levels (ThO^{+}/Th) < 0.2 %. For internal standardization, the isotopes ^{43}Ca was used. Typically, two standard measurements were obtained at the beginning and at the end of an experiment, and 10-20 analyses of unknowns were followed by analyses of one primary

calibration standard and two to four analyses of the secondary standards for quality control purposes. Surficial material was removed using 2 laser pulses prior to each analysis. The following masses were measured (6 samples per peak): ^{29}Si, ^{23}Na, ^{48}Ti, ^{55}Mn, ^{56}Fe, ^{51}V, ^{88}Sr, ^{89}Y, ^{91}Zr, ^{139}La, ^{140}Ce, ^{141}Pr, ^{146}Nd, ^{147}Sm, ^{151}Eu, ^{157}Gd, ^{159}Tb, ^{163}Dy, ^{165}Ho, ^{166}Er, ^{169}Tm, ^{174}Yb, ^{175}Lu, ^{232}Th, ^{238}U. The carbonatite apatite was analyzed in a separate run and the elements ^{29}Si, ^{23}Na, ^{48}Ti, ^{55}Mn, ^{56}Fe, ^{91}Zr were not measured. Analyses were carried out in triple mode, including pulse counting, analog and Faraday cup, depending on signal. Data reduction was performed using the iolite extension (http://www.iolite.org.au) to the software Igor Pro, specifically the data reduction scheme ("DRS") "X_Trace_Elements_IS", proceeding in a series of sequential steps, including data import, selection of integrations, baseline subtraction, drift and down-hole fractionation, calibration and error propagation (Paton et al., 2010, 2011). The Eu anomaly (Eu/Eu*) was calculated as $Eu/Eu^* = Eu_N/(0.5Sm_N + 0.5Gd_N)$.

4.2.3. U-Pb measurements on apatite

Madagascar apatite standard (473.5±0.7 Ma, ID-TIMS, ^{207}Pb/^{206}Pb = 0.8681: Thomson et al., 2021; Chew et al., 2014) served for calibration, and McClure Mountain (523.51 ± 1.47 Ma, ID-TIMS age, ^{207}Pb/^{206}Pb = 0.88198: Schoene and Bowring, 2006) and Durango (31.44 ± 0.18 Ma, ^{207}Pb/^{206}Pb = 0.8376; McDowell et al., 2005) apatite certified reference materials (CMRs) were analyzed as unknowns to evaluate accuracy and precision. The LA-ICPMS system was tuned during line scans using NIST 612 glass for maximum sensitivity for ^{238}U and ^{206}Pb, while maintaining oxide levels (ThO+/Th) < 0.2 % and the Th/U ratio > 0.95. The following masses were measured (4 samples per peak): ^{43}Ca, ^{206}Pb, ^{207}Pb, ^{208}Pb, ^{232}Th and ^{238}U. Magnet settling time was 0.3 (Ca), 0.112 (^{206}Pb,) and 0.001 sec (all other isotopes), and sample times range from 0.003 sec (^{232}Th) to 0.07 sec (^{207}Pb). All isotopes were measured in pulse counting mode, except for ^{238}U and ^{232}Th (analog, counting or Farady cup, depending on signal intensity). Ca was used for internal standardization. Weighted-mean ^{207}Pb-corrected ages for the secondary reference materials are: Durango apatite (32.3 ± 1.4 Ma, n = 9, MSWD = 2.0) and McClure Mountain apatite (529.4 ± 8.1 Ma, n = 9, MSWD = 1.2). For both secondary age reference materials, the ages agree within error with the reference values. Data reduction schemes (DRS) VizualAge (Petrus and Kamber, 2012;

http://www.japetrus.net/va) and VizualAge_UcomPbine (Chew et al., 2014) were employed for common Pb correction in the primary reference material. Graphic presentation and calculation of ages was carried out using the software ISOPLOT-R (Vermeesch, 2018). Uncertainties on individual and mean/regressed ages are 2SE (standard error, absolute).

4.2.4. Sr and Nd isotopic measurements

In-situ Sr and Nd (syenite- and nepheline syenite-hosted apatite only) isotopic analyses on apatite were carried out at the University of Johannesburg, using the same laser system and coupled to a Nu Plasma II MC-ICPMS (Nu Instruments, Wrexham) with 16 Faraday cups and 5 ion counting detectors. A plasma RF power of 1300 W was applied. The following gases were used: coolant Ar gas flow = 13.0 L/min, auxiliary gas flow = 0.80 L/min, nebuliser gas flow = 0.82 L/min and a laser He gas flow of 0.31 L/min. Other laser parameters include a beam energy of 6 mJ and a beam transmittance of 25%.

For Sr isotopic measurements, a spot size of 60 µm was employed with a 10 Hz repetition rate and a fluence of 5.3 J/cm^2. The data acquisition time consisted of a 25 s blank measurement, followed by 70 s of laser ablation. Background correction was done by measuring background signal on mass prior to ablation and subtracting from signal. For interference corrections, Kr interferences were removed during background subtraction, whereas ^{85}Rb was used to calculate and subtract Rb from mass 87. For REE interferences, $^{163}Dy^{2+}$ was used to calculate and subtract doubly-charged Dy from mass 82, while $^{167}Er^{2+}$ was used to calculate and remove $^{166}Er^{2+}$ from ^{83}Kr, $^{168}Er^{2+}$ from mass 84 signal and $^{170}Er^{2+}$ from mass 85 signal. Then $^{171}Yb^{2+}$ was used to calculate and remove $^{168}Yb^{2+}$ from mass 84 signal, $^{170}Yb^{2+}$ from mass 85 signal, $^{172}Yb^{2+}$ from mass 86 signal and to correct $^{174}Yb^{2+}$ on mass 87. Also, $^{71}Yb^{2+}$ was used to calculate and subtract $^{176}Yb^{2+}$ from mass 88, whereas $^{175}Lu^{2+}$ was used to calculate and subtract $^{176}Lu^{2+}$, from mass 88. For mass bias correction, $^{86}Sr/^{88}Sr$ was used to calculate mass bias correction factor for Sr, which was also used for Rb correction after testing and adjustment on the standard. Corrected $^{84}Sr/^{88}Sr$ and $^{86}Sr/^{88}Sr$ values were determined to confirm measurement accuracy. The correction ratios are: $^{166}Er/^{167}Er$ = 1.4658, $^{168}Er/^{167}Er$ = 1.1679, $^{170}Er/^{167}Er$ = 0.6511, $^{168}Yb/^{171}Yb$ = 0.0091, $^{170}Yb/^{171}Yb$ = 0.2129,

$^{172}Yb/^{171}Yb$ = 1.5287, $^{174}Yb/^{171}Yb$ = 2.21559, $^{176}Yb/^{171}Yb$ = 0.88395, $^{176}Lu/^{175}Lu$ = 0.02645, $^{164}Dy/^{163}Dy$ = 1.13212, $^{86}Sr/^{88}Sr$ = 0.1194, $^{87}Rb/^{85}Rb$ = 0.3858. Secondary standards were measured as unknowns to evaluate measurement accuracy, including Durango, MAD, Slyudyanka and McClure apatite (Yang et al., 2014), an apatite from Phalaborwa (Decrée et al., 2020), and BHVO2G glass reference material from the USGS (Elburg et al., 2005).

For Nd isotopic measurements a spot size of 80 to 100 µm was employed depending on the apatite grain size. A 7 Hz repetition rate and a fluence of 2.8 J/cm^2 was applied. The data acquisition time consisted of a 25 s blank measurement followed by 50s of laser ablation. Background correction was done by measuring the background signal on mass prior to ablation and subtracting from the signal. For mass bias correction, ^{147}Sm and ^{149}Sm were used to calculate Sm mass bias factor, whereas ^{146}Nd and corrected ^{144}Nd (after ^{144}Sm removed) were used to calculate Nd mass bias factor. For interference corrections, ^{147}Sm was used to calculate and correct ^{144}Sm interference on ^{144}Nd. The corrected signal for ^{144}Sm was used to calculate ^{148}Sm and correct ^{148}Nd, whereas ^{140}Ce was used to calculate ^{142}Ce and correct ^{142}Nd. The following ratios were used for correction calculations: $^{146}Nd/^{144}Nd$ = 0.7219, $^{147}Sm/^{149}Sm$ = 1.08680, $^{147}Sm/^{144}Sm$ = 4.88, $^{148}Sm/^{144}Sm$ = 3.6574, $^{150}Sm/^{144}Sm$ = 2.401 and $^{142}Ce/^{140}Ce$ = 0.125747. Secondary standards measured as unknowns to evaluate accuracy included Durango apatite (Doucelance et al., 2020) and apatite from Phalaborwa. Solution whole-rock Nd analyses of Phalaborwa rock from the same site, consisting almost exclusively of apatite, produced $^{143}Nd/^{144}Nd$ value of 0.511256 ± 28 (2SD) and $^{147}Sm/^{144}Nd$ value of 0.1174 ± 1 (2SD).

Nd isotope measurements in carbonatite apatite were carried out using a MC-ICP-MS (Neptune, ThermoFisher Scientific) with a desolvating nebulizer and laser ablation dual intake (Aridus II of Teledyne CETAC; and 193 nm excimer laser, COMPex 102F Coherent) sampling system at the Japan Agency for Marine and Earth Science and Technology (JAMSTEC), Yokosuka, Japann. The analytical details were reported by Kimura et al. (2013) and only a summary is presented here. Data were acquired by single spot analysis (100 µm diameter), using a repetition rate of 10 Hz and a fluence of 6 Jcm^{-2}. Gas flows were: Ar carrier gas = 13.0 L/min, Ar auxiliary gas = 1.0 L/min and laser He carrier gas = 0.7 L/min. Mass biases were corrected internally for Sm and Nd. First, the mass bias factor was calculated for Sm using the acquired $^{147}Sm/^{149}Sm$ isotope

ratio and the reported Sm isotope ratio ($^{147}Sm/^{149}Sm$ = 1.08507). The intensity of ^{144}Sm was subsequently calculated by exponential mass bias correction of the mass bias factor and the TIMS-reported ratio ($^{147}Sm/^{144}Sm$ = 4.8771). The calculated ^{144}Sm intensity was subtracted from the 144 mass intensity providing a net ^{144}Nd intensity. The mass bias factor of Nd isotopes was obtained using the measured $^{146}Nd/^{144}Nd$ ratio of 0.7219. Finally, $^{143}Nd/^{144}Nd$ was calculated using the net ^{143}Nd and ^{144}Nd intensities and the exponential mass bias correction from$^{146}Nd/^{144}Nd$ ratio. Standards measured as unknowns include La Jolla solutions (Thirlwall, 1991), NIST SRM 610 synthetic glass (Woodhead and Hergt, 2001) and Durango apatite (Foster and Vance, 2006).

4.3. Results

4.3.1. Host rock characteristics

Detailed petrographic characteristics of the Epembe syenite, nepheline syenite and carbonatite have been provided previously (Tshiningayamwe et al., submitted), so here only summary is provided. The Epembe syenite (Fig. 4.1a) is medium-grained and comprises dominantly alkali feldspar and clinopyroxene with accessory apatite. Apatite occurs as inclusions in clinopyroxene showing an elongated shape up to 0.5 mm. Nepheline syenite is generally medium-grained (Fig. 4.1b). The mineral assemblage includes major to minor alkali feldspar, nepheline, biotite and cancrinite, while plagioclase, apatite, sphene, zircon, calcite and magnetite occur as accessory phases. Alkali feldspar is the dominant mineral and shows sometimes show perthitic exsolution textures (Fig. 4.1c). Medium-grained anhedral and subrounded nepheline is usually disseminated or occurs as interstitial grains between alkali feldspars. Biotite may occur in clusters, where grains display a mosaic arrangement but are mostly disseminated within the alkali feldspar matrix. Anhedral calcite occupies interstices between alkali feldspar grains (Fig. 4.1c). Apatite is elongated, up to 0.5 mm in size and occurs as scattered grains. Fractures are observable in apatite grains.

The typical major and minor mineral assemblage of the carbonatite samples includes variable calcite, apatite, pyrochlore, aegirine, biotite, zircon and alkali feldspars and plagioclase. Magmatic calcite is observed in the samples, as a fine to/or medium-grained matrix, with a modal

abundance of 64 to 83 vol%. Calcite can also occupy interstices between apatite and pyrochlore cumulates. Porphyroblastic (core and mantle structures) textures are common in these samples and are characterized by twinned calcite porphyroblasts fringed by smaller calcite grains devoid of twinning. Apatite is the second most abundant phase occurring throughout the carbonatite, with ovoid, elongate, euhedral hexagonal and subhedral grain shapes. On average, the grain size of apatite is 0.5 mm. The apatite grains (Fig. 4.1d) are disseminated in a calcite matrix or display a flow texture. Occasionally apatite occurs in clusters and as inclusions within pyrochlore and zircon. Zircon occurs as disseminated fine- to medium-sized grains with subhedral and euhedral grain shapes. Mineral inclusions of calcite are common in zircon. Biotite appears as dark or brownish large grains in clusters with a basal cleavage, which is in some cases bent. Alkali-feldspars occur as dispersed anhedral grains or form globular structures, which are up to 6 mm in diameter.

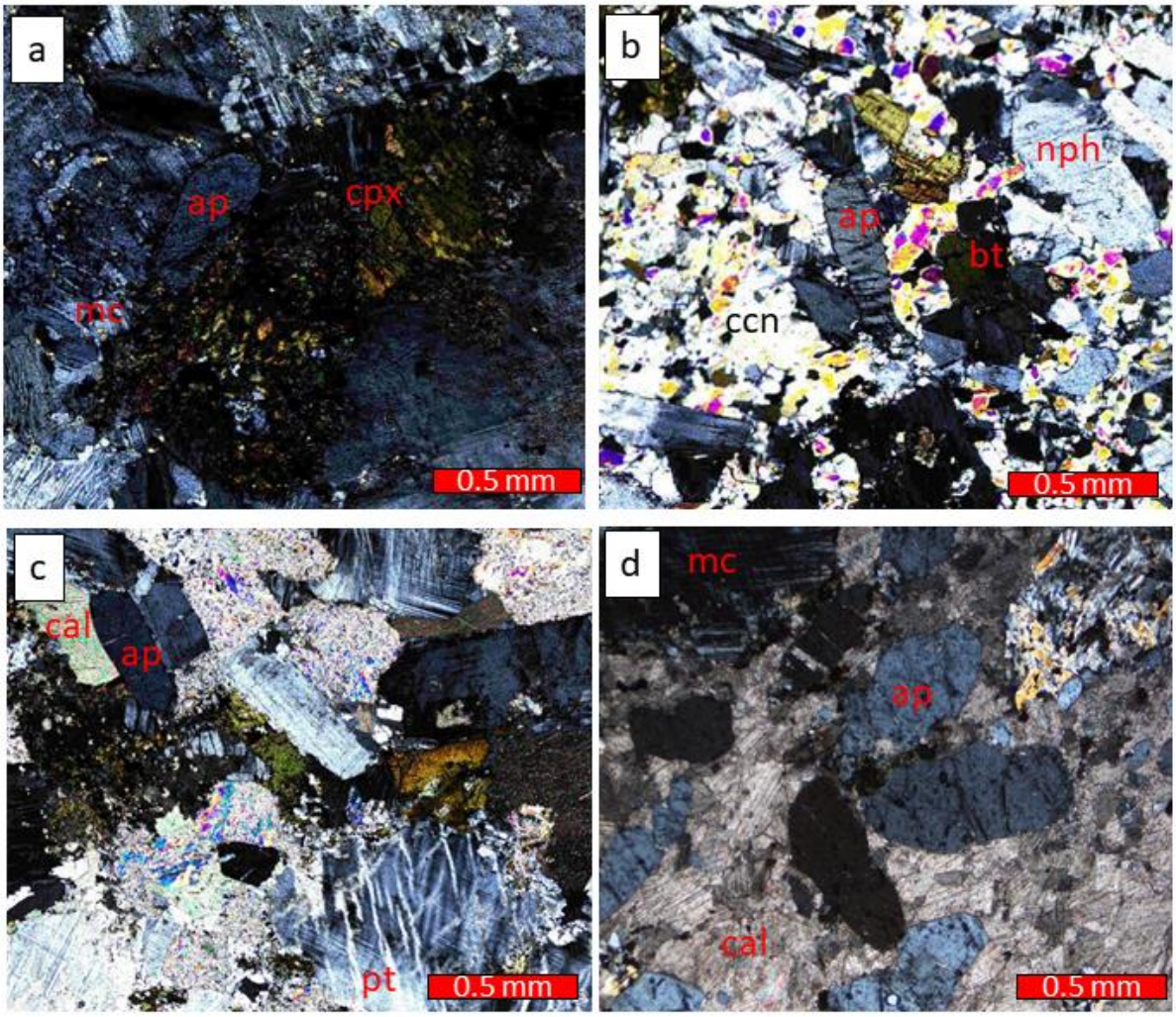

Fig. 4.1: Selected thin section photomicrographs (in XPL) of Epembe syenite (a), nepheline syenite (b, c) and carbonatite (d) showing apatite. (a) Sample BX 01. (b) Sample SNT 09. (c) Very coarse-grained texture in sample SNT 06. Note the presence of calcite. (d) Sample EC 29. Abbreviations: ap=apatite, cpx=clinopyroxene, bt=biotite, nph=nepheline, ccn=cancrinite, pt=perthite, cal=calcite.

4.3.2. Imaging of apatite

Apatite grains are colourless, but sometimes display a yellowish tint. Some of the apatite grains display irregular external shapes attributed to breaking during sample processing. Apatite is commonly observed in igneous rocks as either equant to sub-equant, or acicular grains that rarely

exceed 1 mm in their longest dimension (Piccoli and Candela, 2002). Apatite from syenite sample BX 01 occurs as anhedral, subrounded to elongate grains with grain size variations of 200 to 250 µm. In BSE and CL mode, the apatite grains are typically homogeneous grey (Fig. 4.2a, b).

Apatite from nepheline syenite samples display subhedral and anhedral grain morphologies, which are either elongated, angular or sub-rounded (Fig. 4.2c-f). The predominant grain size is ca. 250 µm reaching up to 400 µm**.** In terms of internal make up, apatite from all nepheline syenite samples are homogeneous grey in BSE and CL mode, however a few grains display zonations in CL**.** In CL core-rim zoning is observed, whereby the core is dark grey and the rim is relatively light grey (Fig. 4.2c), for instance in apatite grains from sample SNT 03. In the nepheline syenite with a pegmatitic texture (sample SNT 06), an additional apatite generation with a patchy texture in CL is observed (Fig. 4.2f). The patchy texture consists of irregular light grey and dark grey CL luminescent areas.

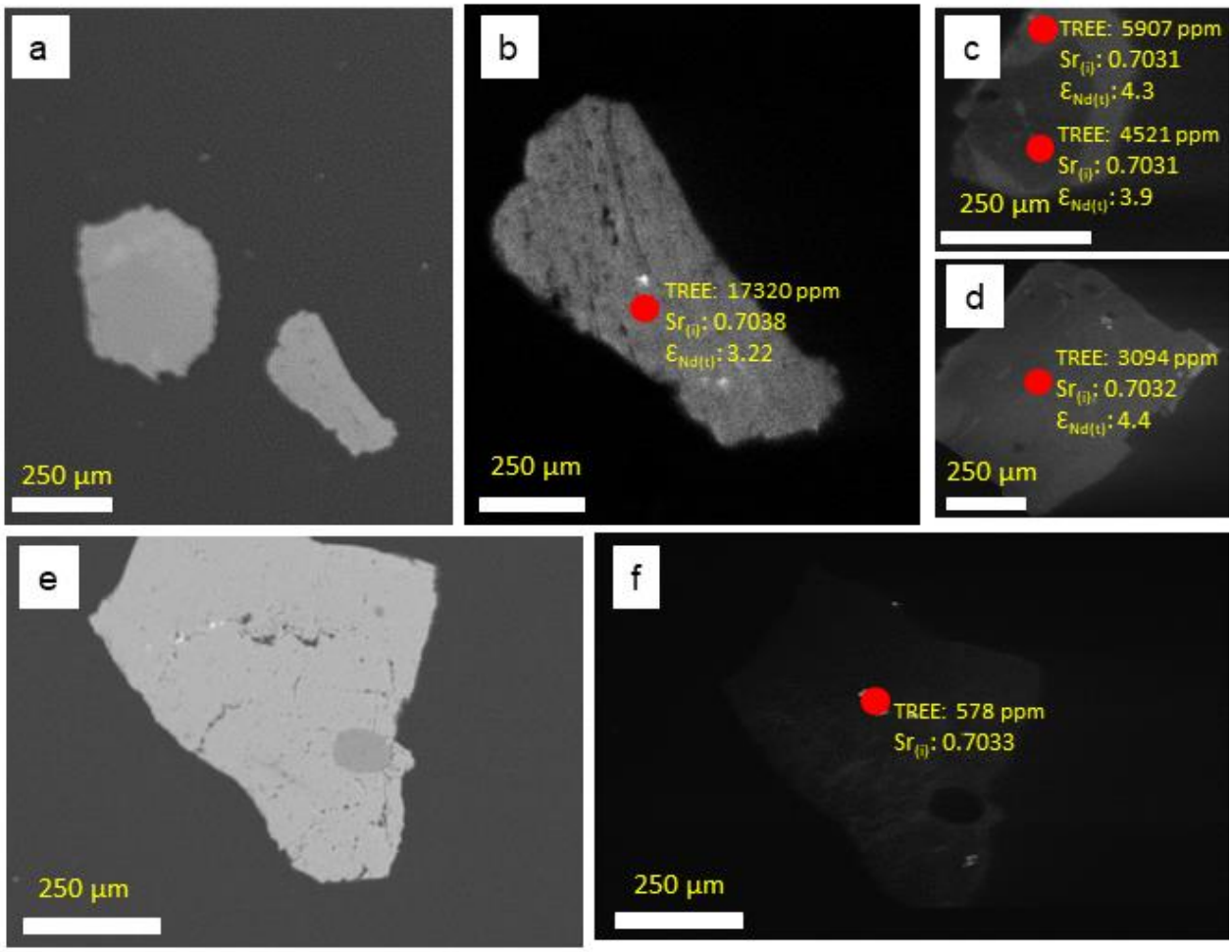

Fig. 4.2: Selected back-scattered (a, e) and cathodoluminescence (b, c, d, f) images of apatite from the Epembe syenitic rocks. (a) Homogeneous sub-rounded and elongated apatite in syenite. (b) Homogeneous grey CL luminescent syenite apatite. (c) Dark core and light grey rim in zoned apatite from nepheline syenite sample SNT 03. (d) Unzoned apatite apatite in nepheline syenite sample SNT 04. (e) Anhedral apatite grain from nepheline syenite sample SNT 06. (f) Patchy zoned apatite from nepheline syenite sample SNT 06. Red dots on apatite grains show location of trace element and isotope ratio analysis. TREE = total rare earth element concentration.

Carbonatite-hosted apatite shows an external ovoid morphology. In BSE mode, apatite grains are typically homogeneous grey, but occasionally show fractures. The fractures are commonly filled with calcite, but in some instances monazite is also observed (Fig. 4.3a, e). Most

of the apatite grains are homogenous in CL (e.g. Fig. 4.3f), however core-rim zoning patterns are observed in apatite from carbonatite sample EC 29 (Fig. 4.3b, d). The transition between zones is sharp and core outlines can be embayed.

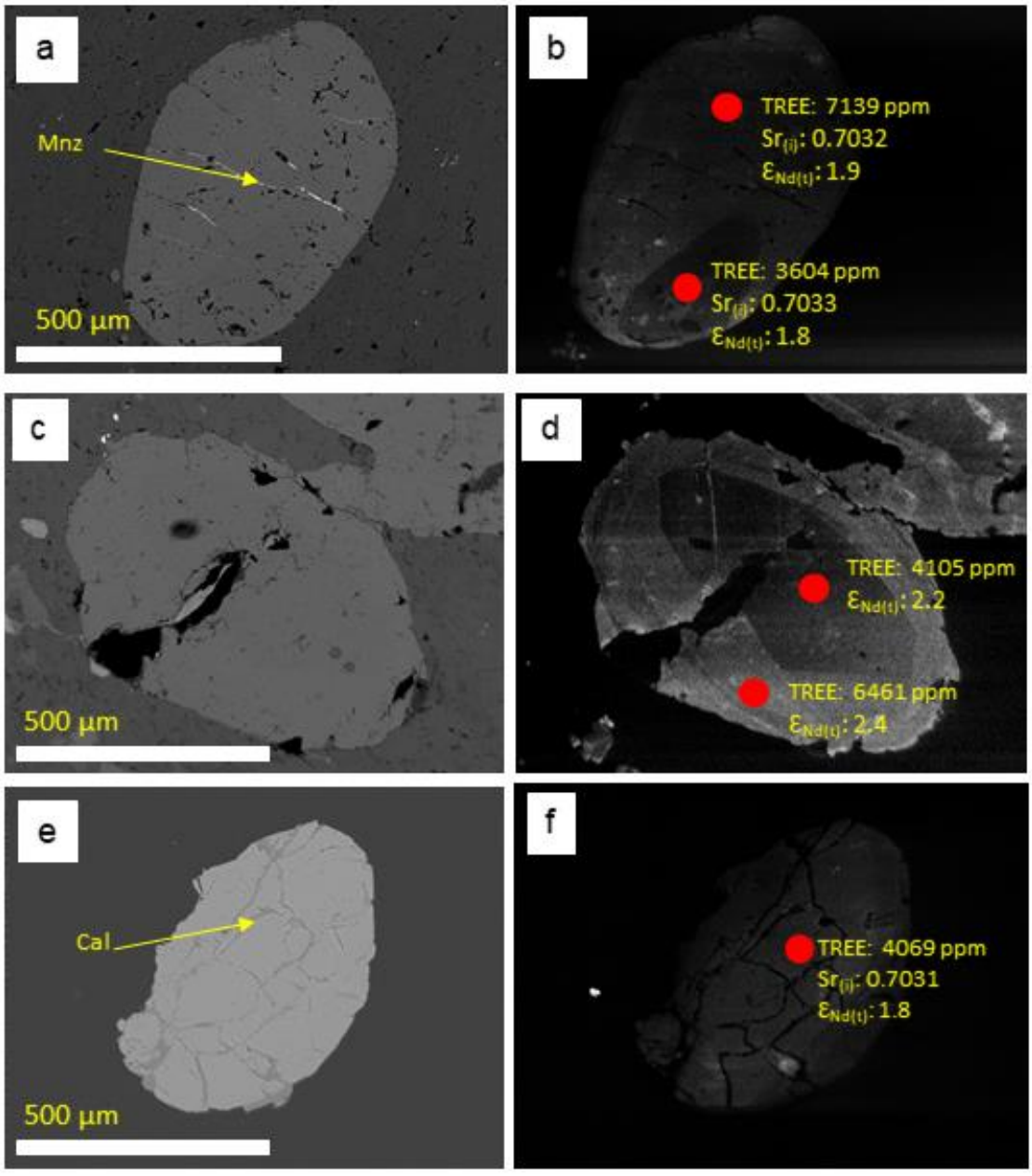

Fig. 4.3: Selected back scattered (a, c, e) and cathodoluminescence (b, d, f)) images of ovoid apatite from Epembe carbonatite. (a) Apatite displaying fractures, partially filled with monazite (mnz). (c) Dark core and light grey rim in zoned apatite. (c) Apatite with absent filled fractures.

(d) Core rim zoned apatite with a partially embayed core. (e) Apatite displaying calcite (cal) filled cracks. (f) Unzoned grey CL luminescent fractured apatite. Images a, b, c, and d show apatite in carbonatite EC 29, whereas e and f show apatites in carbonatite sample EC 23. The red dots are locations for trace element and isotope ratio analysis. TREE = total rare earth element concentration.

4.3.4. Apatite composition

Apatite major and trace element data are presented in Table 4.1 and Appendices 3 and 4. Chondrite-normalized REE patterns are shown in Fig. 4.4. Regarding syenite apatite, major elements P_2O_5 (40 wt%) and CaO (53 wt%) show little variation**,** whereas F varies from 3.43 to 3.61 wt% with Cl levels less than 0.04 wt%. Based on trace element data by LA-ICPMS, all apatite analyses are enriched in Si (8310-50000 ppm, $\bar{x}$ = 15207 ppm) relative to Na (536-1740 ppm, $\bar{x}$ = 969 ppm). All apatite grains are characterized by elevated REE (9189-44100 ppm) concentrations and are LREE enriched relative to HREE with La_N/Yb_N of 41 to 91 and distinctive negative Eu anomalies (Eu/Eu* = 0.36-0.86, $\bar{x}$ = 0.6). Trace elements, including Sr (1480-6630 ppm), Mn (53-1470 ppm), Fe (19-3900 ppm, except one analysis with 44000 ppm), Y (513-2590), Pb (9-97 ppm), Th (27-890 ppm), and U (3-109 ppm) are variable. Other trace elements, Ti, V, Zr and Rb are less than 84 ppm in abundance, although values of 660 ppm and 630 ppm of Ti and 110 ppm Zr are noted.

Nepheline syenite apatite grains are characterized by similar major geochemical characteristics. The major elements P_2O_5 and CaO show a range from 38-42 wt% and 50-54 wt%, respectively. Fluorine is variable, from 2.0-3.9 wt%, and Cl is less than 0.3 wt%. Based on trace element data by LA-ICPMS, apatite from nepheline syenite samples SNT 03, SNT 04, SNT 05, SNT 07 and SNT 09 are geochemically similar. They are enriched in Si (6340-175000 ppm) relative to Na (657-17200 ppm). They are characterized by LREE enrichment (La_N/Yb_N = 32-94) over HREE with a total REE range of 2625-8304 ppm, and Eu anomalies are close to unity. The trace element contents of Sr (6790-15840 ppm), Y (133-430 ppm), Pb (1-16 ppm), Th (3-126 ppm) and U (0-17 ppm) show variability among apatite grains. The majority of Mn and Fe concentrations fall within

100s of ppm, however, a few analyses with greater than 1000 ppm have been observed. Other trace elements, including Ti, V, Zr and Rb, are less than 100 ppm in abundance, however values of up to 3400 Rb, 480 ppm Ti and 1100 Zr are noted in some analyses and are attributed to accidental analyses of mineral inclusions or impurities of associated feldspar, zircon and sphene. A closer examination of zoned apatite from sample SNT 03 shows that the lighter grey CL domains on the rim are enriched in REE and Y relative to the darker grey cores.

Patchy apatite grains from nepheline syenite sample SNT 06 are depleted in Na (34-92 ppm), Ti (< 1.5 ppm), V (< 1 ppm), Y (39-60 ppm), Zr (< 0.08 ppm), Th (< 0.05 ppm), U (< 0.2 ppm), total REE (147-578 ppm), La_N/Yb_N (4-19) relative to homogeneous grey apatite from the same sample (as well as other nepheline syenite apatite), whereas Mn (2540-7040 ppm), Fe (2610-7040 ppm) and Sr (11410-14600 ppm) are higher. Concentration of Rb (0-0.6 ppm), Si (6970-8390 ppm) and Eu/Eu* (= 1) is similar to other nepheline syenite apatite.

With regards to carbonatite apatite, major elements (P and Ca) show little variation, specifically CaO ranges from 51 to 56 wt%, while P_2O_5 ranges from 42.3 to 43.8 wt%. Fluorine varies from 2.3 to 3.3 wt%, while Cl is generally very low (≤0.02 wt%) in all the samples. Most of the apatite grains within Epembe carbonatite are characterized by Na_2O of 0.16 to 0.23 wt% and SrO of 1.02 to 1.96 wt%. The SiO_2 content is low (<0.07 wt%) in most of the apatite grains, except for a few grains with values of up to 0.4 wt%. Analysis by WDS yields: Ce_2O_3 of up to 0.42 wt% and La_2O_3 less than 0.15 wt%. Apatite trace element results indicate that apatite from the carbonatite samples are geochemically similar, with variable Y (50-331 ppm), V (0-35 ppm), Pb (1-54 ppm) and Th (0-27 ppm). U is very low (< 26 ppm) in most grains, except in three cases that contain high values (71, 830 and 2470 ppm). The 71 and 2470 ppm are recorded in apatite from carbonatite EC 21, whereas a concentration of 830 ppm is from EC 5 apatite. Measured LREE data by EPMA are in agreement with those of LA-ICPMS. LA-ICPMS results show total REE in the range of 1161-8618 ppm, La_N/Yb_N between 24 and 164. Europium is not anomalous relative to neighbouring REE with an overall average Eu/Eu* = 1. A closer examination of zoned apatite from sample EC 29 shows that the lighter grey CL domains on the rim are enriched in REE and Y relative to the darker grey cores.

Table 4.1: LA-ICPMS results (averages in ppm) of apatite from Epembe syenite, nepheline syenite and carbonatite

	Syenite		Nepheline syenite							
Sample	BX 01		SNT 03	2SE	SNT 03		SNT 04		SNT 05	
Description-CL	Homogeneous grey CL		Dark grey CL core		Light grey CL rim		Homogeneous grey CL		Homogeneous grey CL	
	n=29	2SE	n=3		n=3	2SE	n=42	2SE	n=11	2SE
Na	969	41	1545	89	1708	188	1415	151	1120	66
Si	15207	2054	7977	497	11037	2063	11932	2113	8968	888
Ti	62.09	30.15	11.03	4.21	17.63	3.92	20.95	10.49	8.36	2.47
V	3	0.47	5.5	0.55	21.79	27.37	5.78	0.8	5.12	0.44
Mn	197	30	265	4.93	302	20.1	239	11.9	377.9	51.7
Fe	2356	585	300	51	383	50	539	137	276	62
Rb	2.6	0.64	0.37	0.18	1134	1533	1.02	0.29	0.28	0.19
Sr	3581.1	114	8032	128	10137	447	8371.4	224.3	8232	169.18
Y	1063	43.7	204.4	4.4	345	44.3	192.4	7	228	5.91
Zr	9.6	6.2	1.97	0.18	367.68	500.19	3.37	0.94	4.61	0.97
La	4537	218	618	14.67	1028	114.33	676	49.5	799	30.4
Ce	9041	405	1707	41.33	2753	300	1656	108	1951	70.45
Pr	841.2	34.42	215.7	5	338.7	36	208.8	11.85	245	8.56
Nd	3041	123	920	22	1417	144	888	44	1047	33.82
Sm	429.61	17.57	155.77	3.83	243	26	154	6.57	183	5.08
Eu	68.4	3.17	44.08	1.13	72.83	8.67	42.36	1.85	49.17	1.44
Gd	297.9	12.6	108.13	2.7	170.7	18.3	108.1	4.94	128	3.39
Tb	37.0	1.64	11.91	0.28	19.23	2.13	11.69	0.55	13.97	0.37
Dy	212.9	9.56	57.73	1.5	94.7	10.6	56.5	2.69	66.6	1.83
Ho	38.8	1.80	8.54	0.21	14.07	1.6	8.33	0.4	9.7	0.26
Er	97.6	4.46	17.87	0.43	29.3	3.3	17.2	0.84	19.7	0.53
Tm	10.8	0.51	1.83	0.05	2.97	0.34	1.73	0.08	2	0.06
Yb	49.1	2.36	8.68	0.24	13.9	1.5	8.15	0.4	9.37	0.29
Lu	4.7	0.23	0.95	0.02	1.47	0.15	0.89	0.05	1.02	0.05
Pb	24.9	2.28	4.17	0.18	4	0.57	4.73	0.47	5.97	0.62
Th	156.5	15.3	27.04	2	21.35	2.01	33.14	4.46	43.68	4.15
U	19.7	1.73	3.19	0.21	0.93	0.38	4.32	0.6	5.93	0.66
REE	18708		3876		6199		3838		4524	
La_N/Yb_N	62.4		48.0		49.9		56.0		57.5	
Eu/Eu*	0.55		0.99		1.04		0.96		0.94	

Table 4.1. Continued

Nepheline syenite								
Sample	SNT 06		SNT 06		SNT 07		SNT 09	
Description-CL	Homogeneous grey CL		Patchy CL		Homogeneous grey CL		Homogeneous grey CL	
	n = 12	2SE	n = 6	2SE	n = 26	2SE	n = 12	2SE
Na	1023	76.3	58.4	8.67	1872	143	1967	393
Si	7608	465	7553	663	16964	3578	10384	1577
Ti	18.39	14.73	1.46	0.7	27.86	9.68	66.97	46.93
V	6.25	0.73	0.36	0.11	5.07	0.45	16.58	1.24
Mn	204.7	6.96	3044	97.8	288.2	17.6	303	13.23
Fe	751.2	318.1	4473	232	587.1	252.02	1484	806
Rb	0.21	0.08	0.25	0.1	2.54	1.11	2.38	1.93
Sr	9199	211	12277	500	8374	257	12523	278
Y	221.63	5.62	48.05	2	188.28	7.72	288.82	13.79
Zr	3.43	0.7	0.08	0.03	1.52	0.29	1.69	0.13
La	774.08	36.5	50.07	18.98	642.27	29.39	1079	38.42
Ce	1911	74.33	119.7	32.35	1581	64.5	2413	91.92
Pr	239.3	8.25	14.12	3.36	201.5	7.76	287.18	11.85
Nd	1013	31.92	60.08	11.12	854	32.52	1182	52.58
Sm	172.72	4.53	12.2	1.31	149.2	6.08	197.09	9.61
Eu	47.5	1.18	3.92	0.32	39.35	1.62	57.41	2.94
Gd	120.36	2.91	11.16	0.82	104.74	4.52	140.32	7.06
Tb	13.23	0.31	1.52	0.09	10.7	0.48	15.68	0.78
Dy	64.18	1.54	9.2	0.45	52.13	2.35	78.72	4.16
Ho	9.5	0.24	1.73	0.08	8.02	0.37	12.08	0.62
Er	19.68	0.52	4.66	0.18	17.05	0.83	26.2	1.32
Tm	2	0.06	0.63	0.03	1.71	0.09	2.78	0.13
Yb	9.42	0.29	4.08	0.15	8.09	0.41	13.74	0.62
Lu	1.02	0.03	0.61	0.02	0.89	0.05	1.55	0.07
Pb	5.71	0.26	4.97	0.21	4.05	0.37	7.39	0.37
Th	48.92	3.03	0.02	0.02	22.42	1.98	38.54	3.38
U	5.79	0.47	0.07	0.03	2.79	0.59	4.67	0.48
REE	4397		294		3671		5506	
La_N/Yb_N	55.4		8.3		53.5		52.9	
Eu/Eu*	0.96		1.01		0.92		1.01	

Table 4.1. continued

	Carbonatite											
Sample	EC 4		EC 5		EC 21		EC 23		EC 29			
Description-CL	Homogeneous grey CL		Homogeneous grey CL		Homogeneous grey CL		Homogeneous grey CL		Dark grey CL core		Light grey CL rim	
	n = 20	2SE	n = 13	2SE	n = 36	2SE	n = 20	2SE	n = 3	2SE	n = 3	2SE
V	3.41	0.59	4.66	0.95	1.79	0.32	5.3	1.42	0.71	0.1	0.12	1.34
Sr	10609	388	8127	718	10869	371	9758	314	11570	507	11777	1247
Y	180.6	4.05	133.8	9.95	234.8	5.08	246.12	6.04	208.7	7.2	289.83	26.77
La	568.77	21.36	612.02	53.08	985.92	33.11	1019.7	55.55	641.67	29.67	1147.67	133.67
Ce	1484.7	40.6	1499.92	143.54	2375.08	80.89	2455.2	113.4	1734.67	113.33	2889.33	314
Pr	184.6	5.17	176.28	15.26	277.95	8.74	296.25	12.19	199	16.67	348.73	40.33
Nd	786.47	24.5	697.54	60.77	1153	42.31	1240.8	47.75	933.67	67.67	1502	165
Sm	150.44	5.08	118.75	10.4	197.1	7.59	216.6	7.81	162.27	13.33	260.13	24.67
Eu	41.82	1.4	32.41	3.46	56.07	2.21	61.03	2.32	44.33	3.4	71.93	7
Gd	101.99	4.69	77.45	8.98	133.8	5.23	148.13	5.82	110.9	6.03	174.43	16.23
Tb	11.54	0.67	8.38	1.01	14.38	0.61	15.9	0.64	11.97	0.73	18.47	1.84
Dy	55.06	3.25	39.37	4.35	67.28	3.21	72.56	3.78	57.83	3.1	85.63	9
Ho	7.91	0.52	5.65	0.57	9.65	0.53	10.37	0.65	8.33	0.76	11.94	1.32
Er	14.61	1.08	11.21	1.38	18.92	1.07	19.92	1.41	16.31	1.6	23.28	2.63
Tm	1.38	0.13	1.09	0.16	1.89	0.14	1.95	0.16	1.69	0.2	2.2	0.28
Yb	6.06	0.61	5.06	0.84	8.4	0.7	8.33	0.75	7.54	0.63	9.71	1.35
Lu	0.6	0.07	0.51	0.1	0.85	0.1	0.84	0.09	0.78	0.12	0.87	0.14
Pb	1.86	0.11	10.73	1.91	4.68	0.44	2.7	0.31	2.82	0.23	16.82	4.51
Th	5.57	0.49	8.26	0.9	13.94	1.08	9.76	1.19	6.77	0.74	5.12	1.67
U	0.09	0.02	64.72	13.28	76.29	7.06	1.14	0.22	0.38	0.11	0.33	0.18
TREE	3416		3286		5300		5568		3931		6546	
La_N/Yb_N	63.3		81.5		79.2		82.5		57		79.7	
Eu*	0.98		0.97		1		0.99		0.96		0.98	

TREE = Total rare earth elements

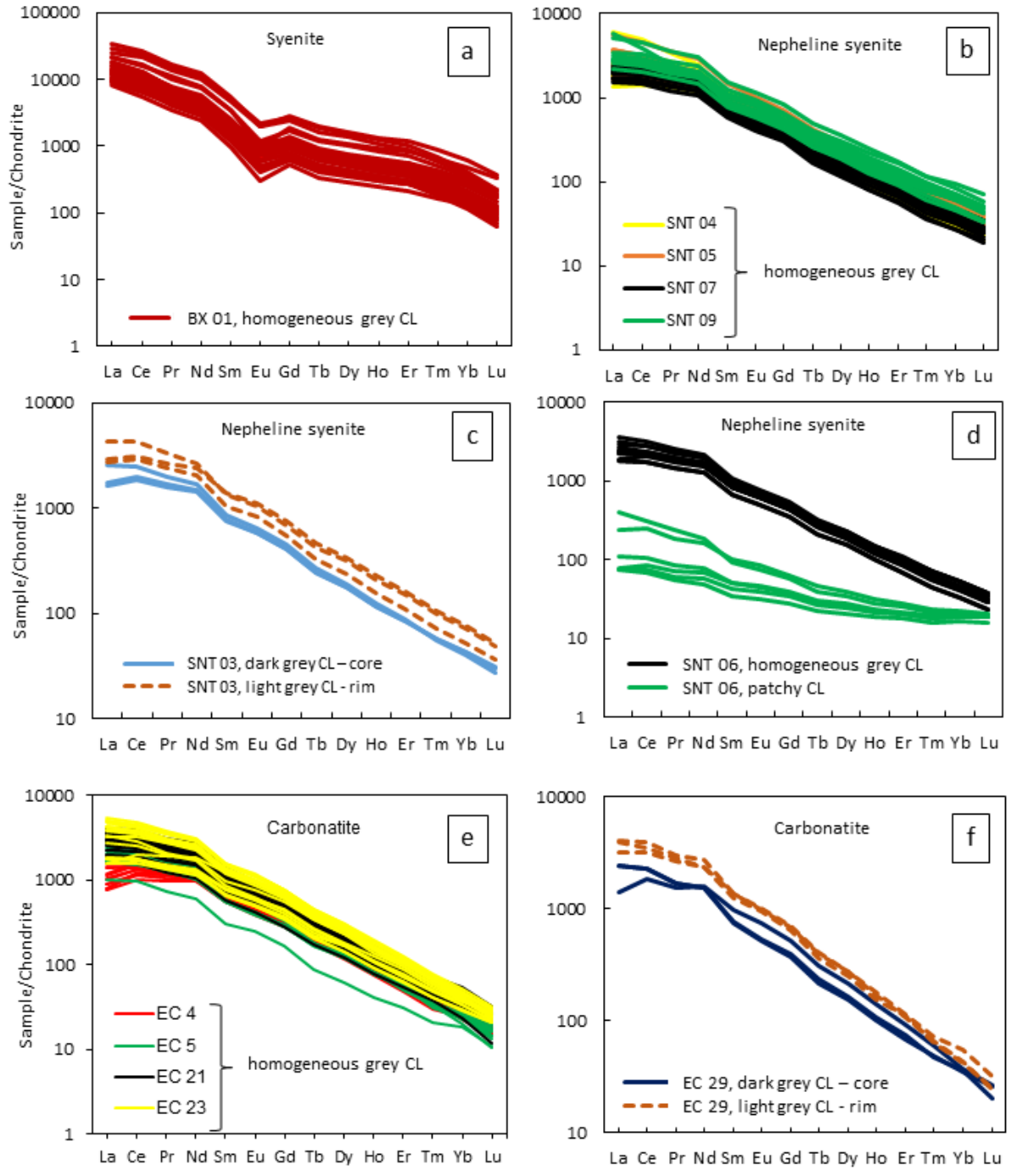

Fig. 4.4: Chondrite-normalized rare-earth element patterns. (a) Homogeneous grey CL luminescent syenite apatite. (b) Homogeneous grey CL luminescent apatite in nepheline syenite (samples SNT 04, SNT 04, SNT 05, SNT 07 and SNT 09). (c) Dark grey core and light grey rim CL

zoned nepheline syenite apatite, sample SNT 03. (d) Homogeneous grey Cl luminescent and patchy apatite, nepheline syenite sample SNT 06. (e) Homogeneous grey CL luminescent apatite in carbonatite (samples EC 4, EC 5, EC 21 and EC 23). (f) Dark grey core and light grey rim CL zoned carbonatite apatite, sample EC 29. Normalization values from Boynton (1984).

4.3.4. Apatite U-Pb geochronology

The U-Pb geochronology results are presented in Appendix 5, and graphically displayed in Tera-Wasserburg-type diagrams (Fig. 4.5). For syenite sample BX 01, 31 analyses define a discordant array between a $^{207}Pb/^{206}Pb$ value of 0.9454 ± 0.0093 at the ordinate intercept and a lower intercept with concordia corresponding to an age of 1216 ± 11 Ma (MSWD = 4.3; n = 26) (Fig. 4.5a). The coupled trace element ratio Sr/Y vs LREE concentration for all apatite grains in this sample plot within the alkali-rich igneous rocks (ALK) field of O'Sullivan et al. (2020) (Fig. 4.5b).

With regards to the nepheline syenites, U-Pb isotopic measurements were performed on apatite from three samples (SNT 06, SNT 07 and SNT 09). U-Pb ages for apatite from samples SNT 06 and SNT 07 have been deduced by anchoring the $^{207}Pb/^{206}Pb$ to that obtained from SNT 09 (0.92) in which the data points spread consistently along the Discordia curve and are not associated with large uncertainties. For sample SNT 06, 24 analyses produce a lower intercept corresponding to an age of 1193 ± 14 Ma (MSWD = 3.2; n = 7: Fig. 4.5c). Apatite grains in sample SNT 06 are homogeneous grey CL luminescent and patchy, and their trace element compositions coincide with the Ultramafic Igneous (UM; homogeneous grey CL luminescent apatite), the low- and medium grade metamorphic and metasomatic (LM; patchy apatite) compositional fields (Fig. 4.5d). This age is based on homogeneous grey CL luminescent apatite only. The patchy apatite measurements do not define any trend and thus no meaningful age could be derived, consistent with their very low Th (< 0.05 ppm) and U (< 0.2 ppm) concentrations. For twenty-six U-Pb analyses for sample SNT 07 a lower intercept age corresponds to 1197 ± 17 Ma (MSWD = 2.3; n = 13) (Fig. 4.5e). The trace element ratios Sr/Y vs LREE concentrations fall within the Ultramafic Igneous rocks field (Fig. 6f). Fourteen U-Pb analyses for sample SNT 09 define a discordant array that spreads between a $^{207}Pb/^{206}Pb$ value of 0.9230 ± 0.0069 at the ordinate intercept and a lower

intercept on the concordia corresponding to 1194 ± 16 Ma (MSWD = 2.8; n = 11) (Fig. 4.5g). In this sample, apatite trace element ratios also plot within the Ultramafic Igneous rocks compositional field (Fig. 4.5h). For carbonatite apatite, no U-Pb ages were obtainable due to very low U concentrations, which is also lower than that of most other apatite grains from syenite and nepheline syenites.

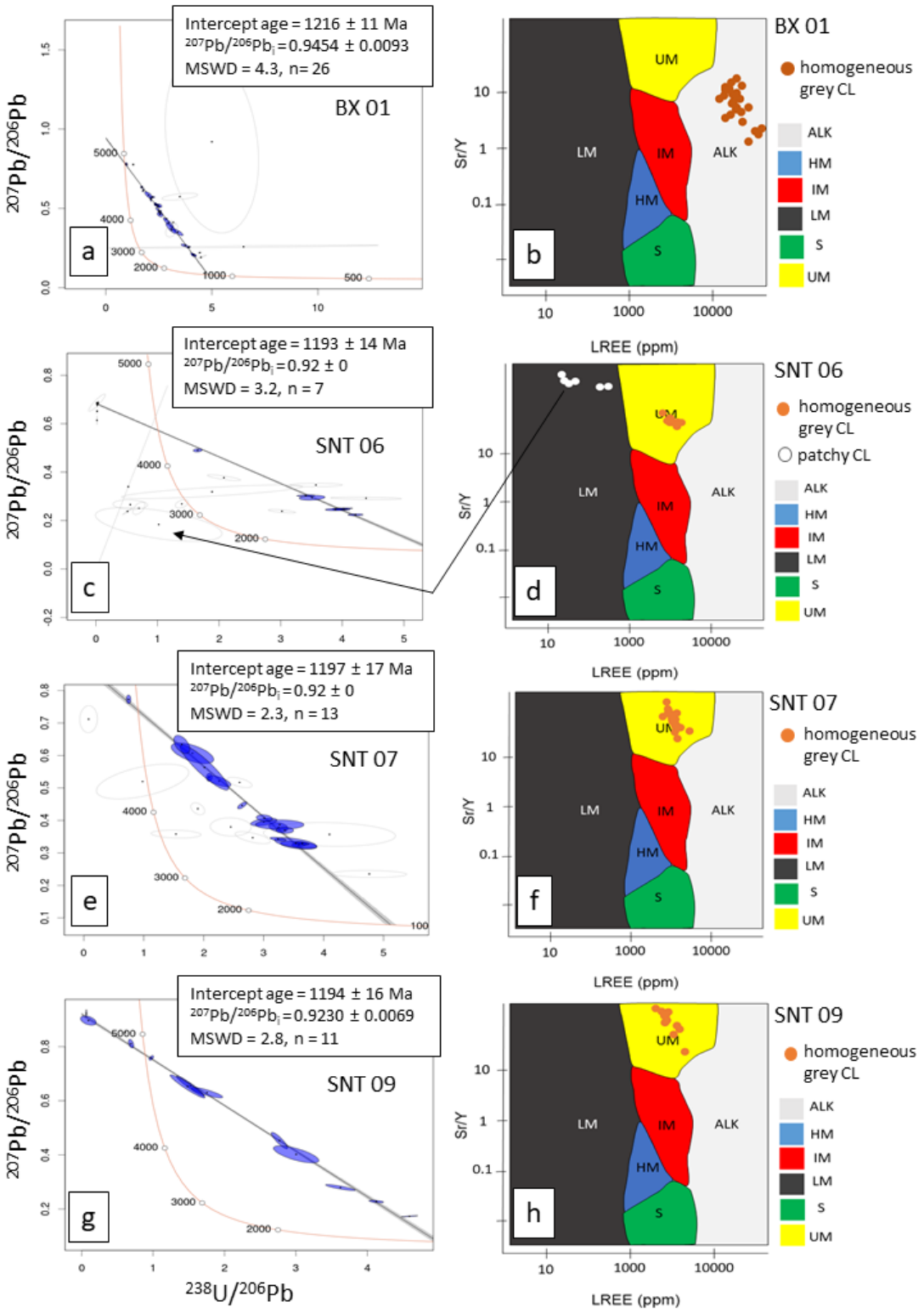

Fig. 4.5: U-Pb Tera-Wasserburg concordia diagrams for syenite apatite (a), nepheline syenite apatite (c, e, g). Error ellipses are 2 SE. Diagrams of Sr/Y ratios vs LREE (La + Ce + Pr + Nd) for

syenite apatite (b) and nepheline syenite apatite (d, f, h) after O'Sullivan et al. (2020). Acronyms: UM = ultramafic igneous; S = felsic granitoids; ALK= alkali rich igneous; IM = mafic granitioids and mafic igneous rocks; HM = high grade metamorphic; LM = low-to medium-grade metamorphic and metasomatic.

4.3.5. Sr and Nd isotope geochemistry

Apatite in syenite, carbonatite and nepheline syenite samples (homogeneous grey CL and CL zoned apatite) are characterized by elevated Sr (1480-15840 ppm) and Nd (627-7200 ppm) contents, Sr and Nd isotopic analyses were undertaken on these apatite grains and the results are presented in Appendix 6. Patchy apatite from nepheline syenite pegmatite contains sufficiently high Sr concentrations (11410-14600 ppm) for Sr isotopic analysis, but low Nd abundances (<112 ppm) prevented reliable Nd isotopic analyses (e.g. Wu et al., 2011). Given that apatite ages may not always give crystallization ages of the host rocks (e.g. Kirkland et al., 2018), zircon crystallization ages (1220 Ma for syenite, 1209 Ma for nepheline syenite and 1198 Ma for carbonatite: Tshiningayamwe et al., submitted) were used to back calculate the initial Sr ($^{87}Sr/^{86}Sr_{(i)}$) and Nd ($^{143}Nd/^{144}Nd_{(i)}$) compositions.

For syenite sample BX 01, four Sr isotope analyses on 3 apatite grains gave $^{87}Sr/^{86}Sr_{(i)}$ from 0.7035 to 0.7048. For nepheline syenites, a total of 15 analyses gives a narrow range of $^{87}Sr/^{86}Sr_{(i)}$ from 0.7031 to 0.7037. Two analyses of patchy apatite from nepheline syenite sample SNT 06 give $^{87}Sr/^{86}Sr_{(i)}$ of 0.7033 similar to other nepheline syenite apatite. A closer examination of zoned apatite shows that both core and rim have similar $^{87}Sr/^{86}Sr_{(i)}$ values, for instance spot SNT 03-1 (core) with $^{87}Sr/^{86}Sr_{(i)}$ of 0.7031 and spot SNT 03-2 (rim) with $^{87}Sr/^{86}Sr_{(i)}$ of 0.7031. In carbonatite apatite, five analyses returned similar $^{87}Sr/^{86}Sr_{(i)}$ of 0.7031 to 0.7033.

Syenite sample BX 01 (one analysis on four apatite grains) produced $^{143}Nd/^{144}Nd$, $^{143}Sm/^{144}Nd$ and $\varepsilon_{Nd(t)}$ of 0.511885–0.512050, 0.084953–0.102921 and +2.5±0.2 to +3.2±0.4 respectively. CL luminescent apatite within the nepheline syenites produced a total of 14 analyses: $^{143}Nd/^{144}Nd$, $^{143}Sm/^{144}Nd$ and $\varepsilon_{Nd(t)}$ of 0.511980-0.512145, 0.087910-0.109819 and +1.5±0.4 to +4.4±0.6, respectively. One analysis of apatite (spot SNT 03-2) is on the rim domain

of core-rim zoned apatite with $^{143}Nd/^{144}Nd$=0.512113, $^{143}Sm/^{144}Nd$= 0.103198 and $\varepsilon_{Nd(t)}$ = 4.3±0.5, similar to the other analyses. For carbonatite-hosted apatite 22 analyses returned similar, but variable $^{147}Sm/^{144}Nd$, $^{143}Nd/^{144}Nd$ and $\varepsilon_{Nd(t)}$ of 0.0950-0.1280, 0.511889-0.512131 and 0.0±0.5 to +3.3±1.1, respectively

4.5. Discussion

4.5.1. Processes forming apatite and controlling its REE content

Cathodoluminescence imaging is well suited for examining mineral textures (e.g. Lu et al., 2021). Magmatic apatite is usually characterized by growth (oscillatory) zoning or homogeneous domains (Gros et al., 2016; Zhang et al., 2020). Magmatic apatite from carbonatite usually displays core-rim zoning in CL, controlled by chemical changes of substituting elements, such as Mn and REE (Chakhmouradian et al., 2017, Lu et al., 2021). In addition, magmatic apatite from carbonatites is enriched in LREE over the REE with La_N/Yb_N from 32 to 853 (Chakhmouradian et al., 2017, Lu et al., 2021)**.** Cooling and crystallizing syenite and carbonatite bodies can release fluids, which in turn metasomatize primary mineral assemblages, including apatite (e.g. Chakhmouradian et al., 2002; Liferovich and Mitchell, 2006). Late-stage metasomatic apatite occurs as turbid, overgrowths or as alteration patches in CL images accompanied by a decrease in REE, Y and Sr relative to its igneous precursor (Harlov et al., 2002; Chakhmouradian et al., 2017; Decrée et al., 2021). However, in some instances, Sr concentration may increase from magmatic to later metasomatic apatite as shown in apatites from Xindigou, northern China (Zhang et al., 2020) as well as in a compilation of apatite trace element data from various kinds of bedrock (O'Sullivan et al., 2020). Primary mineral assemblages can also be altered by meteoric fluids as shown for apatites from syenite satellites to the Phalaborwa Complex, South Africa (Decrée et al., 2020). In this study, Sr isotope composition of magmatic apatite and metasomatic apatite are different indicating that the source of metasomatizing fluids was not derived from the cooling syenite melt. Therefore, metasomatic changes in apatite are preserved texturally, chemically and isotopically (e.g. Chakhmouradian et al., 2002; Liferovich and Mitchell, 2006; Decrée et al., 2020; Broom-Fendley et al., 2017, Harlov et al., 2002). In order to explore the processes controlling

apatite formation at Epembe, a magmatic origin of apatite is first evaluated using textural and chemical criteria.

4.5.1.1. Apatite in syenite

Textural and chemical features of apatite grains from Epembe syenite suggest a magmatic origin. They are homogeneous in BSE (Fig. 4.2a) as well as in CL (Fig. 4.2b) and they are enriched in LREE (La_N/Yb_N = 41-91). Moreover, their Sr/Y ratios vs LREE concentration plot in the field of magmatic apatite derived from alkali-rich igneous rocks (Fig. 4.5b) (O'Sullivan et al., 2020). Therefore, the incorporation of REE in syenite apatite occurred at magmatic stage. Apatite in this sample contains the highest REE concentration among all studied apatite grains and the observed REE patterns in syenite apatite show a markedly negative Eu anomaly (Eu/Eu*=0.36-0.86) similar to apatite formed in a magma that evolved by fractional crystallization of mafic mantle-derived melts (e.g. Permian Oslo rift Belousova et al., 2002b). This implies that apatite grains from syenite BX 01 crystallized from an evolved magma.

A negative Eu anomaly in apatite can arise from early plagioclase formation and removal from the evolving melt as plagioclase can concentrate Eu^{2+} by substituting for Ca (e.g. Belousova et al., 2002; Chakhmouradian et al., 2017). Alternatively, Eu^{2+} together with Y can partition into high-temperature fluids evolving from a melt (Bühn et al., 2001). The negative Eu anomalies in syenite apatite is not likely due to the presence of a high temperature fluid, since the Y/Ho ratio of these apatite grains is chondritic, arguing against the removal of Y (and indirectly Eu^{2+}) from the melt by a high-temperature fluid. Moreover, there is no correlation between Eu/Eu* and Y in these apatite grains (Fig. 4.6). Thus, the explanation for negative Eu anomalies in syenite apatite is earlier plagioclase formation and removal from the evolving melt.

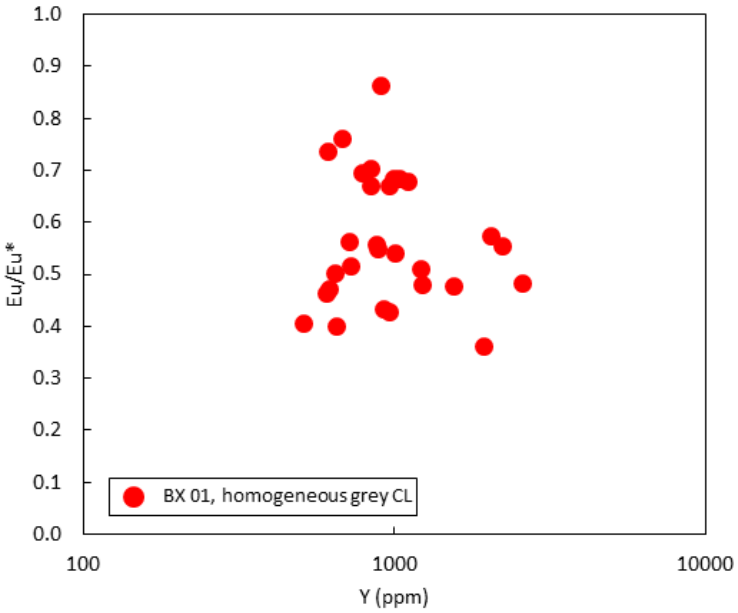

Fig. 4.6: Eu/Eu vs Y diagram for Epembe syenite apatite.*

4.5.1.2. Apatite in nepheline syenite

In CL imaging, apatite grains from samples SNT 04, SNT 05, SNT 07 and SNT 09 are homogeneous grey, whereas sample SNT 03 apatite displays core-rim zoning with a darker grey core and a light grey rim. These features are different from late-stage magmatic/hydrothermal apatite, which commonly displays turbid or conversion textures (Broom-Fendley et al., 2016; Decrée et al. 2020). Moreover, the apatite grains are strongly enriched in LREE (La_N/Yb_N = 61-115) and their Sr/Y ratios vs LREE concentrations plot within the Ultramafic Igneous rocks field (e.g. Figs. 4.5f, h) consistent with apatite grown from a crystallizing magma. We therefore consider the partitioning of REE in these apatite grains to be due to magmatic processes.

Core-rim zoning observed in apatite from sample SNT 03 under CL is accompanied by an increase in REE (Fig. 4.4c) and Y from core to rim. Magmatic-related zoning in apatite can be caused by fractional crystallization or magma mixing (Wang et al., 2014; Chakhmouradian et al. 2017; Décree et al., 2020). Attributing the variation in REE composition of apatite to fractional crystallization requires well- known partition coefficient values for apatite (and other minerals if

any) and the host melt as well as the modal abundance of fractionating mineral assemblage. For instance, Brassiness et al. (2005) showed that the REE content in apatite from the alkaline and carbonatite intrusion of Vuoriyarvi, Russia, increases in the sequence clinopyroxenite-ijolite-carbonatite, with carbonatite being the youngest intrusive phase. This sequential increase in apatite REE content was explained by a variable fractionating assemblage of 98% clinopyroxene + 1% apatite + 1% perovskite changing to 94% clinopyroxene + 5% apatite + 1% perovskite (apatite- and clinopyroxene-carbonatite melt partition coefficient values from Klemme et al., 1995; perovskite-melt partition coefficient values from Nagasawa et al., 1980), such that the overall partition coefficient of the fractionating mineral assemblage is less than 1, which results in REE enrichment in the evolving melt (Brassiness et al., 2005). On the other hand, Decrée et al. (2020) showed that apatite from Phalaborwa pyroxenite and phoscorite rocks are characterized by core-rim CL (light grey core and dark grey rim) zoning with a rim-ward decrease in REE. They proposed that partition coefficient values were greater than unity or a significant proportion of apatite was involved within the crystallizing mineral assemblage in order to account for the decrease in REE content of the evolving melt.

Although the proportion of apatite in the fractionating mineral assemblage cannot be constrained in Epembe nepheline syenites, fractional crystallization of the host magma may not likely explain the rim-ward increase in REE concentration in core-rim zoned apatite, because (1) apatite appears to be the main REE carrier in these rocks as shown by increasing whole rock SiO_2 concentration accompanied by a decrease in P_2O_5 and REE contents among nepheline syenite samples, implying that apatite fractionation lead to a progressive decrease in REE concentration in the evolving melt (Tshiningayamwe et al., submitted). The REE affinity of apatite in silicate melts was shown experimentally by Prowatke and Klemme (2006), indicating that partition coefficient values between apatite and silicate melt are greater than unity. (2) Other elements, such as Na and Si do not define systematic changes between core and rim in apatite along with the REE as should be expected in a magma that is undergoing fractional crystallization. Alternatively, the rim-ward increase of REE in zoned apatite may be explained by formation of early apatite (core) followed by later local intrusion of new magma enriched in REE, such that early formed apatite is re-equilibrated with the new magma, which in turn formed the rim

(Chakhmouradian et al. 2017; Decrée et al., 2020). At Epembe, the carbonatite is enriched in REE compared to the nepheline syenite and was emplaced shortly after the emplacement of the nepheline syenite (Tshiningayamwe et al., submitted) thus, the enrichment of REE in nepheline syenite apatite rims relative to the cores can be attributed to infiltration of carbonatite melts in the nepheline syenite. Since there is no change in initial Sr and Nd isotopic composition between cores and rims, the sources of these magmas were similar. The absence of a negative Eu anomaly in these apatites indicates that differentiation of the primary magma evolved without plagioclase fractionation consistent with apatite from other nepheline syenite occurrences, such as those of Khibiny, Kola Peninsula (Kogarko, 2018).

For nepheline syenite sample SNT 06, two types of apatite were observed in CL, including homogeneous-unzoned and patchy apatite (characterized by areas of different brightness, Fig. 4.2f). Patchy apatite shows REE (147-578 ppm), Y (39-60 ppm), (La_N/Yb_N = 4-19) and Na (34-92 ppm) depletions and high Sr (11410-14600 ppm) contents relative to grey homogeneous CL luminescent apatite (REE = 3262-5840 ppm, Y = 163-255 ppm, La_N/Yb_N = 45-69, Na = 744-1385 ppm, Sr = 7980-10850 ppm) in the same sample (Figs. 4.4d, 4.7). The features of apatite grains with a homogeneous grey CL luminescence are consistent with a magmatic origin. This suggests that incorporation of REE, Y, Na and Sr into this apatite occurred during emplacement and crystallization of the nepheline syenite body as a function of pressure and temperature. The observed textural and chemical characteristics of patchy apatite are suggestive of a metasomatic related origin. The decrease in REE, Y and La_N/Yb_N in patchy apatite relative to homogeneous grey CL luminescent apatite could be due to coupled dissolution and reprecipitation of apatite during late stages of crystallization or after crystallization in the presence of a fluid (e.g. Harlov, 2011; Harlov et al., 2002). In this scenario, re-precipitating secondary apatite, depleted in REE and Y, formed together with a REE-rich phase, such as monazite or xenotime, which partition most of these elements (Harlov, 2011). Given that patchy apatite in the nepheline syenite is not associated with monazite or xenotime as shown by absence of bright phases in BSE images (Fig. 3e) (usually occurring as micro-inclusions in apatite) a coupled dissolution reprecipitation mechanism is not likely. Alternatively, low REE and Y in patchy apatite relative to homogeneous grey CL luminescent apatite are due to fluid flow through the rock, which mobilizes these

elements (Decrée et al., 2020; Harlov et al., 2002). Given that LREE are relatively more mobilized than HREE during fluid rock interactions and show greater stability as chloride or fluoride complexes (Broom-Fendley et al., 2016), a decrease in the La_N/Yb_N ratio of apatite interacting with such fluids is expected as seen patchy apatite from sample SNT 06. Therefore, interaction of apatite with fluids resulting in the mobilization of some elements is the proposed mechanism to explain the REE + Y depletion in patchy apatite. Similar, REE-depleted domains have been observed along the margins of apatite grains in the Port Leyden nelsonite, with no accompanying monazite inclusions (Darling and Florence, 1995). Increasing Sr concentration suggests that the metasomatic fluids were enriched in Sr, and Sr substituted directly for Ca in apatite due to similar size and charge (Pan and Fleet, 2002). Decreasing Na together with REE and Y from unaltered to altered apatite in nepheline syenite SNT 06 apatite suggests that the $Na^{+} + (Y^{3+} + REE^{3+}) = 2Ca^{2+}$ (Pan and Fleet, 2002) coupled substitution was effective. There are no significant changes in $^{87}Sr/^{86}Sr_{(i)}$ between altered and unaltered apatite suggesting that the fluids involved in the metasomatic alteration event were isotopically similar to the melt from which magmatic apatite formed, indicating that the fluids were probably derived from the cooling host magma.

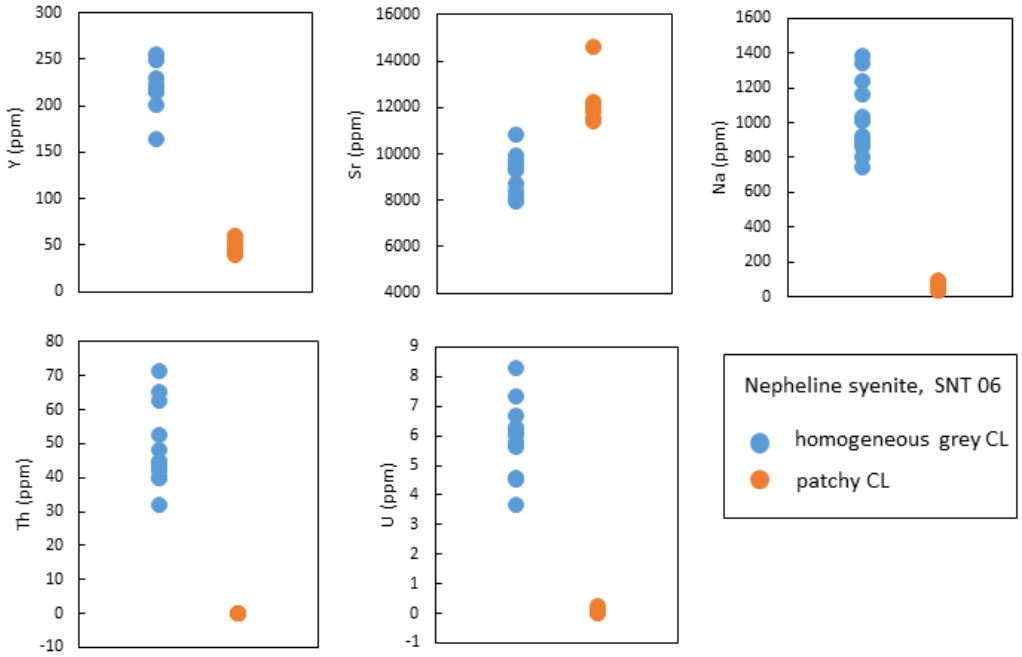

Fig. 4.7: Diagrams showing trace element contents in apatite from Epembe nepheline syenite sample SNT 06.

4.5.1.3. Apatite in carbonatite

A magmatic origin of apatite in the Epembe carbonatite is confirmed by its grey homogeneous or dark grey (core) and light grey (rim) zoning in CL (Fig. 4.3), and the enrichment in LREE relative to HREE (La_N/Yb_N = 24-161). An increase in REE and Y is observed from the core towards the rim in zoned apatite (from sample EC 29) using CL. Increasing REE and Y concentration reflected in core-rim-zoned apatite is common in apatite from carbonatites, and has been noted, for instance, in apatite from Phalaborwa carbonatite (Decrée et al., 2020) and the Songwe Hill carbonatite, Malawi (Broom-Fendley et al., 2017). Such a rim-ward increase in REE is attributed to the formation of early apatite (core) followed by the precipitation of rock forming non-phosphate mineral(s) with low $D^{REE}_{mineral/carbonatite\ melt,}$ such as calcite, which will raise the P_2O_5 and REE concentrations in the melt until P_2O_5 saturation is reached again, and a later, REE-rich apatite is precipitated as crystal rims (Gittins, 1989; Chakhmouradian et al., 2017). The irregular core outlines (Fig. 4.3d) suggest that early-formed apatite underwent abrasion during the hiatus, possibly due to the transport of apatite in a moving magma (Chakhmouradian et al., 2017). A lack of Eu anomalies in carbonatite apatite grains (Fig. 4.4e, f) is consistent with an absence of prior plagioclase formation and removal in the evolution of the Epembe carbonatite, in agreement with absence of Eu anomalies in apatite from other carbonatites (Chakhmouradian et al., 2017, Lu et al., 2021).

4.5.2. U-Pb geochronology

4.5.2.1. Factors affecting U-Pb ages of apatite

Deduced U-Pb apatite ages are always discussed in connection with their closure temperature. The closure temperature of a mineral phase represents the point in time at which a completely mobile daughter product of radiogenic decay becomes completely immobile (Dodson, 1973). The factors affecting when apatite reaches its closure temperature are thermally activated Pb diffusion (e.g. Gawęda et al., 2014; Kirkland et al., 2018), and combined dissolution and reprecipitation (e.g. Kirkland et al., 2018)

According to Kirkland et al. (2018), two general conditions can be considered for thermally-activated Pb diffusion as a response to decreasing temperature and a mineral's passage through its partial retention zone; 1) If the rate of compositional homogenization by diffusion within the mineral fails to keep up with the rate of change of the interface composition then the mineral would not have a single closure temperature, but a closure temperature profile consistent with a slow cooing scenario. 2) In contrast, if the mineral passes quickly through its partial retention zone then a single closure age may be preserved. Rapid cooling shortly after magmatism with a single U-Pb apatite age of ca. 340 Ma has been proposed by Gawęda et al. (2014) for three different granite types from the Tetra Mountains, Poland. In contrast, thermally-activated Pb diffusion accompanied by slow cooling through the apatite partial retention zone after metamorphic peak has been documented for some high-grade, lower to mid-crustal xenoliths from the Bearpaw Mountains, USA (O'Sullivan et al., 2021).

Since Pb loss is generally attributed to thermally-activated diffusion (Blackburn et al., 2011), it is expected that certain grain sizes correspond to certain age groups, for instance the larger grains will have older ages, whereas the smaller grains will have younger ages given the spherical geometry characteristics and Pb diffusion in apatite (Cherniak et al., 1991). However, Kirkland et al. (2018) showed that there is no correlation between grain size and age of apatite. These authors argue that grain size characterization in their study and many other studies is not likely, given the current analytical size constraints. Some authors have signaled that element mobility may be due to fluid-driven activity and that Pb loss by thermally-activated diffusion may be secondary (e.g. Chew et al., 2011; Chen and Simonetti, 2013).

Diffusion of Pb by dissolution and reprecipitation requires new growth of apatite later in the history of a rock. Growth of apatite in this way can be metasomatic in origin, whereby pre-existing apatite breaks down in the presence of infiltrating fluids (e.g. under metamorphic conditions). Reprecipitation of newly formed apatite can have a different chemical composition relative to its igneous precursor depending on factors such as the co-existence with mineral phases, which compete for elements. In the presence of epidote, it was suggested that infiltration of fluids occurred at low temperatures (< 600 °C), close to the closure temperature of apatite (Kirkland et al., 2018). Diffusion of Pb can also be achieved by percolating hydrothermal fluids

that exchange elements with apatite, such as REE, Sr and U. The mobility of Sr, U and REE under hydrothermal conditions well established (this study; Liferovich and Mitchell 2006; Broom-Fendley et al., 2016).

4.5.2.2. Interpretation of apatite U-Pb ages

Syenite sample BX 01 apatite gives a U-Pb age of 1216 ± 11 Ma. The apatite composition and texture is consistent with a magmatic origin (see section 4.5.1). The age is similar to 1220 ± 3 Ma for zircon (Table 4.2) from the same sample (Tshiningayamwe et al. submitted). The similarity in zircon and apatite ages from this sample suggests that the apatite age represents emplacement of the Epembe syenite, i.e fast cooling.

Magmatic apatite from the nepheline syenite samples SNT 06, SNT 07 and SNT 09 give U-Pb ages of 1193 ± 14 Ma, 1197 ± 17 Ma and 1194 ± 16 Ma, respectively. The analytical uncertainties are 1.1-1.4 % and are from low U concentration in apatite, which preferentially partition into coexisting zircon. Apatite (this study) and zircon magmatic U-Pb ages (1209 ± 3 Ma, 1205 ± 13 Ma: Table 4.2.; 1216 - 1213 Ma: Littmann et al., 2000 in Drüppel et al., 2007) from the nepheline syenite show excellent agreement considering analytical uncertainity. Considering the low closure temperature of apatite compared to zircon (Chamberlain and Bowring, 2001; Shoene and Bowring 2007), the apatite ages therefore record the timing of emplacement.

Table 4.2: Comparison of available U-Pb zircon ages with U-Pb apatite ages (this study) from the Epembe area.

	Zircon ages (Ma)	Interpretation	Reference	Apatite ages (Ma)
Carbonatite				
EPG	1173 ± 12	Magmatic	Simon et al. (2017)	
EPG	1184 ± 10	Magmatic	Simon et al. (2017)	
EC 21	1198 ± 5	Magmatic	Tshiningayamwe et al. (submitted)	
Nepheline syenite				
SNT 06	1205 ± 13	Magmatic	Tshiningayamwe et al. (submitted)	1073 ± 15
SNT 04	1209 ± 3	Magmatic	Tshiningayamwe et al. (submitted)	
-	1216 - 1213	Magmatic	Littmann et al. (2000)	
SNT 07				1150 ± 19
SNT 09				1178 ± 16
Syenite				
BX 01	1220 ± 3	Magmatic	Tshiningayamwe et al. (submitted)	1216 ± 11

4.5.3. Isotopic constrains on magma sources

Alkaline magmas can be sourced from the asthenospheric mantle by small degrees of partial melting (Fitton, 1987), or form by partial melting of a metasomatized, LILE- and light REE-enriched upper mantle (Dawson, 1987), or from interaction of asthenospheric mantle-derived magma with the lithosphere during ascent (Menzies, 1987). The generation of the most evolved rock types of alkaline suites such as syenites can be by fractionation from alkali basaltic parents combined with input from the continental crust (Foland et al., 1993; Jung et al., 2007), or by small degree partial melting of the enriched lower continental crust (e.g. Drüppel el., 2007). Available isotope data indicate that carbonatites exhibit large isotopic variations, requiring a number of different sources ranging from enriched to depleted mantle located in the asthenosphere or in the subcontinental lithospheric mantle (e.g. Bell and Simonetti, 2009; Nelson et al., 1988; Wu et al., 2011)

The Sr and Nd isotopic compositions of apatite from Epembe syenite ($^{87}Sr/^{86}Sr_{(i)}$ = 0.7035-0.7048; $\varepsilon_{Nd(t)}$ = +2.5 to +3.2), nepheline syenites ($^{87}Sr/^{86}Sr(i)$ = 0.7031-0.7037; $\varepsilon_{Nd(t)}$ = +1.5 to +4.4) and carbonatite ($^{87}Sr/^{86}Sr(i)$ 0.7031-0.7033; $\varepsilon_{Nd(t)}$ = 0 to +3.3) are similar suggesting a common mantle source. They plot in the time integrated Depleted Mantle quadrant towards CHUR (Fig.

4.8). The generally unradiogenic $^{87}Sr/^{86}Sr_{(i)}$ = 0.7031-0.7048 obtained on apatite from all rock types indicate that the parental mantle-derived magmas were not affected by contamination with evolved crustal material. Also, the high Sr and Nd abundance in syenite, nepheline syenite and carbonatite apatite relative to apatite from continental granites and pegmatites (e.g. Belousova et al., 2002b) argue against crustal contamination as the high Sr and Nd concentrations in the Epembe apatite would prevent significant influence by the continental crust (Wu et al., 2011). The Nb/U (3-584) and Ce/Pb (12-58) ratios of bulk rocks, also reflected in absent negative Nb and positive Pb anomalies in PRIMA-normalized diagrams (Tshiningayamwe et al., submitted) are different from typical crustal rocks and are similar to those of oceanic island basalts (see Hofmann 1997, for a review) suggesting that crustal contribution was unlikely. Furthermore, the nepheline-normative character of nepheline syenites also argues against crustal contribution as nepheline-normative compositions would be erased by interaction with quartz-normative continental crust (e.g. Foland et al., 1993).

Metasomatized subcontinental lithospheric mantle (SCLM) is important in the generation of alkaline rocks and carbonatites. A metasomatized lithospheric mantle can be formed by in-situ interaction of asthenospheric mantle-derived carbonate melts with the subcontinental lithospheric material (Rudnick, 1993) or by element transfer from a subducting oceanic slab and overlying sediments (e.g. Kalfoun et al., 2002). Given that metasomatic agents vary from one locality to another and that multiple metasomatic events can occur within the same mantle volume, Bell and Simonetti (2009) argue against the origin of carbonatite melts from a metasomatized lithospheric mantle, as most carbonatites show isotopic (radiogenic) similarities with HIMU and EMI type oceanic island basalts considered to be located in the sub-lithospheric mantle. The extensive spatial distribution of basalts with similar isotopic composition indicates that isotopic characteristics of their source have remained closed for billions of years (Bell and Simonetti, 2009). Nevertheless, studies which favour an origin of carbonatites or related alkaline rocks from a metasomatized SCLM using Sr and Nd isotopic compositions have shown that the initial Sr isotopic composition is radiogenic, whereas initial Nd isotopic compositions are unradiogenic in the rocks or in their minerals (e.g. Harmer and Gittins, 1998; Wu et al., 2011). In contrast, the unradiogenic initial Sr and radiogenic Nd isotopic compositions in apatite grains

from Epembe render metasomatized lithospheric mantle unlikely as source region. Moreover, it is considered that the parental melts to the Epembe carbonatite and syenites have not interacted with the metasomatized lithospheric mantle significantly, as such interaction would erase the uniform and Depleted Mantle-like Sr and Nd isotopic signature by interaction with isotopically heterogenous material. Conversely, the carbonatites and syenitic rocks of the Epembe carbonatite alkaline complex exhibit Sr and Nd isotopic signatures similar to young East African carbonatites, which track a EM1 and HIMU line on the Sr-Nd isotopic diagram and are related to plume activity (Bell and Tilton, 2001) as well as those from the Blue River carbonatites, Canada (Mitchell et al., 2017), and the Miaoya syenites and carbonatites, China (Zhu et al., 2017). Isotopic similarities between carbonatites and oceanic island basalts have also been reported for some carbonatites from Africa, Australia, Brazil, Europe and the United States ranging in age from Proterozoic to Tertiary (Nelson et al., 1988), for which an asthenospheric mantle origin was proposed. Therefore, on the basis of Nd and Sr isotopic similarities with OIBs and many other carbonatite occurrences worldwide, the preferred origin of the Epembe carbonatite and syenitic rocks is partial melting of an isotopically heterogeneous asthenospheric mantle, comprising both a Depleted and an enriched mantle reservoirs formed by mixing of HIMU and EM1 components (Bell and Simonetti, 2009). Although Sr and Nd isotopic for other Mesoproterozoic carbonatite alkaline complexes occurring in the vicinity of our study area were not entirely intended to establish the exact mantle origin of rocks from those complexes, it is observed that isotopic compositions of the Swartbooisdrif ferrocarbonatite (Fig. 4.8) are similar to those of the Epembe rocks consistent with a common origin. It remains unclear if the Lupongola carbonatite shares a similar origin with Epembe carbonatite, as the Nd isotopic composition of the former was affected by crustal contamination (Alberti et al., 1999).

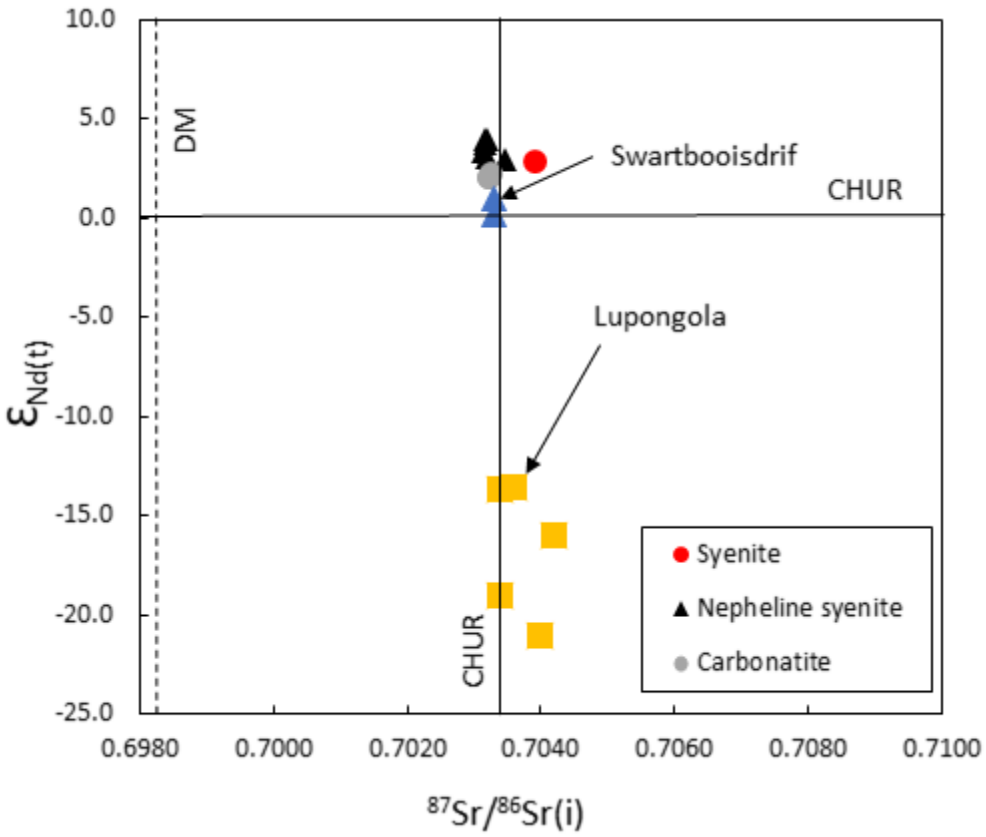

Fig. 4. 8: (a) $\varepsilon_{Nd(t)}$ vs. $^{87}Sr/^{86}Sr_{(i)}$ compositions of Epembe syenite, nepheline syenite and carbonatite apatite. The data are averages per sample. Initial Sr isotopic compositions were calculated using the decay constant $1.393 * 10^{-11}$ y^{-1} (Nebel et al., 2011). For the Bulk Earth, present-day $^{87}Sr/^{86}Sr$ = 0.7045 and $^{87}Rb/^{86}Sr$ = 0.08 were used to calculate the initial Sr of the Bulk Earth (0.7033) ca. 1200 Ma, whereas the DM present day $^{87}Sr/^{86}Sr$ = 0.6995 and $^{87}Rb/^{86}Sr$ of 0.07 were used to calculate the initial Sr of the DM (0.6983) ca. 1200 Ma. Initial ε_{Nd} was calculated using CHUR (chondritic uniform reservoir) parameters of Bouvier et al. (2008): $^{147}Nd/^{144}Sm$ = 0.1960 and $^{143}Nd/^{144}Nd$ = 0.512630, and a decay constant of ^{147}Sm of $\lambda = 6.54 \times 10^{-12}$ (Lugmair and Marti, 1978). Also shown are isotopic data for other Mesoproterozoic carbonatite occurrences in the vicinity of the study area (Lupongola: Alberti et al., 1999, Swartbooisdrif: Thompson et al., 2002).

The majority of carbonatites and related alkaline complexes are associated with large igneous provinces occurring in continental rift settings (Woolley, 1989) and aulocogens

characterized by flood basalts, such as the Damaraland carbonatite and alkaline rocks (Le Roex and Lanyon, 1998). The southern margin of the Congo Craton, into which the Epembe Complex was intruded, was affected by numerous igneous events in the Mesoproterozoic, including the major Kunene event at ca. 1500 to 1220 Ma (Bybee et al., 2019; Drüppel et al., 2007; Maier et al., 2013). The Epembe Complex is located along a fault zone within Palaeproterozoic gneisses and amphibolites south of the Kunene Complex. The Epembe Complex is also age similar (1200 Ma) to the youngest reported ages of the Kunene Complex and it is therefore plausible that faults utilized by the Epembe magmatism were initiated by the emplacement of the Kunene Complex. Such faults can extend down to the base of the lithosphere (Woolley, 1989). The emplacement of some carbonatites along deep-seated faults has also been proposed for some African carbonatites occurring along lineaments (Woolley, 1989).

4.6. Conclusions

The purpose of this work was to characterize apatite from syenitic and carbonatite samples from Epembe Complex by means of cathodoluminescence imaging, trace element and Sr-Nd isotope compositions, as well as U-Pb radiometric age determination. Apatite from syenite is magmatic and shows the highest concentration of REE among all investigated apatite grains. REE enrichment in syenite apatite is attributed to apatite crystallization from an evolved melt, which involves plagioclase fractionation. Magmatic apatite in carbonatite and nepheline syenite is homogeneous in CL, however core-rim zonations with rim-ward increases in REE concentrations are observed. The rim-ward increase in REE concentration in nepheline syenite apatite is attributed to re-equilibration of early-formed apatite with infiltration of a later co-genetic melt rich in REE, whereas in carbonatite apatite REE were controlled by mineral fractionation. Secondary apatite related to interaction with fluids occurs in one nepheline syenite sample shows depleted REE, Y, Na, accompanied by high Sr concentrations at similar initial $^{87}Sr/^{86}Sr_{(i)}$ compositions when compared to magmatic apatite from the same sample, suggesting that the fluids involved in the alteration process were derived from the cooling host magma. U-Pb age determination of apatite gives an emplacement age of 1216 ± 11 Ma (2 SE) of Epembe syenite, while ages of 1178 ± 16 Ma, 1150 ± 19 Ma, and 1073 ± 22 Ma (2 SE) obtained on apatite from

three nepheline syenites suggest a slow cooling event after the emplacement of the associated carbonatite. The Sr and Nd isotopic composition of apatite support an origin of the Epembe syenite, nepheline syenite and carbonatite from a common and heterogeneous mantle source involving HIMU and EMI reservoirs located in the asthenosphere.

5. Investigating the source and evolution of syenites and carbonatite using zircon trace element chemistry, geochronology and Hf isotopic compositions: A case study of the Epembe alkaline-carbonatite complex, NW Namibia

5.1. Introduction

Zircon ($ZrSiO_4$) is almost ubiquitous in the Earth's crust and its low solubility in melts and fluids and durability during transport enables it to survive almost any crustal process (Hanchar and Miller, 1993). However, zircon is not entirely immutable to any major event (e.g. partial dissolution, metamictization, overgrowth) and tends to preserve a record as distinct structural entities on pre-existing grains (Corfu et al., 2003). Because of this, zircon quite commonly consists of distinct segments, each preserving a particular period of zircon formation. Its capability to host significant amounts of U, Th, Hf and REE (Belousova et al., 2002a; Hoskin and Schaltegger, 2003) makes it useful in U-Pb geochronology and determination of magma sources by employing the Lu-Hf isotope system (Kinny and Maas, 2003). Another important application of zircon is the Ti-in-zircon geothermometer (Watson et al., 2006), which relies on the temperature dependent intake of Ti into zircon during crystallization from a melt. Some studies have shown that during hydrothermal alteration or metasomatism, zircon can exchange elements such as REE, Nb and Y with hydrothermal fluids (e.g. Doroshkevich et al., 2021; Hoskin, 2005; Liu et al., 2019). Cathodoluminescence imaging can reveal zircon textures, which can be combined with chemical and isotopic analyses of different segments to retrieve detailed petrogenetic information (Pidgeon et al., 1998; Tichomirowa et al., 2013; Doroshkevich et al., 2021; Bolhar et al., 2021a, b).

The objective of this study is to present trace element and Lu-Hf isotopic compositions of zircons from Epembe Complex as well as U-Pb geochronology. The results are discussed in the context of zircon petrogenesis and its implication for the magma sources and post-magmatic events affecting the Epembe rocks.

5.2. Methodology

Multiple zircons were extracted from seven samples (BX 01, SNT 04, SNT 05, SNT 06, SNT 07, SNT 09 and EC 21) using standard techniques (heavy liquid separation, magnetic separation and hand picking) and were mounted and polished for imaging using cathdololumiscence and back-scattered electron (BSE) imaging to guide in selecting analysis spots.

Trace element analysis on zircons were carried out in the Earthlab at the University of the Witwatersrand, employing an Australian Scientific Instruments (ASI) Resonetics Resolution 193 nm ArF excimer (SE 155) system coupled to a Thermo Scientific Fisher sector-field ICPMS (Element XR). This instrument was also used for U-Pb geochronology on the same zircons. Measurements were performed in low resolution and electrostatic scanning (E-scan) modes. Data were acquired by single spot analysis (60 μm), using a laser repetition rate of 10 Hz and a fluence of 2.5 Jcm^{-2}. Total signal acquisition time was 60 sec to allow data processing and preparation for the next analysis, comprising 15 s of pre- and post-ablation (gas blank) and 20 sec of ablation measurements. Laser sampling took place in a SE155 dual-volume ablation cell (Laurin Technic, Canberra, Australia) using a mixed He-Ar atmosphere and a small volume of N_2 to enhance signal stability and sensitivity. The following gas flows were applied: He (400 ml/min), Ar (1000 ml/min) and N_2 (5 ml/min), respectively. Synthetic glass NIST 612 (Jochum et al., 2011) was used for calibration, while NIST 610 (Gao et al., 2002) and zircon 91500 (Wiedenbeck et al., 1995) were analyzed as unknowns to evaluate accuracy and precision. The LA-ICPMS system was tuned during line scans using NIST 612 glass for maximum sensitivity for ^{6}Li, ^{115}In and ^{238}In, while maintaining oxide levels (ThO^{+}/Th) < 0.2 %. For internal standardization, the isotope ^{29}Si was used. Typically, two analyses of the primary calibration standard were obtained at the beginning and end of an experiment, and 10-20 analyses of unknowns were followed by analyses of one primary calibration standard and two to four analyses of the secondary standards for quality control purposes. Prior to each spot analysis surface material was removed using 2 laser pulses. The following masses were measured (6 samples per peak): ^{48}Ti, ^{31}P, ^{93}Nb, ^{88}Sr, ^{89}Y, ^{139}La, ^{140}Ce, ^{141}Pr, ^{146}Nd, ^{147}Sm, ^{151}Eu, ^{157}Gd, ^{159}Tb, ^{163}Dy, ^{165}Ho, ^{166}Er, ^{169}Tm, ^{174}Yb, ^{175}Lu, ^{232}Th, ^{238}U. All isotopes were measured in triple mode, including pulse counting, analog and Faraday cup, depending on signal. Data reduction was performed using the iolite extension

(http://www.iolite.org.au) to the software Igor Pro (http://www.wavemetrics.com), specifically the data reduction scheme ("DRS") "X_Trace_Elements_IS", proceeding in a series of sequential steps, including data import, selection of integrations, baseline subtraction, drift and down-hole fractionation, calibration and error propagation (Paton et al., 2010, 2011).

The U-Th-Pb measurements were performed in low resolution and electrostatic scanning (E-scan) modes. Data were acquired by single spot analysis (30 µm), using a laser repetition rate of 8 Hz and a fluence of 2.5 Jcm^{-2}. Total signal acquisition time was 50 sec, allowing data processing and preparation for the next analysis, and comprising 10 sec of pre- and post-ablation (gas blank) and 30 sec of ablation measurements. Laser sampling took place in a SE155 dual-volume ablation cell (Laurin Technic, Canberra, Australia) using a mixed He-Ar atmosphere and a small volume of N_2 to enhance signal stability and sensitivity. The following gas flows were applied: He (300-400 ml/min), Ar (800-1100 ml/min) and N_2 (2-5 ml/min), respectively. The LA-ICPMS system was tuned during line scans using NIST 612 glass for maximum sensitivity for ^{238}U and ^{206}Pb, while maintaining oxide levels (ThO^+/Th) < 0.2 % and the Th/U ratio >0.9. Zircon standard GJ1 (Jackson et al., 2004) served for calibration, and Temora-2 (Black et al., 2003, 2004), 91500 (Wiedenbeck et al., 1995) and Plešovice (Sláma et al., 2008) zircon certified reference materials (CMRs) were analyzed as unknowns to evaluate accuracy and precision. Typically, two analyses of the primary calibration standard were obtained at the beginning and end of a sequence, and 10-20 analyses of unknowns were followed by analyses of one primary calibration standard and two to four secondary standards for quality control purposes. Prior to each spot analysis surface material was removed using 2 laser pulses. The following masses were measured (6 samples per peak): ^{202}Hg, ^{204}(Pb+Hg), ^{206}Pb, ^{207}Pb, ^{208}Pb, ^{232}Th, ^{235}U, and ^{238}U. Magnet settling time was 0.001 sec, and sample times range from 0.0002 sec (^{235}U) to 0.003 sec (^{207}Pb). All isotopes were measured in pulse counting mode, except for ^{238}U (analog mode). Data reduction was performed using the iolite extension (http://www.iolite.org. au) to the software Igor Pro (http://www.wavemetrics.com), proceeding in a series of sequential steps, including data import, selection of integrations, baseline subtraction, drift and down-hole fractionation, calibration and error propagation (Paton et al., 2010, 2011). Additionally, the data reduction scheme (DRS) VizualAge (Petrus and Kamber, 2012) was applied to more carefully select

integrations in order to minimize discordance. No common Pb correction was attempted. Graphic presentation and calculation of concordia and upper intercept ages was carried out using the software ISOPLOT-R (Vermeesch, 2018). Uncertainties on individual and mean/regressed ages are reported as 2 SE (standard error, absolute).

The Hf isotope measurements on zircon were performed at the Geology department, University of Johannesburg, using the same laser system as at Wits that was coupled to Nu Plasma LA-MC-IC-PMS with 16 Faraday detectors and 5 ion counting detectors. A plasma RF power of 1300 W was applied. The gas flows were as follow: coolant Ar gas flow = 13.0 L/min, auxiliary gas flow = 0.80 L/min, nebuliser gas flow = 0.82 L/min and laser He gas flow of 0.31 L/min. Data were obtained by a single spot analysis of 60 µm beam diameter, a laser repetition rate of 7 Hz and laser fluence of 5.6 J/cm^2. Other laser parameters include: blank signal (20 s) and ablation signal (70 s). For mass bias correction, ^{171}Yb and ^{173}Yb were used to calculate Yb instrumental mass fractionation and to correct Yb and Lu instrumental mass fractionation; ^{179}Hf and ^{177}Hf were used to calculate Hf instrumental mass fractionation. For interference corrections, ^{171}Yb was used to calculate and correct ^{174}Yb interference on ^{174}Hf and the ^{176}Yb interference on ^{176}Hf; ^{175}Lu used to correct the ^{176}Lu interference on ^{176}Hf. Background correction was done by measuring background signal on mass prior to ablation and subtracting from signal. Zircon certified reference materials Mud Tank, Temora 2 (Woodhead and Hergt, 2005) and LV11 (Heinonen et al., 2010) were measured as unknowns to evaluate accuracy and precision.

Titanium in zircon (T_{zircon}) temperatures were estimated from: T(°C) = [5080 ±30/(6.01± 0.03)- log(Ti)]- 273K (Watson et al., 2006) assuming a TiO_2 activity of 1. The Ce anomaly was calculated as Ce/Ce*, where Ce is the chondrite-normalized Ce value and Ce* is the average of the chondrite-normalized Pr and La concentrations. The Eu anomaly was calculated as Eu/Eu*, where Eu is the chondrite-normalized Eu concentration and Eu* is the average of the chondrite-normalized Gd and Sm concentrations.

5.3. Results

5.3.1. Whole rock petrography

The petrography of the Epembe syenite, nepheline syenite and carbonatite is provided in detail previously in Tshiningayamwe et al. (submitted), so only a summary is provided here.

The Epembe syenite (Fig. 5.1a) is medium-grained and comprises dominantly alkali feldspar and anhedral clinopyroxene. Apatite and magnetite are accessory phases which may occur as inclusions within clinopyroxene. The mineral assemblage of the nepheline syenite (Fig. 5.1b, c) includes major to minor alkali feldspar, nepheline, biotite and cancrinite, while plagioclase, apatite, sphene, zircon, calcite and magnetite occur as accessory phases. Alkali feldspar is the dominant mineral and occurs as euhedral to subhedral elongated grains with a grain size of < 1 to > 5 mm. Nepheline is usually disseminated or occurs as interstitial grains between alkali feldspars. Biotite may occur in clusters, where grains display a mosaic arrangement but are mostly disseminated within the alkali feldspar matrix. Anhedral calcite occupies interstices between alkali feldspar grains (Fig. 5.1c).

The major and minor mineral assemblage of the carbonatite samples includes calcite, apatite, pyrochlore, pyroxene (aegirine), biotite, zircon and alkali feldspars and lath-shaped plagioclase. Calcite is observed in the samples, as a fine to/or medium-grained matrix, with a modal abundance of 64 to 83 vol%. Calcite can also occupy interstices between apatite and pyrochlore cumulates. Porphyroblastic (core and mantle structures) textures are common in these samples and are characterized by twinned calcite porphyroblasts fringed by smaller calcite grains devoid of twinning. Twin lamellae in the porphyroblasts are sometimes bent. Apatite is the second most abundant phase occurring throughout the carbonatite, with ovoid, elongate, euhedral hexagonal and subhedral grain shapes. The apatite grains (Fig. 5.1d) are disseminated in a calcite matrix or display a flow texture. Occasionally apatite occurs in clusters and as inclusions within pyrochlore and zircon. Pyrochlore is brownish or opaque with subhedral shapes (and a dark rim) dispersed in a calcite matrix. Zircon occurs as disseminated fine- to medium-sized grains with subhedral and euhedral grain shapes (Fig. 5.1d). Mineral inclusions of calcite are common in zircon. Biotite appears as dark or brownish large grains in clusters with a basal cleavage, which is bent in some cases. Magnetite occurs as fine-grained opaque grains, which

often occupy micro-fractures. Alkali-feldspars occur as dispersed anhedral grains or form globular structures, which are up to 6 mm in diameter.

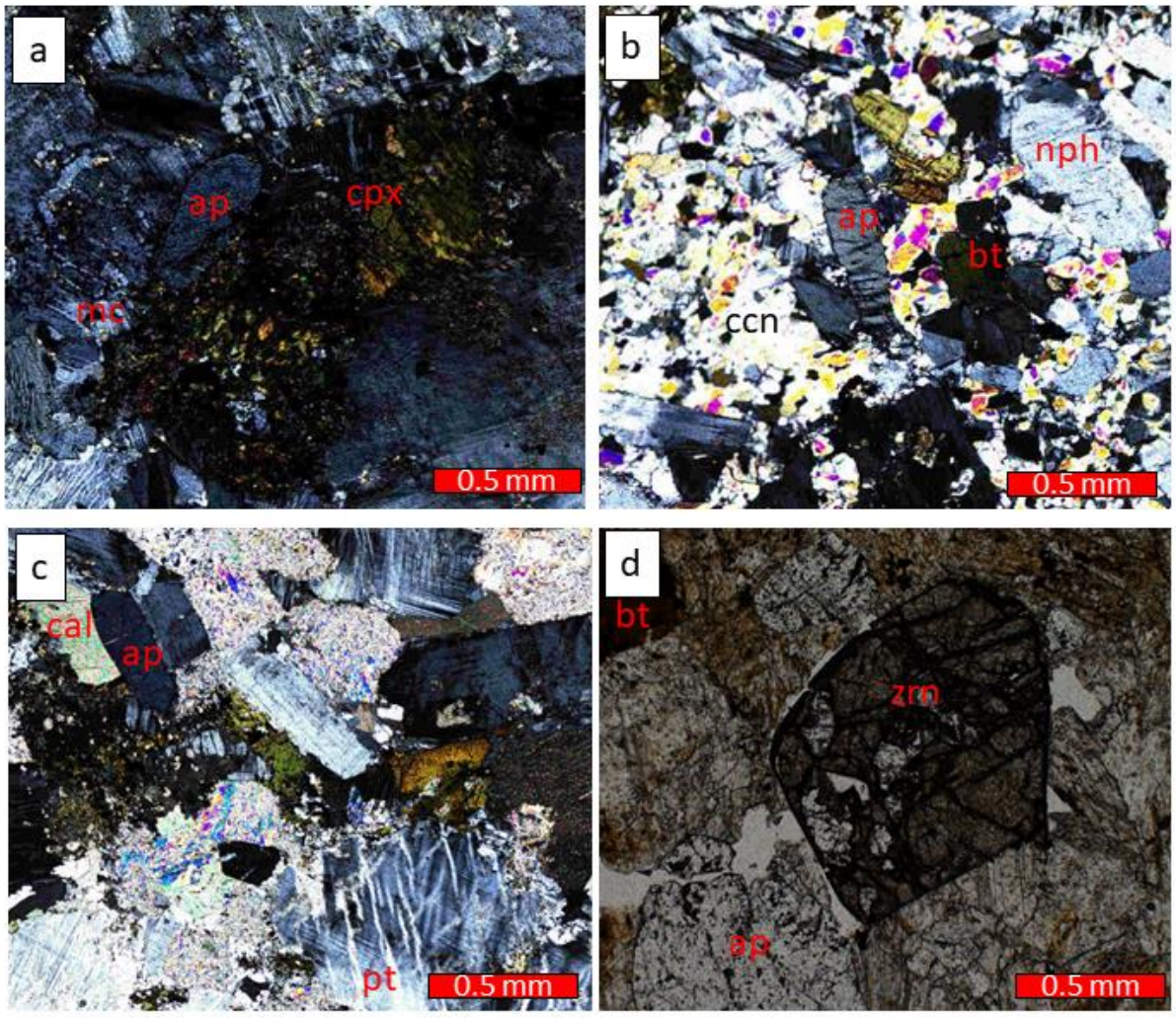

Fig. 5.1: Selected thin section photomicrographs (in XPL) of Epembe syenite (a), nepheline syenite (b, c) and carbonatite (d). (a) Sample BX 01. (b) Sample SNT 09. (c) Sample SNT 06. (d) Sample EC 21 showing euhedral fractured zircon with apatite inclusions. Abbreviations: ap=apatite, cpx=clinopyroxene, bt=biotite, nph=nepheline, ccn=cancrinite, pt=perthite, cal=calcite, zrn=zircon.

5.3.2. Zircon textures

Cathodoluminescence (CL) images of representative zircons from four samples (BX 01, SNT 04, SNT 06 and EC 21 are presented in Fig. 5.2. In contrast to doubly-terminated prismatic zircon crystals found in rapidly crystallized porphyritic, high-level granites, gabbros and subvolcanic intrusions, most of the zircons display stubby and equant forms that are common in slowly cooled deep seated intrusions (Corfu et al., 2003). Inherited cores are lacking in the analyzed grains. The zircons are generally homogenous with respect to their internal make up under BSE examination, although minor fractures are present. However, in CL images, the zircons are characterized by complex internal structures as described below.

Zircons from syenite sample BX 01 (Fig. 5.2a, b) are anhedral to subhedral with grain sizes ranging from 100 to 500 μm. The exterior is irregular in some grains which is attributed to breakage during sample preparation. The internal structures in CL consist of light grey homogeneous zones, oscillatory (growth) zones and patchy zoning characterized by areas of different brightness. Growth zoning is characterized by variable band thickness and can be straight in some grains (Fig. 5.2.a, c). In few grains, a thin homogenous rim is observed where the inner grain show a sharp irregular outline attributed to corrosion.

Zircons from nepheline syenites are anhedral to subhedral in shape (e.g. Fig. 5.2d-i). The grains are dominated by a grain size of approximately 400 - 600 μm, however smaller grains of ~100 μm are also present. Internally, the zircons are characterized by complex zoning patterns including bright domains, homogeneous grey/dark unzoned domains and oscillatory domains. In a few cases, zircons also show an internal structure defined by areas of variable brightness with a cloudy appearance. For the purpose of this study, zircons from the nepheline syenite are grouped into two types on the basis of their CL characteristics and chemical composition. Zircon type 1 refers to the grey/dark homogeneous and oscillatory zoned domains (e.g. Fig. 5.2d), whereas zircon type 2 refers to the zircons with a cloudy appearance (e.g. Fig. 5.2g). Majority of the type 2 zircons were found in sample SNT 06.

Carbonatite zircons (Fig. 5.2j, k) range in size from 200 μm to 500 μm. Most grains are subhedral and anhedral in shape. Internally, carbonatite zircon is characterized by areas of

different CL brightness (light grey and dark grey), or homogeneous grey CL luminescence. Few grains display faint oscillatory zoning. Apatite or calcite inclusions are common in carbonatite zircons.

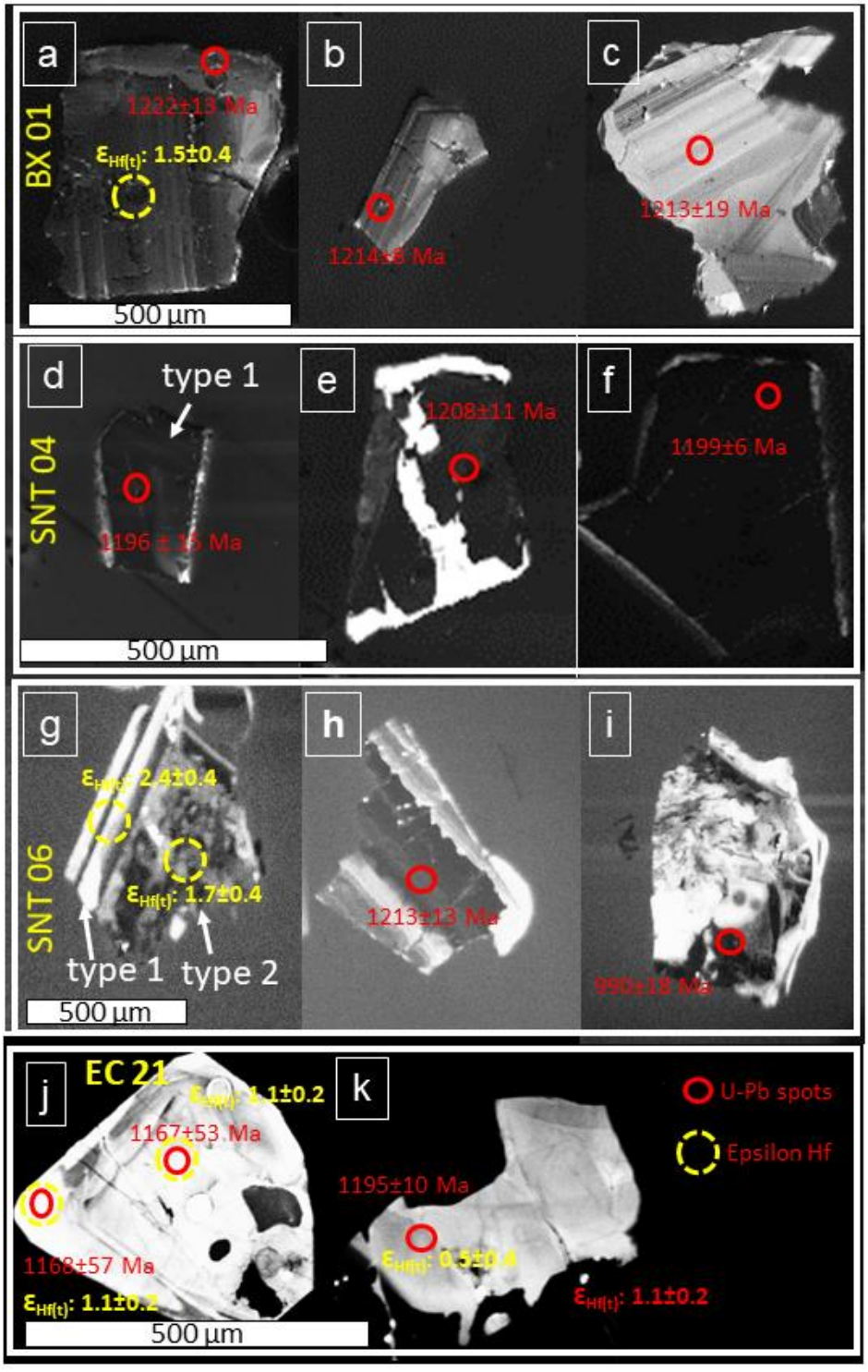

Fig. 5.2: Representative cathodoluminescence images of Epembe zircons. (a-c) Syenite zircon. (d-i) Nepheline syenite zircon. (j, k) Carbonatite zircon. Red circles represent U-Pb ages, while yellow dots are Hf isotopic analyses spots showing $\varepsilon_{Hf(t)}$ values.

5.3.3. Zircon trace element compositions by LA-ICPMS

LA-ICPMS analyses of all zircons are presented in Appendix 8. Chondrite-normalized REE patterns are displayed in Fig. 5.3. Typically, one analysis was obtained per grain, however additional spots were analyzed on different zircon domains in the nepheline syenite zircons. For syenite, nine analyses were carried out and they are characterized by elevated Hf (5130-7710 ppm) concentrations. The concentrations of Th (28-438 ppm) and U (76-389 ppm) vary from tens of ppm to few hundreds ppm. The mean concentration of U (217 ppm) is higher than that of Th (177 ppm). The elements, P, Nb, Sr and Ti show concentrations of less than 54 ppm with some Sr and P concentrations below the limits of detection, ruling out analysis of apatite inclusions. The total REE (138-1843 ppm) and Y (160-2490 ppm) show variable concentrations from few hundred ppm to over a thousand ppm. On the chondrite-normalized REE diagram (Fig. 5.3a), the zircon grains are enriched in HREE (Yb_N/Sm_N = 28-170) relative to LREE with positive Ce anomalies (Ce/Ce* = 1-8) and negative Eu anomalies (Eu/Eu* = 0.2-0.4).

For nepheline syenite type 1 zircon, fifteen analyses are characterized by elevated Hf (3370-9860 ppm) concentrations. Uranium and Th concentrations are variable with higher Th (88-1440 ppm) compared to U (67-448 ppm). The elements, P, Nb, Sr and Ti show concentrations of less than 60 ppm with some Sr and P concentrations below the limits of detection. One analysis (spot SNT 05-2) shows a Sr abundance of 212 ppm. The total REE (513-1308 ppm) and Y (513-1930 ppm) show concentrations from few hundred ppm to over a thousand ppm. On the chondrite-normalized REE diagram (Fig. 5.3b), the zircons are enriched in HREE (Yb_N/Sm_N = 14-56) relative to LREE with positive Ce anomalies (Ce/Ce* = 1-9) and Eu anomalies close to unity (Eu/Eu* = 0.8-1).

Five analyses were carried out on type 2 zircons, yielding elevated Hf (4130-7470 ppm) concentrations. Uranium (187-700 ppm) and Th (170-610 ppm) concentrations are variable and

overlap with those in type 1. These zircons show higher Ti (63-140 ppm), Nb (97-339) and Sr (35-250 ppm) relative to type 1 zircon, while P (29-73 ppm) concentration is similar to zircon type 1. The total REE (367-1301 ppm) and Y (273-556 ppm) concentrations are variable and similar to those in type 1 zircon. However, on the chondrite-normalized REE diagram (Fig. 5.3c), these zircons are relatively enriched in LREE (Yb_N/Sm_N = 2-7) when compared to type 1 zircon. Both the Ce and Eu anomalies are close to unity (Eu/Eu*= ~1).

For carbonatite EC 21, seven zircon trace element analyses were determined. The REE are characterized by HREE enrichment relative to LREE (Fig. 5.3d) with Yb_N/Sm_N of 14-46. Cerium and Eu anomalies (average Ce/Ce* = 2; average Eu/Eu* = 0.8) are typical for carbonatite zircons (Belousova et al., 2002a). Concentrations of Y (316-820 ppm), Pb (0-280 ppm), Th (86-440 ppm) and U (4-84 ppm) are variable.

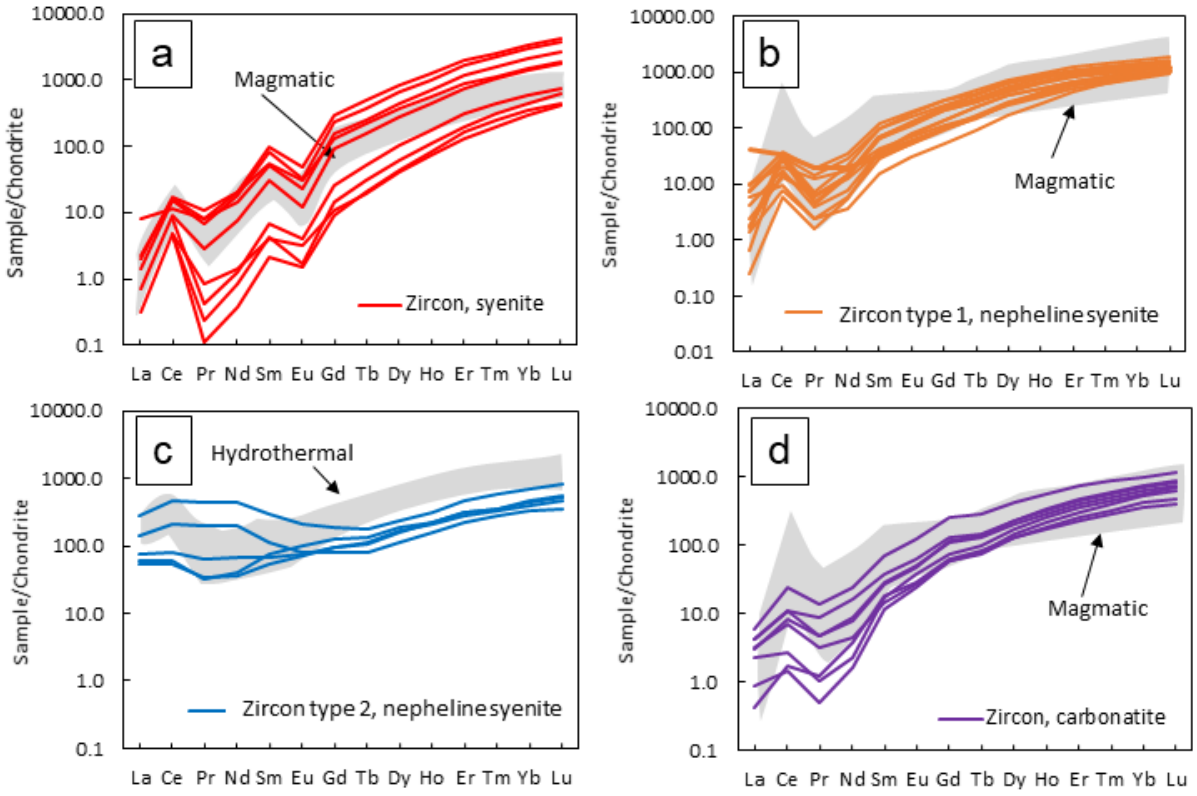

Fig. 5.3: Chondrite-normalized rare-earth element patterns. (a) syenite zircon. (b) Type 1, nepheline syenite zircon. (c) Type 2, nepheline syenite zircon. (d) Carbonatite zircon. Chondrite-normalization values from Boynton (1984). Background shaded values represent the range of REE

patterns in other zircon, in (a) syenite magmatic zircon after Belousova et al. (2002a), in (b-d) magmatic and hydrothermal zircon from alkaline carbonatite complexes (Liu et al., 2019).

5.3.4. U-Pb geochronology by LA-SF-ICPMS

The U-Th-Pb data of the dated zircons are provided in Appendix 9. For syenite sample BX 01, 27 spots were measured on a total of 22 zircons. Out of 15 concordant (< 10% discordance) zircons (Fig. 5.4a), 8 were rejected in the age calculation as they are outliers and a weighted mean age of 1220 ± 3 Ma (MSWD = 1.3) is obtained (Fig. 5.4b).

A total of 28 zircons (34 spot analyses) from the nepheline syenite sample SNT 04 were analyzed for U-Th-Pb. Twenty-five analyses are concordant (< 10% discordance; Fig. 5.4c), and a age of 1209 ± 3 Ma (MSWD = 1.3) was obtained from 8 analyses on the preserved igneous portions of zircons Fig. 5.4d.

In the nepheline syenite sample SNT 06, a total of 27 spots were measured on 13 zircons. On the Wetherill diagram (Fig. 5.4e) the analyses lie along a discordia probably due to variable loss of radiogenic Pb, and an upper intercept age 1205 ± 13 Ma (MSWD = 2) was obtained. The lower intercept age is close to the origin.

In the carbonatite, out of 33 spot analyses, 9 spot ages with < 10% discordance gave a U-Pb concordia age of 1198 ± 5 Ma (MSWD = 1.8) (Fig. 5.5).

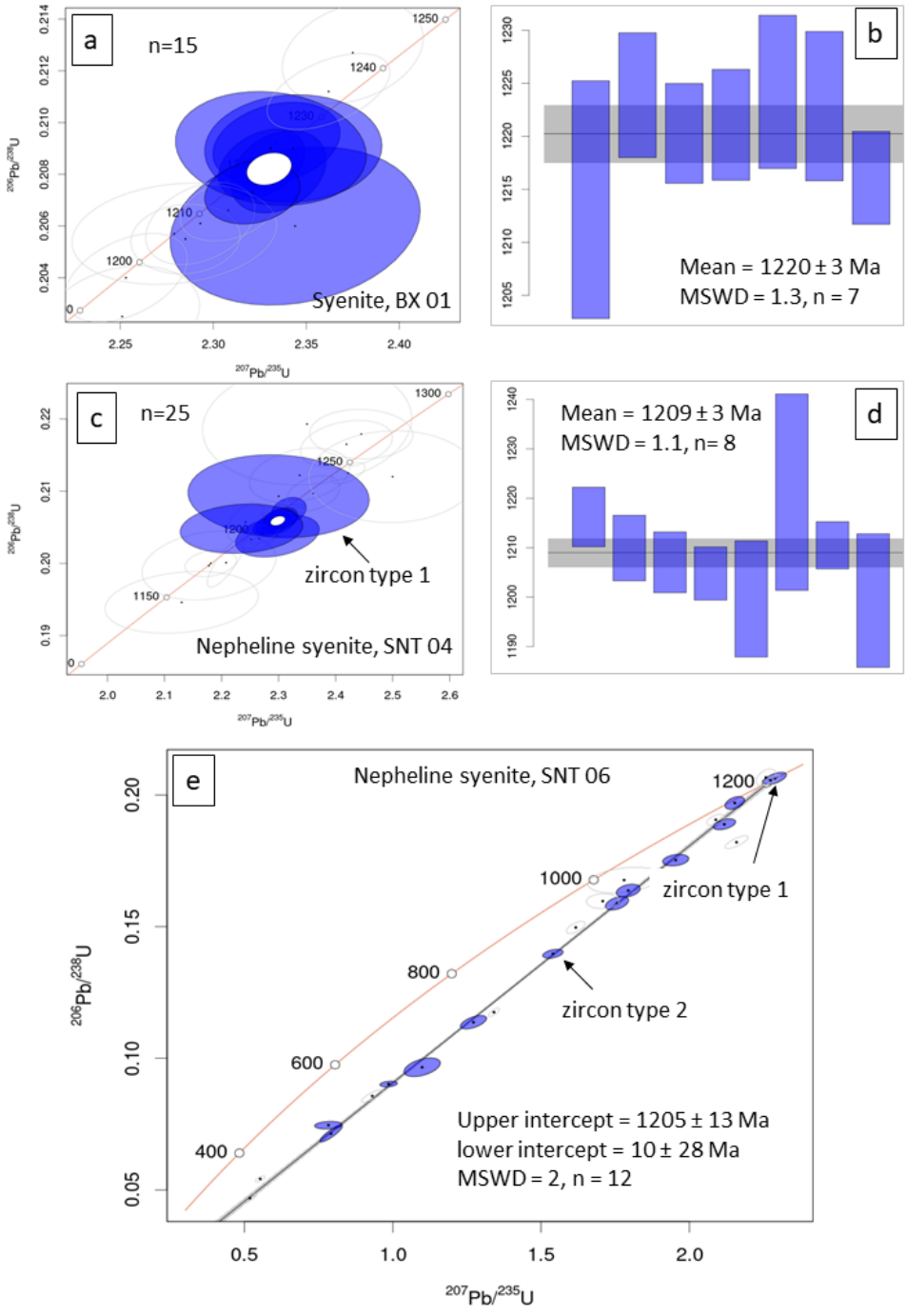

Fig. 5.4: U-Pb Concordia diagrams (a, c, e) and $^{206}Pb/^{238}U$ weighted mean plots (b, d) for zircons from the Epembe syenite (a, b) and nepheline syenites (c-d). Data point error ellipses are 2σ.

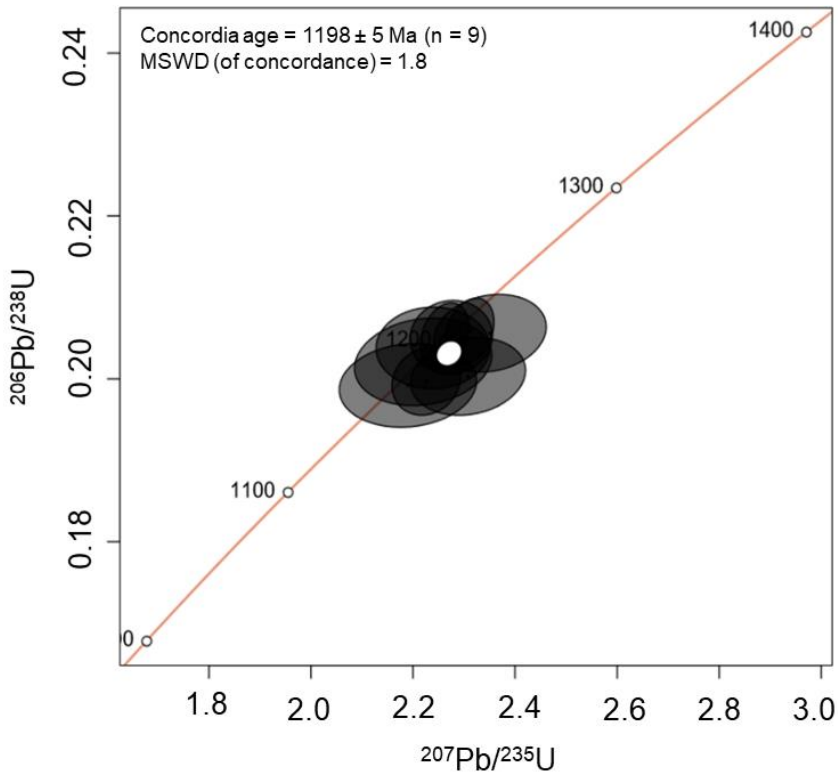

Fig. 5.5: Wetherill-concordia diagram showing analytical data for zircon from sample EC 21. Data point error ellipses are 2σ

5.3.5. Hf isotopes

Zircons extracted from the seven samples were analyzed for Lu-Hf isotopes and the results are reported in Appendix 10. For the syenite sample BX 01, three analyses were carried out on three spots with concordant ages. The $^{176}Hf/^{177}Hf$ ratio varies from 0.282049 to 0.282090, whereas the $^{176}Lu/^{177}Hf$ is from 0.000703 to 0.001604 (Fig. 5.6a), which translates into $\varepsilon_{Hf(1220\ Ma)}$ of +0.5 ± 0.4 to +1.5 ± 0.4 (Fig. 5.6b).

Type 1 and 2 zircons from the nepheline syenite samples have overall similar $^{176}Lu/^{177}Hf$ and $^{176}Hf/^{177}Hf$ ratios (Fig. 5.6a). The $^{176}Hf/^{177}Hf$ in zircon range from 0.282068 to 0.282136, whereas the $^{176}Lu/^{177}Hf$ is from 0.000102 to 0.001830. Obtained $\varepsilon_{Hf(1209\ Ma)}$ of zircons from the nepheline syenites range from +1.6 ± 0.3 to +2.7 ± 0.5 (Fig. 5.6b)

In carbonatite zircon, values for $^{176}Hf/^{177}Hf$ ratios range from 0.2820607 to 0.2820807 (Fig. 5.6a), and for $^{177}Lu/^{177}Hf$ from 0.000167 to 0.001526, translating into $\varepsilon_{Hf(1198)}$ from +0.5 ± 0.4 to +1.9 ± 0.2 (Fig. 5.6b).

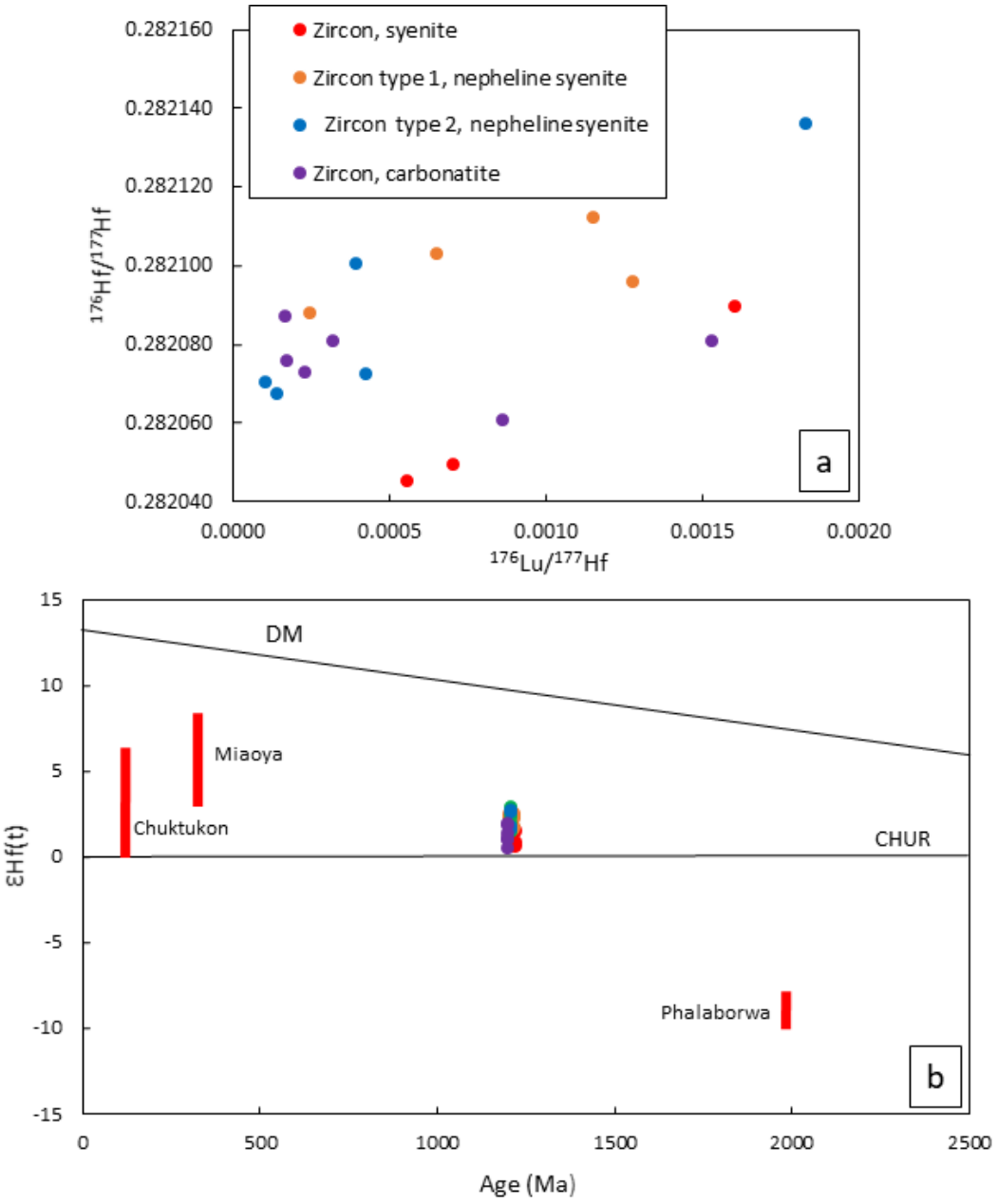

Fig. 5.6: (a) Measured $^{176}Hf/^{177}Hf$ vs.$^{176}Lu/^{177}Hf$ and (b) $\varepsilon_{Hf}(t)$ vs. U-Pb ages for Epembe zircons. Initial ε_{Hf} was calculated using CHUR parameters of Bouvier et al. (2008): $^{176}Hf/^{177}Hf$ = 0.282785 and $^{176}Lu/^{177}Hf$ = 0.0336, and a decay constant of ^{176}Lu of $\lambda=1.867\times10^{-11}$ (Scherer et al., 2001; Söderlund et al., 2004). The Hf isotopic evolution of the Depleted Mantle (DM) is based on

$^{176}Hf/^{177}Hf_{DM}$ = 0.283238 and $^{176}Lu/^{177}Hf_{DM}$ = 0.03976 (Vervoort et al., 2015). Data sources of other alkaline complexes are from Wu et al. (2011); Zhu et al. (2017) and Doroshkevich et al. (2021)

5.4. Discussion

5.4.1. Assessing a magmatic versus non-magmatic origin for zircon

Magmatic zircon can be affected by various fluid-driven processes during late stages of crystallization or after crystallization, which may promote solid-state recrystallization, dissolution-reprecipitation and metasomatism (Corfu et al., 2003; Hoskin, 2005; Liu et al., 2019; Tichomirowa et al., 2013; Bolhar et al., 2021a, b). Given that such fluids may have been derived from various sources with variable chemical and possibly isotopic compositions, textural and geochemical changes are expected in affected zircon domains. Therefore, textural and chemical criteria can be combined to evaluate if zircon grains extracted from the syenite, nepheline syenite and carbonatite of the Epembe Complex are magmatic or non-magmatic in origin. This assessment is made, based on microtextural observation from CL imaging, Th/U ratios and REE compositions.

5.4.1.1. Microtextures

Magmatic zircon is generally characterized by oscillatory zoning, sector zoning and homogeneous CL domains (Pidgeon, 1992; Corfu et al., 2003). On the other hand, post-magmatic recrystallized zircon in solid-state tends to show bright CL domains when compared to igneous zircon and if the recrystallized zircon occurs in the same grain with an igneous origin, the solid-state recrystallized zircon domain is usually irregular and appears to be cutting oscillatory domains discordantly (Pidgeon, 1992; Corfu et al., 2003). In some cases, faint traces of oscillatory-zoned magmatic domains can be preserved in recrystallized domains (Pidgeon et al., 1998). Zircon can also be altered by hydrothermal fluids, which penetrate the zircon structure, along fractures or interfaces between zircon and other mineral inclusions, and along textural discontinuities such as zoning (Corfu et al., 2003; Liu et al., 2019), and such zircon exhibits complex CL characteristics that have been described as irregular, patchy, bulbous, cloudy and feathery (Corfu et al., 2003;

Liu et al. 2019). Zircon with a hydrothermal signature may further show presence of secondary hydrothermal mineral inclusions, such as thorite (Liu et al., 2019). In our study, CL images of syenite zircon suggest a magmatic origin. The zircon grains are homogeneous light grey or show oscillatory zoning (Fig. 5.2a-c). Imaging of nepheline syenite zircon shows complex zoning patterns, which are observed even in a single grain suggestive of presence both magmatic zircon and non-magmatic zircon. Type 1 zircon is characterized by oscillatory or dark homogeneous growth domains in CL interpreted as magmatic. Type 2 is anhedral displaying variable brightness comprising of light and dark areas of cloudy nature and in contact with oscillatory-zoned zircon domains (Fig. 5.2g), suggesting a hydrothermal overprint. Carbonatite zircon is characterized by areas (light grey and dark grey) of different CL brightness, or homogeneous grey CL luminescence. Few grains display oscillatory zoning. Apatite or calcite inclusions are common inclusions in these zircons. Apatite in the carbonatite is magmatic in origin (Tshiningayamwe et al., submitted), therefore, the carbonatite zircon is interpreted as magmatic.

5.4.1.2. Th/U ratios

Several studies have used ratios of Th/U in zircon to identify zircon of igneous origin (Belousova et al., 2002; Bolhar et al., 2008). Magmatic zircon generally has a Th/U ratio > 0.1, although such Th/U ratios have also been reported in zircon from high-grade metamorphic rocks (Rubatto, 2017). More recently, Yakymchuk et al. (2018) compiled Th/U ratios in metamorphic and igneous zircon and showed that distinguishing metamorphic zircon from magmatic zircon on the basis of Th/U ratio can be tricky as reflected in the median Th/U ratios of ~0.7 (5494 analyses) in metamorphic zircon and ~0.4 (1352 analyses) in magmatic zircon. For Epembe syenite zircon, Th/U ratios are from 0.4 to 1.2 (Fig. 5.7) consistent with a magmatic origin. Also, if the Ti-in-zircon crystallization temperature (Watson et al., 2006) is considered, syenite zircon Ti concentration (5 to 10 ppm) return a narrow crystallization temperature range of 680 to 740 °C, overlapping with 700-956 °C obtained for magmatic zircons from Miaoya syenite, China (Zhu et al., 2017). For the nepheline syenite samples, type 1 zircon domains have Th/U ratios ranging from 0.6 to 3.9 (Fig. 5.7). Such elevated Th/U ratios are typical of magmatic zircon. Type 2 zircon with textures typical of hydrothermal alteration is characterized by uniform Th/U ratios of ~0.9 (Fig. 5.7). Although,

the Th/U may have been changed to some extent when compared to igneous zircon type 1 from the same sample, it still corresponds with magmatic origin, indicating that zircon alteration did not cause significant changes in the Th/U systematics. Absence of significant modification of the Th/U ratio has also been shown recently in zircons from the ultramafic-mafic layered Stolzburg Complex, South Africa, which interacted with high-T hydrothermal fluids (Bolhar et al., 2021a). If type 1 and type 2 zircons are considered together, estimated T-in-zircon temperatures are highly variable in these zircons, ranging from 600 to 1042 °C. Some of these estimated temperatures in our nepheline syenite zircon are either higher or lower than the temperature range of 640-956 °C estimated from magmatic zircon from alkaline-carbonatite complexes (Nedosekova et al., 2016; Zhu et al., 2017). Thus, the wide range of temperatures estimated in our nepheline syenite zircon cannot be reconciled by zircon crystallization from a melt only. It requires the presence of other processes, such as cation exchange between zircon and late-stage fluids (e.g. Bolhar et al., 20121c), supporting our interpretation that nepheline syenite zircons have undergone post-magmatic alteration. Epembe carbonatite zircons have Th/U ratios in the range of 1 to 115 (Fig. 5.7). Such a variable Th/U range is consistent with magmatic zircon from carbonatites (Hoskin and Schaltegger, 2003).

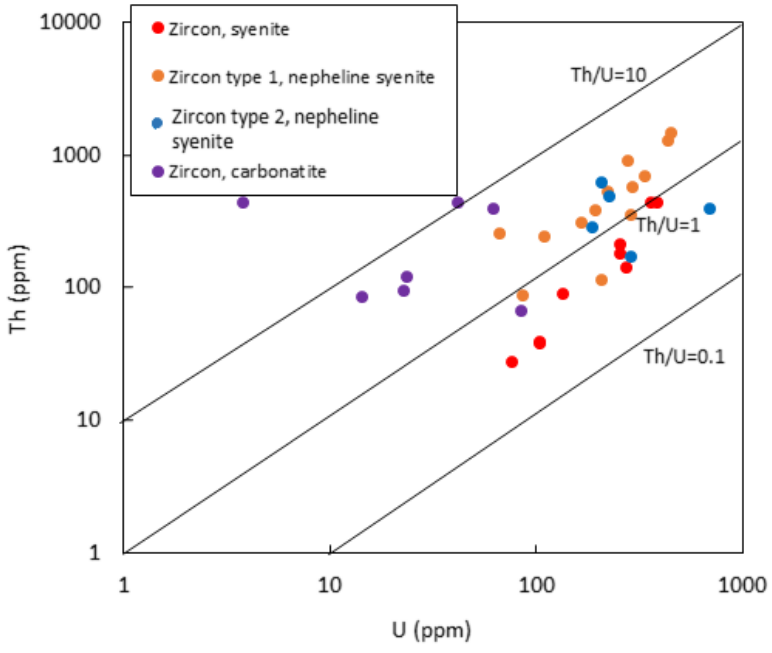

Fig. 5.7: Diagram showing Th vs. U for zircons.

5.4.1.3. Rare earth elements

Rare earth element concentrations in zircon have been used to distinguish magmatic from non-magmatic zircon (e.g. Hoskin, 2005; Fu et al. 2009; Liu et al., 2019; Bolhar et al., 2021a, b). Magmatic zircon is characterized by positively rising chondrite-normalized REE patterns with strong positive Ce anomalies. In contrast, zircon with hydrothermal signatures is characterized by LREE enrichment and subdued Ce anomalies (Hoskin, 2005; Liu et al., 2019). The LREE enrichment relative to HREE in syenite zircon, type 2 nepheline syenite zircon and carbonatite zircon as well as their distinctive positive Ce anomalies are in agreement with a magmatic origin. Moreover, the REE patterns of these zircons overlap with those of magmatic zircon from other studies (Fig. 5.3a, b, d). Type 2 zircon show variable REE compositions, particularly in the LREE with values from less than 100 times chondrite values to around 800 times chondrite values (Fig. 5.3c) with Ce anomalies of close to unity. The REE pattern of type 2 zircon is similar to that of zircons that have undergone hydrothermal alteration in other studies (Fig. 5.3d). Therefore, these features suggest that type 2 zircon have undergone hydrothermal alteration.

5.4.2. Zircon stability in carbonate melt

Based on the low calculated silica activities for a pure carbonatite melt, zircon is unlikely to crystallize from a carbonatite melt, instead baddeleyite and perovskite should form (Barkers, 2001). However, a number of studies have reported zircon in carbonatites interpreted or assumed to have crystallized from the host carbonatite (e.g. Ying et al., 2017). Although these studies have ruled out the possibility of zircon to have been derived from an external source such as the evolved continental crust in which carbonatite have to traverse during magma ascent and emplacement, they have not considered contribution from cogenetic silicate rocks. One way to explain the crystallization of zircon as well as some other silicate phases in a carbonatite melt though, is by local changes in the silica activity (and that of other chemical components) of the melt (Barker, 2001) and this can happen during interaction of carbonate melt with wall rocks (Chakhmouradian et al., 2016; Giebel et al., 2019). Although the Epembe carbonatite zircon is interpreted as magmtic in origin, the possibility that it crystallized from the host carbonatite melt should be assessed, in order to validate the age and Hf isotopic significance obtained from it.

Possible sources of xenocrystal zircon in the Epembe carbonatite is the associated syenite or nepheline syenite. Zircons from the Epembe carbonatite sample are characterized by subhedral to euhedral crystal faces (Fig. 5.2 j, k) which contrasts rounded and resorbed textures which would be expected for xenocryst minerals resulting from modifications from carbonatite magma (Giebel et al., 2019). Some of the Epembe carbonatite zircon grains contain rounded and abraded inclusions of carbonatite apatite and calcite. The REE pattern for carbonatite zircon is different from that of syenite zircon characterized by negative Eu anomalies. However, it is similar to that of nepheline syenite type 1 zircon. This feature is common in zircon from related carbonatite and syenite rocks (e.g. Wu et al., 2011; Ying et al., 2017), and not necessarily due to incorporation of external zircon in the carbonatite. Therefore, considering the above features, carbonatite zircon is likely to have crystallized from carbonatite melt.

5.4.3. Factors controlling zircon growth and its trace element compositions

5.4.3.1. Magmatic zircon

Microtextural and chemical characteristics favour a magmatic origin for zircon from syenite and carbonatite as well as type 1 zircon from nepheline syenite. Therefore, we consider the intake of trace elements and REE in these zircons to have occurred at the magmatic stage, during crystallization from a cooling melt. The chemical composition of magmatic zircon is dependent on melt composition, degree of differentiation of the host magma, co-existence of other mineral phases, cation size and charge (Belousova et al., 2002a, Hoskin et al., 2000). The generally low Ti, Nb, Sr and P concentrations in Epembe igneous zircon compared to other elements, such as Hf, Th and U, is consistent with zircon composition from other studies (e.g. Hoskin and Schaltegger 2003). The elements Ti, Nb, Sr and P partition into other phases co-existing with zircon. Titanium and Nb favour titanite (e.g. Wolff, 1984), whereas Sr and P favour apatite (Prowatke and Klemme, 2006). Titanite and apatite occur as accessory minerals in these rocks (Tshiningayamwe et al. submitted). High average U concentration (217 ppm) in syenite zircon compared to the average Th concentration (177 ppm) is consistent with the higher U compatibility in zircon relative to Th (Hoskin and Schaltegger, 2003). However, in zircons from the nepheline syenites, Th concentrations (average = 550 ppm) are higher than U concentrations (average = 241 ppm)

suggesting that the high Th concentration in zircon relative U is probably due to high Th concentration in the bulk rock composition. From the five zircon host rock samples, three samples have higher Th content relative to U (Tshiningayamwe et al. submitted). For carbonatite, bulk rock samples have higher U concentrations relative to Th (Tshiningayamwe et al., submitted), but zircon show high abundance of Th (average = 234 ppm) relative to U (average = 36 ppm). This instead suggests that U is sequestered into coexisting pyrochlore (Falshaw, 2012).

Anomalous abundances of Ce or Eu are usually features of all igneous zircon (Hoskin and Schaltegger, 2003). These rare earth elements are both redox sensitive and their abundance in zircon is primarily controlled by oxygen fugacity (Hoskin and Schaltegger, 2003; Trail et al., 2012). The abundance of Eu may also be controlled by feldspar fractionation (Hoskin and Schaltegger, 2003; Belousova et al., 2002a). Positive Ce anomalies in syenite, nepheline syenite and carbonatite zircon can therefore be explained by zircon formation under oxidizing conditions in which Ce is Ce^{4+}, which is favoured by zircon over Ce^{3+} (Hoskin and Schaltetegger, 2003). The markedly negative Eu anomalies in syenite zircon can be attributed to prior plagioclase formation and fractionation which can remove Eu from the evolving melt. The negative Eu anomalies can also be related to the oxidation state of the magma from which zircon crystallizes (Trail et al., 2012), however this is unlikely the case for syenite zircon, as the negative Eu anomaly is also displayed in bulk rock Primitive Mantle (PRIMA)-normalized diagrams (Fig. 5.8), consistent with plagioclase fractionation (Tshiningayamwe et al., submitted). Therefore, early plagioclase formation and removal is likely to explain the negative Eu anomalies in syenite zircon. Absence of Eu anomalies in nepheline syenite and carbonatite zircon indicate that plagioclase fractionation was not significant in the evolution of their parental melts.

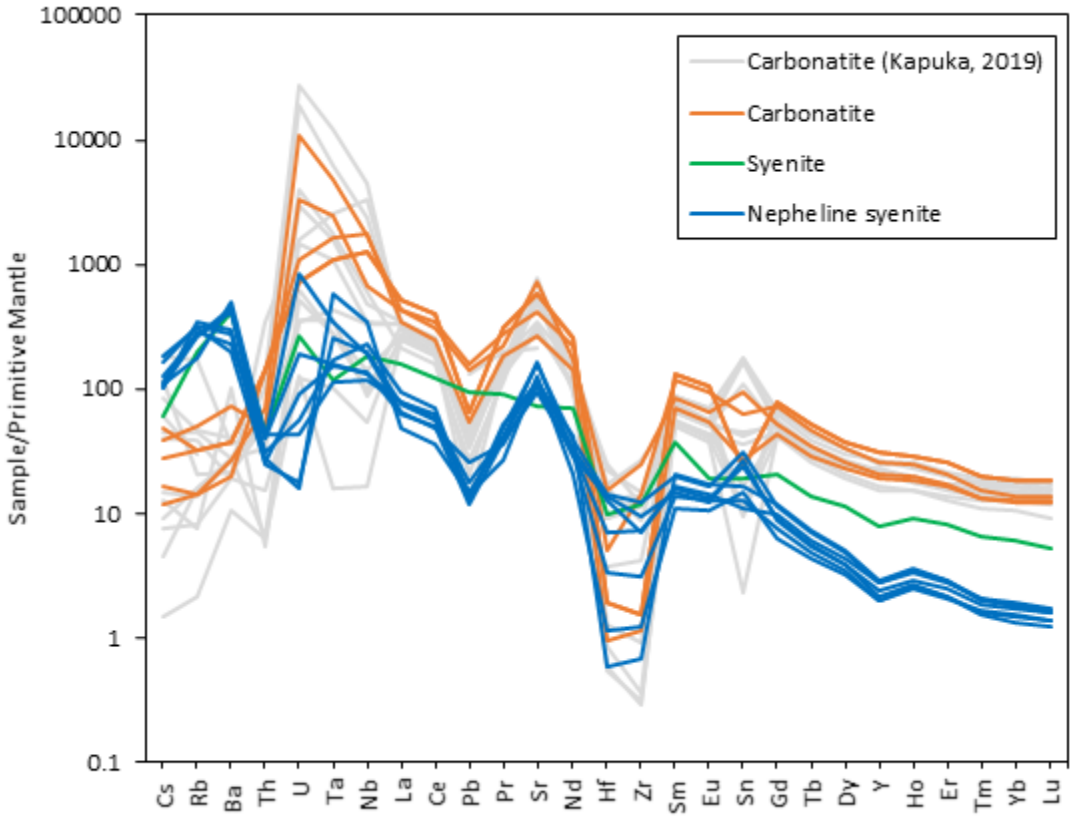

Fig. 5.8: Primitive Mantle-normalized multi-trace element patterns for Nepheline syenite, syenite and carbonatite samples from Epembe. Data from Tshiningayamwe et al. (submitted). Normalization values are from Lyubetskaya and Korenaga (2007).

5.4.3.2. Zircon alteration

Based on CL imaging and REE concentrations of Epembe zircon grains, it was shown earlier that type 2 zircon has been affected by hydrothermal fluids. In addition to LREE enrichment, these zircons are enriched in Nb and Ti relative to type 1 zircon (Fig. 5.9), pointing to enrichments of these elements in the hydrothermal fluids. Fluids responsible for hydrothermal alteration may be independent and unrelated in geologic time to primary magmatic stages. For instance, Ying et al. (2017) showed that the Miaoya carbonatite syenite complex was emplaced ~426 Ma with a metasomatic event having occurred much later at ~240 Ma. Hydrothermal fluids may

alternatively be sourced from the cooling and crystallizing magma resulting in autometasomatism, similar to the Mianing-Dechang carbonatite complex, China (Xie et al., 2015). The Mianing-Dechang carbonatite complex formed from magmatic and magmatic-derived hydrothermal fluids with consistent ages among the carbonatite, pegmatite and syenite (Hou et al., 2006; Liu et al., 2015; Xie et al., 2015). Although no age is determined for type 2 zircon in our study, the source of its elevated LREE, Ti and Nb concentration relative type 1 zircon is unlikely to be unrelated to the nepheline syenite and carbonatite intrusion. This is supported by the similarity in initial Hf isotopic compositions between type 2 and type 1 zircon as well as with carbonatite zircon. Moreover, the elements Nb, LREE and Ti all occur in high concentration in host bulk rock samples (Tshiningayamwe et al., submitted) compared to the surrounding basement units reported in Gleißner et al. (2011). Lastly, carbonatite and associated alkaline rocks are known to release fluids during their emplacement (e.g. Elliot et al., 2018) and it is therefore likely that the formation of type 2 zircon is related to hydrothermal fluids derived from the emplacement of the Epembe complex.

Relatively uniform concentrations of Hf among all zircons, including altered and unaltered zircon (Fig. 5.9), implies that Hf was not affected by post-magmatic processes, presumably because of the near-identical cation size and ionic charge of Hf and Zr, both being main constituents within this mineral (Hoskin and Schaltegger, 2003).

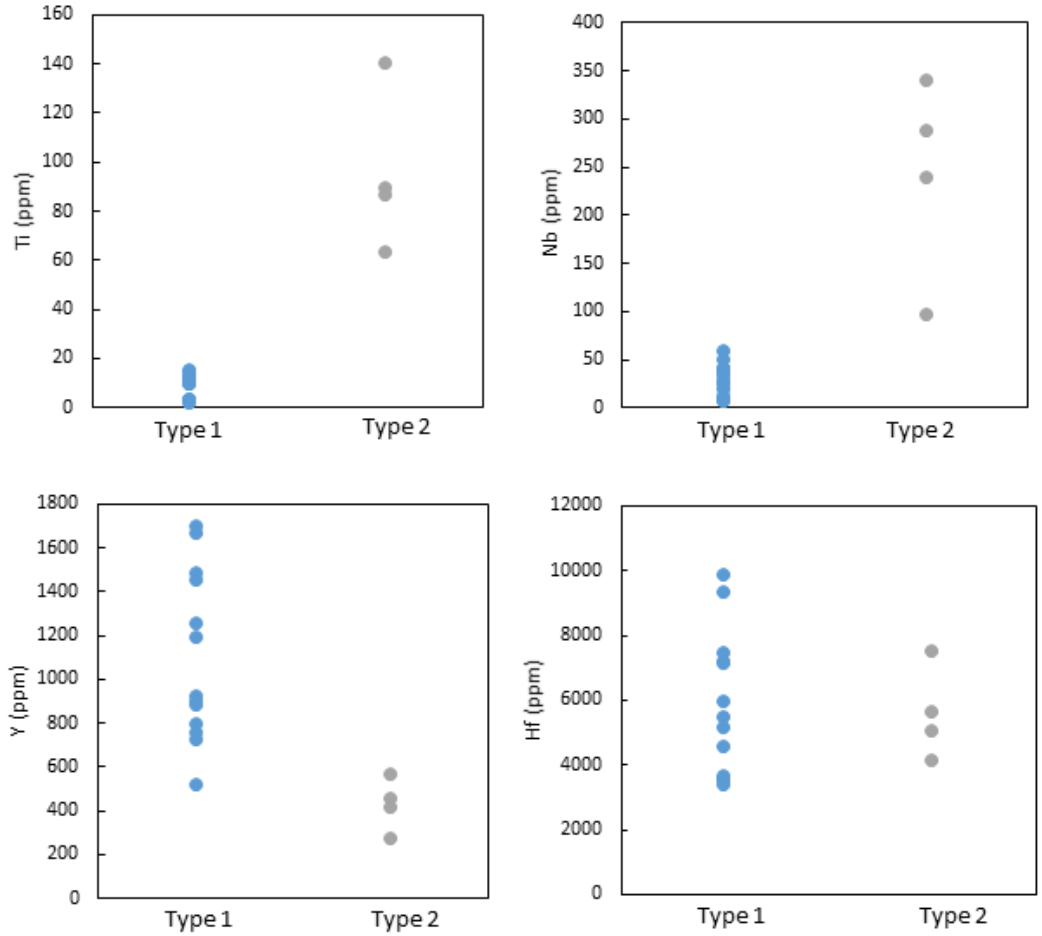

Fig. 5.9: Geochemical variations among different zircon types from Epembe nepheline syenites.

5.4.4. Timing of emplacement

Previous age determinations of nepheline syenites from the Epembe area yielded U-Pb zircon magmatic ages of 1216 ± 2.4 Ma and 1213 ± 2.5 Ma (Littmann et al., 2000 in Drüppel et al., 2005). With respect to the associated carbonatite, a concordant U-Pb zircon age of 1184 ± 10 Ma SIMS (corresponding to a $^{207}Pb/^{206}Pb$ age of 1173 ± 12 Ma) was previously determined by Simon et al. (2017) and interpreted as timing of crystallization of the carbonatite as a whole. These ages are in agreement with the recalculated Rb-Sr age of 1190 Ma (Cahen and Snelling, 1966 in Simon et al., 2017) interpreted as timing of maximum age related to alkaline carbonatite magmatism at Epembe. Based upon a histogram of pooled zircon ages, Simon et al. (2017) further showed that the carbonatite emplacement occurred between 1205 to 1148 Ma. This may indicate a

protracted formation history. Protracted magmatic activity has been observed elsewhere in carbonatite alkaline complexes, for instance, in the Oka Carbonatite Complex (~15 Ma; Chen and Simonetti, 2013), in lamprophyre and carbonatite dykes in the area of Aillik Bay (~35 Ma; Tappe et al., 2006) and in kimberlite and carbonatite from Tikiusaaq and Sarfartoq (40 Ma; Secher et al., 2009; Tappe et al., 2009). The U-Pb ages by LA-ICP-MS on zircons in the present study provide further constraints on magmatism within the area. The age of 1198 ± 5 Ma (sample EC 21) of the carbonatite sample overlaps with the emplacement age range of the carbonatite from previous work and therefore corresponds to magmatic activity within the area. The nepheline-free syenite sample (BX 01) yielded a weighted mean age of 1220 ± 2 Ma, whereas the nepheline syenite sample (SNT 04) gives a weighted mean age of 1209 ± 3 Ma. These ages were obtained from magmatic zircon and approximate magmatic crystallization. The data indicate that the nepheline-free syenite predates the nepheline syenites. The 1216 ± 2.4 Ma and 1213 ± 2.5 Ma age of the nepheline syenites (Littmann et al 2000, in Drüppel et al., 2005) are similar to the presented 1209 ± 3 Ma and 1205 ± 13 Ma age of the nepheline syenites. This similarity or overlap in ages suggests that the syenitic rocks were emplaced continuously over a period of at least 15 Ma**.** Shortly after emplacement of the nepheline syenite, the carbonatite magmatism commences at ~1200 Ma cross-cutting the silicate rocks. The slightly younger age of the carbonatite compared to the nepheline syenite is common in other carbonatite alkaline complexes worldwide and may suggest that the rocks were part of the same magma plumbing system. In the vicinity of the study area, there is an occurrence of ferrocarbonatite dykes in the Swartbooisdrif area, with younger magmatic U-Pb pyrochlore ages of ca. 1140-1120 Ma (Littmann et al., 2000, in Drüppel et al., 2005). Their relationship to the Epembe magmatism remains unclear.

5.4.5. Isotopic constraints on magma source

The similar and narrow initial $\varepsilon_{Hf(t)}$ values of zircon from syenite (0.5 ± 0.4 to +1.5 ± 0.4) and nepheline syenite (+1.6 ± 0.3 to +2.7 ± 0.5) suggest a common mantle source and that the parental melts did not experience significant interaction or mixing between isotopically distinct source components. However, given that on the $\varepsilon_{Hf(t)}$ vs age diagram (Fig. 5.6b), the $\varepsilon_{Hf(t)}$ values of the syenite and nepheline syenite zircon plot towards chondritic uniform reservoir (CHUR)

away from the Depleted Mantle (DM), the mantle source might have been MORB-type depleted upper mantle and parental melts may have been contaminated by evolved continental crust during magma ascent and emplacement. The contribution from continental crust can be evaluated using whole rock primitive mantle normalized multi-element patterns. Pronounced negative Nb anomalies together with strong positive Pb anomalies are expected in mantle derived rocks which have interacted with continental crust (e.g. Maier et al., 2013). Both Epembe syenite and nepheline syenite samples do not show negative Nb and positive Pb anomalies in PRIMA-normalized diagrams (Fig. 5.8: Tshiningayamwe et al., submitted) arguing against crustal contamination of the syenite and nepheline syenite parental melts. Therefore, it is considered that the syenite and nepheline syenite zircon isotopic composition are representative of the primary source, which is a moderately depleted mantle. Given that the syenite did not experience crustal contamination, it appears likely that it did not evolve from the nepheline syenite by assimilation and fractional crystallization process.

Very few Hf isotope data exist for carbonatites. Available data indicate that carbonatites exhibit large isotopic variations, requiring a number of different sources ranging from enriched to depleted mantle located in the asthenosphere or in the subcontinental lithospheric mantle. For instance, Wu et al. (2011) showed that zircon from the Phalaborwa carbonatite, South Africa is characterized by unradiogenic initial Hf isotopic composition with $\varepsilon_{Hf(t)}$ from -7.9 to -10.5. After discounting the involvement of the continental crust, they proposed that the parental melt to the Phalaborwa carbonatite was derived from an enriched mantle (Wu et al., 2011). On the other hand, Zhu et al. (2017) showed that zircons from the Miaoya carbonatite complex China, have variable radiogenic initial Hf isotopic compositions with $\varepsilon_{Hf(t)}$ ranging from +3.1 to +8.9. They proposed an isotopically heterogeneous mantle source involving both enriched and depleted mantle components. Similarly, involvement of both depleted and enriched mantle components has been proposed for the Chuktukon carbonatite complex, Siberia based on variable $\varepsilon_{Hf(t)}$ (-0.6 to +6.3) in zircon (Doroshkevich et al., 2021). Although depleted mantle components have been proposed as mantle sources to carbonatites, so far the typical MORB-type DM has not been invoked (Hoernle et al., 2002). While variable Nb in whole rock PRIMA-normalized diagram is attributed to variable pyrochlore abundance and compositions in the Epembe carbonatite, strong

negative Pb anomalies (Tshiningayamwe et al., submitted) are consistent with the absence of crustal contamination of the carbonatite magma during emplacement. The narrow $\varepsilon_{Hf(t)}$ for the Epembe carbonatite (+0.5 ± 0.4 to +1.9 ± 0.2) suggest that that the parental melt did not experience significant interaction or mixing between isotopically distinct source components. Radiogenic initial Hf isotopic composition of carbonatite zircon thus indicate that the Epembe carbonatite was derived from a slightly depleted mantle source. The isotopic similarity between the Epembe syenite, nepheline syenite and carbonatite suggest an isotopically similar but compositionally heterogeneous mantle source. As shown earlier, the mantle source location for alkaline rocks and carbonatites is usually a metasomatized or asthenospheric mantle. Studies which invoke a metasomatized mantle have shown that the initial Hf isotope composition is unradiogenic (e.g. Wu et al., 2011). In contrast, the radiogenic of $\varepsilon_{Hf(t)}$ for Epembe zircons rather suggest an asthenospheric mantle origin of the parental melts.

5.5. Conclusion

Combined cathodoluminescence imaging and geochemistry of zircon is used to constrain magma sources and post-igneous processes of the Epembe Complex. Zircons were extracted from syenite, nepheline syenite and carbonatite samples. U-Pb geochronology of zircon shows that the order of emplacement of the Epembe complex was in the following order: syenite, nepheline syenite and carbonatite. Textural and chemical characteristics suggest that zircons from syenite and carbonatite are magmatic, and the incorporation of trace elements is controlled by crystallization from a melt**.** In nepheline syenite, two zircon types can be distinguished. Type 1 zircon crystallized from the cooling nepheline syenite melt, whereas type 2 zircon is a result of hydrothermal alteration. Compared to type 1 zircon, the formation of type 2 zircon was accompanied by the development of a cloudy CL texture, an increase in LREE, Nb and Ti sourced from within the complex. No change is observed in the Hf concentration and $^{176}Hf/^{177}Hf$ ratios among the different zircon types suggesting that zircon retained the Hf isotopic composition of its parental melt. Initial radiogenic $\varepsilon_{Hf(t)}$ values of zircon from syenite (0.5 ± 0.4 to +1.5 ± 0.4),

nepheline syenite (+1.6 ± 0.3 to +2.7 ± 0.5) and carbonatite (+0.5 ± 0.4 to +1.9 ± 0.2) suggest an isotopically similar, moderately depleted mantle source.

6. Summary of the petrogenesis of the Epembe syenite, nepheline syenite and carbonatite

6.1. Petrology (with emphasis on apatite and zircon) and emplacement

The syenite is medium-grained, with a granular texture and comprises dominantly alkali feldspar and clinopyroxene with accessory apatite and magnetite. The nepheline syenite is texturally variable, although the most common variety is a medium-grained massive rock. The mineral assemblage comprises major to minor alkali feldspar, nepheline, biotite and cancrinite, while plagioclase, apatite, sphene, zircon, calcite and magnetite are accessory phases. The textural evolution of the carbonatite is diverse and involves both magmatic textures (cumulates, porphyritic, massive and flow textures) and post-magmatic deformation textures (core and mantle structures, mechanical twinning in calcite). However, the mineralogy is generally simple, consisting of major to minor calcite, apatite, pyrochlore, aegirine, biotite, zircon, alkali feldspar and plagioclase. Apatite and zircon are generally rare in the syenite and nepheline syenite under the petrographic microscope, thus the studied grains were obtained from mineral separates. In the carbonatite though, magmatic apatite is ubiquitous, showing ovoid, elongate and subhedral grain shapes. Carbonatite apatite grains are disseminated in a calcite matrix or display a flow texture. Occasionally apatite occurs in clusters and as inclusions within pyrochlore and zircon. Zircon in carbonatite occurs as disseminated fine- to medium-sized grains with subhedral and euhedral grain shapes. Based on CL imaging, magmatic apatite from syenite sample occurs as anhedral, subrounded to elongate grains with grain size variations of 200 to 250 µm and homogeneous grey luminescence. Magmatic nepheline syenite-hosted apatite samples display subhedral and anhedral grain morphologies, which are either elongated, angular or sub-rounded with a predominant grain size of ca. 250 µm. Most of the magmatic nepheline syenite and carbonatite apatite grains are homogeneous grey in CL mode, however, a few grains display core-rim zonations. Magmatic zircons from syenite, nepheline syenite and carbonatite are anhedral to subhedral in shape, with grain sizes ranging from 100 to 600 µm. The internal structures in CL consists of light grey homogeneous zones, oscillatory zones and patchy zoning characterized by areas of different brightness.

Zircon U-Pb dating by LA-ICPMS yields a $^{206}Pb/^{238}U$ weighted mean emplacement age of 1220 ± 3 Ma for the syenite corresponding with the Tera-Wasserburg lower intercept LA-ICPMS U-Pb age of 1216 ± 11 Ma obtained on apatite from the same sample. Two nepheline syenite samples give similar zircon magmatic ages of 1209 ± 3 Ma ($^{206}Pb/^{238}U$ weighted mean age) and 1205 ± 13 Ma (concordia upper intercept age). Zircon from one carbonatite sample yields a magmatic concordia age of 1198 ± 5 Ma similar to that of the associated nepheline syenite. The similarity in ages between the carbonatite compared to the nepheline syenite is common in some other carbonatite alkaline complexes worldwide and may suggest that these rocks were part of the same magma plumbing system. Magmatic apatite from three nepheline syenite samples give U-Pb ages of 1193 ± 14 Ma, 1197 ± 17 Ma and 1194 ± 16 Ma. These apatite ages show excellent agreement with zircon ages from the same samples considering analytical uncertainty and therefore record the timing of emplacement.

6.2. Evolution of the syenite and nepheline syenite

The formation of evolved rock types of alkaline suites including syenites may be by fractionation from alkali basaltic parents combined with input from the continental crust (Foland et al., 1993; Jung et al., 2007), or by small degree partial melting of the enriched lower continental crust (e.g. Drüppel el., 2007).

The whole rock REE pattern of the Epembe syenite as well as that of magmatic apatite and zircon from the syenite show negative Eu anomalies, consistent with prior plagioclase formation and fractionation. The whole rock geochemical characteristics indicate that the syenite was not contaminated by continental crust during magma ascent and emplacement. It is characterized by absence of a negative Nb anomaly on a PRIMA-normalized diagram with Ce/Pb and Nb/U ratios of 12 and 19, respectively. These features are different from crustal rocks which are characterized by pronounced negative Nb anomalies in PRIMA-normalized diagrams with Nb/U ratios of 10 and Ce/Pb < 6 (Hofmann, 1997). The absence of a crustal signature in the evolution of the syenite therefore indicates that the syenite is not related to the nepheline

syenite by combined assimilation and fractional crystallization and was likely emplaced as a distinct magma batch derived from the mantle.

The nepheline-normative syenite samples on the other hand define broadly linear trends in Harker plots consistent with evolution by fractional crystallization involving pyroxene and apatite. The whole rock total REE decrease with increasing SiO_2, suggesting that the REE have been fractionated by apatite. However, core-rim zoned apatite is characterized by rim-ward increase in REE concentration, which is rather attributed to re-equilibration of early formed apatite with local infiltration of a melt rich in REE, which resulted in the formation of apatite overgrowths. Nickel and Cr values in whole rock are low (< 3 ppm), even in the most primitive nepheline syenite samples, which implies that these rocks are the product of crystallization from an evolved magma, consistent with their low Mg# (0.20-0.29).

Whole rock REE patterns of the syenite and nepheline syenite show LREE enrichment relative to HREE. In addition, on a PRIMA-normalized multi-element diagram both the syenite and nepheline syenite display depletions in Zr and Hf. These features are consistent with the presence of garnet in mantle source region, which can retain HREE, well as Hf and Zr during partial melting.

6.3. Evolution of the carbonatite

Although the Epembe carbonatite displays post-magmatic deformation textures, its magmatic geochemical characteristics appear to have been preserved and are seen in the enrichment of incompatible elements up to 10 000 times Primitive Mantle values, depletion in Zr and Hf, LREE abundances of up to 100 times chondrite values with $La_N/Yb_N > 24$, and Y/Ho = 28, similar to many other magmatic carbonatite occurrences worldwide (e.g. Nelson et al., 1988; Woolley and Kempe, 1989). The occurrence of feldspar, biotite and disaggregated silicate lithologies in the carbonatite are interpreted to be due to interaction with associated nepheline syenite during carbonatite emplacement rather than with the surrounding basement units. This is supported by the unradiogenic Sr isotope composition in carbonatite apatite. Several features suggest that that the Epembe carbonatite and nepheline syenite are related: (1) Similar emplacement ages, (2) similar initial Sr-Nd and Hf isotopic compositions of apatite and zircon, respectively, (3) similar

whole-rock REE and multi-element patterns (including Sr, Pb and Hf-Zr), (4) REE abundances in magmatic apatite from both rock types are also similar. Carbonatite magmas are thought to form by direct partial melting of a carbonated mantle peridotite (Harmer et al., 1999; Harmer and Gittins 1998, Wallace and Green, 1988), or represent residual melts that fractionated from a nephelinite parental magma (Gittins and Jago, 1998; Brassiness et al., 2005; Mitchell 2005; Wang et., 2014). Carbonatites may also be viewed as a product of liquid immiscibility arising from a carbonate-saturated silicate melt (Lee and Wyllie, 1998; Bodeving et al., 2017). Studies which invoke the formation of a carbonatite magma by direct partial melting of carbonated mantle peridotite show that the resulting carbonatite is dolomitic in composition (e,g. Wallace and Green, 1988; Wyllie and Green, 1988). Given that the Epembe carbonatite is calcitic in composition rules out this hypothesis. Moreover, the low Cr and Ni abundances in the Epembe carbonatite also argue against the origin of this carbonatite from a mantle peridotite as these elements are enriched in the latter rock. Geochemical characteristics of the carbonatite and nepheline syenite also suggest that the origin of the Epembe carbonatite is not a product of immiscible separation between a carbonate and silicate melt, because during immiscible separation between a carbonated silicate liquid, Ba, REE and HFSE concentrations are expected to be high in the silicate unit (Veksler et al., 2012), which is not the case at Epembe. It has however been shown experimentally that carbonate melts have low viscosities and can separate from their source even at low degrees of partial melting and are capable of percolating through wall rocks (Hunter and Mackenzie, 1989; Hammouda and Laporte, 2000). Therefore, it is proposed that the Epembe carbonatite magma formed after partial crystallization of the associated nepheline syenites and then intruded the nepheline syenite rocks. A similar scenario has been proposed for the origin of the Dahomeyide orogen carbonatite, Ghana (Nude et al., 2009).

6.4. Post-magmatic alteration

Interaction of primary mineral assemblages with fluids is common around carbonatite alkaline complexes (e.g. Broom-Fendley et al., 2016; Elliot et al., 2018; Lu et al., 2021). In our study, some of the apatite and zircon grains obtained from the nepheline syenite show alteration features

related to interaction with fluids. Hydrothermally altered apatite display a patchy texture in CL and is depleted in Na, Y and REE, particularly the LREE and is enriched in Sr relative to magmatic apatite. Given that there are no differences in $^{87}Sr/^{86}Sr_{(i)}$ between altered apatite and magmatic apatite the fluids involved were likely derived from the cooling nepheline syenite magma. Hydrothermally altered zircon displays a cloudy appearance in CL. It is characterized by enrichment in LREE, Nb and Ti at similar initial Hf isotopic composition when compared to magmatic zircon, suggesting that it formed by interaction with fluids enriched in LREE, Nb and Ti, sourced from within the complex.

6.5. Magma source constraints

The Sr and Nd isotopic composition of apatite in syenite ($^{87}Sr/^{86}Sr_{(i)}$ = 0.7035-0.7048; $\varepsilon_{Nd(t)}$ = +2.5 to +3.2), nepheline syenite ($^{87}Sr/^{86}Sr_{(i)}$ = 0.7031-0.7037; $\varepsilon_{Nd(t)}$: +1.5 to +4.4) and carbonatite ($^{87}Sr/^{86}Sr_{(i)}$ = 0.7031-0.7033; $\varepsilon_{Nd(t)}$ = 0 to +3.3) as well as Hf isotopic ratios of zircon from syenite (+0.5 ± 0.4 to +1.5 ± 0.4), nepheline syenite (+1.6 ± 0.3 to +2.7 ± 0.5) and carbonatite (+0.5 ± 0.4 to +1.9 ± 0.2) overlap, suggesting a common but heterogeneous mantle source for the three rock types. The unradiogenic $^{87}Sr/^{86}Sr_{(i)}$ values obtained on apatite from all rock types indicate that the parental mantle-derived magmas were not affected by contamination with evolved crustal material. Also, the high Sr and Nd abundance in syenite and nepheline syenite apatite relative to apatite from continental granites and pegmatites (e.g. Belousova et al., 2002b) argue against crustal contamination as the high Sr and Nd concentrations in the Epembe apatite would prevent significant influence by the continental crust (Wu et al., 2011). Our isotope data are also different from radiogenic initial Sr and unradiogenic Nd-Hf isotopic composition from other carbonatite alkaline complexes, such as the Phalaborwa Igneous Complex, for which a metasomatized lithospheric origin has been proposed (Wu et al., 2011). The unradiogenic initial Sr and radiogenic Nd isotopic compositions in apatite grains as well radiogenic Hf isotopic composition zircon from Epembe thus render metasomatized lithospheric mantle unlikely as a source region. However, the presented Sr and Nd isotopic characteristics are similar to many other carbonatites and oceanic island basalts from Africa, Australia, Brazil, Europe and the United States ranging in age from Proterozoic to Tertiary (Nelson et al., 1988), for which an asthenospheric mantle origin was

proposed. Thus, an asthenospheric mantle source region is considered for the Epembe syenite, nepheline syenite and carbonatite.

Geological events associated with the petrogenesis of the Epembe Complex based on data from this study are summarized in Fig 6.1.

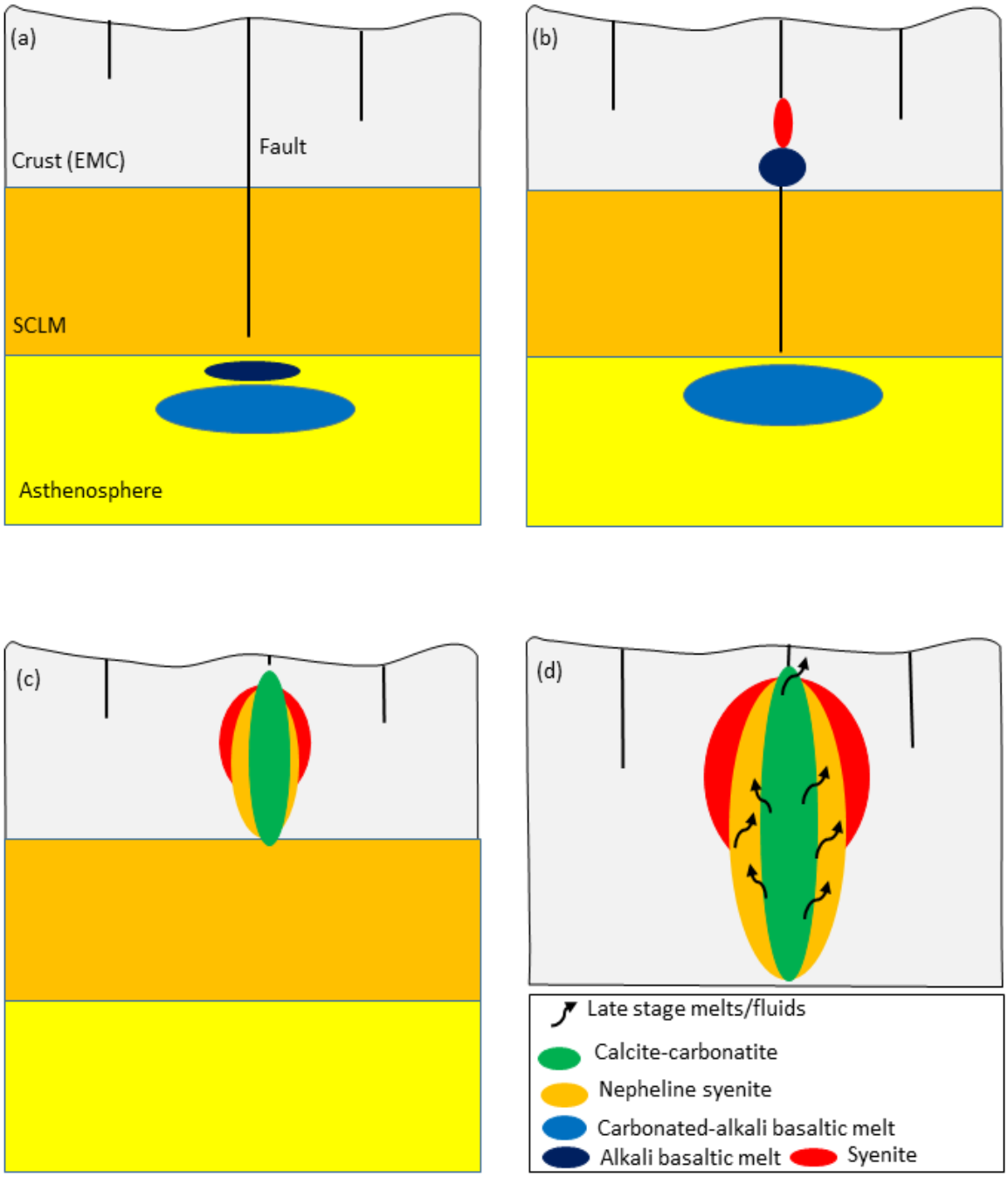

Fig. 6.1: (a) Partial melting of a heterogeneous asthenospheric mantle resulted in the formation an alkali basaltic melt and a carbonated-alkali basaltic melt. The alkali basaltic melt is the parental melt to the syenite (sample BX 01), whereas the carbonated-alkali basaltic melt is the parental melt to the nepheline syenite (samples SNT 03, SNT 04, SNT 05, SNT 06, SNT 07, SNT 08, SNT 09) and the calcite-carbonatite (samples EC 4, EC 5, EC 21, EC 23, EC 29). (b) The syenite parental melt ascends first and evolves by fractional crystallization involving plagioclase without significant crustal contamination and crystallizes at 1220 Ma. (c) Following the syenite formation, emplacement of the nepheline syenite commences at 1209 involving fractional crystallization of apatite and pyroxene leaving behind a carbonatite melt. Subsequently the carbonatite magma intrudes the nepheline syenite at 1198 Ma. (d) Finally, melts or fluids emanating from carbonatite and to some extent the nepheline syenite causes alteration of primary mineral assemblages, recorded in both apatite and zircon.

6.6. Conclusions

The aim of this study was to use whole rock geochemistry, accessory mineral (apatite, zircon) geochronology (U-Pb) and geochemistry (Sr, Nd and Hf isotopes and trace elements) in order to refine aspects of the petrogenesis of the Epembe syenite, nepheline syenite and carbonatite.

- Age constraints from zircon U-Pb dating show that the syenite (1220 ± 3 Ma) was emplacement first followed by the nepheline syenite (1209 ± 3 Ma, 1205 ± 13 Ma) and then the carbonatite (1198 ± 5 Ma).
- Whole rock, apatite and zircon trace element characteristics of the syenite indicate that it crystallized from an evolved mantle melt involving plagioclase fractionation without significant contamination by the continental crust. Lack of crustal contamination in the evolution of the syenites further suggests that the syenite did not evolve from the nepheline syenite by combined crustal assimilation and fractional crystallization.
- Whole rock geochemistry of the nepheline syenite is consistent with fractional crystallization involving apatite and pyroxene. Furthermore, the geochemical characteristics suggest that the carbonatite is not a product of immiscible separation

between a carbonate and silicate melt nor is it primary, but likely a melt fraction that formed after partial crystallization of the nepheline syenite.

- Different apatite and zircon textures from the nepheline syenite combined with geochemistry suggest that this unit was affected by late-stage melts or fluids.
- The combined isotopic composition of apatite (Sr, Nd isotopes) and zircon (Hf isotopes) support an origin of the Epembe syenite, nepheline syenite and carbonatite from a common and heterogeneous mantle source involving a depleted and enriched component located in the asthenosphere.

6.7. Recommendations for future work

In order to further explore the petrogenesis of the Epembe Complex, the following recommendations should be considered for future work:

- Whole rock and isotope geochemistry should be performed on the associated pyroxenite unit and lamprophyres, in order establish its genetic implication with the carbonatite and syenites. In addition, geochemical studies should be used to explore the relationship between the Epembe syenite and Kunene anorthiste considering the age similarities.
- Geochemical analyses should be carried out on other phases (e.g. calcite, pyroxene, and biotite) across the different rock types to explore the relationship between carbonatite and syenites especially the nepheline syenite.
- Fluid inclusion study within the ovoid apatite grains may be used to ascertain the temperature and salinity of hydrothermal fluids. This could be assisted by stable O and H isotopes analysis to identify the source and degree of fluid-rock interaction.
- It will also be of interest to carry out whole rock Sr-Nd-Hf isotopic composition on the samples from which apatite and zircon was previously extracted in order to compare the isotopic compositions with those determined in apatite and zircon.

7. References

Alberti, A., Castorina, F., Censi, P., Comin-Chiaramonti, P., & Gomes, C. (1999). Geochemical characteristics of Cretaceous carbonatites from Angola. Journal of African Earth Sciences, 29, 735–759.

Ashwal, L. D., & Twist, D. (1994). The Kunene complex, Angola/Namibia: A composite massif-type anorthosite complex. Geological Magazine, 131(5), 579–591.

Barker, D. S. (2001). Calculated silica activities in carbonatite liquids. Contributions to Mineralogy and Petrology, 141(6), 704–709.

Bell, K., Kjarsgaard, B., & Simonetti, A. (1999). Carbonatites—Into the Twenty-First Century. Journal of Petrology, 39, 1839-1845.

Bell, K., & Tilton, G. R. (2001). Nd, Pb and Sr Isotopic Compositions of East African Carbonatites: Evidence for Mantle Mixing and Plume Inhomogeneity. Journal of Petrology, 42(10), 1927–1945.

Bell, K., & Simonetti, A. (2009). Source of parental melts to carbonatites–critical isotopic constraints. Mineralogy and Petrology, 98, 77–89.

Belousova E, A., Griffin W, L., Suzanne Y, O., & Fisher N, I. (2002a). Igneous zircon: trace element composition as an indicator of source rock type. Contributions to Mineralogy and Petrology, 143, 602-622.

Belousova, E. A., Griffin, W. L., O'Reilly, S. Y., & Fisher, N. I. (2002b). Apatite as an indicator mineral for mineral exploration: Trace-element compositions and their relationship to host rock type. Journal of Geochemical Exploration, 76(1), 45–69.

Black, L. P., Kamo, S. L., Allen, C. M., Aleinikoff, J. N., Korsch, R. J., & Foudoulis, C. (2003). TEMORA 1: a new standard for Phanerozoic U-Pb geochronology. Chemical Geology, 200(1-2), 155-170.

Black, L. P., Kamo, S. L., Allen, C. M., Aleinikoff, J. N., Korsch, R. J., & Foudoulis, C. (2004). Improved 206Pb/238U microprobe geochronology by the monitoring of a trace-element-related

matrix effect: SHRIMP, ID-TIMS, ELA-ICP-MS and oxygen isotope documentation for a series of zircon standards. Chemical Geology, 205(1-2), 115-140.

Bodeving, S., Williams-Jones, A. E., & Swinden, S. (2017). Carbonate–silicate melt immiscibility, REE mineralising fluids, and the evolution of the Lofdal Intrusive Suite, Namibia. Lithos, 268–271, 383–398.

Bolhar, R., Tappe, S., Wilson, A., Ireland, T., Avila, J., & Anhaeusser, C. (2021a). A petrochronology window into near-surface fluid/rock interaction within Archaean ultramafic-mafic crust: Insights from the 3.25 Ga Stolzburg Complex, Barberton Greenstone Belt. Chemical Geology, 569, 120130.

Bolhar, R., Cawthorn, R. G., (2021b). Zircon geochronology and geochemistry of pre- Bushveld sills in the eastern Transvaal Supergroup, South Africa. South African Journal of Geology.

Bolhar, R., Hofmann, A. & Allen, C. M., Maas, R. (2021c). A LA-ICPMS zircon record of magmatic crystallization and compositional alteration in meta-igneous rocks of the eastern Kaapvaal Craton. South African Journal of Geology.

Bolhar, R., Weaver, S. D., Palin, J. M., Cole, J. W., & Paterson, L. A. (2008). Systematics of zircon crystallisation in the Cretaceous Separation Point Suite, New Zealand, using U/Pb isotopes, REE and Ti geothermometry. Contributions to Mineralogy and Petrology, 156(2), 133–160.

Bouvier, A., Vervoort, J. D., & Patchett, P. J. (2008) The Lu-Hf and Sm-Nd isotopic composition of CHUR: Constraints from unequilibrated chondrites and implications for the bulk composition of terrestrial planets. Earth and Planetary Science Letters, 273, 48-57

Boynton, W.V. (1984). Cosmochemistry of the rare Earth elements: Meteorite studies. Dev. Geochem. 2, 63–114.

Brandt, S., Klemd, R., & Okrusch, M. (2003). Ultrahigh-Temperature Metamorphism and Multistage Evolution of Garnet–Orthopyroxene Granulites from the Proterozoic Epupa Complex, NW Namibia. Journal of Petrology, 44(6), 1121–1144.

Brassinnes, S., Balaganskaya, E., & Demaiffe, D. (2005). Magmatic evolution of differentiated ultramafic, alkaline and carbonatite intrusion of the Vuoriyarvi (Kola Peninsula, Russia) A LA-ICP-MS study of apatite. Lithos, 85, 76-92.

Broom-Fendley, S., Brady, A. E., Wall, F., Gunn, G., & Dawes, W. (2017). REE minerals at the Songwe Hill carbonatite, Malawi: HREE-enrichment in late-stage apatite. Ore Geology Reviews, 81, 23–41.

Broom-Fendley, S., Styles, M. T., Appleton, J. D., Gunn, G., & Wall, F. (2016). Evidence for dissolution-reprecipitation of apatite and preferential LREE mobility in carbonatite-derived late-stage hydrothermal processes. American Mineralogist, 101(3), 596–611.

Brower, A. (2017). Understanding Magmatic Timescales and Magma Dynamics in Proterozoic Anorthosites: a Geochronological and Remote Sensing Investigation of the Kunene Complex, Angola. MSc thesis, University of the Witwatersrand, Johannesburg.

Bühn, B., Wall, F., & Le Bas, M. J. (2001). Rare-earth element systematics of carbonatitic fluorapatites, and their significance for carbonatite magma evolution. Contributions to Mineralogy and Petrology, 141(5), 572–591.

Bull, J. (2013). Detailed Geological Mapping and Petrological Study of the Nb-Ta-U Epembe Carbonatite-Syenite Complex, North-West Namibia. MSc thesis, University of Exeter, Penryn.

Bybee, G. M., Hayes, B., Owen-Smith, T. M., Lehmann, J., Ashwal, L. D., Brower, A. M., Hill, C. M., Corfu, F., & Manga, M. (2019). Proterozoic massif-type anorthosites as the archetypes of long-lived (≥100 Myr) magmatic systems—New evidence from the Kunene Anorthosite Complex (Angola). Precambrian Research, 332, 105393.

Chakhmouradian, A. R., Reguir, E. P., & Mitchell, R. H. (2002). Strontium-apatite: new occurrences, and the extent of Sr-for-Ca substitution in apatite-group minerals. The Canadian Mineralogist, 40(1), 121–136.

Chakhmouradian, A. R., Reguir, E. P., & Zaitsev, A. N. (2016). Calcite and dolomite in intrusive carbonatites. I. Textural variations. Mineralogy and Petrology, 110(2), 333–360.

Chakhmouradian, A. R., Reguir, E. P., Zaitsev, A. N., Couëslan, C., Xu, C., Kynický, J., Mumin, A. H., & Yang, P. (2017). Apatite in carbonatitic rocks: Compositional variation, zoning, element partitioning and petrogenetic significance. Lithos, 274–275, 188–213.

Chamberlain, K., & Bowring, S. (2001). Apatite–feldspar U–Pb thermochronometer: A reliable, mid-range (~450°C), diffusion-controlled system, 172, 173-200.

Chen, W., & Simonetti, A. (2013). In-situ determination of major and trace elements in calcite and apatite, and U–Pb ages of apatite from the Oka carbonatite complex: Insights into a complex crystallization history. Chemical Geology, 353, 151–172.

Cherniak, D. J., Lanford, W. A., & Ryerson, F. J. (1991). Lead diffusion in apatite and zircon using ion implantation and Rutherford Backscattering techniques. Geochimica et Cosmochimica Acta, 55(6), 1663–1673.

Cherniak, D. J., & Watson, E. B. (2001). Pb diffusion in zircon. Chemical Geology, 172(1), 5–24.

Chew, D. M., Sylvester, P. J., & Tubrett, M. N. (2011). U–Pb and Th–Pb dating of apatite by LA-ICPMS. Chemical Geology, 280(1), 200–216.

Chew, D. M., Babechuk, M. G., Cogné, N., Mark, C., O'Sullivan, G. J., Henrichs, I. A., Doepke, D., & McKenna, C. A. (2016). (LA,Q)-ICPMS trace-element analyses of Durango and McClure Mountain apatite and implications for making natural LA-ICPMS mineral standards. Chemical Geology, 435, 35–48.

Corfu, F., Hanchar, J. M., Hoskin, P. W. O., & Kinny, P. (2003). Atlas of Zircon Textures. Reviews in Mineralogy and Geochemistry, 53(1), 469–500.

Dalton, J. A., & Wood, B. J.(1993). The compositions of primary carbonate melts and their evolution through wallrock reaction in the mantle. Earth and Planetary Science Letters, 119(4), 511–525.

Darling, R. S., & Florence, F. P. (1995). Apatite light rare earth element chemistry of the Port Leyden nelsonite, Adirondack Highlands, New York; implications for the origin of nelsonite in anorthosite suite rocks. Economic Geology, 90(4), 964–968.

Dawson, J. B. (1987). The kimberlite clan: Relationship with olivine and leucite lamproites, and inferences for upper-mantle metasomatism. In Fitton, J. G., & Upton, B. G. J. (eds), Alkaline igneous rocks. Geological Society of London Special Publications, 30, 95–101.

Decrée, S., Cawthorn, G., Deloule, E., Mercadier, J., Frimmel, H., & Baele, J. M. (2020). Unravelling the processes controlling apatite formation in the Phalaborwa Complex (South Africa) based on combined cathodoluminescence, LA-ICPMS and in-situ O and Sr isotope analyses. Contributions to Mineralogy and Petrology, 175, 34.

Dodson, M. H. (1973). Closure temperature in cooling geochronological and petrological systems. Contributions to Mineralogy and Petrology, 40(3), 259–274.

Doroshkevich, A. G., Sharygin, V. V., Belousova, E. A., Izbrodin, I. A., & Prokopyev, I. R. (2021). Zircon from the Chuktukon alkaline ultramafic carbonatite complex (Chadobets uplift, Siberian craton) as evidence of source heterogeneity. Lithos, 382–383, 105957.

Dostal, J. (2017). Rare Earth Element Deposits of Alkaline Igneous Rocks. Resources, 6(3), 34.

Doucelance, R., Bruand, E., Matte, S., Bosq, C., Auclair, D., & Gannoun, A. M. (2020). In-situ determination of Nd isotope ratios in apatite by LA-MC-ICPMS: Challenges and limitations. Chemical Geology, 550, 119740.

Drüppel, K., Hoefs, J., & Okrusch, M. (2005). Fenitizing Processes Induced by Ferrocarbonatite Magmatism at Swartbooisdrif, NW Namibia. Journal of Petrology, 46(2), 377–406.

Drüppel, K., Littmann, S., Romer, R. L., & Okrusch, M. (2007). Petrology and isotope geochemistry of the Mesoproterozoic anorthosite and related rocks of the Kunene Intrusive Complex, NW Namibia. Precambrian Research, 156(1), 1–31.

Eby, G. N., Woolley, A. R., Din, V., & Platt, G. (1998). Geochemistry and Petrogenesis of Nepheline Syenites: Kasungu–Chipala, Ilomba, and Ulindi Nepheline Syenite Intrusions, North Nyasa Alkaline Province, Malawi. Journal of Petrology, 39(8), 1405–1424.

Elburg, M., Vroon, P., van der Wagt, B., & Tchalikian, A. (2005). Sr and Pb isotopic composition of five USGS glasses (BHVO-2G, BIR-1G, BCR-2G, TB-1G, NKT-1G). Chemical Geology, 223(4), 196–207.

Elliot, H. A. L., Wall, F., Chakhmouradian, A. R., Siegfried, P., Dahlgren, S., Weatherley, S., Finch, A. A., Marks, M. A. W., Dowman, E., & Deasy, E. (2018). Fenites associated with carbonatite complexes: A review. Ore Geology Reviews, 93, 38-59

Falshaw, S. (2012). The Geology and rare metal metallogenesis of the Epembe carbonatite dyke, NW Namibia. MSc thesis, University of Exeter, Penryn.

Ferguson, J., McIver, J., & Danchin, R. (1975). Fenitisation associated with the Alkaline-Carbonatite Complex of Epembe, South West Africa. Annals of the South Africa Museum, 78, 111-121.

Fitton, J. (1987). The Cameroon Line, West Africa: A comparison between oceanic and continental alkaline volcanism. In Fitton, J. G., & Upton, B. G. J. (eds), Alkaline igneous rocks. Geological Society of London Special Publications, 30, 273–291.

Foland, K. A., Landoll, J. D., Henderson, C. M. B., & Chen, J. (1993). Formation of cogenetic quartz and nepheline syenites. Geochimica et Cosmochimica Acta, 57(3), 697–704.

Foster, G., & Vance, D. (2006). In situ Nd isotopic analysis of geological materials by laser ablation MC-ICP-MS. Journal of Analytical Atomic Spectrometry, 21, 288-296.

Fosu, B. R., Ghosh, P., Chew, D. M., & Viladkar, S. G. (2019). Composition and U—Pb ages of apatite in the Amba Dongar carbonatite–alkaline complex, India. Geological Journal, 54(6), 3438–3454.

Frost, B., Barnes, C., Collins, W., Arculus, R., Ellis, D., & Frost, C. (2001). A Geochemical Classification for Granitic Rocks. Journal of Petrology, 42, 2033–2048.

Gao, S., Liu, X., Yuan, H., Hattendorf, B., Günther, D., Chen, L., & Hu, S. (2002). Determination of Forty Two Major and Trace Elements in USGS and NIST SRM Glasses by Laser Ablation-Inductively Coupled Plasma-Mass Spectrometry. Geostandards Newsletter, 26(2), 181–196.

Gawęda, A., Szopa, K., & Chew, D. (2014). LA-ICP-MS U-Pb dating and REE patterns of apatite from the Tatra Mountains, Poland as a monitor of the regional tectonomagmatic activity. Geochronometria, 41(4), 306–314.

Giebel, R, J., Parsapoor, A., Walter, B, F., Braunger, S., Marks, M, A, W., Wenzel, T., & Markl, G. (2019). Evidence of Magma-Wall Rock Interaction in Carbonatites from the Kaiserstuhl Volcanic Complex (Southwest Germany). Journal of Petrology, 60(6), 1163-1194.

Gittins, J. (1989). The origin and evolution of carbonatite magmas. In Bell, K. (Ed.), Carbonatitites: Genesis and Evolution. Unwin Hyman. London, pp 580-600.

Gittins, J., & Jago, B. (1998). Differentiation of natrocarbonatite magma at Oldoinyo Lengai volcano, Tanzania. Mineralogical Magazine - Mineralogical Magazine, 62, 759–768.

Gleißner, P., Drüppel, K., & Romer, R. L. (2011). The role of crustal contamination in massif-type anorthosites, new evidence from Sr–Nd–Pb isotopic composition of the Kunene Intrusive Complex, NW Namibia. Precambrian Research, 185(1), 18–36.

Hammouda, T., Chantel, J., & Devidal, J.-L. (2010). Apatite solubility in carbonatitic liquids and trace element partitioning between apatite and carbonatite at high pressure. Geochimica et Cosmochimica Acta, 74(24), 7220–7235.

Hanchar, J. M., & Miller, C. F. (1993). Zircon zonation patterns as revealed by cathodoluminescence and backscattered electron images: Implications for interpretation of complex crustal histories. Chemical Geology, 110(1), 1–13.

Harlov, D. E. (2011). Formation of monazite and xenotime inclusions in fluorapatite megacrysts, Gloserheia Granite Pegmatite, Froland, Bamble Sector, southern Norway. Mineralogy and Petrology, 102(1), 77.

Harlov, D. E., Andersson, U. B., Förster, H.-J., Nyström, J. O., Dulski, P., & Broman, C. (2002). Apatite–monazite relations in the Kiirunavaara magnetite–apatite ore, northern Sweden. Chemical Geology, 191(1), 47–72.

Harmer, R. E., & Gittins, J. (1998). The Case for Primary, Mantle-derived Carbonatite Magma. Journal of Petrology, 39(11–12), 1895–1903.

Harmer, R. E. (1998). The Petrogenetic Association of Carbonatite and Alkaline Magmatism: Constraints from the Spitskop Complex, South Africa. Journal of Petrology, 40, 525–548.

Heinonen, A. P., Andersen, T., & Rämö, O. T. (2010). Re-evaluation of rapakivi petrogenesis: Source constraints from the Hf isotope composition of zircon in the rapakivi granites and associated mafic rocks of Southern Finland. Journal of Petrology, 51(8), 1687–1709.

Hoernle, K., Tilton, G., Bas, M. J. L., Duggen, S., & Garbe-Schönberg, D. (2002). Geochemistry of oceanic carbonatites compared with continental carbonatites: Mantle recycling of oceanic crustal carbonate. Contributions to Mineralogy and Petrology, 142, 520-542.

Hofmann, A. W. (1997). Mantle geochemistry: The message from oceanic volcanism. Nature, 385, 219-229.

Hoskin, P. W. O. (2005). Trace-element composition of hydrothermal zircon and the alteration of Hadean zircon from the Jack Hills, Australia. Geochimica et Cosmochimica Acta, 69(3), 637–648.

Hoskin, P. W. O., & Schaltegger, U. (2003). The Composition of Zircon and Igneous and Metamorphic Petrogenesis. Reviews in Mineralogy and Geochemistry, 53(1), 27–62.

Hou, Z., Tian, S., Yuan, Z., Xie, Y., Yin, S., Yi, L., Fei, H., & Yang, Z. (2006). The Himalayan collision zone carbonatites in western Sichuan, SW China: Petrogenesis, mantle source and tectonic implication. Earth and Planetary Science Letters, 244(1), 234–250.

Ihlen, P., Schiellerup, H., Gautneb, H., & Skåat, Ø. (2013). Characterization of apatite resources in Norway and their REE potential—A review. Ore Geology Reviews, 58, 126-147.

Jackson, S. E., Pearson, N. J., Griffin, W. L., & Belousova, E. A. (2004). The application of laser ablation-inductively coupled plasma-mass spetrometry to insitu U-Pb zircon geochronology. Chemical Geology, 211(1-2), 47-69.

Jochum, K. P., Weis, U., Stoll, B., Kuzmin, D., Yang, Q., Raczek, I., Jacob, D. E., Stracke, A., Birbaum, K., Frick, D. A., Günther, D., & Enzweiler, J. (2011). Determination of Reference Values for NIST SRM 610–617 Glasses Following ISO Guidelines. Geostandards and Geoanalytical Research, 35(4), 397–429.

Jung, S., Hoffer, E., & Hoernes, S. (2007). NeoProterozoic rift-related syenites (Northern Damara Belt, Namibia): Geochemical and Nd–Sr–Pb–O isotope constraints for mantle sources and petrogenesis. Lithos, 96, 415–435.

Kalfoun, F., Ionov, D., & Merlet, C. (2002). HFSE residence and Nb/Ta ratios in metasomatised, rutile-bearing mantle peridotites. Earth and Planetary Science Letters, 199(1), 49–65.

Kapuka, R. R. (2019). Rare element distribution in the Epembe carbonatite dyke, Namibia. MSc thesis, University of the Witwatersrand, Johannesburg.

Kimura, J.-I., Chang, Q., & Kawabata, H. (2013). Standardless determination of Nd isotope ratios in glasses and minerals using laser-ablation multiple-collector inductively coupled plasma mass spectrometry with a low-oxide molecular yield interface setup. Journal of Analytical Atomic Spectrometry, 28(9), 1522–1529.

Kinny, P. D., & Maas, R. (2003). Lu–Hf and Sm–Nd isotope systems in zircon. Reviews in Mineralogy and Geochemistry, 53(1), 327–341.

Kirkland, C. L., Yakymchuk, C., Szilas, K., Evans, N., Hollis, J., McDonald, B., & Gardiner, N. J. (2018). Apatite: A U-Pb thermochronometer or geochronometer? Lithos, 318–319, 143–157.

Klemme, S., van der Laan, S. R., Foley, S. F., & Günther, D. (1995). Experimentally determined trace and minor element partitioning between clinopyroxene and carbonatite melt under upper mantle conditions. Earth and Planetary Science Letters, 133(3), 439–448.

Kogarko, L. (2018). Chemical Composition and Petrogenetic Implications of Apatite in the Khibiny Apatite-Nepheline Deposits (Kola Peninsula). Minerals, 8(11), 532.

Le Bas, M. J. (1987). Nephelinites and carbonatites. In: Fitton, J. G., & Upton, B. G. J. (eds), Alkaline igneous rocks. Geological Society of London Special Publications, 30, 53-83.

Le Roex, A. P., & Lanyon, R. (1998). Isotope and Trace Element Geochemistry of Cretaceous Damaraland Lamprophyres and Carbonatites, Northwestern Namibia: Evidence for Plume—Lithosphere Interactions. Journal of Petrology, 39(6), 1117–1146.

Lee, W.-J., & Wyllie, P. J. (1998). Processes of Crustal Carbonatite Formation by Liquid Immiscibility and Differentiation, Elucidated by Model Systems. Journal of Petrology, 39(11–12), 2005–2013.

Liferovich, R. P., & Mitchell, R. H. (2006). Apatite-group minerals from nepheline syenite, Pilansberg alkaline complex, South Africa. Mineralogical Magazine, 70(5), 463–484.

Liu, Y., Zhu, Z., Chen, C., Zhang, S., Sun, X., Yang, Z., & Liang, W. (2015). Geochemical and mineralogical characteristics of weathered ore in the Dalucao REE deposit, Mianning–Dechang REE Belt, western Sichuan Province, southwestern China. Ore Geology Reviews, 71, 437–456.

Liu, Y., Hou, Z., Zhang, R., Wang, P., Gao, J., & Raschke, M. B. (2019). Zircon Alteration as a Proxy for Rare Earth Element Mineralization Processes in Carbonatite-Nordmarkite Complexes of the Mianning-Dechang Rare Earth Element Belt, China. Economic Geology, 114(4), 719–744.

Lu, J., Chen, W., Ying, Y., Jiang, S., & Zhao, K. (2021). Apatite texture and trace element chemistry of carbonatite-related REE deposits in China: Implications for petrogenesis. Lithos, 398–399, 106276.

Lugmair, G.W., & Marti, K. (1978) Lunar intitial $^{143}Nd/^{144}Nd$: differential evolution of the lunar crust and mantle. Earth and Plateary Science Letters, 39, 349-357

Lyubetskaya, T., Korenaga, J. (2007). Chemical composition of Earth's primitive mantle and its variance:. Journal of Geophysical Research, 112, 1-21.

Maier, W. D., Rasmussen, B., Fletcher, I. R., Li, C., Barnes, S.-J., & Huhma, H. (2013). The Kunene Anorthosite Complex, Namibia, and Its Satellite Intrusions: Geochemistry, Geochronology, and Economic Potential. Economic Geology, 108(5), 953–986.

Mariano, A. N. (1989). Nature of economic mineralization in carbonatites and related rocks. In Bell, K. (Ed.), Carbonatites: Genesis and Evolution. Unwin Hyman. London, pp 147-176.

Mariano, A. N., & Mariano, A., Jr. (2012). Rare Earth Mining and Exploration in North America. Elements, 8(5), 369–376.

Martin, L.H.J., Schmidt, M.W., Mattsson, H.B., & Guenther, D., (2013). Element partitioning between immiscible carbonatite and silicate melts for dry and H_2O bearing system t 1-3 GPa. Journal of Petrology, 54, 2301-2338.

Menge, G. F. (1998). The antformal structure and general aspects of the Kunene Complex, Namibia. Journal of Applied and Regional Geology, 3, 431-448.

Menzies, M. (1987). Alkaline rocks and their inclusions: A window on the Earth's interior. In Fitton, J. G., & Upton, B. G. J. (eds), Alkaline igneous rocks. Geological Society of London Special Publications, 30(1), 15–27.

Middlemost, E. A. K. (1994). Naming materials in the magma/igneous rock system. Earth-Science Reviews, 37(3), 215–224.

Mitchell, R. H. (2005). Carbonatites, Carbonatites and Carbonatites. The Canadian Mineralogist, 43, 2049-2068.

Mitchell, R., Chudy, T., McFarlane, C. R. M., & Wu, F.-Y. (2017). Trace element and isotopic composition of apatite in carbonatites from the Blue River area (British Columbia, Canada) and mineralogy of associated silicate rocks. Lithos, 286–287, 75–91.

Nagasawa, H., Schreiber, H. D., & Morris, R. V. (1980). Experimental mineral/liquid partition coefficients of the rare earth elements (REE), Sc and Sr for perovskite, spinel and melilite. Earth and Planetary Science Letters, 46(3), 431–437.

Nebel, O., Scherer, E. E., & Mezger, K. (2011). Evaluation of the 87Rb decay constant by age comparison against the U–Pb system. Earth and Planetary Science Letters, 301(1), 1–8.

Nedosekova, I., Belyatsky, B., & Belousova, E. (2016). Trace elements and Hf isotope composition as indicators of zircon genesis due to the evolution of alkaline-carbonatite magmatic system (Ilmeny-Vishnevogorsky complex, Urals, Russia). Russian Geology and Geophysics, 57, 891–906.

Nelson, D. R., Chivas, A. R., Chappell, B. W., & McCulloch, M. T. (1988). Geochemical and isotopic systematics in carbonatites and implications for the evolution of ocean-island sources. Geochimica et Cosmochimica Acta, 52(1), 1–17.

Nude, P. M., Shervais, J. W., Attoh, K., Vetter, S. K., & Barton, C. (2009). Petrology and geochemistry of nepheline syenite and related carbonate-rich rocks in the Pan-African Dahomeyide orogen, southeastern Ghana, West Africa. Journal of African Earth Sciences, 55(3), 147–157.

O'Sullivan, G., Chew, D., Kenny, G., Henrichs, I., & Mulligan, D. (2020). The trace element composition of apatite and its application to detrital provenance studies. Earth-Science Reviews, 201, 103044.

O'Sullivan, G. J., Thakurdin, Y., Bolhar, R., Horváth, P., Hoare, B. C., & Collerson, K. D. (2021). The Great Falls Tectonic Zone after the assembly of Laurentia: Evidence for long-term tectonic stability from xenolith apatite. Lithos, 384–385, 105977.

Pan, Y., & Fleet, M. E. (2002). Compositions of the Apatite-Group Minerals: Substitution Mechanisms and Controlling Factors. Reviews in Mineralogy and Geochemistry, 48(1), 13–49.

Paton, C., Hellstrom, J., Paul, B., Woodhead, J., & Hergt, J. (2011). Iolite: Freeware for the visualisation and processing of mass spectrometric data. Journal of Analytical Atomic Spectrometry, 26(12), 2508–2518.

Paton, C., Woodhead, J. D., Hellstrom, J. C., Hergt, J. M., Greig, A., & Maas, R. (2010). Improved laser ablation U-Pb zircon geochronology through robust downhole fractionation correction. Geochemistry, Geophysics, Geosystems, 11(3).

Paulick H, Machacek E (2017) The global REE exploration boom: An analysis of resources of China and discussion of development perspectives. Resources Policy, 52, 134-153

Pell, J. (1996). Mineral deposits associated with carbonatites and related alkaline igneous rocks. In: Mitchell, R. H. (Ed), Undersaturated Alkaline Rocks: Mineralogy, Petrogenesis, and Economic Potential. Short Course Series 24. Mineralogical Association of Canada, 24, 271–310.

Petrus, J. A., & Kamber, B. S. (2012). VizualAge: A novel approach to laser ablation ICP-MS U-Pb geochronology data reduction. Geostandards and Geoanalytical Research, 36(3), 247-270.

Piccoli, P., & Candela, P. (2002). Apatite in Igneous Systems. Reviews in Mineralogy and Geochemistry, 48, 255-292.

Pidgeon, R. T. (1992). Recrystallisation of oscillatory zoned zircon: Some geochronological and petrological implications. Contributions to Mineralogy and Petrology, 110(4), 463–472.

Pidgeon, R. T., Nemchin, A. A., & Hitchen, G. J. (1998). Internal structures of zircons from Archaean granites from the Darling Range batholith: Implications for zircon stability and the interpretation of zircon U-Pb ages. Contributions to Mineralogy and Petrology, 132(3), 288–299.

Prowatke, S., & Klemme, S. (2006). Trace element partitioning between apatite and silicate melts. Geochimica et Cosmochimica Acta, 70(17), 4513–4527.

Rubatto, D. (2017). Zircon: The Metamorphic Mineral. Reviews in Mineralogy and Geochemistry, 83(1), 261–295.

Rudnick, R.L., McDonough, W.F., Chappel, B. W. (1993). Carbonatite metasomatism in the northern Tanzanian mantle: petrographic and geochemical characteristics. Earth and Planetary Science Letters, 114, 463-475.

Schoene, B., & Bowring, S. A. (2007). Determining accurate temperature–time paths from U–Pb thermochronology: An example from the Kaapvaal craton, southern Africa. Geochimica et Cosmochimica Acta, 71(1), 165–185.

Scherer, E., Münker, C., & Mezger, K. (2001). Calibration of the lutetium-hafnium clock. Science, 293, 683–687

Secher, K., Heaman, L. M., Nielsen, T. F. D., Jensen, S. M., Schjøth, F., & Creaser, R. A. (2009). Timing of kimberlite, carbonatite, and ultramafic lamprophyre emplacement in the alkaline province located 64°–67° N in southern West Greenland. Lithos, 112, 400–406.

Seth, B., Armstrong, R. A., Brandt, S., Villa, I. M., & Kramers, J. D. (2003). Mesoproterozoic U–Pb and Pb–Pb ages of granulites in NW Namibia: Reconstructing a complete orogenic cycle. Precambrian Research, 126(1), 147–168.

Seth, B., Armstrong, R. A., Büttner, A., & Villa, I. M. (2005). Time constraints for Mesoproterozoic upper amphibolite facies metamorphism in NW Namibia: A multi-isotopic approach. Earth and Planetary Science Letters, 230(3), 355–378.

Simon, S. J., Wei, C., Ellmies, R., Yang, H., & Soh Tamehe, L. (2017). New SIMS U-Pb age on zircon from the Epembe carbonatite dyke, NW Namibia: Implications for Mesoproterozoic evolution of carbonatites at the southern margin of the Congo Craton. Journal of African Earth Sciences, 135, 108–114.

Smith, M., Moore, K., Kavecsanszki, D., Finch, A., Kynicky, J., & Wall, F. (2016). From mantle to critical zone: A review of large and giant sized deposits of the rare earth elements. Geoscience Frontiers, 7, 315-334.

Söderlund, U., Patchett, P. J., Vervoort, J.D., & Isachsen, C. E. (2004). The ^{176}Lu decay constant determined by Lu–Hf and U–Pb isotope systematics of Precambrian mafic intrusions. Earth and Planetary Science Letters, 219, 311–324.

Shand, S. J. (1927). Eruptive Rocks. D. Van Nostrand Company, NewYork.

Stacey, J. S., & Kramers, J. D. (1975). Approximation of terrestrial lead isotope evolution by a two-stage model. Earth and Planetary Science Letters, 26(2), 207–221.

Streckeisen, A. (1976). To each plutonic rock its proper name. Earth-Science Reviews, 12(1), 1–33.

Sweeney, R. J., Green, D. H., & Sie, S. H. (1992). Trace and minor element partitioning between garnet and amphibole and carbonatitic melt. Earth and Planetary Science Letters, 113(1), 1–14.

Tappe, S., Foley, S. F., Jenner, G. A., Heaman, L. M., Kjarsgaard, B. A., Romer, R. L., Stracke, A., Joyce, N., & Hoefs, J. (2006). Genesis of Ultramafic Lamprophyres and Carbonatites at Aillik Bay, Labrador: A Consequence of Incipient Lithospheric Thinning beneath the North Atlantic Craton. Journal of Petrology, 47(7), 1261–1315.

Tappe, S., Pearson, D. G., Nowell, G., Nielsen, T., Milstead, P., & Muehlenbachs, K. (2011). A fresh isotopic look at Greenland kimberlites: Cratonic mantle lithosphere imprint on deep source signal. Earth and Planetary Science Letters, 305(1), 235–248.

Tappe, S., Steenfelt, A., Heaman, L. M., & Simonetti, A. (2009). The newly discovered Jurassic Tikiusaaq carbonatite-aillikite occurrence, West Greenland, and some remarks on carbonatite–kimberlite relationships. Lithos, 112, 385–399.

Tegtmeyer, A., & Kröner, A. (1985). U-Pb ages for granitoid gneisses in northern Namibia and their significance for proterozoic crustal evolution of southwestern Africa. Precambrian Research, 28, 311-326.

Thirlwall, M. F. (1991). Long-term reproducibility of multicollector Sr and Nd isotope ratio analysis. Chemical Geology, 94(2), 85–104.

Thompson, R., Smith, P., Gibson, S., Mattey, D., & Dickin, A. (2002). Ankerite carbonatite from Swartbooisdrif, Namibia: The first evidence for magmatic ferrocarbonatite. Contributions to Mineralogy and Petrology, 143(3), 377–396.

Tichomirowa, M., Whitehouse, M. J., Gerdes, A., Götze, J., Schulz, B., & Belyatsky, B. V. (2013). Different zircon recrystallization types in carbonatites caused by magma mixing: Evidence from U–Pb dating, trace element and isotope composition (Hf and O) of zircons from two Precambrian carbonatites from Fennoscandia. Chemical Geology, 353, 173–198.

Trail, D., Watson, E. & Tailby, N. (2012). Ce and Eu anomalies in zircon as proxies for the oxidation state of magmas. Geochimica et Cosmochimica Acta, 97, 70-89.

Tshiningayamwe, M., Bolhar, R., & Nex, P. A. M. Petrology, geochemistry and

Geochronology of the Epembe carbonatite and syenitic rocks, northwest Namibia. Journal of African Earth Sciences. (submitted)

Veksler, I. V., Dorfman, A. M., Dulski, P., Kamenetsky, V. S., Danyushevsky, L. V., Jeffries, T., & Dingwell, D. B. (2012). Partitioning of elements between silicate melt and immiscible fluoride, chloride, carbonate, phosphate and sulfate melts, with implications to the origin of natrocarbonatite. Geochimica et Cosmochimica Acta, 79, 20–40.

Vermeesch, P. (2018). IsoplotR: a free and open toolbox for geochronology. Geoscience Frontiers, 9, 1479-1493.

Verplanck, P. L. (2017). The role of fluids in the formation of rare earth element deposits. Earth and Planetary Science, 17, 758-761.

Vervoort, J. D., Patchett, P. J., Blichert-Toft, J., & Albarede, F. (1999). Relationships between Lu-Hf and Sm-Nd isotopic systems in the global sedimentary system. Earth and Planetary Science Letters, 168, 79-99.

Vervoort, J., Kemp, A., Fisher, C., Bauer, A., & S, B. (2015). The Rock Record Has It About Right-No Significant Continental Crust Formation Prior to 3.8 Ga. Abstract V43D-05, AGU Fall meeting 2015. San Francisco.

Wallace, M., & Green, D. (1988). Wallace, M. E. & Green, D. H. An experimental determination of primary carbonatite magma composition. Nature 335, 343-346. Nature, 335, 343–346.

Wang, L., Marks, M., Wenzel, T., Von Der Handt, A., Keller, J., Teiber, H., & Markl, J. (2014). Apatites from the Kaiserstuhl Volcanic Compolex, Germany: new constraints on the relationship between carbonatites and associated silicate rocks. European Journal of Mineralogy, 26, 397-414.

Watson, E. B., Wark, D. A., & Thomas, J. B. (2006). Crystallization thermometers for zircon and rutile. Contributions to Mineralogy and Petrology, 151(4), 413-433.

Wiedenbeck, M. A., Alle, F., Corfu, W. L., Griffin, M., Meier, F. V., Oberli, A., & Spiegel. (1995). Three natural zircon standards for U-Th-Pb, Lu-Hf, trace element and REE analyses. Geostandards Newsletter, 19, 1-23.

Woolley, A. R., Kjarsgaard, B. A. (2008). Carbonatite occurrences of the world: map and database. Geological Survey of Canada, Open File # 5796, p 28

Woolley, A. R. (1989). The Spatial and Temporal Distribution of Carbonatites. In Bell, K. (Ed.), Carbonatites: Genesis and Evolution. Unwin Hyman. London, pp 15-37

Woolley, A. R., & Kempe, R. C. (1989). Carbonatites: Nomenclature, Average chemical, and element distribution. In Bell, K. (Ed.), Carbonatites: Genesis and Evolution. Unwin Hyman, London, pp 1-14.

Woodhead, J. D., & Hergt, J. M. (2001). Strontium, Neodymium and Lead Isotope Analyses of NIST Glass Certified Reference Materials: SRM 610, 612, 614. Geostandards Newsletter, 25(2–3), 261–266.

Woodhead, J. D., & Hergt, J. M. (2005). A Preliminary Appraisal of Seven Natural Zircon Reference Materials for In Situ Hf Isotope Determination. Geostandards and Geoanalytical Research, 29(2), 183–195.

Wu, F.-Y., Yang, Y.-H., Li, Q.-L., Mitchell, R. H., Dawson, J. B., Brandl, G., & Yuhara, M. (2011). In situ determination of U–Pb ages and Sr–Nd–Hf isotopic constraints on the petrogenesis of the Phalaborwa carbonatite Complex, South Africa. Lithos, 127(1), 309–322.

Xie, Y., Li, Y., Hou, Z., Cooke, D. R., Danyushevsky, L., Dominy, S. C., & Shuping Yin. (2015). A model for carbonatite hosted REE mineralisation—The Mianning–Dechang REE belt, Western Sichuan Province, China. Ore Geology Reviews, 70, 595–612.

Yakymchuk, C., Kirkland, C. L., & Clark, C. (2018). Th/U ratios in metamorphic zircon. Journal of Metamorphic Geology, 36(6), 715–737.

Yang, Y. H., Wu, F. Y., Yang, J. H., Chew, D. M., Xie, L. W., Chu, Z. Y., Zhang, Y. Bin, & Huang, C. (2014). Sr and Nd isotopic compositions of apatite reference materials used in U-Th-Pb geochronology. Chemical Geology, 385, 35–55.

Ying, Y., Chen, W., Lu, J., Jiang, S.-Y., & Yang, Y. (2017). In situ U–Th–Pb ages of the Miaoya carbonatite complex in the South Qinling orogenic belt, central China. Lithos, 290–291, 159–171.

Zhang, F., Li, W., White, N. C., Zhang, L., Qiao, X., & Yao, Z. (2020). Geochemical and isotopic study of metasomatic apatite: Implications for gold mineralization in Xindigou, northern China. Ore Geology Reviews, 127, 103853.

Zhu, J., Wang, L., Peng, S., Peng, L., Wu, C., & Qiu, X. (2017). U–Pb zircon age, geochemical and isotopic characteristics of the Miaoya syenite and carbonatite complex, central China. Geological Journal, 52(6), 938–954.

Appendix 1: Thin section images of the studied samples

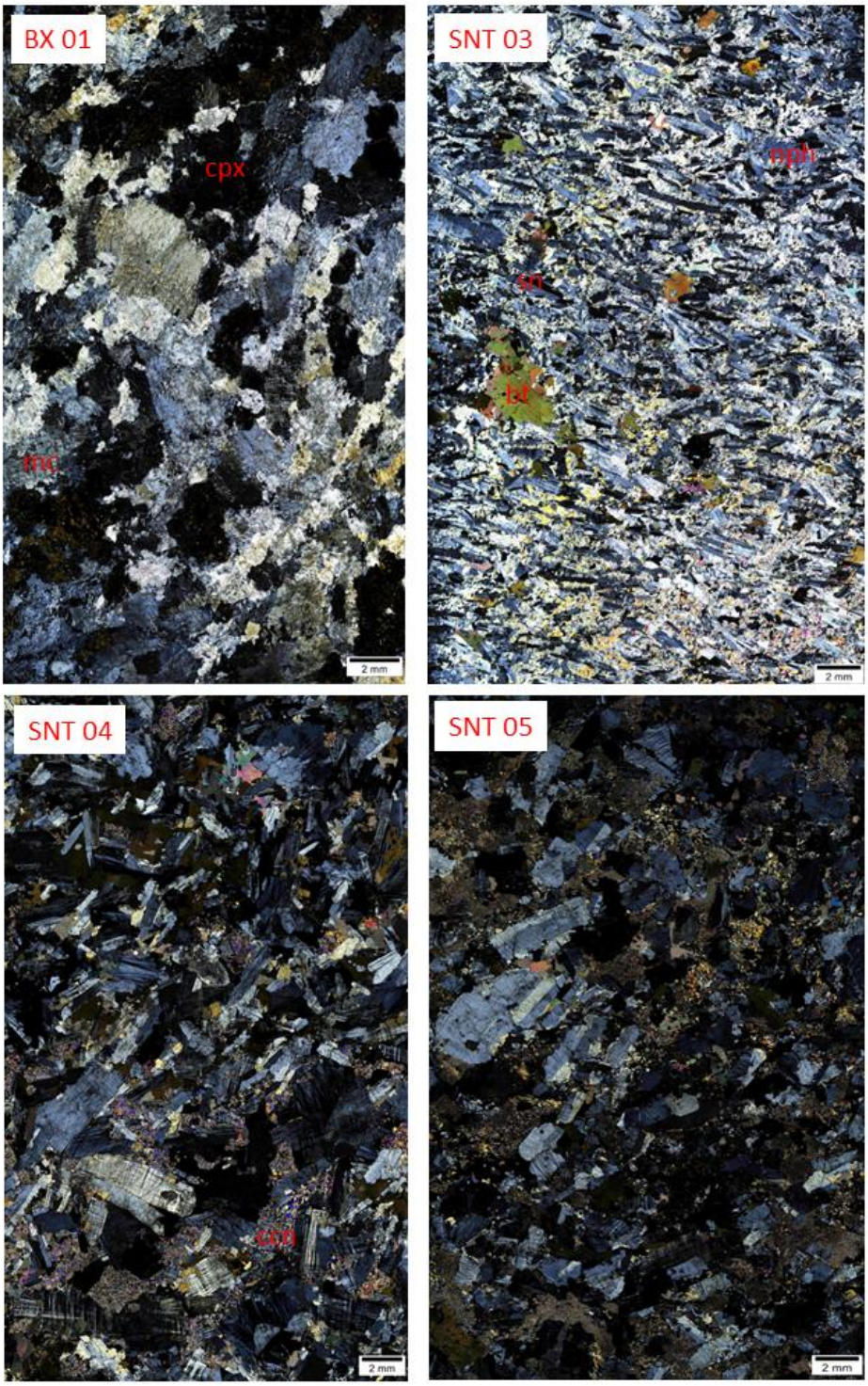

All images are in XPL. Abbreviations: mc=microcline, sn=sanidine, cpx = clinopyroxene, bt = biotite, nph = nepheline, ccn = cancrinite.

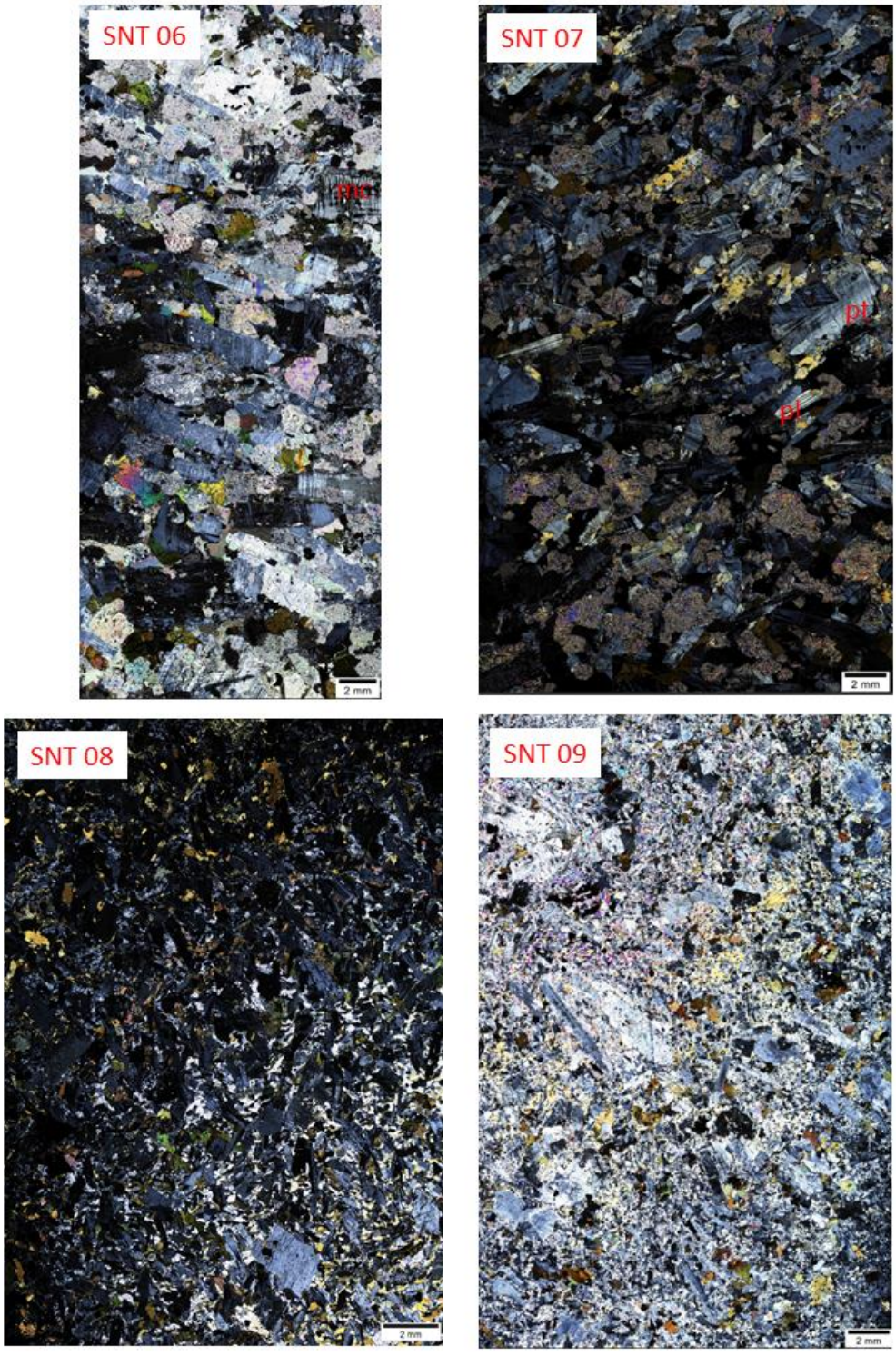

All images are in XPL. Abbreviations: mc=microcline, pl=plagioclase, pt=perthite

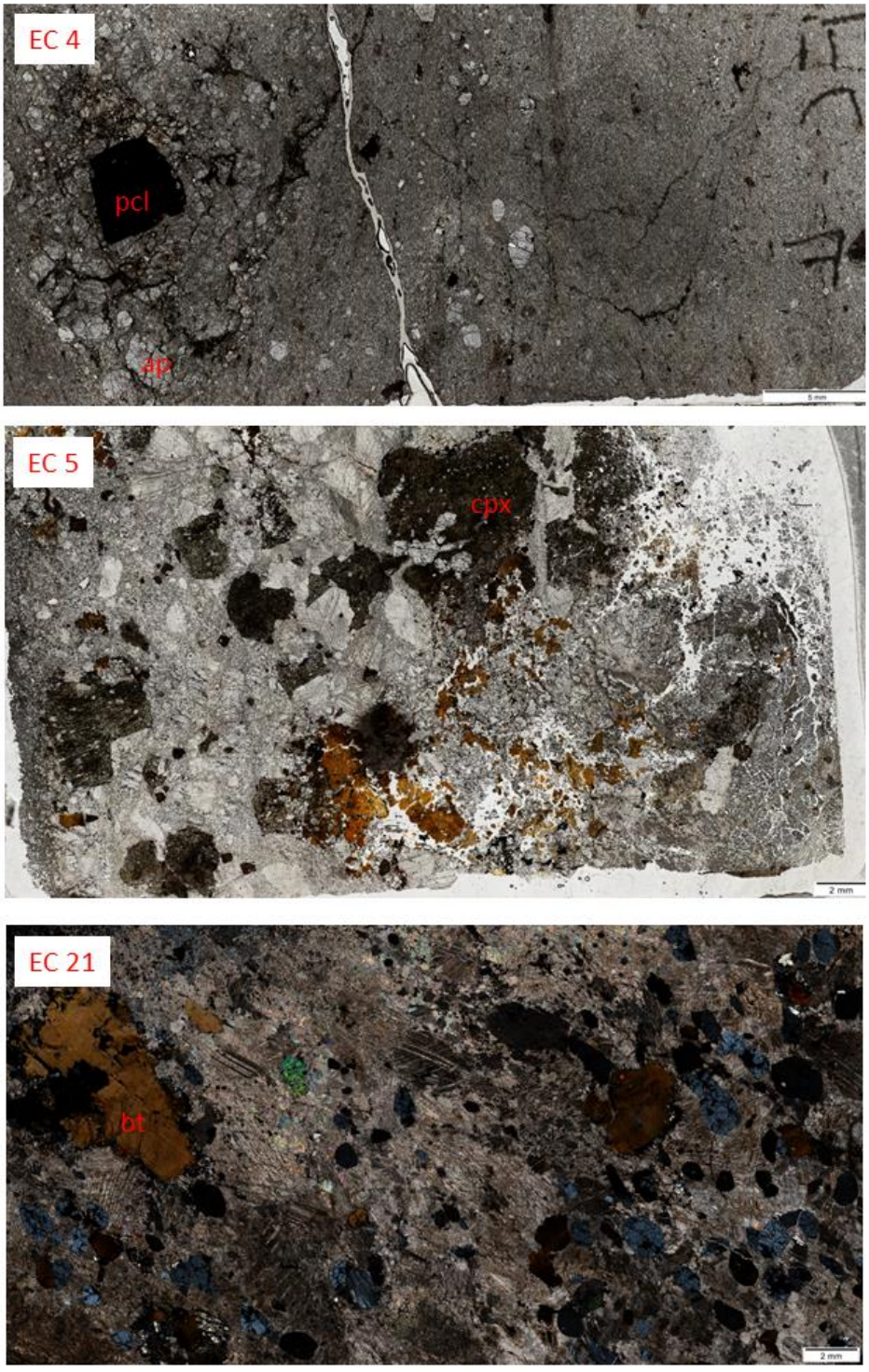

All images are in PPL. Abbreviations: cpx=clinopyroxene, bt=biotite, ap=apatite, pcl=pyrochlore, zrn=zircon.

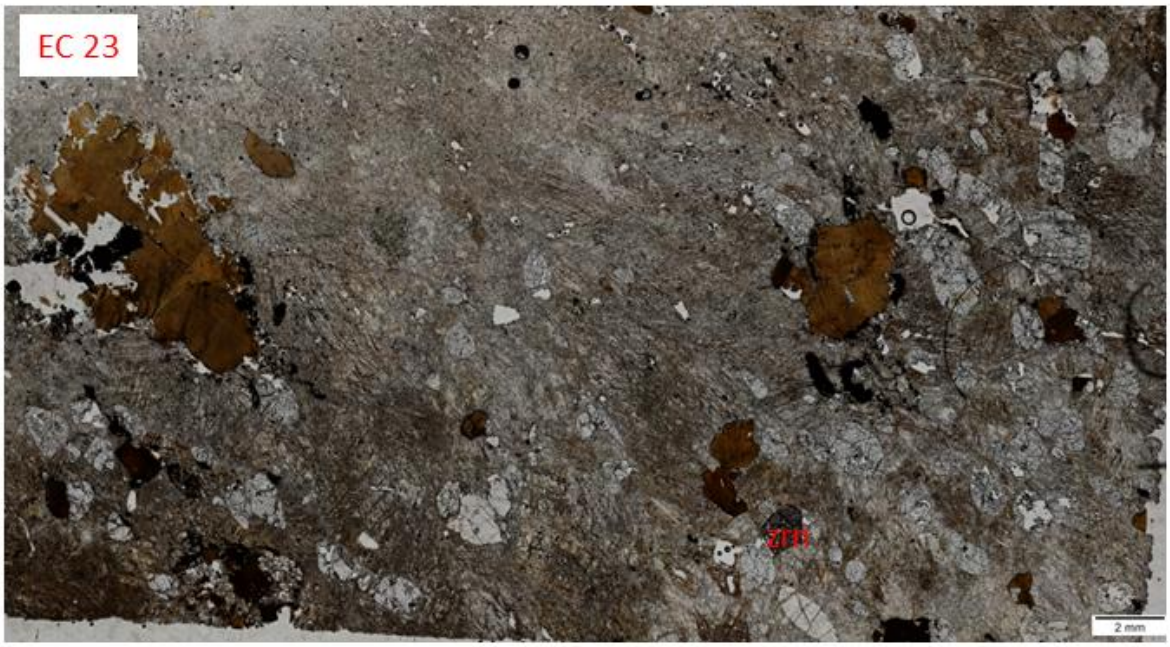

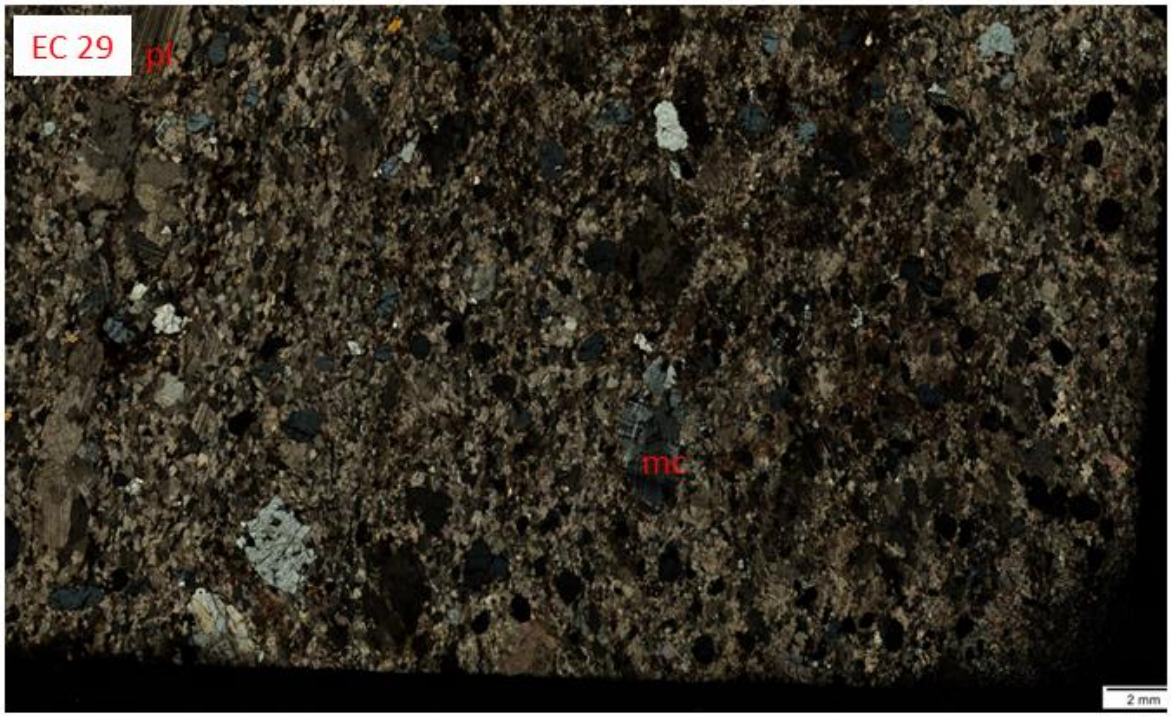

Sample EC 23 image is in PPL, while sample EC 29 image is in XPL. Abbreviations: mc=microcline, pl=plagioclase, zrn=zircon.

Appendix 2: Whole rock major (in wt%) and trace element (in ppm) results for studied samples as well as for standards

	Carbonatite					Syenite			Nepheline syente				
	EC 4	EC 5	EC 21	EC 32	EC 29	BX 01	SNT 03	SNT 04	SNT 05	SNT 06	SNT 07	SNT 08	SNT 09
SiO_2	2.32	4.36	5.65	4.64	5.72	59.14	49.08	50.46	50.04	48.42	47.55	51.58	49.70
$Al2O_3$	0.48	0.69	1.14	1.29	0.49	17.85	20.47	18.31	19.17	19.18	18.46	20.61	21.17
Fe_2O_3	1.66	2.69	3.26	2.04	3.76	5.19	2.63	4.59	6.09	6.56	5.86	4.16	4.14
MnO	0.34	0.25	0.32	0.38	0.30	0.11	0.06	0.08	0.11	0.11	0.10	0.09	0.08
MgO	0.16	0.27	0.53	0.29	0.48	0.73	0.53	0.79	0.87	0.97	1.08	0.51	0.66
CaO	53.46	48.74	48.04	49.95	48.94	2.60	5.54	5.68	4.65	6.34	5.78	2.66	3.09
Na_2O	0.00	0.37	0.22	0.20	0.23	5.29	7.74	4.69	3.72	3.27	5.24	6.12	8.33
K_2O	0.23	0.30	0.65	0.60	0.17	6.14	6.72	8.67	8.50	7.39	8.18	8.86	6.34
TiO_2	0.03	0.07	0.13	0.09	0.13	0.57	0.26	0.37	0.55	0.49	0.64	0.74	0.92
P_2O_5	1.15	1.17	3.88	3.18	3.38	0.27	0.48	0.68	0.85	0.90	0.91	0.15	0.13
LOI	40.51	38.88	34.44	36.27	35.75	1.08	5.99	5.06	4.88	5.40	5.18	3.59	4.09
Total	100.34	97.78	98.26	98.93	99.36	98.97	99.50	99.38	99.43	99.04	98.98	99.09	98.66
Li	0.54	0.70	2.31	1.63	0.87	3.15	5.21	10.73	39.29	79.95	17.94	3.59	3.61
P	6505	7085	25577	14141	19130	1071	2051	2689	3502	3524	3703	627	530
Sc	0.76	5.80	6.40	6.86	1.30	3.46	0.69	2.09	1.45	3.80	0.62	0.94	0.90
Ti	299	478	974	1345	641	2990	1428	1620	2579	2000	2903	3937	5169
V	35.1	79.9	69.4	52.0	7.3	9.5	19.9	59.8	58.4	93.0	58.1	15.4	22.0
Cr	0.68	1.84	9.34	12.86	1.69	6.85	1.36	1.17	3.13	1.08	1.46	1.03	1.27
Co	3.16	2.22	8.12	16.91	5.28	3.99	2.57	3.15	3.83	3.89	4.27	4.10	4.71
Ni	3.31	0.71	19.84	34.70	7.98	3.96	1.81	1.14	1.73	1.26	1.28	1.16	1.41
Cu	3.39	1.75	37.46	75.45	16.83	6.83	1.50	2.47	2.87	2.36	1.66	3.71	5.26
Zn	7.8	18.5	35.2	20.9	13.1	86.0	42.3	54.9	71.4	77.3	73.8	49.0	47.0
Ga	22.8	28.5	35.6	34.4	38.3	26.9	27.1	32.2	32.5	37.4	36.2	20.8	22.6
Rb	6.6	6.5	23.1	26.0	14.7	91	82	130	140	121	146	156	120
Sr	4242	11261	6512	6142	9038	1161	1847	1659	1503	2510	1774	2597	2003
Y	65.3	70.2	85.1	103.3	104.1	26.37	9.21	8.04	7.22	9.52	9.81	6.75	6.66
Zr	7.96	130.72	42.75	2.20	16.38	82.88	108.5	116.6	60.2	119.9	4.88	28.08	9.71

Nb	797	784	304	86	575	85	55	87	63	60	106	92	160
Sn	2.80	9.82	6.48	1.40	2.41	1.99	1.14	2.80	2.49	3.25	1.68	1.31	1.54
Sb	0.12	0.07	0.11	0.07	0.04	0.11	0.09	0.09	0.06	0.06	0.05	0.07	0.09
Cs	0.19	0.27	0.62	0.78	0.44	0.95	1.73	1.80	2.90	1.70	2.62	1.60	2.04
Ba	99	134	366	491	188	2072	2517	1181	997	2250	1425	1498	2107
La	176.4	219.9	220.9	262.1	258.8	79.5	40.4	32.6	31.9	40.3	48.1	38.4	24.4
Ce	335.5	411.5	468.6	508.2	539.9	163.7	78.1	65.7	66.5	84.0	94.6	74.4	48.0
Pr	37.5	44.3	55.7	56.6	63.7	18.6	8.56	7.28	7.79	9.74	10.59	8.09	5.34
Nd	140.7	167.2	222.8	223.7	250.8	70.1	33.5	28.9	31.2	39.0	41.1	29.8	20.6
Sm	23.0	27.3	38.6	38.0	42.6	11.2	5.30	4.86	5.23	6.39	6.67	4.49	3.55
Eu	6.71	8.12	11.42	11.31	12.73	3.29	1.74	1.50	1.63	2.01	2.09	1.58	1.29
Gd	18.88	22.34	31.17	31.31	33.97	8.80	4.18	3.78	4.00	4.96	5.12	3.33	2.77
Tb	2.32	2.72	3.68	3.86	4.11	1.11	0.48	0.44	0.45	0.56	0.57	0.39	0.34
Dy	12.2	13.9	17.9	19.9	20.3	6.14	2.34	2.09	2.07	2.62	2.69	1.85	1.72
Ho	2.19	2.37	2.95	3.54	3.49	1.09	0.40	0.36	0.33	0.43	0.43	0.31	0.30
Er	5.63	5.89	7.02	9.17	8.80	2.79	0.96	0.86	0.74	0.99	1.00	0.75	0.73
Tm	0.71	0.71	0.82	1.16	1.07	0.36	0.11	0.10	0.08	0.11	0.11	0.09	0.09
Yb	4.33	4.21	4.78	7.11	6.39	2.09	0.66	0.59	0.46	0.63	0.61	0.51	0.53
Lu	0.70	0.67	0.74	1.15	1.00	0.29	0.09	0.09	0.07	0.09	0.09	0.07	0.07
Hf	0.26	5.52	3.20	0.10	0.36	2.68	1.61	2.18	1.63	2.82	0.16	0.70	0.28
Ta	49.88	144.32	74.26	12.20	32.98	3.51	3.48	10.25	4.67	4.69	5.11	7.70	17.66
W	0.15	0.11	0.05	0.15	3.46	0.14	0.06	0.11	0.04	0.03	0.05	2.93	0.15
Tl	0.04	0.04	0.12	0.24	0.06	0.31	0.61	0.51	0.49	0.41	0.56	0.44	0.48
Pb	7.88	20.5	22.8	22.3	9.3	13.4	2.60	3.72	1.73	1.83	1.93	2.15	2.02
Th	8.85	4.43	3.13	5.11	8.83	2.68	2.68	2.54	1.61	2.50	1.92	1.55	1.75
U	19.1	184.6	57.3	25.0	12.7	4.53	0.74	14.59	1.57	3.29	0.96	0.31	0.27
TREE	767	931	1087	1177	1248	369	177	149	152	192	214	164	110
Mg #	0.16	0.17	0.24	0.22	0.20	0.22	0.29	0.25	0.22	0.23	0.27	0.20	0.24
Y/Ho	29.8	29.7	28.9	29.2	29.8	24.2	23.1	22.6	22.1	22.2	22.8	21.8	22.5
Nb/U	41.7	4.2	5.3	3.5	45.4	18.7	74.3	6.0	40.4	18.2	110.2	296.2	585
Ce/Pb	42.6	20.1	20.6	22.8	57.9	12.2	30.1	17.7	38.4	46.0	49.1	34.6	23.8
La_N/Yb_N	27.5	35.2	31.2	24.9	27.3	25.6	41.2	37.3	47.1	43.1	53.4	50.9	31.3

Eu/Eu*	0.96	0.98	0.98	0.98	0.99	0.67	1.10	1.03	1.05	1.05	1.05	1.20	1.22

	EC 1	EC 2	EC 6	EC 7	EC 8	EC 9	EC 10	EC 11	EC 12	EC 13	EC 14	EC 15	EC 16
SiO_2	3.83	6.84	2.51	9.22	3.10	5.07	3.18	6.59	50.09	49.31	4.15	8.57	25.19
$Al2O_3$	0.95	2.13	0.54	2.63	0.72	0.54	0.70	1.85	21.49	14.16	0.97	2.38	7.24
Fe_2O_3	2.24	2.45	1.65	2.24	1.13	3.56	2.87	1.58	2.86	1.17	1.97	3.52	4.91
MnO	0.38	0.35	0.31	0.34	0.23	0.24	0.27	0.26	0.07	0.16	0.41	0.54	0.41
MgO	0.27	0.29	0.18	0.32	0.19	0.35	0.16	0.22	0.63	0.14	0.23	0.47	0.41
CaO	50.54	48.41	52.57	45.80	52.55	48.86	51.90	49.16	6.60	14.34	50.05	44.35	30.27
Na_2O	0.10	0.00	0.00	0.12	0.00	0.40	0.07	0.12	0.64	7.55	0.08	0.55	1.94
K_2O	0.50	1.25	0.31	1.79	0.37	0.02	0.34	1.11	11.31	1.25	0.56	1.06	3.22
TiO_2	0.03	0.09	0.03	0.09	0.05	0.06	0.04	0.03	0.33	0.04	0.04	0.30	2.70
P_2O_5	0.38	0.84	0.55	2.54	1.69	0.29	1.25	2.85	0.91	2.16	1.22	0.94	1.62
Cr_2O_3	0.00	0.00	0.00	0.00	0.00	0.00	0.00	0.00	0.00	0.00	0.00	0.00	0.00
NiO	0.00	0.00	0.00	0.00	0.00	0.00	0.00	0.00	0.00	0.00	0.00	0.00	0.00
LOI	40.10	37.60	40.77	34.00	40.02	39.10	39.24	35.95	5.71	9.63	39.23	35.63	22.38
TOTAL	99.33	100.24	99.40	99.08	100.05	98.49	100.02	99.72	100.64	99.92	98.92	98.30	100.29

	EC 17	EC 18	EC 19	EC 20	EC 22	EC 24	EC 25	EC 26	EC 27	EC 28	EC 30	EC 31
SiO_2	3.66	3.14	42.05	1.45	13.33	14.74	1.60	4.19	4.23	2.34	6.72	1.37
$Al2O_3$	0.85	0.74	12.34	0.24	3.39	4.33	0.26	1.05	0.99	0.69	1.43	0.21
Fe_2O_3	2.88	1.35	7.98	1.32	5.00	4.11	2.26	4.06	1.39	2.10	4.55	1.78
MnO	0.51	0.38	0.40	0.31	0.29	0.38	0.35	0.34	0.23	0.34	0.24	0.37
MgO	0.35	0.31	0.52	0.20	0.95	0.59	0.34	0.86	0.13	0.60	0.82	0.27
CaO	50.53	51.45	12.91	53.28	41.40	41.27	51.93	49.44	51.17	52.92	47.96	51.68
Na_2O	0.00	0.08	4.27	0.00	1.11	1.26	0.01	0.03	0.14	0.00	0.55	0.00
K_2O	0.57	0.37	4.09	0.09	1.16	1.56	0.12	0.62	0.58	0.32	0.75	0.09
TiO_2	0.09	0.02	6.34	0.02	0.37	0.34	0.03	0.30	0.02	0.05	0.26	0.02
P_2O_5	0.34	0.65	0.08	0.39	3.48	1.23	0.39	3.66	1.25	1.28	6.06	1.98

Cr_2O_3	0.00	0.00	0.00	0.00	0.00	0.00	0.00	0.00	0.00	0.00	0.00	0.00
NiO	0.00	0.00	0.01	0.00	0.00	0.00	0.00	0.00	0.00	0.00	0.00	0.00
LOI	39.96	40.52	9.87	41.90	29.69	30.88	41.26	35.51	39.05	40.04	30.82	39.85
TOTAL	99.74	99.02	100.86	99.20	100.17	100.69	98.54	100.05	99.19	100.68	100.17	97.62

Standard	SiO_2	Al_2O_3	Fe_2O_3	FeO	MnO	MgO	CaO	Na_2O	K_2O	TiO_2	P_2O5	Cr_2O_3	NiO	TOTAL	LOI
NIM-P	51.75	4.38	1.28	10.33	0.22	25.55	2.64	0.35	0.09	0.2	0.03	3.51	0.08	100.39	-0.23
NIM-D	38.71	0.33	1.71	13.86	0.22	43.91	0.31	0.05	0.01	0.03	0.02	0.48	0.26	99.91	-0.51
W2	53.15	15.81	1.09	8.83	0.17	6.45	10.95	2.24	0.61	1.08	0.13	0	0.01	100.52	0.19
NIM-S	64.91	17.81	0.14	1.12	0.01	0.47	0.67	0.37	15.53	0.05	0.12	0	0	101.18	0.42
GSP2	67.35	15.31	0.49	4	0.05	0.98	2.14	2.82	5.49	0.67	0.29	0	0	99.57	0.87
BCR2	55.06	13.95	1.4	11.3	0.2	3.63	7.19	3.2	1.81	2.27	0.36	0	0	100.34	0.1
NIM-N	53.44	17.02	0.91	7.34	0.18	7.58	11.59	2.43	0.24	0.2	0.02	0	0.02	100.95	0.04
NIM-G	76.31	12.46	0.2	1.6	0.02	0.05	0.79	3.31	5.05	0.1	0.02	0	0	99.88	0.73
PCC1	44.89	0.76	0.87	7.05	0.13	45.87	0.6	0.04	0	0.01	0.01	0.5	0.33	101.08	5.09
BHVO2	50.46	13.98	1.24	10.07	0.17	7.31	11.45	2.22	0.52	2.77	0.27	0.04	0.02	100.52	-0.48
AGV2	60.02	17.51	0.68	5.51	0.1	1.81	5.26	4.3	2.93	1.05	0.48	0	0	99.61	1.8
G2	69.94	15.8	0.27	2.17	0.03	0.77	1.94	4.07	4.55	0.49	0.14	0	0	100.15	0.64
DTS1	40.51	0.27	0.87	7.04	0.13	49.89	0.17	0.07	0	0.01	0.01	0.7	0.31	99.98	-0.02
SIO2	98.91	0.13	0	0	0	0.05	0.03	0	0	0.0068	0.02	0	0.0007	99.15	

Standard	BCR2 Meas	BHVO2 Meas	BIR-1 Meas	BCR2 Recom	BHVO2 Recom	BIR-1 Recom
Li	10.15	4.89	3.44	9.90	5.00	3.4
P	1576	1175	89	1571	1178	100
Sc	33.3	29.8	38.1	32	31	44
Ti	13186	15413	5408	13005	15621	5755
V	431	317	324	414	329	313
Cr	16.2	300.9	411.1	17	285.0	382
Co	38.2	44.3	52.6	35.8	47.0	51.4

Ni	12.1	118.4	171.8	12.7	112.0	166
Cu	19.7	139.9	133.6	19.4	142.0	126
Zn	146.4	107.5	75.3	147	107	71
Ga	23.0	20.7	13.6	22.7	21	
Rb	52.64	9.45	0.21	49	10.1	0.25
Sr	332	370	98	321	382	108
Y	32	22.3	11.8	31	23	16
Zr	187.9	165.4	12.1	194	160	15.5
Nb	11.96	17.63	0.46	12.8	16.4	0.6
Sn	3.42	1.95	0.74	2.1	2.7	0.65
Sb	0.55	0.18	0.85	0.62	0.16	0.58
Cs	1.26	0.10	0	1.17	0.11	
Ba	662	125	6	641	129	7
La	25.32	15.11	0.62	24.50	15.60	0.62
Ce	51.58	36.25	1.78	50.50	37.00	1.95
Pr	6.43	4.90	0.34	6.30	5.00	0.38
Nd	27.87	23.27	2.22	27	24	2.5
Sm	6.38	5.73	1.03	6.3	5.80	1.10
Eu	1.95	1.96	0.50	1.91	2.00	0.54
Gd	6.57	5.84	1.67	6.50	5.90	1.85
Tb	0.97	0.85	0.32	0.95	0.86	0.36
Dy	5.98	4.92	2.29	6	4.90	2.50
Ho	1.21	0.91	0.51	1.20	0.91	0.57
Er	3.33	2.28	1.47	3.30	2.3	1.70
Tm	0.47	0.29	0.22	0.46	0.3	0.26
Yb	3.34	1.94	1.57	3.20	2.02	1.65
Lu	0.47	0.26	0.22	0.47	0.26	0.26
Hf	4.85	4.23	0.53	5	4.1	0.6
Ta	0.71	1.04	0.06	0.78	0.94	0.04
W	0.38	0.32	0.03	0.44	0.27	0.01
Tl	0.54	0.04	0	0.3	0.06	0.01
Pb	9.37	1.67	2.66	10.9	1.4	3

Th	5.58	1.17	0.03	5.5	1.18	0.03
U	1.76	0.43	0.01	1.73	0.44	0.01

Appendix 3: Major and minor element compositions (in wt%) of apatite by WDS

	Carbonatite											
	EC 4							EC 5				
	1	2	3	4	5	6	7	1	2	3	4	5
CaO	53.40	53.62	53.69	54.40	54.90	55.47	51.79	52.15	49.62	51.36	52.55	54.05
Na_2O	0.13	0.18	0.23	0.22	0.11	0.08	0.16	0.11	0.29	0.13	0.23	0.25
La_2O_3	0.04	0.09	0.18	0.10	0.07	0.07	0.09	0.08	0.20	0.03	0.16	0.23
Ce_2O_3	0.08	0.16	0.28	0.17	0.18	0.14	0.12	0.12	0.26	0.24	0.41	0.40
P_2O_5	42.06	42.80	42.16	43.48	43.31	43.37	38.80	42.35	41.51	42.20	42.14	43.06
SiO_2	0.05	0.15	0.14	0.02	0.06	0.08	2.33	0.03	0.00	0.00	0.03	0.02
F	3.30	3.13	3.03	2.89	3.00	3.13	2.27	2.93	3.20	2.88	2.97	2.96
Cl	0.01	0.00	0.01	0.01	0.00	0.00	0.00	0.01	0.00	0.00	0.00	0.00
Total	99.96	100.94	101.02	102.55	102.71	103.32	96.42	98.69	96.32	98.21	99.71	102.50

	EC 5											
	6	7	8	9	10	11	12	13	14	15	16	17
CaO	54.07	52.55	52.77	53.71	54.27	53.00	50.80	51.59	51.02	52.29	53.90	54.71
Na_2O	0.22	0.09	0.16	0.22	0.24	0.16	0.09	0.17	0.18	0.23	0.20	0.16
La_2O_3	0.18	0.07	0.08	0.15	0.17	0.11	0.06	0.13	0.20	0.22	0.16	0.12
Ce_2O_3	0.26	0.18	0.18	0.29	0.31	0.29	0.16	0.26	0.43	0.45	0.29	0.17
P_2O_5	42.86	43.27	42.61	42.63	42.49	42.86	42.27	41.92	42.28	42.11	42.92	42.81
SiO_2	0.01	0.02	0.00	0.01	0.08	0.01	0.00	0.16	0.01	0.00	0.03	0.03
F	2.87	2.95	3.02	2.98	2.96	2.99	2.83	2.97	3.33	2.91	2.73	2.92
Cl	0.00	0.00	0.00	0.00	0.02	0.00	0.00	0.01	0.00	0.01	0.00	0.00
Total	101.66	100.34	99.82	101.13	101.97	100.58	97.53	98.10	98.72	99.25	101.46	102.07

	EC 21			EC 23		EC 29							
	1	2	3	1	2	1	2	3	4	5	6	7	8
CaO	50.37	51.30	52.95	55.71	54.47	47.86	50.72	51.09	50.71	49.24	50.61	56.67	52.23
Na_2O	0.26	0.22	0.21	0.21	0.18	0.15	0.18	0.21	0.26	0.14	0.22	0.24	0.14
La_2O_3	0.13	0.14	0.13	0.10	0.20	0.07	0.11	0.18	0.14	0.06	0.12	0.21	0.00
Ce_2O_3	0.52	0.44	0.30	0.19	0.33	0.29	0.28	0.40	0.35	0.32	0.27	0.39	0.10
P_2O_5	43.34	43.80	44.27	43.18	42.33	43.48	41.85	41.62	40.98	43.11	41.27	42.24	43.97
SiO_2	0.05	0.02	0.01	0.07	0.02	0.02	0.26	0.00	0.05	0.02	0.01	0.21	0.01
F	2.49	2.80	2.69	2.94	2.57	3.03	2.99	3.08	3.01	2.80	3.22	2.86	3.04
Cl	0.02	0.01	0.00	0.00	0.02	0.00	0.00	0.00	0.01	0.00	0.01	0.00	0.03
Total	99.17	100.86	102.37	103.77	101.90	96.22	97.55	98.09	96.94	96.79	97.15	104.39	100.83

	Syenite			Nepheline syenite									
	BX 01			SNT 03			SNT 04						
	1	2	3	1	2	3	1	2	3	4	5	6	7
CaO	52.12	53.50	53.60	50.56	51.36	51.86	51.66	51.20	50.56	51.36	51.86	53.19	51.73
Na_2O	0.07	0.07	0.08	0.02	0.03	0.08	0.09	0.11	0.11	0.11	0.10	0.05	0.10
La_2O_3	0.50	0.42	0.24	0.01	0.09	0.13	0.07	0.00	0.07	0.11	0.09	0.07	0.11
Ce_2O_3	1.06	0.76	0.38	0.09	0.09	0.13	0.14	0.16	0.18	0.14	0.16	0.23	0.15
P_2O_5	39.87	40.77	40.00	40.60	40.53	39.12	39.70	40.05	40.60	40.53	39.12	38.07	39.72
SiO_2	1.16	1.00	0.43	0.23	0.93	0.22	0.13	0.65	0.19	0.36	0.22	0.13	0.15
F	3.59	3.43	3.61	3.32	3.46	3.60	3.88	3.69	3.74	3.69	3.72	3.75	3.61
Cl	0.02	0.04	0.01	0.27	0.13	0.10	0.02	0.03	0.02	0.04	0.02	0.05	0.02
Total	98.39	100.00	98.36	95.12	96.61	95.25	95.69	95.89	95.48	96.35	95.28	95.54	95.60

	SNT 05			SNT 06				SNT 07					
	1	2	3	1	2	3	4	1	2	3	4	5	6
CaO	52.31	50.61	50.86	51.80	51.70	53.11	52.38	50.62	50.12	50.76	51.33	52.73	50.18
Na_2O	0.07	0.04	0.07	0.09	0.06	0.05	0.09	0.12	0.10	0.08	0.06	0.26	0.12
La_2O_3	0.00	0.13	0.07	0.17	0.17	0.08	0.00	0.03	0.15	0.08	0.05	0.00	0.22
Ce_2O_3	0.17	0.13	0.19	0.26	0.22	0.11	0.17	0.15	0.19	0.17	0.14	0.08	0.20
P_2O_5	39.25	38.65	38.21	40.11	39.28	39.58	39.95	40.96	41.43	41.68	41.80	40.41	41.60
SiO_2	1.76	0.39	0.31	0.44	0.28	0.35	0.18	0.12	0.26	0.21	0.18	1.92	0.16
F	3.30	3.71	3.45	3.64	3.93	3.56	3.45	3.68	3.69	3.68	3.59	3.48	3.44
Cl	0.12	0.03	0.01	0.03	0.00	0.00	0.02	0.03	0.00	0.02	0.01	0.02	0.01
Total	96.97	93.69	93.16	96.52	95.66	96.84	96.25	95.71	95.94	96.69	97.16	98.90	95.93

	SNT 09				
	1	2	3	4	5
CaO	50.76	52.33	53.73	52.18	52.18
Na_2O	0.42	0.27	0.62	0.08	0.24
La_2O_3	0.08	0.18	0.00	0.21	0.13
Ce_2O_3	0.17	0.21	0.31	0.29	0.15
P_2O_5	39.84	40.06	38.77	39.42	40.39
SiO_2	0.67	0.16	1.41	1.04	0.13
F	2.00	2.32	2.51	2.39	2.60
Cl	0.01	0.01	0.00	0.01	0.02
Total	93.94	95.54	97.35	95.62	95.85

Appendix 4: Apatite trace element data (in ppm)

	Syenite BX 01 - 1.	BX 01 - 2	BX 01 - 3	BX 01 - 4	BX 01 - 6	BX 01 - 7	BX 01 - 8	BX 01-10	BX 01-11	BX 01 - 12	BX 01 - 13
CL texture	Homogeneous grey CL										
Na	920	935	882	919	759	1088	817	1185	1104	1095	1032
Si	11100	13790	11800	10430	9450	8460	10590	11600	13200	11170	8810
Ti	7.78	22	84	7.7	8.18	6.5	12.1	29	8.7	26	6.65
V	0.23	1.4	12.7	2.78	0.79	2.11	0.51	4.72	2.71	5.21	2.08
Mn	72.2	560	118	121.1	114.6	108.6	111.2	189	149	370	77.2
Fe	25.9	1760	3280	52.8	187	39.8	194	2670	800	3900	36
Rb	0.54	2.45	1.25	0.2	0.51	0.16	0.53	1.39	0.76	1.86	0.18
Sr	4840	4225	4380	2880	3530	3800	2478	6060	6630	4080	4520
Y	1553	2590	968	934	608	722	1223	1016	889	886	682
Zr	5.49	22.5	7.4	2.61	1.32	1.15	4.68	9.4	2.11	4.56	0.68
La	6620	10570	4190	4340	2950	3175	5750	5390	4240	3670	3558
Ce	13160	21300	8400	8560	5570	6570	10590	10110	8630	7480	6990
Pr	1210	1970	765	755	486	575	904	896	785	665	604
Nd	4450	7200	2801	2720	1711	2052	3143	3220	2840	2410	2139
Sm	652	1060	396	375	224.8	278.7	427	439	387	341	285.6
Eu	88.3	145	76.4	46.5	30	44.9	62.5	68	61.1	55.1	62.8
Gd	446	718	278.4	263	159.6	192.9	298.7	306	272.5	247	203.2
Tb	55.7	91.2	34.2	32.48	19.37	23.84	37.6	37	32.6	30.8	24.13
Dy	320.4	523	197.5	188	112.5	138.3	223	211	184.6	179	135.8
Ho	58.46	95.4	35.8	34.9	21.23	25.46	42.5	38.4	33.6	32.9	24.88
Er	147.3	244	89.1	91.2	55.9	64.3	113	94.5	82.3	82.5	61.3
Tm	16.43	27.8	9.77	10.86	6.64	7.17	13.58	10.04	8.67	9.04	6.36
Yb	73.2	127.7	42.6	53.9	33	32.07	67.6	42.8	36.4	40	26.25
Lu	6.65	12.05	3.9	5.58	3.53	3	7.08	3.83	3.22	3.71	2.25
Pb	33.56	97	33.6	21.7	11	11.87	24.1	25.5	14.7	25.7	10.58
Th	250.9	890	148.2	136	43.9	44.9	172	209	83.3	114	46.34

U	49.03	109.2	23.92	20.4	7.21	8.69	21.3	22.1	11.72	19.8	7.65

	Syenite BX 01-14	BX 01 - 16	BX 01 - 17	BX 01-18	BX 01 - 19	BX 01 - 20	BX 01 - 21.	BX 01 - 22	BX 01 - 23	BX 01-24	BX 01 - 25
CL texture	Homogenous grey CL										
Na	889	890	784	536	1013	971	605	1385	867	1205	1740
Si	10800	9740	8960	8660	22900	9160	45000	23800	50000	8310	16500
Ti	660	6.94	39	7.57	4.84	9.05	6.4	6.4	630	6.49	84
V	2.91	5.9	4.65	0.69	0.8	1.04	2.01	1	13.1	1.49	1.21
Mn	176	63.3	78.1	53.3	89	80	139.2	258	1470	115.3	292
Fe	1030	18.9	1180	143	100	630	760	325	44000	76	1410
Rb	0.41	0.26	0.59	0.43	0.23	0.26	0.51	0.43	54	0.27	1.39
Sr	1480	4510	4769	2241	2970	2979	2157	3103	2760	3941	3104
Y	656	1110	999	905	842	795	1949	2056	616	726	2239
Zr	24	3.04	4.1	1.73	1.32	2.15	7.76	6.49	27	2.76	8.75
La	2830	4820	4200	3255	3690	3690	6530	7520	2780	3080	9140
Ce	5340	9730	8530	6970	6830	7670	12730	17060	5070	6630	19190
Pr	541	875	771	631	693	680	1314	1648	513	598	1845
Nd	1970	3182	2800	2326	2510	2451	4720	6070	1850	2160	6760
Sm	271	447.7	395	331	345	336	682	901	254	297	1025
Eu	31	87.3	77.7	82.8	66.3	67	70.5	146.7	53.6	43.5	160.5
Gd	188	314.9	279	237.4	240	234.3	475	612	177	203	684
Tb	22.6	39.09	34.7	29.78	30.2	28.5	60.3	77.5	21.8	24.88	87.6
Dy	128	226.2	200	173.4	172	162	350	446	124.5	140.6	500
Ho	23.1	41.72	36.5	32.46	31.3	29.4	64.7	78.4	22.7	25.32	88.4
Er	58.1	105.7	91.7	85.4	77.3	71.8	171	186.6	55.5	62.1	211.7
Tm	6.84	11.63	9.99	10.47	8.16	7.51	20.3	19.05	5.75	6.85	21.73
Yb	34.5	51.4	44.4	53.5	34.4	30.5	101.3	76.2	24.1	30	86.8
Lu	3.77	4.66	4.03	5.74	2.98	2.59	10.52	6.27	1.98	2.77	7.17
Pb	10.2	26.15	22.4	22.48	12.9	14.8	30.5	46.4	48	9.4	54.4

Th	43	219	161	172.6	72	87	194	333	82	26.7	392
U	8.8	31.3	24.2	28.82	11.3	12.8	36.3	3.33	11.5	5.58	3.35

	Syenite							Nepheline syenite			
	BX 01-26	BX 01 - 28	BX 01-30	BX 01 - 31	BX 01 - 32	BX 01 - 34	BX 01 - 35	SNT 03 - 1	SNT 03 - 8	SNT 03 - 14	SNT 03 - 2
CL texture	Homogenous grey CL							Dark Grey CL core			light grey CL rim
Na	960	887	824	939	836	865	1166	1389	1790	1456	1584
Si	11940	9280	14400	18200	19700	11750	21500	7410	8660	7860	10300
Ti	17.6	6.31	12.7	6.6	42	30	6.1	5.46	5.62	22	41
V	1.64	1.45	1.03	8.13	2.06	1.95	0.71	0.68	3.4	12.41	1.1
Mn	166	103.2	166.8	77.2	174	144.3	64.3	319.8	244.8	231.4	406
Fe	1230	61	830	400	1870	1230	80	359	222	320	780
Rb	2.6	0.23	1.97	0.36	0.82	0.27	0.57	0.07	0.35	0.69	1.1
Sr	3584	2866	2072	4277	3360	3306	2950	8990	7750	7355	8840
Y	647	971	513	1047	1232	621	843	210	205.1	198.2	405
Zr	2.66	3.21	2.84	3.24	110	3.36	1.98	0.97	1.86	3.08	1.24
La	3035	4150	2494	4180	4940	2930	3870	806	499	548	903
Ce	5910	8270	4303	7930	10030	5540	7110	2003	1496	1621	2490
Pr	527	736	411.7	815	948	509	724	245.1	195	207.1	327
Nd	1862	2640	1434	2948	3420	1813	2580	1025	849	886	1441
Sm	249.6	367	189.8	414	490	243.5	354	168.9	147.6	150.8	268
Eu	36.1	44.8	22.01	81.1	67.7	32.98	70.4	47.35	42.5	42.4	82.2
Gd	176.6	255	132.5	289	347	170.3	238	115.4	104.4	104.6	194
Tb	21.47	31.7	16.04	35.9	42.5	20.67	29.2	12.59	11.67	11.46	22
Dy	123.9	185	92.1	206.4	246	118.7	165	59.9	57	56.3	109
Ho	23.06	34.4	17.16	37.3	45.1	21.83	29.5	8.78	8.45	8.39	16.3
Er	59.4	89.6	45.1	93.2	113.4	56	71.5	18.06	17.74	17.82	33.7
Tm	6.81	10.7	5.41	10.11	12.77	6.53	7.35	1.82	1.83	1.83	3.41
Yb	32.35	53.5	28.25	44.4	60.3	31.55	29.8	8.4	8.84	8.81	15.9
Lu	3.32	5.57	3.18	4.04	5.99	3.27	2.51	0.89	0.97	0.99	1.67

Pb	12.84	16.6	9.26	24.5	25.44	11.49	15.3	3.59	3.66	5.26	3.48
Th	51.2	91	31	170	151.4	31.03	92	17.6	24.2	39.31	13.79
U	7.85	16	5.89	24.8	20.5	6.1	13.1	0.58	4.03	4.96	0.19

	Nepheline syenite										
	SNT 03 - 9	SNT 03 - 15	SNT 04 - 1	SNT 04 - 2	SNT 04 - 3	SNT 04 - 4	SNT 04 - 5	SNT 04 - 6	SNT 04 - 7	SNT 04 - 8	SNT 04 - 9
CL texture	light grey CL rim		Homogeneous grey CL								
Na	1630	1910	1184	1167	1317	1297	1059	1840	1333	1210	947
Si	7710	15100	7030	7210	8500	9680	7400	8600	7780	7630	7870
Ti	5.94	5.95	9.44	9.63	22	39	8.99	11.9	9.42	9.08	9.5
V	2.26	62	4.49	2.77	3.69	7.66	6.22	3.93	8.1	8.38	4.4
Mn	281	219.7	231.9	269	152.9	155	227.8	224.9	219.1	243.2	209.2
Fe	259	109.5	275	359.3	540	940	272	307	431	367	208.3
Rb	0.19	3400	0.06	0.07	1.11	2.7	0.07	0.35	0.08	0.07	0.09
Sr	9250	12320	7690	8250	11400	9220	7870	8210	7450	7710	8380
Y	269	360	160.1	159.9	266.6	203.7	155.3	154.6	200.2	181.6	194.1
Zr	1.79	1100	1.21	0.75	1.21	1.62	1.68	1.1	6.97	3.17	1.26
La	840	1340	528	528.5	570	524	576	567	666.4	633	520.2
Ce	2340	3430	1323	1310	1398	1326	1441	1400	1682	1582	1375
Pr	290	399	170.4	167.3	180.1	173.3	184.2	178.3	216.1	202.8	183.3
Nd	1220	1590	732	716	800	768	789	764	929	870	815
Sm	202	259	127.6	123.3	154.4	140.2	133.2	129.4	160.7	151.2	149.6
Eu	61	75.3	34.58	33.3	42.3	38.5	35.97	35.58	43.69	41.13	42
Gd	141	177	91.2	87.2	128.8	106.1	92.3	90	112.5	106.7	109
Tb	15.5	20.2	9.5	9.15	13.54	11.37	9.61	9.36	11.89	11.29	11.76
Dy	75	100.2	46.3	44.26	66.8	56.2	45.73	45.17	58	54.1	57.6
Ho	11	14.9	6.99	6.63	10.39	8.63	6.74	6.74	8.61	8	8.48
Er	23	31.3	14.59	13.94	22.19	18.07	13.95	13.92	17.9	16.59	17.56
Tm	2.31	3.18	1.5	1.42	2.24	1.82	1.43	1.43	1.84	1.67	1.78
Yb	10.9	14.9	7.08	6.71	10.56	8.72	6.72	6.79	8.67	7.94	8.2

Lu	1.18	1.56	0.76	0.76	1.2	0.98	0.74	0.75	0.94	0.86	0.9
Pb	5.51	3.01	2.88	2.56	2.81	2.82	3.71	2.75	6.57	5.05	4.11
Th	36.1	14.17	14.3	8.79	11.43	26.1	23.7	13.44	55.4	36.1	28.3
U	2.1	0.51	1.82	1.44	0.98	2.96	2.7	1.71	7.42	4.7	3.9

	Nepheline syenite										
	SNT 04 - 10	SNT 04 - 11	SNT 04 - 12	SNT 04 - 13	SNT 04 - 14	SNT 04 - 16	SNT 04 - 17	SNT 04 - 18	SNT 04 - 19	SNT 04 - 20	SNT 04 - 21
CL texture	Homogeous grey CL										
Na	3900	952	1531	1126	1335	1520	1179	1000	1328	1015	1288
Si	48400	7900	52100	6930	7960	8660	7750	9300	7920	15100	7750
Ti	10.8	12.9	22.3	9	10.3	11.6	8.47	130	8.17	35	8.13
V	5.52	5.28	3.49	3.84	11.6	6.2	7.11	13.2	6.04	7.6	6.81
Mn	200.7	217.3	248	258.4	232.6	256.6	215	178	238.1	233	231.9
Fe	404	390	395	307.7	660	537	279.9	350	321	1040	354
Rb	0.57	0.26	20.2	0.12	0.1	0.61	0.07	0.32	0.06	1.7	0.05
Sr	8180	8099	8480	7580	7640	7850	7300	8000	7540	7330	7270
Y	223	172.5	180.2	156.2	205.1	189.2	165.4	209.6	173.2	176.6	184.7
Zr	2.07	1.71	2.09	1.63	5.9	3.05	3.02	5.06	4.58	3.44	6.71
La	613	578	589	542	701	635	582	600	674	598	659
Ce	1561	1464	1401	1368	1774	1574	1465	1567	1670	1498	1656
Pr	203.8	188.1	178.3	175.7	226.7	202	187.7	207	213	194	212.7
Nd	906	810	768	757	964	861	800	913	903	833	901
Sm	168	141.9	139.1	131.5	165	150.1	137.7	166.2	154.6	146.1	156.3
Eu	46.1	39.08	37.2	35.78	45.16	41.7	38	45.47	42.5	40.2	43.04
Gd	121	99.5	101.9	90.7	114.2	104.2	94	118.1	104	100.8	106.6
Tb	13.2	10.75	10.91	9.71	12.4	11.35	10.2	12.75	11.27	10.96	11.82
Dy	65.8	51.7	52.8	46.6	60.6	54.9	49.3	61.7	53.9	52.5	57.1
Ho	9.9	7.58	7.78	6.89	8.96	8.07	7.17	9.15	7.71	7.74	8.13
Er	20.9	15.66	15.79	14.04	18.77	16.71	14.68	18.69	15.52	15.9	16.08
Tm	2.1	1.56	1.57	1.43	1.92	1.72	1.49	1.87	1.54	1.55	1.59

Yb	9.4	7.41	7.37	6.83	9.07	8.08	7.06	8.84	7.25	7.32	7.32
Lu	1.01	0.81	0.81	0.75	0.98	0.88	0.78	0.95	0.77	0.8	0.77
Pb	4.61	4.16	3.52	3.27	7.36	5.24	4.93	5.58	6.9	4.81	7.24
Th	34.5	29	18.6	19.3	64.4	32.6	38.4	48.7	52.8	35	61.6
U	4.62	2.87	3.32	3.47	8.5	3.9	5.43	7.78	7.13	5.4	9.08

	Nepheline syenite										
	SNT 04 - 22	SNT 04 - 23	SNT 04 - 25	SNT 04 - 26	SNT 04 - 27	SNT 04 - 28	SNT 04 - 29	SNT 04 - 30	SNT 04 - 31	SNT 04 - 32	SNT 04 - 33
CL texture	Homogeneous grey CL										
Na	1144	1070	1235	1177	1205	1053	1188	1067	2020	5000	1243
Si	9200	7150	13300	34000	7420	7800	8040	7880	9960	18100	7430
Ti	7.79	13.7	7.81	3.5	7.75	7.68	7.53	7.97	8.71	11	7.78
V	0.62	5.01	8.9	4.92	0.44	10.93	9.47	5.71	6.1	4.2	4.83
Mn	209	230.3	227	230.2	236.6	221.4	213.4	220.7	207	118	230.2
Fe	242	480	507	410	262.9	307.9	277.5	287.6	420	199	349
Rb	0.1	0.29	0.11	Below LOD	0.08	0.05	0.16	0.05	0.13	0.31	0.06
Sr	10230	8110	7910	7070	10010	7520	7340	7610	8130	8430	8020
Y	269	168.9	231	204	214.9	186.9	217.3	163.8	203	263	214.6
Zr	0.5	1.61	6.34	6.65	0.38	3.33	4.99	1.73	2.32	0.9	2.39
La	1108	583	810	703	1030	665	681	564	642	420	735
Ce	2590	1437	2000	1743	2284	1643	1708	1412	1601	1140	1822
Pr	323	182.6	256	224.1	272	207.5	216.8	179.5	204.2	163	226.9
Nd	1370	781	1090	962	1106	875	926	766	876	800	965
Sm	236	134.4	187	169	179.9	148.6	161.5	130.5	155	183	162.8
Eu	67.6	37.4	51.4	46.7	50.5	41.03	44.94	36.1	43.2	53.8	44.38
Gd	167	93.8	131	117.7	122.9	103.6	114.3	91	109	148	113.9
Tb	17.9	10.22	14.6	12.99	13.06	11.25	12.69	9.93	12	16	12.54
Dy	84	49.9	72	62.3	62	54.7	61.94	47.6	57.2	76	60.9
Ho	11.9	7.34	10.7	9.33	8.99	8.12	9.2	6.95	8.37	10.8	9.15
Er	23	15.09	22.3	19.3	18.26	16.77	19.05	14.43	17	21.1	19.24

Tm	2.22	1.53	2.27	1.98	1.86	1.72	1.97	1.47	1.69	1.99	1.98
Yb	10	7.2	10.8	9.04	8.72	8.13	9.37	6.96	7.9	8.74	9.37
Lu	1.1	0.8	1.18	0.98	1.02	0.87	1.02	0.75	0.86	0.91	1.04
Pb	4.77	2.7	5.57	6.08	4.65	4.85	6.7	3.53	4.25	2.55	5.42
Th	17.5	15.15	53	46.7	19.35	38	56.56	21.3	28.4	16.9	41.6
U	0.5	2.46	7.8	7.04	0.6	4.43	7.48	2.82	3.75	2.2	4.68

	Nepheline syenite										
	SNT 04 - 34	SNT 04 - 35	SNT 04 - 36	SNT 04 - 37	SNT 04 - 38	SNT 04 - 39	SNT 04 - 40	SNT 04 - 42	SNT 04 - 43	SNT 04 - 44	SNT 04 - 45
CL texture	Homogeneous grey CL										
Na	3000	1109	1095	1229	1072	991	1505	1202	1140	1079	1077
Si	35000	7190	7260	7800	7100	11000	8240	9300	7670	6340	12500
Ti	63	7.69	7.1	7.33	14.5	253	7.18	9.7	9.4	7.4	6.91
V	10.4	5.22	1.39	0.75	1.47	10.2	8.25	4.58	5.44	4.64	2.81
Mn	242	242.4	276.3	437	317.6	520	286.5	214.3	207.8	212.5	282.1
Fe	2600	355	388	358	497	4000	480	416	418	272.6	367
Rb	1.07	0.05	0.04	0.07	0.22	9	0.09	0.11	0.09	0.04	Below LOD
Sr	13430	7990	9490	10810	8380	8470	7670	8670	8520	7880	8460
Y	221.5	144.9	178.4	211	156.2	180.1	177.2	213.8	210.6	172.5	166.9
Zr	30	1.65	0.56	0.61	1.4	2.4	3.54	4.14	4.59	1.78	1.56
La	1870	525	764	964	618	570	667	678	652	584	692
Ce	4000	1315	1800	2124	1504	1426	1665	1692	1632	1485	1676
Pr	420	167.2	220	252	188.5	183	211.4	216.3	207.4	190.7	211
Nd	1500	719	915	1026	805	790	902	935	893	821	894
Sm	198	123.4	150.7	167.5	134.3	139.2	153.7	164.9	157.6	141.4	150.5
Eu	50.3	34.12	41.6	46.6	36.77	38.6	42.54	46.2	43.7	38.84	41.6
Gd	127	84.3	101.8	113.2	92.5	98.1	105.2	117.3	111.9	97.4	101.9
Tb	13.9	9.13	10.92	12.46	9.75	10.82	11.39	12.99	12.43	10.55	10.86
Dy	68	43	51.8	60.1	45.98	53	54.48	63.7	60.8	50.43	52.1
Ho	10.3	6.24	7.49	8.93	6.67	7.89	7.93	9.45	9.06	7.36	7.48

Er	21.8	12.8	15.28	18.82	13.48	16.4	16.18	19.5	18.9	15.04	15.15
Tm	2.26	1.31	1.53	1.98	1.37	1.68	1.63	1.97	1.93	1.5	1.52
Yb	10.9	6.06	7.32	9.61	6.52	8.05	7.71	9.25	9.12	7.14	7.09
Lu	1.25	0.66	0.78	1.11	0.73	0.91	0.86	0.98	0.99	0.77	0.79
Pb	11.8	2.87	3.24	8.51	2.47	4.3	5.2	5.88	5.21	3.93	3.42
Th	119	15.9	11.6	45.6	7.01	22.8	34.9	44.3	43.9	25.72	14.05
U	7.4	3.06	0.99	0.36	1.98	5.33	4.3	7.9	12	3.41	1.64

	Nepheline syenite										
	SNT 05 - 1	SNT 05 - 3	SNT 05 - 4	SNT 05 - 5	SNT 05 - 6	SNT 05 - 7	SNT 05 - 8	SNT 05 - 9	SNT 05 - 10	SNT 05 - 11	SNT 05 - 12
CL texture	Homogeneous grey CL										
Na	909	1043	988	873	860	659	2710	971	657	889	1758
Si	7780	11310	15790	8770	7680	7140	9220	10300	6590	7300	6770
Ti	5.22	24	22.3	5.35	6.31	4.8	4.53	4.7	4.88	5.8	4.12
V	7.1	6.6	6.13	5.53	7	1.6	3.15	6.64	4.3	6.39	1.92
Mn	221	770	1260	369	252	91.1	163.5	296	163	296	274.7
Fe	149	720	690	196	176.4	37.6	97	270	134	235	330.9
Rb	0.07	0.61	0.67	0.11	0.06	0.09	0.3	0.9	0.06	0.12	0.07
Sr	7420	8030	6920	7402	7430	9290	11570	7330	7780	7295	10090
Y	201.2	258	219.4	184.7	191	300.6	320.8	194.4	222.8	196.7	218.8
Zr	14.7	4.43	4.64	4.07	6.33	0.2	1.6	5.26	4.4	4.47	0.58
La	673	847	764	644	624.5	531	1736	638	517	656	1163
Ce	1765	2210	1963	1649	1615	1366	3725	1632	1340	1675	2522
Pr	224	281	251.4	210.7	206.7	190	433.3	209.3	178	215.1	295.5
Nd	957	1200	1077	898	886	931	1746	895	804	922	1197
Sm	163.6	206	182.1	153.5	152.7	207.6	280.6	154.9	157.1	159.3	191.1
Eu	44.8	56.2	50.6	42.17	41.93	51.9	76	42.49	39.3	43.96	51.57
Gd	112.2	140.8	123.4	104.7	104.8	171.5	184.5	107.8	121.6	110.6	124.8
Tb	12.29	15.55	13.49	11.37	11.6	18.57	19.8	12.08	13.42	12.2	13.3
Dy	59.5	75	64.4	54.5	55.84	87.2	92.6	58.36	64.2	58.8	62.68

Ho	8.71	11	9.35	7.85	8.22	12.47	13.1	8.51	9.41	8.57	8.91
Er	18.02	23.1	19.64	16.24	17.01	24.26	26.33	17.6	19.01	17.92	18.05
Tm	1.87	2.4	2.04	1.67	1.77	2.26	2.63	1.82	1.85	1.84	1.83
Yb	8.8	11.47	9.94	7.96	8.52	9.76	12.19	8.64	8.5	8.74	8.59
Lu	0.97	1.26	1.14	0.88	0.94	1.04	1.31	0.89	0.93	0.96	0.93
Pb	8	9.9	8.38	6.46	6.94	1.33	3.66	6.6	4.8	6.54	3.03
Th	67.7	71.1	49	49.7	61.6	2.98	17.02	56.9	40	56.3	8.18
U	8.2	12	6.37	5.49	10.04	0.13	3.44	5.37	4.7	7.57	1.96

	Nepheline syenite										
	SNT 07 - 1	SNT 07 - 2	SNT 07 - 3	SNT 07 - 4	SNT 07 - 5	SNT 07 - 6	SNT 07 - 8	SNT 07 - 9	SNT 07 - 10	SNT 07 - 11	SNT 07 - 12
CL texture	Homogeneous grey CL										
Na	920	1003	1300	1523	1058	1059	17200	1660	1096	1040	1014
Si	7230	7530	8210	8650	8600	7840	175000	11120	6980	32000	7750
Ti	14.12	14.06	45	17.9	15	28	32.9	150	11.93	28.5	23.6
V	3.9	6.18	3.86	2.8	5.34	4.03	1.34	6.1	3.97	5.32	12.53
Mn	211.3	192.5	212.5	227.6	200.2	183.4	194	314	239.7	213	214
Fe	201	248	740	388	272	440	520	2100	278.1	2100	470
Rb	0.06	0.04	2	0.4	1.6	0.64	46	4.8	0.06	1	0.63
Sr	7693	7980	8330	8710	8460	8450	11360	9080	8150	6790	8530
Y	148.6	169.4	230	213.9	205	191.1	308.7	197.7	148.2	140	216.4
Zr	1.37	2.05	0.63	0.55	0.75	0.65	0.67	0.67	1.01	0.89	2.75
La	541	633	653	659	654	600	1076	683	557	476	804
Ce	1358	1545	1636	1630	1656	1516	2454	1665	1366	1170	1906
Pr	174.1	194.6	211.3	208.8	214.9	198.7	302.9	212	173.3	148	235.9
Nd	732	812	901	887	928	861	1259	898	725	627	980
Sm	127.9	140.6	162.2	156.8	166.5	157	218.1	156.3	125.7	111	166.4
Eu	31.77	35.1	42.3	40.4	42.2	40.1	58.4	40.5	32.13	29.2	43.6
Gd	88.4	97.8	116.1	112.1	117.1	110.3	152.6	109.3	86.3	78.7	116.2
Tb	8.5	9.43	11.6	11.08	11.51	10.88	15.58	10.88	8.6	8	11.85

Dy	41.4	46.2	58.4	55.2	56.1	52.7	78.6	53	41.4	37.8	57.7
Ho	6.43	7.2	9.33	8.74	8.63	8.19	12.45	8.27	6.33	5.86	8.96
Er	13.72	15.56	20.66	19.15	18.4	17.26	26.9	17.7	13.36	12.3	19.31
Tm	1.36	1.53	2.09	1.93	1.79	1.68	2.66	1.76	1.32	1.19	1.96
Yb	6.5	7.24	10.02	9.02	8.31	7.75	12.35	8.29	6.25	5.71	9.5
Lu	0.72	0.81	1.13	1.02	0.91	0.86	1.3	0.92	0.69	0.66	1.09
Pb	3.72	4.23	2.49	2.95	3.13	2.64	2.11	2.8	2.79	2.44	5.38
Th	25.6	31.9	11.38	10.4	21.3	16.04	8.5	15.4	12.36	12.01	41.4
U	1.76	2.9	1.9	1.13	1.85	1.56	1.12	2.78	1.37	1.77	3.19

	SNT 07 - 13	SNT 07 - 14	SNT 07 - 15	SNT 07 - 16	SNT 07 - 17	SNT 07 - 18	SNT 07 - 19	SNT 07 - 20	SNT 07 - 21	SNT 07 - 22	SNT 07 - 23
CL texture	Homogeneous grey CL										
Na	945	1076	1110	1188	1140	1138	1173	1146	1190	1130	1045
Si	8020	14200	21000	8280	8060	7190	9640	8040	8040	7180	24000
Ti	21.2	40	16.1	15.1	18.9	10.81	88.5	49	10.51	13.1	17.7
V	6.94	6.17	6.98	4.08	1.48	4.88	4.27	7.96	6.24	3.5	3.13
Mn	203.8	218	208	211.8	194	235.7	1910	220.6	224.8	240.4	226
Fe	357	530	396	305	370	295.2	1970	670	279.4	366	440
Rb	0.37	0.51	0.21	0.33	0.63	0.05	2.26	1.05	0.08	0.18	2
Sr	8170	7980	7860	8270	10020	8100	9000	7720	7870	8350	8070
Y	186.5	203	204	183.9	227	157.2	173	166.5	179.4	148.8	158
Zr	1.92	2.52	3.09	0.75	0.38	1.9	2.13	1.91	1.47	0.77	1.16
La	647.9	685	688	599	652	579	740	593	619	546	545
Ce	1602	1710	1714	1511	1541	1430	1760	1486	1544	1344	1365
Pr	203.8	224	224	196.5	193.6	182.2	212	191	198.3	170.3	173.9
Nd	855.6	963	956	846	816	770	869	813	842	723	749
Sm	147	171	169	149.3	148.1	131.7	146	140	144.4	123.3	131.1
Eu	38.46	44.8	44.9	40.1	43.1	34.89	39.1	37.3	38.2	32.88	35.1
Gd	103.5	120	119.2	104.7	107	91.7	101.7	97.4	100.7	86.1	91.4

Tb	10.64	12.5	12.5	10.8	11.47	9.44	10.37	10.04	10.41	8.88	9.58
Dy	51.5	61.2	60.6	51.9	57.2	45.4	49.3	48.2	51.1	42.74	45.9
Ho	7.87	9.5	9.34	7.89	8.95	6.82	7.37	7.2	7.75	6.45	7.05
Er	16.89	20.1	19.9	16.7	19.55	14.23	15.3	15	16.29	13.54	14.8
Tm	1.69	2.07	2	1.67	2.04	1.44	1.53	1.51	1.69	1.37	1.53
Yb	8	10.1	9.52	7.9	9.96	6.74	7.23	7.14	8.01	6.59	7.05
Lu	0.88	1.12	1.05	0.87	1.13	0.75	0.79	0.79	0.88	0.72	0.79
Pb	4.26	5.6	5.42	2.96	2.03	3.65	16.3	4.03	4.15	2.58	3.13
Th	30.49	39.1	39.8	17.65	9.12	22.9	16.2	28.09	28.3	12.15	13.6
U	3.83	4.37	4.45	1.56	3.2	2.58	1.11	3.1	3.6	1.41	2.01

	Nepheline syenite										
	SNT 07 - 24	SNT 07 - 25	SNT 07 - 26	SNT 07 - 27	SNT 09 - 1	SNT 09 - 2	SNT 09 - 3	SNT 09 - 5	SNT 09 - 8	SNT 09 - 9	SNT 09 - 10
CL texture	Homogeneous grey CL										
Na	929	1103	1144	4330	1462	2090	1489	1800	1840	1311	2040
Si	7380	7130	8200	13800	8370	9230	8670	9440	8510	10440	16000
Ti	9.57	10.45	10.23	12.2	6.38	32.7	6.04	8.1	36	14.9	89
V	1.51	4.09	6.18	8.96	0.15	0.75	0.28	0.5	0.82	95.4	87.1
Mn	265.8	224	277	229.9	361.9	377.3	350	323.4	340.6	126.2	155
Fe	297	319	383	530	541.6	900	539	550	960	482	1810
Rb	0.04	0.05	0.88	0.21	0.12	1.33	0.07	0.16	0.98	0.45	2.7
Sr	8540	8250	8480	7520	12570	12500	14920	12840	12110	9640	9430
Y	133.3	167	204.2	234.5	230.2	280	274.5	255.1	279	254.2	229.8
Zr	0.31	1.26	2.4	5.6	0.34	0.69	0.44	0.8	0.84	6.52	6.34
La	504	587	684	694	797	865	988	885	866	1812	1650
Ce	1281	1456	1695	1755	1929	2130	2311	2091	2091	3175	2960
Pr	166.1	186.5	215.8	226.5	242	270	286.5	258	261.3	308	292
Nd	712	794	920	976	1016	1148	1202	1076	1102	1110	1077
Sm	122.4	136.3	159.2	171.8	172.8	197	200.4	177.7	188.4	161.3	155.5
Eu	32.38	36.16	42.8	47.1	50.3	58.3	59.6	52.5	55.9	45.64	43.1

Gd	83.7	95.3	111.7	124.2	122.4	139.6	141.1	125.6	134.8	113.3	108.7
Tb	8.51	9.97	11.65	13.41	13.64	15.7	15.71	14.09	15.28	12.48	11.66
Dy	40.1	48.6	56.5	66.7	67	78.9	77.9	71.4	77.8	63.5	58
Ho	5.87	7.35	8.57	10.18	9.93	12.18	11.71	11	11.96	10.11	9.16
Er	11.89	15.27	18.07	21.5	20.89	26.4	24.92	24.1	26.2	22.67	20.41
Tm	1.17	1.53	1.83	2.15	2.19	2.84	2.62	2.6	2.8	2.47	2.22
Yb	5.55	7.12	8.56	9.91	10.47	14.2	12.64	12.84	14.09	13.06	11.54
Lu	0.6	0.79	0.95	1.05	1.13	1.57	1.38	1.42	1.58	1.56	1.39
Pb	1.79	2.86	4.49	7.48	4.22	5.16	5.63	6.88	5.52	14.6	15.15
Th	4.6	16.4	29	69.1	6.48	20.2	15.44	25.4	24.2	126.4	116.7
U	0.12	5.7	3.69	10.5	0.12	3.18	0.98	2.59	3.01	17.7	15.5

	Nepheline syenite										
	SNT 09 - 11	SNT 09 - 12	SNT 09 - 17	SNT 09 - 18	SNT 09 - 19	SNT 06-1	SNT 06 - 2	SNT 06 - 3	SNT 06 - 4	SNT 06 - 5	SNT 06 - 6
CL texture	Homogeneous grey CL										
Na	1440	1411	1601	5600	1520	1030	1340	1160	744	867	800
Si	7670	7460	8020	20600	10200	8700	6850	5030	7460	7820	8560
Ti	6.01	6.45	28	480	90	6.29	12.5	7.65	65	18	33
V	0.16	0.09	0.38	5.7	7.6	7.11	3.95	6.64	6.9	6.99	7.02
Mn	363	340.9	306.3	378	213	261.6	216	247.3	176	182.5	168.3
Fe	594	816	690	8600	1320	381	960	360	2200	890	880
Rb	0.07	0.09	0.79	20	1.79	0.08	0.35	0.06	0.29	0.22	0.26
Sr	12360	15840	12320	15540	10210	7980	9400	8690	10850	8400	9280
Y	211	316	366	340	430	255	222.6	215.8	229.3	222.3	215.1
Zr	0.34	0.58	1.7	0.32	1.33	3.56	2.14	2.99	5.4	4.42	5.8
La	681	861	1066	891	1580	897	728	766	717	808	771
Ce	1658	2128	2646	2194	3640	2222	1830	1892	1780	1917	1846
Pr	206.4	269.3	332	280.6	440	277	232	239.1	226	236.2	229.2
Nd	863	1141	1404	1215	1830	1166	992	1016	976	994	966
Sm	150	203.1	239.9	217	302	195.2	172.2	175.1	173.2	169	164.4

Eu	43.4	60.9	69.5	64.8	85	52.9	48.1	47.6	48.2	46.77	45.59
Gd	107.3	146.4	169.6	163	212	135	120.9	120.4	127.5	119.9	115.4
Tb	12.02	16.82	19.49	18.2	23.1	14.84	13.19	13.14	13.9	13.21	12.68
Dy	59.5	85.2	99.4	91	115	72.2	64.1	63.9	67.7	64.44	62.2
Ho	8.91	12.98	15.55	14	17.5	10.85	9.4	9.38	10	9.55	9.25
Er	19.1	28.29	34.6	30	36.8	22.88	19.35	19.49	20.49	19.79	19.42
Tm	2	3.02	3.8	3.12	3.74	2.35	1.95	1.98	2.07	2	2.03
Yb	9.68	14.99	19.38	14.6	17.43	11.11	9.12	9.36	9.4	9.28	9.63
Lu	1.07	1.68	2.28	1.61	1.89	1.2	0.98	1.01	1.01	0.99	1.1
Pb	4.29	5.9	7.98	5.09	8.28	7.91	4.64	5.61	4.17	6.06	5.59
Th	6.39	10.63	52.2	9.46	49	62.8	40	44.9	43.1	52.6	47.99
U	0.14	0.7	6.97	0.58	4.6	6.16	4.55	6.02	5.8	6.69	6.29

	Nepheline syenite											
	SNT 06 - 13	SNT 06 - 15	SNT 06 - 16	SNT 06 - 21	SNT 06 - 26	SNT 06 - 27	SNT 06 - 10	SNT 06 - 11	SNT 06 - 12	SNT 06 - 17	SNT 06 - 18	SNT 06 - 25
CL texture	Homogeneous grey CL						Patchy CL					
Na	1240	903	1385	1010	882	919	67.2	81	33.7	36.9	39.7	92
Si	7630	6560	8130	8440	8190	7920	8160	7240	7250	7310	6970	8390
Ti	8.4	7.55	40	6.82	7.71	7.7	1.46	Below LOD	Below LOD	Below LOD	Below LOD	Below LOD
V	7.35	7.63	9.55	5.04	3.44	3.41	0.92	0.15	0.05	0.34	0.25	0.47
Mn	258.5	167.2	264.2	197.6	197.4	119.7	4480	2690	2989	2584	2978	2540
Fe	611	246	1020	710	376	380	7040	4310	4440	4070	4370	2610
Rb	0.13	0.2	0.26	0.15	0.24	0.27	0.34	0.04	Below LOD	0.13	0.11	0.62
Sr	9390	9680	9690	9930	8144	8950	12260	11410	11860	11510	12020	14600
Y	201.4	249.9	254.5	163.9	215	214.8	59.9	54	43	47.4	44.9	39.1
Zr	2.69	3.82	3.99	1.63	2.77	1.95	0.08	Below LOD	Below LOD	Below LOD	Below LOD	Below LOD
La	692	964	1100	569	682	595	73	123	22.9	24.4	34.1	23
Ce	1755	2286	2590	1407	1774	1630	199	250	59	70	85.3	55

Pr	223.8	280.3	313	178.3	225.6	210.9	22.7	29	7.31	8.8	10.29	6.6
Nd	956	1163	1295	759	966	912	97.4	112	34.5	41	46.1	29.5
Sm	164.3	193	210.2	131.1	165.9	159	19.95	18.4	8.41	9.9	9.9	6.61
Eu	44.91	53.16	56.2	36.36	45.96	44.3	6.21	5.43	2.92	3.34	3.29	2.33
Gd	113.2	133	139.8	91.5	114.9	112.8	16.36	14.7	8.92	10.1	9.62	7.27
Tb	12.26	14.65	15.24	10.1	12.83	12.7	2.16	1.89	1.26	1.43	1.36	1.04
Dy	59.17	71.2	73.1	48.9	61.45	61.8	12.63	10.89	7.99	8.78	8.31	6.6
Ho	8.67	10.65	10.79	7.14	9.11	9.19	2.23	1.97	1.56	1.68	1.59	1.32
Er	17.91	22.15	22.35	14.6	18.88	18.89	5.8	5.23	4.32	4.54	4.36	3.7
Tm	1.81	2.3	2.27	1.46	1.93	1.88	0.76	0.69	0.59	0.63	0.59	0.51
Yb	8.62	10.94	10.82	6.93	8.92	8.93	4.69	4.42	3.88	4.07	3.96	3.45
Lu	0.93	1.19	1.18	0.75	0.96	0.94	0.66	0.65	0.6	0.61	0.6	0.51
Pb	5.64	7.63	8.72	3.88	4.67	3.96	8.97	4.64	4.56	4.25	4.07	3.32
Th	44.7	65.3	71.6	31.9	42	40.1	0.05	0.02	Below LOD	Below LOD	0	Below LOD
U	4.59	7.32	8.3	3.65	5.63	4.5	0.23	0.11	0.03	0.03	0.03	0.01

	Carbonatite										
	EC4-1	EC4-2	EC4-3	EC4-4	EC4-5	EC4-6	EC4-7	EC4-8	EC4-9	EC4-10	EC4-11
CL texture	Homogeneous grey CL										
V	26.4	4.3	1.86	0.34	1.21	Below LOD	2.52	4.32	4.39	Below LOD	1.41
Sr	11850	11320	10340	10310	9210	11940	11750	7770	10470	11240	8690
Y	205.1	211.1	148.7	139.9	144.4	228.3	215.7	121.1	166.3	191.2	153.7
La	1044	250	237	620	618	1285	1074	439	273.3	311.8	436
Ce	2502	984	826	1514	1445	2815	2433	1114	914	1086	1163
Pr	286.6	143.1	118.7	176.8	170.6	322.3	280.2	139.7	129.2	152.2	148.1
Nd	1161	696	576	740	709	1279	1090	595	600.8	692	615
Sm	192	158	124.4	126.6	123.3	212.6	185.2	109	133.2	152.5	122.3
Eu	52.2	47	36.6	34.5	33.16	56.4	50	30.1	37.6	43.4	33.2
Gd	124.1	115.5	90.3	84.2	80.1	129.6	123	71.4	91.4	105.8	86.5
Tb	13.19	13.05	9.69	9.31	9.13	14.6	13.4	8.06	10.18	12.3	9.69

Dy	62.4	60.1	47.1	40.8	45.8	69.3	62.8	38.1	52	59.2	46.1
Ho	8.71	9.09	6.66	6.16	6.88	9.65	9.47	5.4	7.17	8.15	6.85
Er	15.6	16.4	11.28	12.01	12.51	17	17.3	10.28	13.5	16.13	12.8
Tm	1.45	1.55	1.12	1.16	1.25	1.55	1.64	0.98	1.26	1.47	1.25
Yb	6.73	6.72	4.8	5.21	6.05	6.77	7.13	5.04	5.42	5.85	5.19
Lu	0.67	0.64	0.47	0.55	0.6	0.76	0.73	0.48	0.51	0.55	0.58
Pb	2.24	1.42	2.68	1.79	2.76	1.9	1.64	2.74	1.72	1.26	1.7
Th	7.04	2.74	7.05	2.3	19.44	5.07	3.02	12.7	2.35	0.89	4.3
U	Below LOD	0.13	0.33	0.01	0.15	0	0	0.25	0.04	Below LOD	0.2

	Carbonatite										
	EC4-12	EC4-13	EC4-14	EC4-15	EC4-16	EC4-17	EC4-18	EC4-19	EC4-20	EC5-1	EC5-2
CL texture	Homogeneous grey CL										
V	9.3	1.23	0.12	0.03	0.04	0.22	0.04	2.19	1.43	0.55	3.2
Sr	11330	11630	11830	11980	11760	10520	11310	8200	8730	8470	7000
Y	212	224.3	208	213.3	177.2	198.5	178.8	138	137	159.2	151
La	241.9	346	364	1238	1006	318	273.5	516.3	483.5	744	1000
Ce	944	1220	1287	2730	2172	1054	967	1302	1222	1860	2410
Pr	140.8	169	178.3	309.1	243.3	145.8	135.9	156.8	145.4	211	269
Nd	688	771	839	1225	952	657	627	633	583.5	827	1040
Sm	160.8	163.6	175.5	203.5	161.4	142.3	138.3	116.4	107.8	146.9	162
Eu	47.3	48.4	49.38	54.1	43.5	41.3	39.4	30.44	28.43	39.3	44
Gd	118.9	121.3	123.5	124.9	100.7	101.2	96.6	78.8	72	89.5	93
Tb	13.28	14.06	13.76	13.84	11.17	12.4	11.83	9.23	8.69	10.19	9.9
Dy	63.8	65.1	65.9	66.3	56	58.4	54.8	45.1	42.1	46.3	44
Ho	8.9	10.26	9.18	9.28	7.93	8.34	7.92	6.34	5.91	6.51	5.5
Er	15.3	18.6	17.12	17.1	13.63	16.2	15.14	12.59	11.65	12.4	11.3
Tm	1.46	1.77	1.57	1.52	1.22	1.55	1.37	1.24	1.12	1.16	1.09
Yb	6.73	7.38	6.39	6.3	5.8	7.08	5.82	5.49	5.22	5.23	4.1
Lu	0.65	0.77	0.57	0.65	0.58	0.7	0.6	0.55	0.5	0.46	0.34

Pb	1.48	2.06	1.57	2.12	1.77	1.68	1.34	1.73	1.63	3.62	21.4
Th	2.69	7.99	1.84	6.87	4.48	6.46	1.51	6.83	5.9	5.74	5.9
U	0.1	0.02	0.01	0	0	0	0	0.3	0.04	0.16	1.18

	EC5-3	EC5-4	EC5-5	EC5-6	EC5-7	EC5-8	EC5-9	EC5-10	EC5-11	EC5-12	EC5-13
CL texture	Homogeneous grey CL										
V	9.79	6.35	4.13	2.48	2.96	7.8	5.52	0.89	13	0.19	3.66
Sr	8670	4600	8150	9580	10560	2430	8170	9420	9220	10110	9270
Y	167	74	130.9	136.6	129.2	50	139.3	163.9	132	176.8	129.3
La	645	312	501	549.5	516	210	681	881	517.7	879	520
Ce	1691	770	1230	1351	1274	550	1650	2050	1280	2067	1316
Pr	197	90	153.2	163.6	152.4	64	198	234	154.4	247.3	157.7
Nd	787	362	605	654	617	234	781	922	619	979	641
Sm	136	59	109.5	114.1	106.6	41	136	157.4	106.6	158.1	110.6
Eu	40.3	18.4	28.2	30.1	28.9	12.4	37.7	40.4	30.4	42	29.2
Gd	94.3	43	71.5	74.9	74.4	25	84.1	99.4	72.1	109.8	75.9
Tb	10.6	4.2	7.75	8.63	7.95	3	8.68	10.69	8.28	10.9	8.12
Dy	54.1	19.5	38.4	38.7	38.9	13.2	41.3	49.3	39.4	50.3	38.4
Ho	7.67	3	5.87	5.56	5.7	1.73	5.88	7.12	5.66	7.62	5.65
Er	15	6.6	11.97	11.7	11.03	4.1	10.4	13.9	11.26	14.7	11.38
Tm	1.51	0.67	1.02	1.17	1.13	0.37	1.1	1.35	1.12	1.38	1.07
Yb	6.84	3.8	4.96	5.35	4.72	2.7	5.14	6.1	5.5	5.95	5.44
Lu	0.62	0.36	0.43	0.46	0.54	Below LOD	0.53	0.66	0.55	0.58	0.57
Pb	13.7	34.2	2.35	1.83	1.94	41.7	9.2	2.43	2.58	2.49	2.03
Th	20.5	6.3	11.8	6.07	7.33	3.94	5.43	9.8	6.51	8.53	9.5
U	830	2.46	0.74	0.08	0.41	2.11	1.44	0.29	2.14	0.07	0.3

	Carbonatite											
	EC21-1	EC21-2	EC21-3	EC21-4	EC21-5	EC21-6	EC21-7	EC21-8	EC21-9	EC21-10	EC21-11	EC21-12
CL texture	Homogeneous grey CL											
V	0.08	1.49	0.27	0.79	1.55	0.03	0.72	0.69	5.3	Below LOD	3.9	11.34
Sr	11380	10940	11450	11090	9840	10950	11260	11290	11050	11390	11740	8500
Y	249.6	215.8	267.2	221.2	162.6	205.3	284.6	213.2	250.8	268.8	295.4	194.4
La	1136	972	1167	983	622	877	1246	936	812	1221	680	696
Ce	2661	2274	2764	2269	1514	2044	2962	2196	2005	2865	2020	1728
Pr	319.6	271.4	336	264.7	179.9	236.4	351.2	252.3	241	334.9	246	207.2
Nd	1298	1110	1361	1065	771	964	1444	1038	1034	1385	1133	890
Sm	216.1	188.1	233.9	180.5	136	165.1	244.9	177.5	191.7	231.4	229	150.6
Eu	63.7	54.55	67.89	50.9	37.4	45.2	68.7	49.2	54.9	65.1	67.5	41.1
Gd	149.7	130.9	159.4	122.7	94.6	109	163.3	116.6	134.6	152	170.1	103.8
Tb	15.46	13.68	17	13.5	10.23	11.95	17.6	12.73	14.75	16.37	18.72	11.18
Dy	72.1	64.7	79.1	62	48.3	55.9	83.1	59.9	69.9	76.3	86.2	53
Ho	10.52	9.18	10.93	9.09	7.03	8.17	11.68	8.83	10.17	11.07	12.66	7.87
Er	20.3	17.99	21.2	18.91	14.11	15.8	23.02	17.27	19.7	21.87	24.33	15.77
Tm	1.98	1.69	2.1	1.89	1.43	1.69	2.33	1.89	2.01	2.2	2.29	1.6
Yb	8.78	7.51	9.38	8.71	6.87	7.55	9.9	7.97	8.54	9.95	9.75	7.92
Lu	0.85	0.66	0.88	0.88	0.7	0.73	1.04	0.77	0.86	1.01	1.01	0.86
Pb	2.99	2.52	3.08	2.52	1.67	1.83	3.98	2.35	2.58	2.34	1.92	3.79
Th	17.78	13.04	18.78	9.55	7.61	6.57	27.1	9.86	13.87	10.17	3.15	23
U	0.02	0.05	0.02	0.24	0.24	0.01	3.2	0.08	0.52	0.02	2.5	1.93

	Carbonatite											
	EC21-13	EC21-14	EC21-15	EC21-16	EC21-17	EC21-18	EC21-19	EC21-20	EC21-21	EC21-22	EC21-23	EC21-24
CL texture	Homogeneous grey CL											
V	1.49	0.3	0.42	1.58	3.63	0.11	0.07	6.81	0.94	0.05	0.36	1.27
Sr	11500	9340	11610	11260	6200	11090	11100	11770	11880	11210	11310	10380

Y	273.7	264.2	243	239.2	143	223.7	225.6	226.4	275.2	262.3	219.4	197.1
La	1213	1240	1155	988	479	986	1030	1032	870	1189	982	784
Ce	2840	2920	2780	2580	1280	2340	2416	2526	2353	2810	2213	1867
Pr	338	337	291.7	273.8	147	281.9	287	280.2	298.3	335.8	255.2	217.9
Nd	1385	1327	1250	1242	640	1149	1165	1131	1278	1379	1025	901
Sm	233	223	197.2	198	112	193.2	193.5	190.4	236.4	233.4	176.6	156.9
Eu	65	64.2	57.5	57.3	30.4	57	55.8	54.15	68.3	66.2	50.48	42.6
Gd	155	145	134.5	139.6	72	134.2	132.2	130.4	167.1	156.4	121.1	102.7
Tb	16.6	15.66	14.29	14.34	8.1	13.99	13.99	13.85	17.94	16.88	13.08	11.18
Dy	78.2	75.6	67	67.6	38.5	65.7	64.6	65.2	82.1	78.5	62	52.9
Ho	10.9	10.99	9.3	9.53	5.6	9.2	9.23	9.53	11.79	10.99	8.9	7.71
Er	21.7	21.1	18.3	18	11.6	18.1	18.47	18.82	23.1	21.4	17.62	16.6
Tm	2.29	1.98	1.6	1.77	1.22	1.83	1.8	1.92	2.13	2.1	1.87	1.71
Yb	9.8	9.6	8.2	7.6	4.9	7.77	7.89	8.68	9.74	9.57	8.14	7.82
Lu	1.01	0.84	0.8	0.74	0.39	0.78	0.81	0.91	1.01	0.94	0.84	0.78
Pb	3.15	4.29	2.5	2.95	14.9	2.58	2.32	54	2.09	3.62	2.31	1.99
Th	19.2	7.62	8.4	14.3	18.2	13.3	9.71	23.11	7.8	24.8	9.65	6.57
U	0.51	0.13	0.99	3.8	6	0.03	0.01	2470	0.38	0.01	0.06	0.04

	Carbonatite											
	EC21-25	EC21-26	EC21-27	EC21-28	EC21-29	EC21-30	EC21-31	EC21-32	EC21-33	EC21-34	EC21-35	EC21-36
CL texture	Homogeneous grey CL											
V	0.18	2.93	0.46	0.36	3.4	1.77	4.1	0.13	0.4	0.06	Below LOD	3.82
Sr	11890	11130	11150	11878	11640	11790	7780	11320	11090	10220	11300	10560
Y	218	247	216.5	254.9	256.6	251	172.5	248.7	240	250.6	236.2	238.3
La	840	1126	907	1022	1272	906	581	1146	1162	1139	1066	1030
Ce	2018	2614	2162	2447	2950	2320	1486	2666	2702	2700	2481	2730
Pr	239	307.7	252.5	291.2	344	281	181.2	315.1	320.5	315.7	282.9	291
Nd	984	1258	1049	1221	1416	1219	793	1292	1249	1251	1162	1257
Sm	172.7	213.4	180.8	210.1	225.7	214.8	142.2	215.8	206.2	206	196	222

Eu	49.7	60.41	50.3	59.49	63	60	39.14	60.2	58.5	61.4	58.7	62.5
Gd	118.6	139.3	118.6	142	145.9	144.6	98.3	143.8	140.1	153.9	136.4	138.3
Tb	12.99	15.03	12.78	15.3	15.63	15.66	10.56	15.51	15.69	15.82	14.52	14.99
Dy	61.5	71.1	60.6	72	74	71.5	49.4	72	71.2	72.2	68.3	69.7
Ho	8.94	10.06	8.63	10.26	10.98	10.31	7.41	10.39	10.27	10.06	9.56	9.75
Er	17.46	19.68	16.67	20.48	20.4	19.7	14.79	20.1	19.7	19.5	19.29	18.2
Tm	1.7	1.92	1.71	2.02	1.99	2.05	1.55	2.01	1.96	2.03	1.84	1.79
Yb	7.63	8.84	7.78	8.91	9.6	8.1	7.35	8.56	9	8.31	8.04	7.63
Lu	0.78	1	0.76	0.88	1.01	0.9	0.79	0.94	0.85	0.9	0.86	0.77
Pb	2.27	3.23	2.21	3.22	2.03	2.26	3.91	3.1	3.35	3.25	2.62	8.9
Th	10.23	19	10.22	17.09	10.7	8.7	13.1	18.2	18.8	19.8	12.62	20.06
U	0.03	0.66	0.05	0.21	0.37	71	4.48	0.03	0.25	Below LOD	Below LOD	26

	Carbonatite											
	EC23-1	EC23-2	EC23-3	EC23-4	EC23-5	EC23-6	EC23-7	EC23-8	EC23-9	EC23-10	EC23-11	EC23-12
CL texture	Homogeneous grey CL											
V	1.57	3	0.61	0.36		0.2	0.22	0.19	1.7	0.21	9.2	35
Sr	7420	11260	10780	11270	11200	11120	11340	10730	11020	8800	7400	8780
Y	146.8	276.2	246.5	318.2	267.2	273.2	320.9	275.5	331.2	191.3	154.3	246.3
La	541	1454	1180	1547	1320	1303	1371	1237	1643	851	568	1040
Ce	1378	3245	2785	3597	3024	3064	3330	3031	3910	2020	1419	2270
Pr	166.7	382.7	330.3	432.3	352.2	366.7	413	361.8	455	240	174.2	256
Nd	723	1549	1352	1761	1414	1495	1739	1497	1854	1018	749	1040
Sm	128.5	259	231.3	296.8	240.9	252.7	302	251.5	303.3	167.7	130.3	189
Eu	35.39	72.1	64.2	82.1	67	71.4	84.3	71.1	85.3	46	35.7	55.3
Gd	89.1	173	153	199.2	160.9	169.6	202.3	164.6	195.3	114.6	90.7	143.5
Tb	9.72	18.1	16.14	21.03	17.09	17.73	21.4	17.93	21.48	12.23	9.87	16.01
Dy	45.3	80.7	72.4	96	78.4	82.1	96.2	82.3	96.2	55.6	45.5	73.8
Ho	6.66	11.6	9.94	13.1	11.24	11.24	13.66	11.47	14.2	8.11	6.6	10.52
Er	13.1	22.5	20	25.1	21.56	21.8	24.3	22.5	26.6	16.13	13.4	19.91

Tm	1.35	2.23	1.93	2.47	2.22	2.19	2.32	2.1	2.55	1.6	1.33	1.87
Yb	6.24	9.67	7.83	9.7	9.27	8.65	9.61	8.9	10.81	7.66	6.06	8.2
Lu	0.68	0.96	0.75	0.99	0.94	0.8	0.88	0.85	1.05	0.9	0.67	0.88
Pb	1.971	2.51	2.328	2.24	2.91	2.47	2.54	2.61	2.94	2.06	2.78	5.4
Th	7.6	9.41	8.3	7.56	7.76	9.87	10.1	10.58	14.8	4.92	12.7	17
U	0.591	0.0416	0.215	0.0039	0.215	0.0197	0.024	0.289	0.039	0.262	2.29	8.9

	Carbonatite							
	EC23-13	EC23-14	EC23-15	EC23-16	EC23-17	EC23-18	EC23-19	EC23-20
CL texture	Homogeneous grey CL							
V	Below LOD	0.09		0.51	6.2	20.7	0.04	10.3
Sr	11300	11410	9530	10080	6700	6670	11240	7100
Y	277.2	316.5	212	262	138	184.2	306.8	178.1
La	493	1543	556	515	670	475	1514	573
Ce	1616	3564	1431	1598	1520	1269	3630	1403
Pr	229.7	426.1	180.3	216	172	159	436	175
Nd	1097	1739	799	1038	730	668	1781	773
Sm	237.4	289.4	153.7	209	107	130	303	148.5
Eu	67.7	80.7	44	62.3	31	37.3	84.7	43
Gd	177.9	192.7	115	153	70	97	195.6	105.5
Tb	18.98	20.44	12.55	16.4	7.7	10.5	20.68	11.49
Dy	85.7	91.8	58.8	74.6	37	52.6	92	54.1
Ho	11.91	12.94	8.9	10.97	5.8	7.8	13.04	7.7
Er	22.45	25	18.2	21.3	10.4	15	24	15.2
Tm	2.1	2.43	1.76	1.94	1.17	1.59	2.27	1.59
Yb	8.52	9.96	8	8.7	4.9	7	9.88	7.05
Lu	0.79	0.95	0.85	0.89	0.62	0.69	0.93	0.74
Pb	1.56	2.42	2.35	2.45	2.06	4.71	2.7	3.05
Th	1.109	8.6	3.07	8.72	5.4	16.2	12	19.6
U	0.00242	0.0096	0.51	0.0074	0.0089	3.97	0.0154	5.3

	Carbonatite					
	EC29-1	EC29-3	EC29-5	EC29-2	EC29-4	EC29-6
CL texture	Dark grey core			Light grey rim		
V	0.47	0.91	0.76	0.23	0.07	0.07
Sr	12020	11410	11280	13180	10720	11430
Y	255.9	184.9	185.3	314.1	264.3	291.1
La	432	748	745	1253	1210	980
Ce	1510	1850	1844	3190	2858	2620
Pr	188	204	205	373	343.2	330
Nd	970	916	915	1648	1428	1430
Sm	190	149	147.8	266	245.6	268.8
Eu	55.1	39.4	38.5	71.9	69.2	74.7
Gd	134.8	101.6	96.4	177	164.8	181.5
Tb	14.6	11.23	10.09	18.59	17.28	19.55
Dy	69.9	53.2	50.4	89.7	80.1	87.1
Ho	10.01	7.66	7.32	12.8	11.06	11.97
Er	19.1	15.44	14.4	24.1	23	22.74
Tm	1.94	1.55	1.59	2.35	2.07	2.17
Yb	7.7	7.51	7.4	11.46	8.68	9
Lu	0.85	0.66	0.82	1.02	0.81	0.77
Pb	3.53	2.69	2.24	2.261	43.1	5.1
Th	12.61	2.01	5.7	4.66	5.9	4.8
U	0.34	0.684	0.121	0.00283	0.84	0.138

Standard	Durango_1	Durango_2	Durango_3	**Durango av.**	**Durango ref.**	G_NIST612_1	G_NIST612_2	G_NIST612_3	G_NIST612_4	G_NIST612_5	**NIST612 av.**	**NIST 612 ref.**
Na	1196	1206	1285	**1229**		103900	103870	103800	103900	103900	**103874**	
Si	9210	11000	9970	**10060**		336100	336100	336000	336100	336100	**336080**	
Ti	6.97	6.02	6.35	**6.4**		44	44.01	43.99	44	44	**44**	
V	31.9	31.8	49.5	**37.8**	**30.7**	39	39	39	39	39	**39**	**40**
Mn	93.5	94.5	93.6	**93.9**	**104.6**	38	38	38	38	38	**38**	
Fe	272.4	271.4	293.3	**279**		51	51	51	50.99	51	**51**	
Rb	0.24	0.24	0.24	**0.2**		31.4	31.4	31.4	31.4	31.4	**31**	
Sr	485.6	510	506.4	**501**	**517**	78.4	78.4	78.4	78.4	78.4	**78**	
Y	1135	1168	878	**1060**	**824**	38	38	38	38	38	**38**	**40**
Zr	1.75	1.83	1.46	**1.7**		38	37.98	38	38	38	**38**	
La	4460	4340	4350	**4383**	**3720**	35.8	35.8	35.8	35.8	35.8	**36**	**35**
Ce	6640	6720	5760	**6373**	**5184**	38.7	38.7	38.7	38.7	38.7	**39**	**37**
Pr	515	537	420.5	**491**	**452**	37.2	37.2	37.2	37.2	37.2	**37**	**37**
Nd	1850	1903	1435	**1729**	**1567**	35.9	35.9	35.89	35.9	35.9	**36**	**35**
Sm	279.1	288	209.5	**259**	**224**	38.1	38.1	38.1	38.1	38.1	**38**	**37**
Eu	19.34	20.14	17.29	**18.9**	**18.9**	35	35	35	35	35	**35**	
Gd	242.1	248.3	182	**224.1**	**189**	36.7	36.7	36.69	36.7	36.7	**37**	
Tb	31.5	32.5	23.3	**29.1**	**23**	36	36	36	36	36	**36**	**40**
Dy	194	201	143	**179**	**136**	36	36	36	36	36	**36**	
Ho	38.11	39.5	28.37	**35.3**	**26.6**	38	38	38	38	38	**38**	**39**
Er	104.7	107	77.9	**96.5**	**71.9**	38	38	38	38	38	**38**	
Tm	13.0	13.3	9.8	**12.1**	**9.0**	38	38	38	38	38	**38**	
Yb	68.5	69.9	52.7	**63.7**	**47.8**	39	39	39	39	39	**39**	
Lu	7.3	7.4	6.1	**6.9**	**5.4**	37	37	37	37	37	**37**	
Pb	1.2	1.3	1.1	**1.2**	**0.7**	39	39	39	39	39	**39**	
Th	406.0	414.0	369.1	**396.4**	**253.0**	38	38	38	38	38	**38**	
U	23.5	24.1	16.6	**21.4**	**13.1**	37	37	37	37	37	**37**	

Reference values from Chew et al. (2016) for Durango and Jochum et al. (2011) for NIST 612

Standard	NIST610_1	NIST610_2	NIST610_3	NIST610_4	**NIST 610 av.**	**NIST 610 ref.**
Na	100300	100500	100100	101200	**100525**	**97174**
Si	328700	318400	329000	320700	**324200**	
Ti	501	493	506	500	**500**	
V	455	454	459	460	**457**	**442**
Mn	442	431	442	427	**435**	**435**
Fe	465	471	481	500	**479**	
Rb	408	407	422	429	**417**	**431**
Sr	507	506	522	520	**514**	**497**
Y	451	449	463	455	**454**	**450**
Zr	434	441	451	445	**443**	**439**
La	435	430	442	432	**435**	**457**
Ce	463	452	463	456	**459**	**448**
Pr	453	438	450	438	**445**	**430**
Nd	446	433	443	432	**438**	**430**
Sm	466	453	464	453	**459**	**449**
Eu	437	433	447	432	**437**	**460**
Gd	436	427	437	429	**432**	**420**
Tb	409	413	426	413	**415**	**442**
Dy	427	429	446	430	**433**	**426**
Ho	434	431	450	437	**438**	**448**
Er	439	434	449	441	**441**	**426**
Tm	427	425	436	431	**430**	**420**
Yb	450	450	461	456	**454**	**460**
Lu	417	411	416	417	**415**	**435**
Pb	416	414	410	418	**414**	**413**
Th	427	421	426	417	**423**	**451**
U	425	441	446	448	**440**	**457**

Reference values from Gao et al. (2002) for NIST 610

Appendix 5: Apatite U-Pb data

Spot	Description - CL	$^{207}Pb/^{235}U$	2SE	$^{206}Pb/^{238}U$	2SE	Rho	$^{238}U/^{206}Pb$	2SE	$^{207}Pb/^{206}Pb$	2SE	Rho
Syenite											
BX 01 – 1	Homogeneous grey CL	7.17	0.41	0.2427	0.0059	0.89354	4.120313	0.1	0.21	0.0078	-0.72187
BX 01 - 2	Homogeneous grey CL	7.02	0.39	0.2411	0.0056	0.87159	4.147657	0.1	0.2045	0.0068	-0.4872
BX 01 - 3	Homogeneous grey CL	10.02	0.69	0.268	0.011	0.9342	3.731343	0.15	0.2651	0.0088	-0.68838
BX 01 - 4	Homogeneous grey CL	25.4	1.4	0.392	0.017	0.91003	2.55102	0.11	0.462	0.012	-0.38664
BX 01 - 5	Homogeneous grey CL	13.1	0.25	0.2988	0.0077	0.81459	3.34672	0.083	0.3142	0.0048	0.6705
BX 01 - 6	Homogeneous grey CL	48.64	0.81	0.568	0.011	0.76344	1.760563	0.027	0.6135	0.0085	0.49335
BX 01 - 7	Homogeneous grey CL	30.2	1.5	0.415	0.016	0.98624	2.409639	0.096	0.5207	0.0076	-0.64787
BX 01 - 8	Homogeneous grey CL	21.28	0.24	0.3511	0.0049	0.6384	2.848191	0.04	0.4344	0.0048	0.61704
BX 01 - 9	Homogeneous grey CL	5.98	0.64	0.223	0.011	0.66938	4.484305	0.21	0.192	0.011	0.98026
BX 01 - 10	Homogeneous grey CL	29	1.6	0.401	0.018	0.95534	2.493766	0.12	0.5176	0.0093	-0.3016
BX 01 - 11	Homogeneous grey CL	22.7	2.8	0.287	0.039	0.97509	3.484321	0.69	0.574	0.018	0.55124
BX 01 - 12	Homogeneous grey CL	40.6	3.7	0.496	0.031	0.98402	2.016129	0.15	0.584	0.018	-0.7254
BX 01 - 13	Homogeneous grey CL	27.4	2.2	0.401	0.019	0.98324	2.493766	0.12	0.485	0.017	-0.91686
BX 01 - 16	Homogeneous grey CL	26	19	0.2	0.06	0.68899	5	1.8	0.92	0.47	-0.20821
BX 01 - 17	Homogeneous grey CL	6.88	0.17	0.2259	0.0041	0.72133	4.426737	0.078	0.2208	0.0045	0.45569
BX 01 - 18	Homogeneous grey CL	5.2	1.4	0.154	0.043	0.99763	6.493506	5.2	0.2586	0.0082	0.87294
BX 01 - 19	Homogeneous grey CL	25.49	0.43	0.391	0.009	0.99039	2.557545	0.055	0.4774	0.0085	0.77113
BX 01 - 20	Homogeneous grey CL	17.69	0.89	0.315	0.01	0.96843	3.174603	0.1	0.411	0.01	-0.58016
BX 01 - 21	Homogeneous grey CL	8.98	0.16	0.2555	0.0039	0.89204	3.913894	0.06	0.2561	0.0047	0.47557
BX 01 - 22	Homogeneous grey CL	82.6	2.8	0.775	0.025	0.97433	1.290323	0.043	0.7767	0.007	-0.067732
BX 01 - 23	Homogeneous grey CL	15.2	2.1	0.295	0.017	0.95076	3.389831	0.2	0.351	0.018	-0.8307
BX 01 - 24	Homogeneous grey CL	29.3	1.9	0.409	0.02	0.98554	2.444988	0.1	0.5177	0.0099	-0.80396
BX 01 - 25	Homogeneous grey CL	110.9	5.5	1.032	0.043	0.97664	0.9689922	0.041	0.7789	0.0095	-0.29798
BX 01 - 26	Homogeneous grey CL	51.7	1.6	0.591	0.016	0.93698	1.692047	0.045	0.6338	0.0066	-0.10292
BX 01 - 27	Homogeneous grey CL	16.65	0.31	0.329	0.011	0.68992	3.039514	0.11	0.364	0.0099	0.82291
BX 01 - 28	Homogeneous grey CL	19.7	2.9	0.339	0.027	0.97714	2.949853	0.2	0.41	0.026	-0.89332
BX 01 - 29	Homogeneous grey CL	14	0.56	0.3023	0.0079	0.88911	3.307972	0.088	0.3377	0.0061	-0.14246
BX 01 - 30	Homogeneous grey CL	36.6	1.2	0.4721	0.0074	0.8298	2.118195	0.033	0.559	0.012	-0.45243
BX 01 - 31	Homogeneous grey CL	17.3	2.3	0.325	0.022	0.96045	3.076923	0.2	0.374	0.027	-0.83815
BX 01 - 32	Homogeneous grey CL	31.33	0.92	0.4279	0.0085	0.80917	2.336995	0.046	0.5268	0.009	-0.20406
BX 01 - 34	Homogeneous grey CL	36	1.1	0.453	0.013	0.986	2.207506	0.083	0.5716	0.0043	-0.096736
BX 01 - 35	Homogeneous grey CL	16.4	1.9	0.322	0.043	0.88084	3.10559	0.23	0.364	0.036	0.34596
Nepheline syenite											

SNT 06- 1	Homogeneous grey CL	8.47	0.3	0.2513	0.0073	0.95279	3.979308	0.12	0.247	0.0038	-0.10114
SNT 06 - 2	Homogeneous grey CL	11.49	0.55	0.285	0.01	0.661	3.508772	0.17	0.2944	0.0082	0.22001
SNT 06 - 3	Homogeneous grey CL	40.3	1.4	0.605	0.02	0.94281	1.652893	0.058	0.49	0.0055	0.14651
SNT 06 - 4	Homogeneous grey CL	24.9	2.8	0.481	0.045	0.98792	2.079002	0.22	0.377	0.01	-0.80535
SNT 06 - 5	Homogeneous grey CL	8.37	0.17	0.2507	0.0058	0.91715	3.988831	0.08	0.2463	0.0026	0.54976
SNT 06 - 6	Homogeneous grey CL	9.02	0.86	0.228	0.02	0.99098	4.385965	0.47	0.2921	0.0041	-0.33562
SNT 06 - 7	Homogeneous grey CL	26	1.7	0.717	0.046	0.76938	1.3947	0.086	0.269	0.014	0.41348
SNT 06 - 8	Homogeneous grey CL	22.3	4.7	0.53	0.12	0.97064	1.886792	1.2	0.319	0.023	0.76678
SNT 06 - 9	Homogeneous grey CL	62.2	5.1	1.95	0.26	0.99363	0.5128205	0.062	0.238	0.011	0.97658
SNT 06 - 10	Patchy CL	4400	1200	51	14	0.99833	0.01960784	0.0097	0.6515	0.0082	0.27824
SNT 06 - 11	Patchy CL	2340	140	25.4	1.6	0.98963	0.03937008	0.0023	0.685	0.0064	0.40468
SNT 06 - 12	Patchy CL	4680	460	57.3	6.8	0.97923	0.01745201	0.0021	0.614	0.015	0.6164
SNT 06 - 13	Homogeneous grey CL	11.94	0.38	0.2936	0.0093	0.95822	3.405995	0.12	0.303	0.0029	0.25117
SNT 06 - 14	Homogeneous grey CL	67	18	1.79	0.44	0.92197	0.5586592	0.23	0.266	0.016	-0.10803
SNT 06 - 15	Homogeneous grey CL	8.35	0.23	0.2487	0.0071	0.94583	4.020909	0.12	0.25	0.0018	0.24077
SNT 06 - 16	Homogeneous grey CL	8.46	0.29	0.2575	0.0079	0.93497	3.883495	0.13	0.2456	0.0034	0.13732
SNT 06 - 17	Patchy CL	4080	450	44.9	5	0.99693	0.02227171	0.0023	0.6776	0.0066	-0.15737
SNT 06 - 18	Patchy CL	4900	1200	55	13	0.99627	0.01818182	0.11	0.687	0.029	0.91144
SNT 06 - 19	Homogeneous grey CL	47.4	3.2	1.43	0.15	0.71235	0.6993007	0.081	0.251	0.021	0.53171
SNT 06 - 21	Homogeneous grey CL	12.85	0.72	0.28	0.016	0.94311	3.571429	0.35	0.3468	0.0058	0.024426
SNT 06 - 22	Homogeneous grey CL	26	17	0.98	0.44	0.89074	1.020408	0.84	0.184	0.057	-0.54668
SNT 06 - 23	Homogeneous grey CL	88	88	1.9	1.9	-1	0.5263158	0.52	0.34	0.34	1
SNT 06 - 26	Homogeneous grey CL	7.14	0.16	0.2373	0.0056	0.67516	4.214075	0.1	0.2241	0.0029	0.14846
SNT 06 - 27	Homogeneous grey CL	10.86	0.98	0.331	0.02	0.9479	3.021148	0.18	0.2386	0.006	-0.67459
SNT 07 - 1	Homogeneous grey CL	11.44	0.94	0.279	0.014	0.94082	3.584229	0.25	0.324	0.01	-0.41954
SNT 07 - 2	Homogeneous grey CL	15	0.78	0.308	0.011	0.90054	3.246753	0.13	0.379	0.012	-0.24686
SNT 07 - 3	Homogeneous grey CL	43.7	6	0.552	0.06	0.97627	1.811594	0.29	0.607	0.026	-0.60564
SNT 07 - 4	Homogeneous grey CL	32.57	0.79	0.478	0.0093	0.68443	2.09205	0.041	0.533	0.01	0.061126
SNT 07 - 5	Homogeneous grey CL	21.56	0.36	0.3787	0.0087	0.6936	2.640613	0.061	0.4463	0.0086	0.693
SNT 07 - 6	Homogeneous grey CL	16.47	0.99	0.333	0.022	0.99437	3.003003	0.18	0.3952	0.0097	0.47849
SNT 07 - 8	Homogeneous grey CL	19.9	2.8	0.408	0.044	0.91483	2.45098	0.28	0.38	0.023	-0.053512
SNT 07 - 9	Homogeneous grey CL	11.9	2.2	0.244	0.036	0.84447	4.098361	0.9	0.357	0.03	-0.12334
SNT 07 - 10	Homogeneous grey CL	11.55	0.37	0.2784	0.0078	0.87778	3.591954	0.1	0.3264	0.0065	0.19973
SNT 07 - 11	Homogeneous grey CL	12	1.2	0.283	0.02	0.92827	3.533569	0.29	0.33	0.014	-0.56578
SNT 07 - 12	Homogeneous grey CL	15.1	1.1	0.306	0.021	0.91807	3.267974	0.33	0.387	0.012	-0.0003023
SNT 07 - 13	Homogeneous grey CL	13.85	0.69	0.2982	0.0099	0.90946	3.353454	0.12	0.3696	0.0079	-0.0065497
SNT 07 - 14	Homogeneous grey CL	15.9	2	0.355	0.031	0.94133	2.816901	0.24	0.347	0.015	-0.62838

SNT 07 - 15	Homogeneous grey CL	24.6	5.6	0.65	0.31	0.94589	1.538462	0.34	0.358	0.01	-0.16764
SNT 07 - 16	Homogeneous grey CL	25.6	1.9	0.385	0.022	0.96703	2.597403	0.17	0.517	0.013	-0.57312
SNT 07 - 17	Homogeneous grey CL	29.7	2.5	0.443	0.029	0.96882	2.257336	0.16	0.521	0.014	-0.65963
SNT 07 - 18	Homogeneous grey CL	38.7	8.4	0.497	0.069	0.98989	2.012072	0.33	0.563	0.057	-0.90891
SNT 07 - 19	Homogeneous grey CL	1130	660	12.6	7.6	0.99439	0.07936508	0.12	0.712	0.034	0.030571
SNT 07 - 20	Homogeneous grey CL	13.62	0.55	0.3085	0.0099	0.94715	3.241491	0.11	0.3426	0.0049	-0.53805
SNT 07 - 21	Homogeneous grey CL	11.74	0.3	0.2743	0.0075	0.92204	3.645643	0.089	0.3293	0.0038	-0.48533
SNT 07 - 22	Homogeneous grey CL	17.46	0.8	0.332	0.013	0.89326	3.012048	0.11	0.4072	0.0084	-0.21331
SNT 07 - 23	Homogeneous grey CL	64	25	1.02	0.46	0.99427	0.9803922	0.63	0.52	0.044	0.52337
SNT 07 - 24	Homogeneous grey CL	134.9	6.4	1.338	0.057	0.95329	0.7473842	0.031	0.773	0.011	-0.059228
SNT 07 - 25	Homogeneous grey CL	49.7	5.1	0.612	0.044	0.95087	1.633987	0.11	0.634	0.023	-0.49885
SNT 07 - 26	Homogeneous grey CL	29.6	1.8	0.526	0.025	0.85455	1.901141	0.094	0.436	0.015	-0.37729
SNT 07 - 27	Homogeneous grey CL	6.44	0.77	0.21	0.021	0.92029	4.761905	0.51	0.2351	0.0089	-0.096952
SNT 09 - 1	Homogeneous grey CL	23	2.2	0.361	0.013	0.96539	2.770083	0.094	0.453	0.025	-0.88454
SNT 09 - 2	Homogeneous grey CL	61.5	8.9	0.657	0.066	0.9965	1.52207	0.16	0.654	0.031	-0.95777
SNT 09 - 3	Homogeneous grey CL	108.3	2.5	1.025	0.027	0.95113	0.9756098	0.027	0.7581	0.0071	0.51954
SNT 09 - 5	Homogeneous grey CL	50.5	5.6	0.57	0.05	0.99461	1.754386	0.18	0.63	0.016	-0.8441
SNT 09 - 8	Homogeneous grey CL	63	11	0.674	0.084	0.99556	1.48368	0.2	0.653	0.035	-0.95213
SNT 09 - 9	Homogeneous grey CL	5.225	0.069	0.2179	0.0043	0.87701	4.589261	0.096	0.1733	0.002	0.80332
SNT 09 - 10	Homogeneous grey CL	7.65	0.25	0.2424	0.0049	0.95255	4.125413	0.084	0.2279	0.004	-0.49882
SNT 09 - 11	Homogeneous grey CL	1965	89	15.43	0.74	0.97314	0.06480881	0.0033	0.922	0.012	0.14061
SNT 09 - 12	Homogeneous grey CL	162.4	8.2	1.446	0.06	0.95609	0.6915629	0.031	0.811	0.013	-0.44787
SNT 09 - 15	Homogeneous grey CL	1320	390	10.6	3.1	0.99937	0.09433962	0.09	0.896	0.014	-0.42492
SNT 09 - 17	Homogeneous grey CL	18.7	2.4	0.333	0.026	0.93709	3.003003	0.26	0.402	0.026	-0.70977
SNT 09 - 18	Homogeneous grey CL	190	24	1.63	0.2	0.99635	0.6134969	0.1	0.8523	0.0085	-0.28317

Standard	$^{207}Pb/^{235}U$	2SE	$^{206}Pb/^{238}U$	2SE	Rho	$^{238}U/^{206}Pb$	2SE	$^{207}Pb/^{206}Pb$	2SE	Rho
MAD - 1	0.596	0.023	0.0777	0.0017	0.45603	12.87	0.27	0.0572	0.002	0.11222
MAD - 2	0.608	0.021	0.0786	0.0012	0.51457	12.7227	0.19	0.0573	0.0017	-0.0782
MAD - 3	0.6	0.014	0.07476	0.00099	0.067355	13.3761	0.18	0.0574	0.0014	0.42832
MAD - 4	0.604	0.02	0.0759	0.001	0.094452	13.1752	0.18	0.0574	0.0019	0.31967
MAD - 5	0.601	0.011	0.07563	0.0009	0.11959	13.2223	0.16	0.0566	0.0012	0.29301
MAD - 6	0.6	0.017	0.0747	0.0013	0.029178	13.3869	0.23	0.0573	0.0018	0.51209
MAD - 7	0.603	0.016	0.07653	0.00071	-0.35824	13.0668	0.12	0.0574	0.0019	0.67203

MAD - 8	0.601	0.012	0.07493	0.00068	0.30591	13.3458	0.12	0.0574	0.0011	0.15586
MAD - 10	0.601	0.018	0.0796	0.0012	0.68361	12.5628	0.19	0.0574	0.0013	-0.182
MAD - 12	0.603	0.015	0.08061	0.00089	0.5127	12.4054	0.14	0.0576	0.0014	0.00726
MAD - 13	0.6	0.013	0.0743	0.001	0.37369	13.459	0.18	0.0575	0.0013	0.27522
MAD - 14	0.601	0.013	0.0754	0.0011	0.12917	13.2626	0.19	0.0561	0.0014	0.09377
MAD - 15	0.602	0.013	0.0756	0.0012	-0.27464	13.2275	0.21	0.0569	0.0015	0.67685
MAD - 16	0.602	0.033	0.0764	0.0012	0.15705	13.089	0.21	0.0575	0.0032	0.11675
MAD - 17	0.596	0.039	0.07401	0.00098	0.079306	13.5117	0.18	0.0581	0.0039	0.1019
MAD - 19	0.603	0.022	0.078	0.0011	0.45726	12.8205	0.17	0.057	0.0015	0.06316
MAD - 20	0.601	0.015	0.0757	0.001	0.010289	13.21	0.18	0.0578	0.0017	0.46702
DURANGO - 1	0.294	0.037	0.00713	0.00029	0.017608	140.253	5.8	0.294	0.035	0.33463
DURANGO - 2	0.07	0.025	0.00484	0.00029	-0.3886	206.612	13	0.107	0.041	0.50137
DURANGO - 3	0.106	0.01	0.00551	0.0002	0.28822	181.488	6.8	0.137	0.012	0.45822
DURANGO - 4	0.218	0.011	0.00673	0.0002	0.82052	148.588	4.3	0.238	0.013	-0.1278
DURANGO - 5	0.215	0.011	0.0066	0.00015	0.80381	151.515	4	0.234	0.011	-0.2668
DURANGO - 6	0.257	0.015	0.00709	0.00023	0.37645	141.044	4.9	0.272	0.016	0.2898
DURANGO - 7	0.251	0.02	0.00713	0.00025	0.94338	140.253	4.7	0.275	0.017	-0.639
DURANGO - 8	0.281	0.033	0.00725	0.00029	-0.04115	137.931	5.6	0.288	0.024	0.10574
DURANGO - 9	0.157	0.028	0.00596	0.00032	0.53351	167.785	8.6	0.183	0.027	-0.0689
DURANGO - 10	0.266	0.014	0.00718	0.00027	0.99998	139.276	5.8	0.266	0.014	-0.5219
DURANGO - 11	0.297	0.066	0.00716	0.00041	0.38991	139.665	7.4	0.28	0.02	0.23941
DURANGO - 12	0.373	0.069	0.00822	0.00077	0.9798	121.655	9.3	0.339	0.038	-0.8642
DURANGO - 13	0.227	0.017	0.00677	0.00032	0.52659	147.711	7.1	0.251	0.018	0.13581
DURANGO - 14	0.234	0.013	0.00675	0.00016	0.10489	148.148	3.4	0.251	0.014	0.32261

Appendix 6: Rb and Sr isotope data by LA-MC-ICPMS

	Description - CL	$^{143}Nd/^{144}Nd$	2SE	$^{147}Sm/^{144}Nd$	2SE	$\varepsilon_{Nd(t)}$	2SE	$^{87}Rb/^{86}Sr$	$^{87}Sr/^{86}Sr$	SE	$^{87}Sr/^{86}S_{(i)}$
Syenite											
BX 01-1	Homogeneous grey CL	0.511885	0.000009	0.086877	0.000007	2.51	0.18	0.008922	0.704926	0.000021	0.7048
BX 01-3	Homogeneous grey CL	0.512050	0.000020	0.102921	0.000029	3.22	0.40	0.000630	0.703855	0.000023	0.7038
BX 01-24	Homogeneous grey CL	0.511892	0.000017	0.084953	0.000026	2.94	0.33	0.000011	0.703549	0.000023	0.7035
BX 01-16	Homogeneous grey CL	0.511887	0.000015	0.085438	0.000030	2.77	0.28	0.000055	0.703497	0.000034	0.7035
Nepheline syenite											
SNT 03-1	Light grey CL core	0.512096	0.000024	0.103763	0.000026	3.86	0.48	0.000015	0.703115	0.000015	0.7031
SNT 03-2	Dark grey CL - rim	0.512113	0.000024	0.103198	0.000041	4.27	0.48	0.000001	0.703135	0.000015	0.7031
SNT 03-13	Light grey CL core							0.000007	0.703141	0.000016	0.7031
SNT 03-14	Dark grey CL - rim							0.000009	0.703121	0.000015	0.7031
SNT 04-1	Homogeneous grey CL	0.512127	0.000026	0.104410	0.000040	4.35	0.52	0.000021	0.703163	0.000008	0.7032
SNT 04-3	Homogeneous grey CL	0.512128	0.000025	0.109819	0.000040	3.54	0.50	0.000003	0.703132	0.000014	0.7031
SNT 05-2	Homogeneous grey CL	0.512070	0.000026	0.107045	0.000041	2.84	0.51	0.000022	0.703106	0.000019	0.7031
SNT 03-8	Homogeneous grey CL	0.512098	0.000029	0.107541	0.00011	3.30	0.58				
SNT 06-1	Homogeneous grey CL	0.512029	0.000028	0.103225	0.000039	2.63	0.54	0.000035	0.703468	0.000011	0.7035
SNT 06-2	Homogeneous grey CL	0.512036	0.000023	0.100485	0.000036	3.19	0.46	0.000025	0.703262	0.000014	0.7033
SNT 06-10	Patchy CL							0.000007	0.703270	0.000011	0.7033
SNT 06-11	Patchy CL							0.000000	0.703261	0.000011	0.7033
SNT 06-13	Homogeneous grey CL							0.000024	0.703666	0.000011	0.7037
SNT 07-18	Homogeneous grey CL	0.512088	0.000024	0.103165	0.000028	3.79	0.47	0.000003	0.703181	0.000008	0.7032
SNT 07-20	Homogeneous grey CL	0.511980	0.000028	0.104339	0.000040	1.49	0.54				
SNT 07-1	Homogeneous grey CL	0.512004	0.000029	0.100883	0.000088	2.50	0.56				
SNT 09-2	Homogeneous grey CL	0.512078	0.000021	0.103398	0.000035	3.56	0.41	0.000061	0.703208	0.000009	0.7032
SNT 09-3	Homogeneous grey CL	0.512145	0.000025	0.109056	0.000044	3.99	0.48	0.000027	0.703281	0.000009	0.7033
SNT 09-10	Homogeneous grey CL	0.512000	0.000024	0.087910	0.000029	4.43	0.47				
Carbonatite											
EC 4-2	Homogeneous grey CL	0.511974	0.000041	0.1021	0.0001	1.62	0.8				
EC 4-3	Homogeneous grey CL	0.512016	0.000051	0.1066	0.0004	1.75	1				
EC 4-4	Homogeneous grey CL	0.511997	0.000041	0.1019	0.0004	2.1	0.8	0.000349	0.703140	0.000013	0.7031
EC 5-1	Homogeneous grey CL	0.511973	0.000055	0.1063	0.0002	0.95	1.08				

EC 5-2	Homogeneous grey CL	0.51192	0.000046	0.1044	0.0004	0.21	0.9				
EC 5-3	Homogeneous grey CL	0.511922	0.000041	0.1034	0.0002	0.4	0.8				
EC 5-4	Homogeneous grey CL	0.511899	0.000047	0.1033	0.0001	-0.04	0.92				
EC 5-6	Homogeneous grey CL	0.511941	0.000046	0.1028	0.0002	0.86	0.9				
EC 21-3	Homogeneous grey CL	0.511949	0.000034	0.0975	0.0003	1.83	0.67				
EC 21-4	Homogeneous grey CL	0.512088	0.000034	0.1169	0.001	1.57	0.67				
EC 21-5	Homogeneous grey CL	0.511958	0.000023	0.0995	0.0007	1.7	0.45				
EC 21-6	Homogeneous grey CL	0.511976	0.000036	0.1025	0.0001	1.59	0.7				
EC 23-10	Homogeneous grey CL	0.511975	0.000035	0.1012	0.0009	1.77	0.68	0.000003	0.703230	0.000014	0.7032
EC 23-13	Homogeneous grey CL	0.512032	0.000038	0.1084	0.0012	1.78	0.74	0.000015	0.703283	0.000023	0.7033
EC 23-5	Homogeneous grey CL	0.511997	0.000039	0.095	0.0019	3.16	0.76				
EC 23-16	Homogeneous grey CL	0.512004	0.000028	0.1001	0.0002	2.51	0.55				
EC 23-17	Homogeneous grey CL	0.512131	0.000034	0.128	0.0005	0.7	0.67				
EC 23-19	Homogeneous grey CL	0.511975	0.000034	0.0992	0.0003	2.08	0.67				
EC 29-1	Light grey CL core	0.511942	0.00003	0.0966	0.0001	1.84	0.59	0.000143	0.703255	0.000008	0.7033
EC 29-2	Dark grey CL - rim	0.511962	0.000033	0.0987	0.0003	1.9	0.65	0.000033	0.703186	0.000009	0.7032
EC 29-3	Light grey CL core	0.511969	0.00003	0.0976	0.0001	2.21	0.59				
EC 29-4	Dark grey CL - rim	0.511991	0.000037	0.0993	0.0002	2.38	0.72				
EC 29-5	Light grey CL core	0.511942	0.000023	0.0981	0.0002	1.61	0.45				

Standard	^{146}Nd (V)	^{147}Sm (V)		^{143}Nd/^{144}Nd	2SE
Glass Standard					
NIST610_1	0.5	0.44		0.511933	0.000038
NIST610_2	0.49	0.42		0.511909	0.000054
NIST610_3	0.48	0.42		0.511906	0.000042
NIST610_6	0.48	0.42		0.51192	0.00005
NIST610_7	0.48	0.42		0.511944	0.000055
NIST610_8	0.5	0.44		0.511941	0.000042
			av	**0.511925**	
			2SD	**0.000033**	
Apatite Reference Material		**Ref.**	**0.511927 ± 0.000004** (Woodhead & Hergt 2007, TIMS)		
Durango_1	1.41	0.16		0.512489	0.000032

Durango_2	1.43	0.16		0.512507	0.000028
Durango_3	1.4	0.15		0.512493	0.000031
Durango_4	1.37	0.15		0.512477	0.000022
Durango_5	1.32	0.14		0.512499	0.000025
Durango_6	1.34	0.15		0.512513	0.000032
Durango_7	1.29	0.14		0.512475	0.000028
Durango_8	1.28	0.14		0.512468	0.000028
Durango_9	1.35	0.15		0.512522	0.000036
Durango_10	1.29	0.14		0.512498	0.000025
Durango_11	0.68	0.08		0.512493	0.000047
Durango_12	0.73	0.08		0.512467	0.000032
Durango_13	0.79	0.09		0.512475	0.000041
			av	**0.51249**	
			2SD	**0.000035**	
	Ref. 0.512483 ± 0.000026		(Foster & Vance 2006, MC-ICP-MS)		

Standard	$^{143}Nd/^{144}Nd$	2SE	$^{147}Sm/^{144}Nd$	2SE	$\varepsilon_{Nd(t)}$	2SE
PhAp1-1	0.511233	0.000014	0.112513	0.000016	-5.2	0.3
PhAp1-2	0.511206	0.000015	0.112077	0.000023	-5.6	0.3
PhAp1-3	0.511208	0.000016	0.112221	0.000022	-5.6	0.3
PhAp-average (2SD)	**0.511216**	**0.00003**	**0.11227**	**0.00044**		
PhAp-refererence	**0.511256**	**0.000028**	**0.11740**	**0.00001**		
Durango-1	0.512676	0.000018	0.092289	0.000029	1.2	0.4
Durango-2	0.512634	0.000020	0.087042	0.000021	0.4	0.4
Durango-3	0.512635	0.000017	0.092582	0.000020	0.4	0.3
Durango-6	0.512647	0.000024	0.089547	0.000027	0.6	0.5
Durango-4	0.512675	0.000023	0.091220	0.000024	1.2	0.5
Durango-5	0.512604	0.000017	0.092890	0.000022	-0.2	0.3
Durango-average (2SD)	**0.512645**	**0.000055**	**0.090928**	**0.004519**		
Durango-reference	**0.511256**	**0.000028**	**0.1174**	**0.0001**		

Reference values from Doucelance et al. (2020) for Durango apatite

Standard	$^{87}Rb/^{86}Sr$	$^{87}Sr/^{86}Sr$	SE
Phal-1	0.00011	0.70730	0.00015
Phal-2	0.00008	0.70736	0.00015
Phal-3	0.00009	0.70743	0.00014
Phal-average (1SD)	**0.00009**	**0.70736**	**0.00006**
Phal-reference	**0.00002**	**0.70720**	
Slyud-1	**0.00000**	**0.70781**	**0.00004**
Slyud-reference	**0.00010**	**0.70769**	
McClure-1	**0.00000**	**0.70372**	**0.00003**
McClure-reference	**0.00000**	**0.70371**	
BHVO2G-1	0.06780	0.70349	0.00033
BHVO2G-2	0.06826	0.70330	0.00037
BHV02G-average (1SD)	**0.06803**	**0.70339**	**0.00013**
BHV02G-reference	**0.02300**	**0.70347**	
MAD-1	0.00001	0.71195	0.00004
MAD-2	0.00001	0.71199	0.00004
MAD-3	0.00000	0.71195	0.00004
MAD-4	0.00001	0.71197	0.00006
MAD-5	0.00001	0.71199	0.00006
MAD-6	0.00001	0.71207	0.00005
MAD-average (1SD)	**0.00001**	**0.71199**	**0.00005**
MAD-reference	**0.00010**	**0.71180**	
Durango-1	0.00002	0.70694	0.00016
Durango-2	0.00010	0.70687	0.00014
Durango-3	0.00002	0.70727	0.00018
Durango-4	0.00010	0.70686	0.00017
Durango-5	0.00003	0.70713	0.00015
Durango-4	0.00005	0.70743	0.00016
Durango-average (1SD)	**0.00005**	**0.70708**	**0.00023**
Durango-reference	**0.00090**	**0.70634**	

Reference values from Yang et al. (2014) for Durango, MAD, Slyud and McClure, whereas BHV02G and Phal are from Elburg et al. (2005) and Decrée et al. (2020), respectively.

Appendix 7a: CL images of syenite zircon

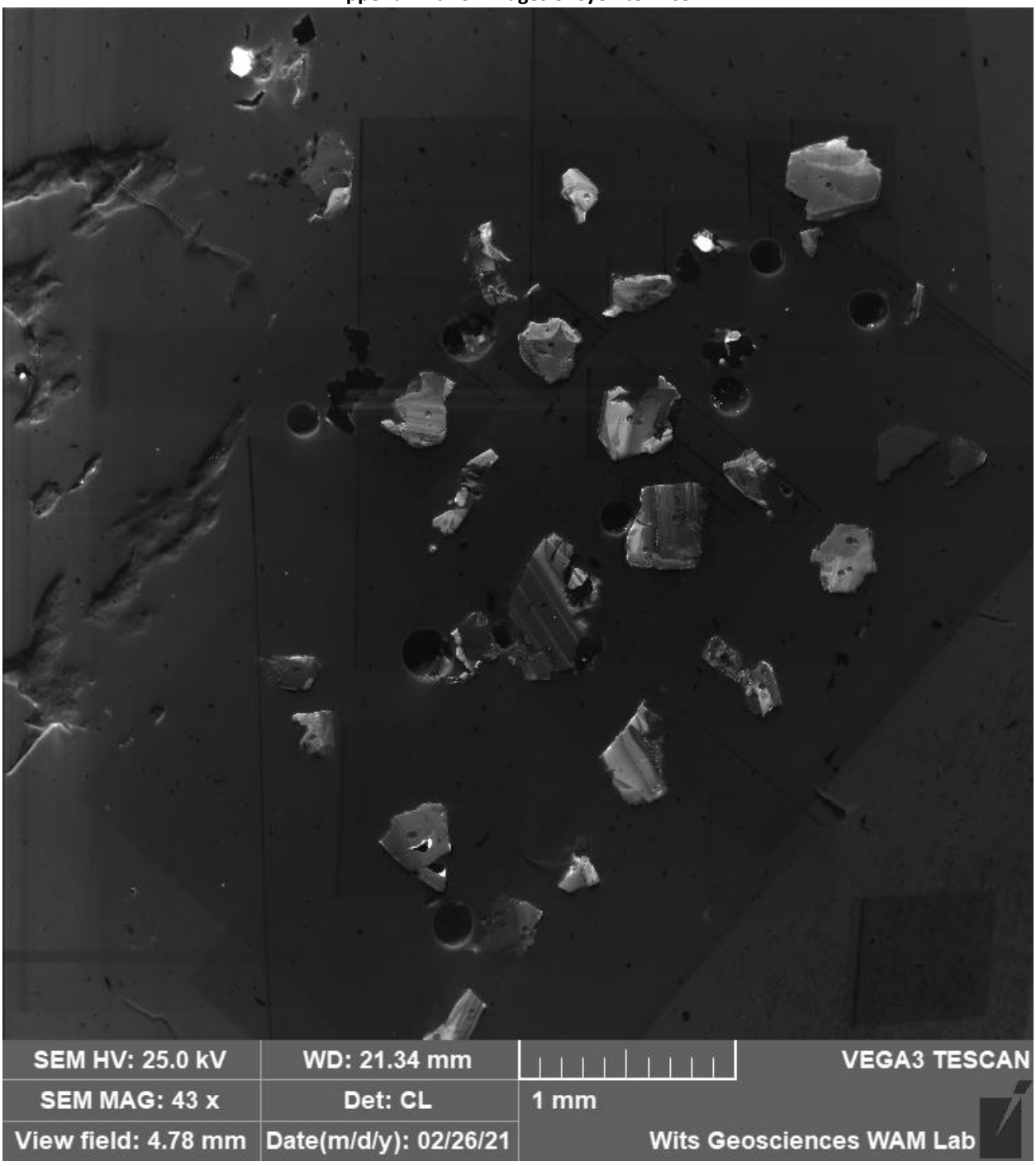

Appendix 7b: CL images of nepheline syenite zircon

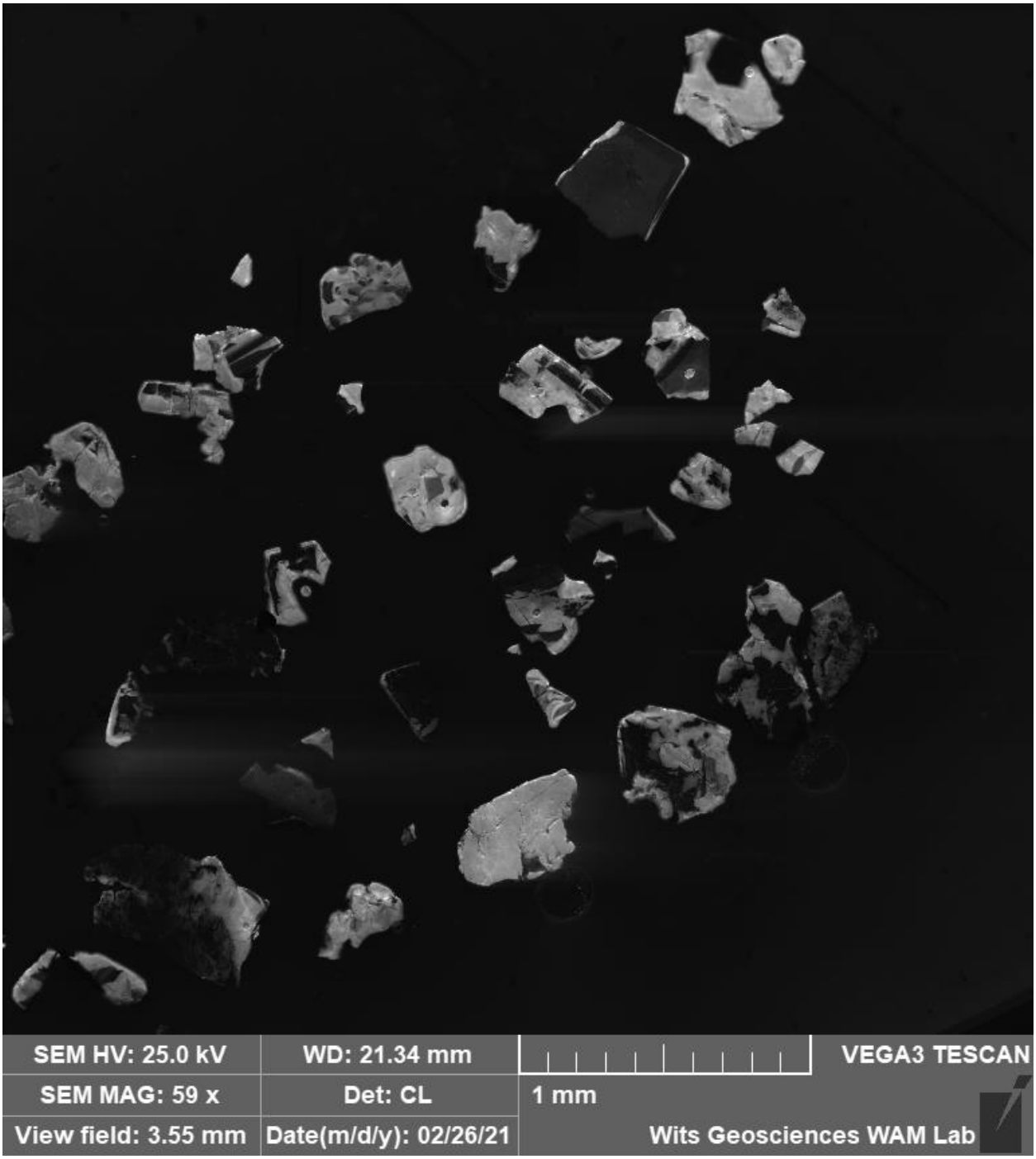

Appendix 7c: CL images of carbonatite zircon

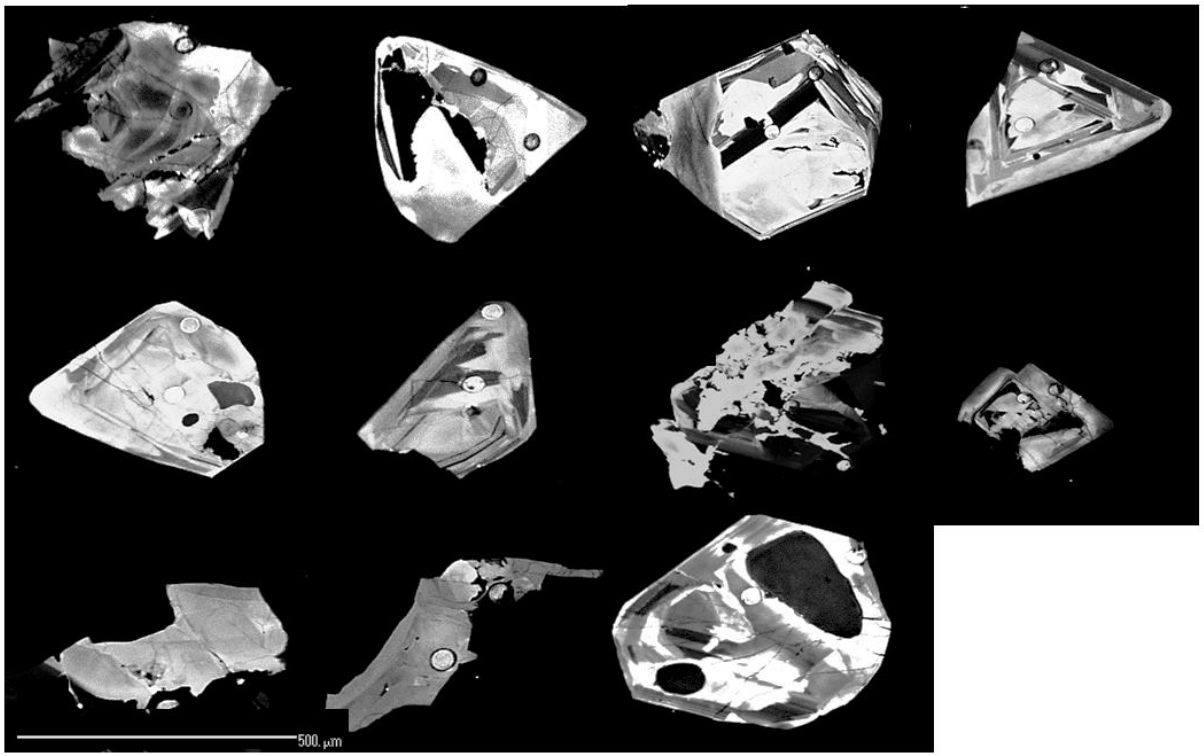

Appendix 8: Zircon trace element data

	Syenite zircon								
	BX 01 - 1	BX 01 - 2	BX 01 - 5	BX 01 - 8	BX 01 - 11	BX 01 - 13	BX 01 - 14	BX 01 - 15	BX 01 - 16
P	36.9	35.03	36.2	45.5	Below LOD	52.4	41.6	53.5	33.8
Ti	5.73	6.4	6.89	7.6	4.8	6.2	10.2	9.69	5.1
Sr	Below LOD	Below LOD	Below LOD	9.5	Below LOD	1.01	Below LOD	Below LOD	Below LOD
Y	252	160	974	1399	370	2120	1141	2490	193
Nb	1.87	2.14	2.97	4.19	1.45	7.89	4.04	8.99	1.43
La	Below LOD	0.1	0.22	2.48	Below LOD	0.45	0.64	0.72	Below LOD
Ce	3.63	3.85	7.18	9.43	6.47	12.44	14	13.1	3.91
Pr	0.03	0.1	0.35	1	0.05	0.83	1.33	0.99	0.01
Nd	0.5	0.87	4.64	8.46	0.78	11.17	12	12.55	0.22
Sm	0.84	0.76	5.93	10	1.33	15.9	10.4	19.3	0.41
Eu	0.12	0.23	0.89	1.64	0.29	2.38	2.26	3.52	0.11
Gd	3.84	2.75	24	39.2	6.67	60.3	34.1	76.4	2.35
Tb	1.44	0.93	7.36	11.96	2.42	18.1	10.26	23.1	0.96
Dy	19.8	12.99	90.1	143	32.7	211	117.4	268.5	14
Ho	8.1	5.18	32.4	51.2	12.4	72.3	39.6	90.8	5.95
Er	41.9	27.4	158.4	246	65	349	186	422	34.2
Tm	10	6.51	34	50.9	14.06	71.3	36.8	83.4	8.06
Yb	95	63.1	296	440	124.6	622	316	695	74.2
Lu	19.7	13.05	57.2	85.7	23.6	122	61	133.7	14.4
Hf	7160	7710	6780	6060	5130	5940	5960	5570	7020
Th	38.5	27.6	179	209.6	88.9	434	141	438	39.6
U	104	76.2	256	255	134.9	389	273	361	104.2
TREE	204.9	137.8	718.7	1101	290.4	1569.2	842	1843.1	158.8
T (°C)	694.28	703.21	709.25	717.41	680.32	700.63	742.72	738.21	685.05
Yb_N/Sm_N	105.52	77.06	46.57	41.05	87.74	36.5	28.35	33.6	170.1
Eu/Eu*	0.18	0.43	0.2	0.22	0.25	0.21	0.33	0.24	0.27

Ce/Ce*		8.29	4.97	1.44		3.73	2.67	3.11		
Th/U	0.37	0.36	0.7	0.82	0.66	1.12	0.52	1.21	0.38	
Sm_N/La_N		12.65	42.85	6.41		56.17	25.87	42.61		

	Nepheline syenite, type 1 zircon												
	SNT 04 - 1	SNT 04 - 2	SNT 04 - 4	SNT 04 - 8	SNT 04 - 9	SNT 04 - 14	SNT 04 - 16	SNT 05 - 2	SNT 06 - 11	SNT 07 - 1	SNT 07 - 3	SNT 07 - 7	SNT 09 - 1
P	27.7	Below LOD	Below LOD	32.1	32.7	37.1	28.1	Below LOD	30.9	33	34.6	26.4	35.4
Ti	3.04	10.3	2.8	15	9	12	12	12.3	1.56	2.75	9.5	14	11.4
Sr	Below LOD	62	23	5.2	30.3	28.6	4	212	Below LOD	14	12.3	13.1	4.1
Y	1696	919	1450	1667	1478	880	1190	751	899	1255	720	793	513
Nb	33.9	59	36.5	40	40	11.49	24	18.6	7.33	28	50	7.07	8.84
La	0.2	0.77	2.2	2.9	2.47	1.3	0.52	13.1	0.08	0.58	3.21	0.43	1.8
Ce	26	10.8	22.3	29.7	25	14.7	23.1	28	4.59	12.4	16.4	6.45	7.9
Pr	0.87	0.75	0.77	2.23	1.75	0.49	0.56	2.4	0.19	0.72	1.54	0.29	0.29
Nd	12.9	7.6	8.4	20.7	16.74	4.56	8.3	11.8	3.25	8.4	10.5	3.46	2.23
Sm	19.7	7.4	13.6	23	19.6	7.3	12.8	6.3	7.28	12.2	8.1	5.36	2.89
Eu	12.87	4.3	9.2	14.3	11.6	5.55	8.5	3.93	5.7	8.7	5	3.94	2.19
Gd	79.1	24.9	59.6	82.6	66.2	36.5	54	24.5	36.6	52.7	28.1	25.5	13.5
Tb	20	7.1	16.1	22.47	18.2	11	14	7.52	11.44	14.3	7.3	7.4	4.36
Dy	211	87	178	236.8	196	120	149	88.1	123.8	160	81	88	54.1
Ho	61.2	31	54.4	69.7	57.8	37.1	45.1	29.4	35.9	49.2	25.3	28.7	19.4
Er	233	136	210	254.9	215	139	172	125.7	136.8	199	108	122	93.4
Tm	39.4	27.1	36.6	46	39.6	25.9	30.6	23	24.8	35	19.9	22.4	19.6
Yb	290	221	276	343	296	192	225	184	193.2	267	160	174	172
Lu	50.4	42.8	48.5	58	50.6	34	38.9	34.2	33.62	46.8	29.5	31.3	34.5
Hf	5480	9860	5130	3530	3520	5930	3370	7430	7160	7110	9330	3640	4540
Th	1288	258	897	682	576	244	1440	385	114.7	523	310	87.8	350
U	438	67	277	334.5	293	110	448	194	209	224	166	85.5	288
TREE	1056.63	608.52	935.67	1206.3	1016.56	629.4	782.38	581.95	617.25	867	503.85	519.23	428.16

T (°C)	646	743	640.2	777	731	757	757	759	600	638	736	771	752
Yb_N/Sm_N	13.73	27.86	18.93	13.91	14.09	24.54	16.4	27.25	24.76	20.42	18.43	30.29	55.53
Eu/Eu*	0.86	0.87	0.83	0.89	0.89	0.85	0.84	0.84	0.87	0.89	0.91	0.85	0.89
Ce/Ce*	8.32	3.1	4.12	2.66	2.77	4.43	9.12	1.12	6.24	3.95	1.77	4.22	2.39
Th/U	2.94	3.85	3.24	2.04	1.97	2.22	3.21	1.98	0.55	2.33	1.87	1.03	1.22
Sm_N/La_N	157.38	15.28	9.83	12.61	12.61	8.93	39.13	0.76	146.5	33.44	4.01	20	2.55

	Nepheline syenite, type 2 zircon					Carbonatite zircon						
	SNT 06 - 3	SNT 06 - 5	SNT 07 - 2	SNT 07 - 4	SNT 07 - 13	EC 21-1	EC 21-2	EC 21-3	EC 21-4	EC 21-5	EC 21-7	EC 21-8
P	73	37.8	34.5	29	Below LOD							
Ti	140.3	89.3	86	63	127							
Sr	80.1	35.4	70	63	250							
Y	566	273.2	409	453	406	600	460	360	316	387	603	820
Nb	239	97	339	287	339							
La	86.2	44.4	18.2	23.1	16.9	1.3	0.72	1	0.13	0.27	1.33	1.9
Ce	379	173	48	63	42.4	9	2.22	5.6	1.44	1.18	9.1	20
Pr	53.7	24.7	3.87	7.8	4.13	1.1	0.13	0.38	0.15	0.06	0.59	1.7
Nd	260	120	23.7	39.9	21.7	9.6	1.35	2.7	2.26	0.97	4.7	15
Sm	57.9	22.4	14.8	13.2	10.6	7.6	3.4	2.9	3.6	2.23	5.26	13.8
Eu	15.9	5.88	7.2	5.4	5.17	4.6	2.75	2.05	2.12	1.8	3.57	9
Gd	48.3	21.1	32.1	24.1	24.5	34	19.7	15.8	16.8	15.31	29.7	66
Tb	8.62	3.85	6.4	5.07	5.39	6.9	4.8	3.6	3.9	3.83	6.49	13.3
Dy	77.6	36.6	59	52.3	52.6	76	55	42	42	46.4	74.2	136
Ho	23.1	11.36	16.4	15.8	15.2	23.9	18.2	13.1	12.5	15.25	23.3	40
Er	97	46.5	65	65.4	60.1	98	76	54	49	64.4	96.7	153
Tm	18.6	8.96	11.5	11.63	11	19.2	14.7	10.6	9.4	13.17	18.65	28
Yb	148	70.2	90	95.9	84.2	152	121	87	74	110.1	149.8	210
Lu	27.2	11.53	16.7	18	15.1	28.4	22.3	15.6	13.3	19.96	27.3	37

Hf	5010	5630	4130	7470	4140	Below LOD	0.21	6	7.1	3.5	280	270
Th	393	170	610	283	480	396	120	86	94	66.9	437	440
U	700	289	207	187	228	62	23.5	14.2	22.6	84.6	3.81	42
TREE	1301	600	413	441	369	472	342	256	231	295	451	745
T (°C)	1042	978	973	933	1027							
Yb_N/Sm_N	2.38	2.92	5.67	6.78	7.41	18.66	33.2	27.99	19.18	46.06	26.57	14.2
Eu/Eu*	0.9	0.81	0.98	0.91	0.94	0.74	0.8	0.74	0.69	0.69	0.69	0.75
Ce/Ce*	1.31	1.24	1.31	1.13	1.19	1.69	1.63	2.18	2.18	2.14	2.47	2.47
Th/U	0.56	0.59	2.95	1.51	2.11	6.39	5.11	6.06	4.16	0.79	114.7	10.48
Sm_N/La_N	3.55	0.8	1.29	0.91	1	9.29	7.51	4.61	44.02	13.13	6.29	11.55

Standard	G_NIST612_1	G_NIST612_2	G_NIST612_3	G_NIST612_4	G_NIST612_5	G_NIST612_6	G_NIST612_7	**NIST 612 av.**	std	**NIST 612 ref.**
P	Below LOD	40.3	50.8	50.4	55.2	44.3	58.3	**49.9**	6.68	
Ti	43.1	44.3	41.9	43.9	46.3	42.8	45.7	**44**	1.58	
Sr	76.2	78.8	77	78	78.1	80.9	78.6	**78.2**	1.49	**78.5**
Y	38.9	37.78	39.2	37.5	37.9	38.3	37.8	**38.2**	0.63	**40.1**
Nb	40.2	39.9	40.1	39.9	40	40.3	39.7	**40**	0.20	**41.5**
La	35.9	35.5	35.8	36.1	35.6	35.8	36.1	**35.8**	0.23	**34.7**
Ce	40.8	40.1	38.45	38.8	38.2	40.3	40.2	**39.6**	1.04	**37.3**
Pr	36.7	37.9	37.2	37.2	37	37.6	37	**37.2**	0.40	**37.3**
Nd	35.7	36.1	36	35.9	35.6	36.2	36.2	**36**	0.24	
Sm	37.8	38.3	38.1	38.1	38.09	38.1	38.2	**38.1**	0.15	
Eu	37.7	33.8	38.5	34.23	34.7	35	36.5	**35.8**	1.81	
Gd	36.9	37.1	36.5	37.2	36.6	36.56	38.3	**37**	0.63	
Tb	38	33	37.02	35.06	35.5	36.02	36	**35.8**	1.58	**40.0**
Dy	39.3	33.5	38.3	35.56	35.7	35.63	34.8	**36.1**	2.01	
Ho	39.3	37.3	38.4	37.81	38.23	37.45	37.5	**38**	0.70	**38.7**
Er	38	38	37.9	38	38	37.98	38	**38**	0.04	
Tm	38.8	37	38.9	37.9	39.3	37.5	37.3	**38.1**	0.90	
Yb	40.2	37.9	40	38.6	39.8	39	38.6	**39.2**	0.86	

Lu	37.5	36.1	37.5	36.66	37.9	36.8	36.4	**37**	0.66
Hf	47	33	45	33.84	35.5	35.3	35.3	**37.8**	5.67
Th	37.9	36.6	38.1	38.1	37.6	37.9	37.3	**37.6**	0.54
U	57.3	33.8	54.2	35.8	36.7	37.1	37.2	**41.7**	9.69

Standard	NIST610_1	NIST610_2	NIST610_3	NIST610_4	NIST610_5	**NIST610 av.**	std	**NIST610 ref**
P	105.2	104.5	130.4	127.5	165.4	**126.6**	24.8	
Ti	499	516	517	553	532	**523.4**	20.3	**434**
Sr	537	541	531	538	519	**533.2**	8.7	**497**
Y	462	472.3	466	453	448	**460.3**	9.8	**450**
Nb	500	506	490	484	478	**491.6**	11.4	
La	426	447	446.6	433	419	**434.3**	12.4	**457**
Ce	476	475	474	482	453	**472**	11.1	**448**
Pr	437	442	461	489	425	**450.8**	25.0	**430**
Nd	423	421	433	467	411	**431**	21.6	**430**
Sm	445	438	451	465	433	**446.4**	12.4	**449**
Eu	411	417	419	446	450	**428.6**	18	**460**
Gd	417	417.7	430	446	446	**431.3**	14.3	**420**
Tb	370	370	420	450	460	**414**	42.8	**442**
Dy	398	396	428	458	479	**431.8**	36.6	**426**
Ho	421	417	441	470	474	**444.6**	26.7	**448**
Er	425	428.3	422	472	442	**437.9**	20.6	**426**
Tm	429	422.4	439	457	450	**439.5**	14.3	**420**
Yb	433	425.2	442	464	455	**443.8**	15.8	**460**
Lu	439	423	433	447	440	**436.4**	9	**435**
Hf	394	375.9	398	417	420	**401.0**	18.1	**418**
Th	471	438	467	484	458	**463.6**	17.1	**451**
U	439	407.8	450	474	487	**451.6**	31	**457**

Standard	Z91500_1	Z91500_2	Z91500_3	Z91500_4	Z91500_5	**Z91500 av**	std	**Z91500 ref.**
P	Below LOD	28.1	35.7	34.5	Below LOD	**32.77**	4.09	
Ti	3.86	4.6	3.06	5.1	4.11	**4.15**	0.77	
Sr	Below LOD	Below LOD	Below LOD	Below LOD	Below LOD			
Y	34	33.6	28.79	31.1	32.26	**31.95**	2.11	
Nb	1.213	1.234	1.103	1.144	1.2	**1.18**	0.05	
La	Below LOD	Below LOD	Below LOD	Below LOD	Below LOD			
Ce	1.801	1.751	1.687	1.66	1.609	**1.70**	0.08	**1.9**
Pr	Below LOD	Below LOD	Below LOD	Below LOD	Below LOD			
Nd	0.05	0.042	0.05	0.032	0.031	**0.04**	0.01	**0.4**
Sm	0.112	0.106	0.098	Below LOD	0.112	**0.11**	0.01	**0.3**
Eu	0.0444	0.0419	0.044	0.049	0.045	**0.04**	0	**0.3**
Gd	0.385	0.388	0.43	0.44	0.39	**0.41**	0.03	**2**
Tb	0.158	0.16	0.1553	0.19	0.172	**0.17**	0.01	
Dy	2.48	2.55	2.269	2.51	2.78	**2.52**	0.18	**8**
Ho	1.09	1.06	1.02	1.06	1.19	**1.08**	0.07	
Er	6.06	6.28	5.67	5.63	6.06	**5.94**	0.28	**20**
Tm	1.546	1.64	1.42	1.47	1.59	**1.53**	0.09	
Yb	16.4	16.7	14.09	14.87	16.28	**15.67**	1.13	**46**
Lu	3.48	3.7	3.09	3.27	3.43	**3.39**	0.23	**12**
Hf	4800	5030	4950	5240	5390	**5082.**	234.24	**589**
Th	12.35	13.69	13.1	13	12.8	**12.99**	0.49	**37**
U	47	49.6	48.4	52.1	54.4	**50.3**	2.96	**< 11**

Reference values are from Jochum et al. (2011) for NIST 612, Gao et al. (2002) for NIST 610 and Wiedenbeck et al. (1995)

Appendix 9: U-Th-Pb zircon data (including standards) by LA-ICPMS

Spot	$^{207}Pb/^{235}U$	± 2σ	$^{206}Pb/^{238}U$	± 2σ	$^{207}Pb/^{206}Pb$	± 2σ	$^{207}U/^{235}Pb$ Age	± 2σ	$^{206}Pb/^{238}U$ Age	± 2σ	$^{207}Pb/^{206}Pb$ Age	± 2σ	discordance (%)	U_ppm	Th_ppm	Th/U
Syenite																
BX 01 - 2	2.17800	0.077	0.18450	0.003	0.08560	0.003	1171	25	1091	14	1326	36	17	30.18	12.10	0.40
BX 01 - 3	2.26700	0.054	0.19830	0.002	0.08220	0.002	1199	17	1166	12	1248	27	6	39.20	17.24	0.44
BX 01 - 4	2.22000	0.140	0.20030	0.006	0.08150	0.005	1184	45	1177	34	1225	53	4	58.60	23.46	0.40
BX 01 - 5	3.00500	0.075	0.20402	0.001	0.10690	0.003	1403	19	1197	5.3	1726	41	29	156.90	140.50	0.90
BX 01 - 6	2.34400	0.055	0.20600	0.003	0.08390	0.002	1225	17	1207	13	1285	26	7	69.80	47.20	0.68
BX 01 - 7	1.93900	0.031	0.16970	0.001	0.08200	0.001	1093	11	1010	7.7	1243	16	18	101.20	64.50	0.64
BX 01 - 8	1.40100	0.019	0.10417	0.001	0.09630	0.001	889	8	639	5.7	1550	18	59	472.20	173.30	0.37
BX 01 - 9	2.33400	0.028	0.20920	0.001	0.08073	0.001	1221	8.4	1224	6.7	1213	12	-1	80.20	79.99	1.00
BX 01 - 10	2.77000	0.170	0.19780	0.003	0.09930	0.006	1339	45	1163	14	1581	93	23	33.12	13.59	0.41
BX 01 - 11	2.32600	0.019	0.20840	0.001	0.08085	0.001	1220	5.7	1220	5.6	1214	7.9	-1	201.70	249.70	1.24
BX 01 - 12	2.25100	0.034	0.20250	0.002	0.08140	0.001	1196	11	1189	8.8	1228	21	3	104.80	101.20	0.97
BX 01 - 13	2.27200	0.067	0.19260	0.002	0.08360	0.002	1201	20	1135	13	1274	27	11	25.77	10.54	0.41
BX 01 - 14	2.28500	0.024	0.20550	0.001	0.08040	0.001	1207	7.4	1205	6.1	1207	13	0	66.70	45.47	0.68
BX 01 - 15	2.37500	0.031	0.21270	0.002	0.08090	0.001	1233	9.5	1243	8.3	1215	16	-3	48.53	20.25	0.42
BX 01 - 16	1.79000	0.032	0.14900	0.002	0.08570	0.002	1040	12	896	8.4	1325	27	32	91.20	36.95	0.41
BX 01 - 17	2.25300	0.027	0.20400	0.001	0.08108	0.001	1197	8.5	1197	7.5	1222	13	2	130.00	56.83	0.44
BX 01 - 18	2.30800	0.021	0.20661	0.001	0.08090	0.001	1214	6.3	1211	5.2	1218	10	0	130.10	108.00	0.83
BX 01 - 19	2.33500	0.021	0.20810	0.001	0.08138	0.001	1222	6.4	1218	6.7	1229	11	1	122.80	129.30	1.05
BX 01 - 20	2.34300	0.039	0.20900	0.002	0.08080	0.002	1223	12	1223	9	1213	19	-2	41.01	20.36	0.50
BX 01 - 21	12.99000	0.880	0.12590	0.007	0.73000	0.024	2663	68	764	41	4800	31	84	17.40	1.42	0.08
BX 01 - 22	14.50000	1.000	0.16400	0.014	0.68400	0.042	2781	72	972	79	4697	40	79	2.54	1.48	0.58
BX 01 - 23	2.33100	0.042	0.20900	0.002	0.08210	0.002	1221	13	1223	9.8	1240	25	1	117.90	88.90	0.75
BX 01 - 24	2.27900	0.045	0.20570	0.002	0.08020	0.002	1202	14	1205	8.3	1202	25	-2	21.90	10.38	0.47
BX 01 - 25	2.36200	0.027	0.21120	0.001	0.08033	0.001	1230	8	1235	6.6	1204	10	-3	206.00	145.80	0.71
BX 01 - 26	2.58200	0.037	0.20030	0.001	0.09330	0.001	1294	10	1177	7.3	1489	15	21	58.11	273.10	4.70
BX 01 - 27	2.29300	0.024	0.20610	0.001	0.08113	0.001	1209	7.4	1208	7	1223	10	1	107.10	61.80	0.58
BX 01 - 28	2.32100	0.021	0.20730	0.001	0.08106	0.001	1218	6.3	1214	5.4	1222	10	1	133.00	82.10	0.62
BX 01 - 29	2.20000	0.058	0.18070	0.002	0.08670	0.002	1178	18	1070	10	1349	27	20	36.79	15.91	0.43

Nepheline syenite																
SNT 04 - 1	2.31800	0.025	0.20730	0.002	0.07990	0.001	1217	7.7	1215	7.9	1196	15	-2	271.30	531.00	1.96
SNT 04 - 2	2.36100	0.038	0.20970	0.002	0.07990	0.001	1230	12	1227	11	1193	16	-3	116.90	265.60	2.27
SNT 04 - 3	2.35000	0.150	0.21930	0.007	0.07810	0.005	1225	45	1278	37	1147	76	-13	64.00	208.50	3.26
SNT 04 - 4	1.30200	0.042	0.12460	0.003	0.07690	0.002	844	18	757	15	1110	34	31	77.80	309.30	3.98
SNT 04 - 5	2.75000	0.180	0.21000	0.005	0.08960	0.006	1326	49	1228	26	1419	63	12	5.41	14.23	2.63
SNT 04 - 6	1.63200	0.082	0.14840	0.003	0.07880	0.004	970	32	891	15	1139	63	17	8.37	6.16	0.74
SNT 04 - 7	2.41900	0.066	0.21650	0.003	0.08000	0.002	1247	19	1263	14	1193	29	-6	97.00	200.20	2.06
SNT 04 - 8	2.33700	0.072	0.21220	0.003	0.07790	0.002	1222	22	1241	16	1144	40	-9	97.60	321.10	3.29
SNT 04 - 9	2.30200	0.026	0.20590	0.002	0.08054	0.001	1212	7.9	1207	7.9	1208	11	0	184.60	524.70	2.84
SNT 04 - 10	2.13000	0.110	0.19460	0.004	0.08040	0.004	1149	36	1146	19	1178	59	-1	6.10	4.77	0.78
SNT 04 - 11	2.25200	0.017	0.20330	0.001	0.08011	0.001	1198	5.4	1194	5.5	1199	6.6	0	217.50	462.00	2.12
SNT 04 - 12	2.29000	0.024	0.20550	0.001	0.07937	0.001	1209	7.4	1205	7.2	1181	13	-2	213.60	749.00	3.51
SNT 04 - 13	2.85000	0.100	0.23590	0.003	0.08810	0.003	1371	24	1365	17	1380	37	0	25.60	23.65	0.92
SNT 04 - 14	2.26200	0.014	0.20441	0.001	0.07990	0.000	1200	4.3	1199	4.5	1194	5.9	0	551.40	673.00	1.22
SNT 04 - 15	2.24200	0.026	0.20570	0.002	0.07977	0.001	1194	8.3	1206	12	1190	9.8	-1	346.70	1311.00	3.78
SNT 04 - 16	1.93000	0.100	0.15550	0.004	0.09160	0.005	1088	34	931	20	1434	65	32	6.75	3.82	0.57
SNT 04 - 17	2.42200	0.024	0.21250	0.001	0.08253	0.001	1249	7.1	1242	6.4	1258	8.9	1	261.90	951.00	3.63
SNT 04 - 18	2.26600	0.025	0.20340	0.001	0.08044	0.001	1202	7.5	1194	7.7	1209	11	1	113.90	215.00	1.89
SNT 04 - 19	4.67000	0.240	0.31910	0.008	0.10420	0.005	1747	42	1783	38	1691	54	-7	3.62	6.70	1.85
SNT 04 - 20	3.04000	0.200	0.20460	0.005	0.10020	0.006	1387	47	1198	25	1610	79	21	4.74	9.80	2.07
SNT 04 - 21	3.18400	0.084	0.24390	0.004	0.08910	0.002	1450	20	1407	21	1398	31	-1	44.20	28.60	0.65
SNT 04 - 22	2.28300	0.023	0.20530	0.001	0.08030	0.001	1206	7	1204	6	1201	9.1	0	126.60	166.50	1.32
SNT 04 - 23	2.20800	0.027	0.20010	0.003	0.08123	0.001	1183	8.6	1176	15	1226	15	4	333.80	879.00	2.63
SNT 04 - 24	2.27200	0.024	0.20410	0.001	0.08020	0.001	1203	7.5	1197	5.9	1205	12	0	82.00	191.10	2.33
SNT 04 - 25	2.18100	0.037	0.20000	0.002	0.07930	0.001	1174	12	1175	8.1	1170	18	-2	38.60	26.33	0.68
SNT 04 - 26	2.17800	0.096	0.19970	0.004	0.08030	0.004	1168	31	1173	21	1189	48	-2	6.00	5.87	0.98
SNT 04 - 27	2.29800	0.060	0.20380	0.002	0.08280	0.002	1208	19	1195	13	1258	25	4	29.45	44.48	1.51
SNT 04 - 28	2.44500	0.074	0.21790	0.003	0.07970	0.003	1255	23	1271	15	1181	38	-9	17.81	4.23	0.24
SNT 04 - 29	2.30000	0.130	0.20930	0.005	0.08060	0.006	1211	44	1224	25	1215	62	-4	7.15	0.81	0.11
SNT 04 - 30	2.30400	0.023	0.20620	0.001	0.08074	0.001	1212	7	1209	5.7	1214	11	0	103.80	200.40	1.93

SNT 04 - 32	2.23500	0.088	0.20480	0.003	0.07810	0.003	1185	28	1200	15	1142	46	-7	11.49	7.44	0.65
SNT 04 - 33	2.50000	0.120	0.21200	0.005	0.08530	0.004	1263	35	1239	28	1326	62	3	10.63	12.82	1.21
SNT 04 - 34	0.91000	0.083	0.10040	0.010	0.06900	0.004	663	49	614	56	885	67	26	45.00	0.23	0.01
SNT 04 - 35	2.42000	0.180	0.21790	0.006	0.07900	0.006	1224	53	1276	32	1110	110	-36	4.89	1.14	0.23
SNT 06 - 1	2.11800	0.031	0.18890	0.002	0.08220	0.001	1154	10	1115	9.3	1253	14	11	82.70	90.30	1.09
SNT 06 - 2	3.75500	0.078	0.25960	0.004	0.10430	0.002	1582	17	1487	20	1699	25	12	57.40	32.60	0.57
SNT 06 - 3	1.66800	0.024	0.13360	0.002	0.09197	0.001	996	9.2	808	11	1466	11	45	537.00	420.50	0.78
SNT 06 - 4	2.15300	0.027	0.19700	0.002	0.08030	0.001	1166	8.8	1159	11	1203	9.9	4	156.90	240.50	1.53
SNT 06 - 5	0.78300	0.038	0.07460	0.001	0.07640	0.004	584	21	464	7.5	1083	58	55	36.76	33.08	0.90
SNT 06 - 6	0.93100	0.030	0.08570	0.002	0.08020	0.001	667	15	530	12	1202	18	56	454.00	558.00	1.23
SNT 06 - 7	1.61700	0.026	0.14970	0.002	0.07930	0.001	976	10	899	11	1184	18	24	300.00	157.60	0.53
SNT 06 - 8	0.98600	0.024	0.09024	0.001	0.07920	0.002	695	12	557	5.3	1169	26	52	46.99	31.55	0.67
SNT 06 - 9	1.54000	0.028	0.13970	0.001	0.07910	0.001	945	11	843	7.8	1176	18	28	82.70	23.40	0.28
SNT 06 - 10	1.27200	0.036	0.11370	0.002	0.08230	0.002	831	16	694	12	1244	28	44	79.40	17.20	0.22
SNT 06 - 11	0.51800	0.019	0.04690	0.002	0.08040	0.002	420	13	295	9.5	1199	26	75	77.30	21.04	0.27
SNT 06 - 12	2.28800	0.032	0.20630	0.002	0.08119	0.001	1207	9.9	1209	10	1225	13	1	99.60	65.70	0.66
SNT 06 - 13	1.78000	0.100	0.16770	0.004	0.07590	0.004	1029	36	999	22	1082	58	5	10.31	7.58	0.74
SNT 06 - 14	2.25800	0.027	0.20670	0.003	0.08070	0.001	1199	8.6	1211	14	1213	13	0	228.30	27.13	0.12
SNT 06 - 15	2.27400	0.025	0.20560	0.002	0.07983	0.001	1203	7.8	1205	8.4	1196	7.3	-1	253.10	34.70	0.14
SNT 06 - 16	1.95400	0.036	0.17530	0.002	0.08150	0.002	1098	13	1041	9.8	1225	21	14	92.30	34.61	0.37
SNT 06 - 17	1.79400	0.033	0.16370	0.002	0.07980	0.001	1042	12	977	11	1192	20	18	150.40	99.20	0.66
SNT 06 - 19	1.75600	0.032	0.15890	0.002	0.08120	0.001	1028	12	951	12	1234	18	23	169.90	93.70	0.55
SNT 06 - 20	1.09900	0.050	0.09660	0.003	0.08350	0.004	748	24	594	17	1267	45	52	22.90	4.98	0.22
SNT 06 - 21	0.55300	0.013	0.05420	0.001	0.07210	0.001	447	8.1	340	5.8	990	18	65	651.00	979.00	1.50
SNT 06 - 22	0.79200	0.031	0.07140	0.003	0.08150	0.002	590	17	444	15	1238	24	64	368.00	407.00	1.11
SNT 06 - 23	1.07000	0.110	0.06590	0.004	0.11500	0.012	728	53	411	21	1840	120	77	8.16	1.48	0.18
SNT 06 - 24	1.34100	0.015	0.11750	0.001	0.08183	0.001	863	6.4	716	7.6	1241	9.1	42	398.30	471.30	1.18
SNT 06 - 25	2.15900	0.032	0.18210	0.002	0.08118	0.001	1167	10	1078	11	1225	13	12	235.80	565.10	2.40
SNT 06 - 26	1.70800	0.045	0.15970	0.002	0.07910	0.002	1009	17	955	13	1176	31	18	32.56	8.62	0.26
SNT 06 - 27	2.08900	0.025	0.19060	0.002	0.08079	0.001	1145	8.1	1124	9.4	1216	11	8	210.10	158.00	0.75
Carbonatite																

EC 21 - 1	1.77300	0.100	0.09620	0.003	0.13560	0.008	1027	36	592	20	2153	58	73	10.05	1.84	0.18
EC 21 - 2	1.17500	0.051	0.06930	0.002	0.12310	0.005	781	24	432	10	1998	40	81	16.20	3.30	0.20
EC 21 - 3	1.28300	0.078	0.10490	0.003	0.08970	0.006	828	33	643	16	1366	76	29	10.55	6.28	0.60
EC 21 - 4	1.79000	0.069	0.13850	0.003	0.09350	0.003	1032	25	836	16	1477	41	23	21.60	57.34	2.65
EC 21 - 5	2.27500	0.066	0.20510	0.004	0.08120	0.002	1202	21	1202	20	1209	31	0	13.24	89.30	6.74
EC 21 - 6	2.23900	0.091	0.20380	0.004	0.08050	0.003	1182	29	1195	22	1209	44	-1	6.69	5.19	0.78
EC 21 - 7	2.45000	0.150	0.19980	0.005	0.08990	0.006	1213	47	1172	28	1425	68	3	3.01	27.10	9.00
EC 21 - 8	2.47000	no data	0.21060	no data	0.08540	no data	1269	no data	1231	no data	1309	no data	3	9.89	100.00	10.11
EC 21 - 9	2.22600	0.055	0.19970	0.003	0.08090	0.002	1184	17	1173	18	1210	23	1	27.29	84.30	3.09
EC 21 - 10	2.56000	0.160	0.20790	0.005	0.09040	0.006	1236	50	1215	29	1378	66	2	2.78	15.10	5.44
EC 21 - 11	2.71000	0.240	0.21090	0.008	0.09650	0.008	1261	70	1234	42	1490	92	2	1.66	1.73	1.04
EC 21 - 12	2.44200	0.063	0.20940	0.004	0.08500	0.002	1252	19	1225	19	1311	23	2	25.87	26.30	1.02
EC 21 - 13	2.19000	0.110	0.19920	0.004	0.08010	0.004	1162	34	1171	23	1167	53	-1	6.29	3.56	0.57
EC 21 - 14	2.58000	0.430	0.20700	0.013	0.09500	0.016	1150	120	1204	65	1770	140	-4	0.74	3.43	4.63
EC 21 - 15	2.22000	0.110	0.20210	0.004	0.08030	0.004	1169	34	1186	24	1168	57	-1	5.69	3.59	0.63
EC 21 - 16	2.30800	0.092	0.20030	0.004	0.08370	0.003	1199	29	1176	21	1276	44	2	9.41	18.00	1.91
EC 21 - 17	1.05000	0.110	0.07600	0.003	0.10200	0.011	700	56	472	18	1620	120	48	6.32	3.68	0.58
EC 21 - 18	2.82000	0.360	0.21080	0.010	0.10100	0.014	1298	95	1228	53	1770	130	6	0.72	0.33	0.45
EC 21 - 19	2.90000	0.380	0.22010	0.010	0.10200	0.014	1190	130	1275	53	1750	130	-7	0.82	171.70	209.65
EC 21 - 20	0.57300	0.057	0.04640	0.002	0.09220	0.010	440	38	292	11	1420	110	51	7.26	23.30	3.21
EC 21 - 21	3.69000	0.670	0.27600	0.020	0.10700	0.021	1360	190	1555	99	1960	200	-13	0.50	1.04	2.07
EC 21 - 22	1.34100	0.094	0.05630	0.002	0.17300	0.011	858	42	353	12	2578	62	143	28.86	285.90	9.91
EC 21 - 23	2.75400	0.110	0.18520	0.004	0.10830	0.004	1334	28	1095	21	1752	43	22	16.35	27.07	1.66
EC 21 - 24	2.16100	0.089	0.13860	0.004	0.11320	0.004	1153	28	836	20	1842	34	38	13.21	16.81	1.27
EC 21 - 25	2.31100	0.039	0.20587	0.003	0.08128	0.001	1215	12	1207	17	1227	9.8	1	174.50	582.00	3.34
EC 21 - 26	1.38500	0.081	0.11950	0.003	0.08560	0.005	855	34	727	16	1279	61	18	4.78	5.65	1.18
EC 21 - 27	2.26200	0.039	0.20529	0.003	0.07993	0.001	1200	12	1204	17	1195	10	0	150.20	666.00	4.43
EC 21 - 28	4.25000	0.160	0.21790	0.005	0.14190	0.006	1666	31	1270	24	2226	41	31	6.89	1.12	0.16
EC 21 - 29	2.35100	0.090	0.20560	0.004	0.08370	0.003	1215	28	1205	21	1267	41	1	7.85	0.78	0.10
EC 21 - 30	2.63000	0.250	0.18470	0.007	0.10500	0.011	1284	70	1091	40	1690	100	18	5.16	402.50	78.00
EC 21 - 31	11.45000	0.260	0.62600	0.014	0.13275	0.001	2556	22	3124	58	2137	5.6	-18	182.80	69.90	0.38

EC 21 - 32	10.16000	0.640	0.62300	0.031	0.11830	0.004	2431	60	3110	120	1933	37	-22	14.50	3.76	0.26
EC 21 - 33	1.74200	0.050	0.14900	0.003	0.08500	0.002	1018	19	895	16	1303	27	14	21.55	22.98	1.07

Spot	$^{207}Pb/^{235}U$	± 2σ	$^{206}Pb/^{238}U$	± 2σ	$^{207}Pb/^{206}Pb$	± 2σ	$^{207}U/^{235}Pb$ Age	± 2σ	$^{206}Pb/^{238}U$ Age	± 2σ	$^{207}Pb/^{206}Pb$ Age	± 2σ	discordance (%)	U_ppm	Th_ppm	Th/U
Ples - 1	0.3939	0.0081	0.0535	0.00051	0.0523	0.0011	336.8	6	335.9	3.1	302	23	-24	239.2	26.31	0.11
Ples - 2	0.3911	0.0055	0.05354	0.00035	0.05292	0.00074	334.9	4	336.2	2.2	327	17	-10.3	258.5	27.91	0.11
Ples - 3	0.3979	0.0078	0.05346	0.0004	0.053	0.001	339.8	5.7	335.7	2.5	328	23	-14	246.2	26.96	0.11
Ples - 4	0.3976	0.0064	0.05343	0.00034	0.05428	0.00093	339.6	4.6	335.5	2.1	377	25	-2.2	261.1	27.87	0.11
Ples - 5	0.3945	0.0053	0.05377	0.00033	0.05313	0.00072	337.4	3.9	337.6	2	334	18	-15.9	256.2	27.41	0.11
Ples - 6	0.3938	0.0059	0.05373	0.00031	0.05335	0.00079	336.8	4.3	337.4	1.9	344	20	-17	261.7	28.44	0.11
Ples - 7	0.395	0.011	0.05423	0.00059	0.0532	0.0013	337.8	7.9	340.4	3.6	335	31	-13	264.8	29.55	0.11
GJ-1 - 1	0.7967	0.009	0.09747	0.00055	0.05934	0.00064	594.5	5.1	599.6	3.2	575	14	-6.3	280.1	9.26	0.03
GJ-1 - 2	0.8026	0.0083	0.09876	0.00047	0.05896	0.00059	597.9	4.7	607.1	2.7	564	13	-10.1	292.1	9.7	0.03
GJ-1 - 3	0.8605	0.0088	0.09842	0.00058	0.06348	0.00063	630.6	4.9	605.1	3.4	723	13	15.5	288.7	9.59	0.03
GJ-1 - 4	0.8093	0.0076	0.0986	0.00053	0.05962	0.00058	602.3	4.4	606.2	3.1	591	12	-4.1	286.2	9.41	0.03
GJ-1 - 5	0.8218	0.0074	0.09655	0.00052	0.06182	0.00062	608.8	4.1	594.1	3.1	665	12	10.3	282.6	9.44	0.03
GJ-1 - 6	0.811	0.008	0.09722	0.00053	0.06038	0.00056	602.6	4.5	598	3.1	617	10	2	297.1	9.75	0.03
GJ-1 - 7	0.815	0.0082	0.09725	0.00052	0.06075	0.00061	604.9	4.6	598.3	3.1	626	12	4.3	284.6	9.38	0.03
GJ-1 - 8	0.8212	0.0086	0.09755	0.00054	0.06098	0.00064	608.3	4.8	600	3.2	636	14	4.2	285.6	9.5	0.03
GJ-1 - 9	0.8085	0.0079	0.0979	0.00047	0.05985	0.00061	601.2	4.5	602.1	2.8	596	13	-2.9	293.4	9.8	0.03
GJ-1 - 10	0.8011	0.0079	0.09781	0.00057	0.05947	0.00061	597.6	4.5	601.5	3.3	582	13	-5	296.4	9.83	0.03
GJ-1 - 11	0.8042	0.009	0.09759	0.00056	0.05969	0.00059	598.7	5	600.2	3.3	594	14	-2.9	297.9	9.77	0.03
GJ-1 - 12	0.8292	0.0083	0.09836	0.00048	0.0611	0.00065	612.8	4.6	604.8	2.8	641	15	3.8	280.6	9.09	0.03
GJ-1 - 13	0.8024	0.0085	0.09776	0.00054	0.05955	0.00058	598.3	4.9	601.2	3.2	588	12	-3.9	280.7	9.2	0.03
GJ-1 - 14	0.8189	0.0092	0.09867	0.00055	0.06026	0.00063	606.9	5.1	606.6	3.2	610	13	-1.2	290.5	9.81	0.03
GJ-1 - 15	0.8367	0.009	0.09817	0.00056	0.06196	0.00068	616.9	5	603.7	3.3	673	14	9.8	269.6	8.96	0.03
GJ-1 - 16	0.8025	0.0083	0.09686	0.00052	0.06007	0.00058	597.8	4.7	595.9	3	607	11	0.7	282.6	9.29	0.03
GJ-1 - 17	0.82	0.008	0.09832	0.00049	0.06064	0.00054	607.7	4.5	604.5	2.9	624	11	1.8	307.8	10.13	0.03
91500 - 1	1.828	0.048	0.1791	0.0017	0.0734	0.002	1055	17	1062	9	1026	34	-6.8	24.9	7.24	0.29

91500 - 2	1.86	0.055	0.1806	0.0019	0.0748	0.0022	1063	20	1070	10	1055	35	-2.9	27.09	7.85	0.29
91500 - 3	1.857	0.082	0.1791	0.0029	0.0765	0.0035	1062	30	1062	16	1100	54	1.2	30.6	8.84	0.29
91500 - 5	1.87	0.045	0.1795	0.0016	0.0762	0.0019	1066	16	1064.3	8.8	1089	32	0	25.79	7.42	0.29
91500 - 6	1.859	0.071	0.1808	0.0024	0.0758	0.0028	1063	25	1071	13	1078	40	-1.2	28.73	8.24	0.29

Appendix 10: Zircon Lu-Hf data by LA-MC-ICPMS

Spot	$^{176}Hf/^{177}Hf$	1SE	$^{176}Lu/^{177}Hf'$	1SE	$\varepsilon_{Hf(t)}$	1SE
Syenite zircon						
BX 01-9	0.282090	0.000011	0.001604	0.000003	1.5	0.4
BX 01-20	0.282045	0.000011	0.000556	0.000001	0.8	0.4
BX 01-19	0.282049	0.000011	0.000703	0.000004	0.5	0.4
Nepheline syenite type 1 zircon						
SNT 04-1	0.282112	0.000011	0.001147	0.000002	2.4	0.4
SNT 04-9	0.282096	0.000013	0.001274	0.000001	1.7	0.5
SNT 05-5	0.282103	0.000011	0.000649	0.000000	2.5	0.4
SNT 09-4	0.282088	0.000011	0.000245	0.000005	2.3	0.4
Nepheline syenite type 2 zircon						
SNT 06-14	0.282073	0.000013	0.000420	0.000004	1.6	0.4
SNT 06-21	0.282136	0.000015	0.001830	0.000003	2.7	0.5
SNT 07-10	0.282070	0.000009	0.000102	0.000003	1.8	0.3
SNT 06-13	0.282068	0.000012	0.000139	0.000003	1.7	0.4
SNT 07-14	0.282101	0.000013	0.000388	0.000008	2.6	0.5
Carbonatite zircon						
EC 21-5	0.282076	0.000004	0.000168	0.000006	1.9	0.2
EC 21-6	0.282073	0.000004	0.000229	0.000001	1.8	0.1

EC 21-13	0.282087	0.000004	0.000167	0.000002	1	0.2
EC 21-15	0.282081	0.000004	0.000316	0.000004	1.1	0.2
EC 21-25	0.282081	0.000007	0.001526	0.000001	1.4	0.2
EC 21-27	0.282061	0.000012	0.000862	0.000005	0.5	0.4

Standard	$^{176}Hf/^{177}Hf$	1SE	$^{176}Lu/^{177}Hf'$	1SE	$\varepsilon_{Hf(t)}$	1SE
Mud Tank-1	0.282505	0.000007	0.000032	0.000000	6.4	0.2
Mud Tank-2	0.282518	0.000008	0.000035	0.000000	6.9	0.3
Mud Tank-3	0.282507	0.000009	0.000032	0.000000	6.5	0.3
Mud Tank-4	0.282517	0.000008	0.000032	0.000000	6.9	0.3
av Mud Tank (1SD)	**0.2825118**	**0.000007**				
Mud Tank reference	**0.282507**	**0.000006**				
Temora-1	0.282663	0.000008	0.000917	0.000006	4.7	0.3
Temora-2	0.28267	0.00001	0.001737	0.000008	4.8	0.3
Temora-3	0.282672	0.000011	0.001759	0.000003	4.8	0.4
Temora-4	0.282674	0.000009	0.00148	0.000008	5	0.3
Temora-5	0.28267	0.00001	0.000886	0.000001	5	0.3
Temora-6	0.282693	0.000011	0.001372	0.000002	5.7	0.4
Temora-7	0.282683	0.000012	0.001404	0.000002	5.3	0.4
av Temora (1SD)	**0.282675**	**0.000010**				
Temora reference	**0.282671**	**0..000008**				
LV11-1	**0.282834**	**0.000007**	**0.002059**	**0.000001**	**7.8**	**0.3**

LV11 reference	**0.282801**	**0.000009**

Reference values from Woodhead and Hergt (2005) for Mud Tank and Temora, while LV11 is from Heinonen et al. (2010)